WARRIP
WESTERN AUSTRALIAN ROAD RESEARCH
AND INNOVATION PROGRAM

Evaluation and characterisation of nanosilica-modified asphalt materials

2018-005

Final Report

AN INITIATIVE BY:

THE GOVERNMENT OF WESTERN AUSTRALIA
mainroads
WESTERN AUSTRALIA
arrb

Evaluation and characterisation of nanosilica-modified asphalt materials

2018-005

for Main Roads Western Australia

Reviewed

Project Leader

James Grenfell

Quality Manager

Elsabe van Aswegen

PRP18049-
March 2020

ABN 68 004 620 651

Victoria
500 Burwood Highway
Vermont South VIC 3133
Australia
P: +61 3 9881 1555
F: +61 3 9887 8104
info@arrb.com.au

Western Australia
191 Carr Place
Leederville WA 6007
Australia
P: +61 8 9227 3000
F: +61 8 9227 3030
arrb.wa@arrb.com.au

New South Wales
2-14 Mountain St
Ultimo NSW 2007
Australia
P: +61 2 9282 4444
F: +61 2 9280 4430
arrb.nsw@arrb.com.au

Queensland
21 McLachlan St
Fortitude Valley QLD 4006
Australia
P: +61 7 3260 3500
F: +61 7 3862 4699
arrb.qld@arrb.com.au

South Australia
Level 11,
101 Grenfell Street
Adelaide SA 5000
Australia
P: +61 8 7200 2659
F: +61 8 8223 7406
arrb.sa@arrb.com.au

SUMMARY

Nanotechnology is enabling innovative approaches in science and engineering. Nanosized particles can be developed and utilised to create or manipulate existing or new properties of materials.

Nanoparticles alter the engineering properties of material, because as the particle size reduces, it results in a change in surface energies and interaction between particle matrixes.

This study aimed to systematically review available data in numerous sources, focussing on nanosilica (NS) improved bitumen binder.

From the literature review, the following was concluded:

- The experimental data does not show any controversial results, and there is general agreement when performance parameters are evaluated.
- Achieving a balance between cohesion and adhesion of aggregate and bitumen is a good approach to determine the optimal NS content. However, asphalt mix performance tests are the main criteria to indicate the optimal NS content.
- Details of mixing methods indicate that the best method depends upon achieving a balance between dispersion qualities and ageing, which may occur during mixing.

During the study, bitumen binder properties such as penetration, softening point, rutting resistance and fatigue resistance were evaluated. Binders investigated were virgin class C320, C600 and polymer modified A15E binder. Four ageing conditions were evaluated, namely unaged, short-term rolling thin film oven (RTFO) aged, long-term 3 x RTFO and pressure ageing vessel (PAV) aged.

Some of the key conclusions from the study and the experimental work are:

- The addition of NS causes bitumen binder to become stiffer and more viscous. The results obtained from penetration tests for all samples before ageing, after RTFO ageing and after 3 x RTFO ageing show a similar decreasing trend.
- The enhancements in viscosity vary from 15% (for 2% NS 60 nm) to 55% (for 6% NS 60 nm) in the unaged condition with respect to virgin C320.

  For wet mixed samples, the viscosity increases are typically between 20% and 140% (for 2% NS 20 nm with couplant), depending on the NS content. The larger the NS, the higher the viscosity for the NS-modified C320.
- The larger size of NS (i.e. 60 nm) results in an increase of the complex shear modulus (G*). However, the use of the couplant with the 20 nm NS is highly effective to offset the size effect by increasing G* even more than the 60 nm NS without couplant. This effect is only observed for the unaged or RTFO aged condition. In the PAV aged condition, the 60 nm NS is superior to the 20 nm NS with couplant.

- The increases in G* vary from 10% (for 6% NS 20 nm) to 45% (for 6% NS 20 nm with couplant) in the unaged condition with respect to virgin C320. Significant increases in G* are seen for frequencies either higher than 100 Hz or lower than 0.01 Hz.
- NS-modified C320 batches generally have lower G* than C600 or A15E. However, after PAV ageing, these exhibit a higher G* than C600 or A15E.
- Considering only G*, the optimum dosage of NS is between 4% and 6% considering all ageing conditions. The wet mixing method shows the biggest increase in G* at 6%.
- The most suitable NS size is 60 nm. However, the use of a couplant is likely to increase its performance even more.
- The results support the claim that wet mixed samples are better for dispersion efficiency, which is inherently poor for nanoparticles that tend to agglomerate. This finding is based on evidence from both mechanical tests and scanning electron microscope (SEM) observations.
- Dry mixed samples do not show consistent trends during rheological testing. Thus, the findings in the literature involving uniform trends for dry mixes cannot be verified. This can be attributed to the efficiency of different mixers or the quality of the dry mixing process and agglomeration of particles. An advanced Silverson mixer was used in this testing to ensure the highest quality mixes.
- A field emission gun scanning electron microscope (FEGSEM) with a cryogenic stage was shown to be a good tool to directly monitor the binders under different conditions. The observation of the dispersion quality of NS within the modified binders was a unique aspect of this research.
- The dynamic shear rheometer (DSR) results for binders blended with NS showed an increase in the G*/Sin(δ) parameter, which is indicative of an increased resistance to rutting.
- The increase of G*/Sin(δ) or decrease in the complex shear compliance (J_{nr}) value in the multiple stress creep recovery (MSCR) test indicates that NS particles can reduce rutting by about 25% to 45%.
- The fatigue parameter (G*.sinδ) has a direct relationship with NS content. NS seems to make the binder more rigid. However, this finding cannot be confirmed without fatigue tests on real asphalt mixtures.

Some areas of future work have been highlighted below.

Asphalt mix testing

- Consider three mix designs for each NS of asphalt mixes with a maximum nominal aggregate size of 20 mm (AC20); the testing will include the following:
  - Marshall testing for 10 samples (stability and flow changes)
  - 4-point bending beam testing, which will provide flexural modulus and fatigue performance data. It will be important to undertake this at standard conditions to give comparative data, but also at lower temperatures than standard to determine the effects at low temperatures, where fatigue becomes the definitive failure mode (for 10 samples)
  - Hamburg wheel tracking tests to determine rutting resistance for 10 samples
  - large wheel tracking tests to determine rutting resistance for 10 samples
  - indirect tensile testing (ITS) which will give data on the resilient modulus of different mixes for 10 samples
  - development of master curves using the asphalt mix performance tester (AMPT) dynamic modulus test results for 10 samples.

Trial section construction and testing

- The trial section will consist of the construction of an asphalt layer consisting of NS. All aspects of the asphalt production, paving and post-construction testing will be evaluated. The details of this stage are not contained in this report and will be outlined in a detailed project plan to be developed at the time.

CONTENTS

1 INTRODUCTION 1
1.1 Background 1
1.2 Scope and Objectives 1
1.3 Structure of the Report 2
2 BITUMEN COMPOSITION 3
3 MICROSTRUCTURE OF BITUMEN 6
3.1 Colloidal model 6
3.2 Dispersed fluid model 8
4 BITUMEN PROPERTIES 9
4.1 Ageing 9
4.2 Rutting and fatigue 9
4.3 Adhesion and cohesion 10
5 FEATURES OF NANOSILICA 13
6 EFFECTS OF COUPLANT 15
7 MIXING CONDITION 16
7.1 Dry or wet 16
7.2 Temperature and speed of stirring 17
8 ADVANCED OBSERVATION TECHNIQUES 18
8.1 Commonly used 18
8.2 Thermogravimetric analysis (TGA) 21
8.3 Differential scanning calorimetry (DSC) 21
8.4 Gel permeation chromatography (GPC) 21

ACKNOWLEDGEMENTS

The authors would like to thank Meda Sicoe, Technical Manager of Downer Group for her participation and support, especially in terms of access to Downer's bitumen testing facilities. Without her passionate participation, the tests could not have been successfully conducted in time.

8.5 Nuclear magnetic resonance analysis (NMR) 21

8.6 X-ray fluorescence spectroscopy 22

8.7 Scanning electron microscopy 23

8.8 Atomic force microscopy 25

9 MICROSTRUCTURAL INTERACTION OF NANOSILICA AND BITUMEN 27

10 SUMMARY OF RESULTS FOR NS-MODIFIED BITUMINOUS MIXES 28

11 IMPORTANT LESSONS FROM THE LITERATURE REVIEW 32

12 METHODOLOGY 33

12.1 Introduction 33

12.2 Materials 33
- *12.2.1 Bitumen 33*
- *12.2.2 Nanosilica 33*
- *12.2.3 Details of batches 34*

12.3 Sample Preparation 35
- *12.3.1 Dry mixing method 35*
- *12.3.2 Wet mixing method 36*
- *12.3.3 Short-term ageing (RTFO) 41*
- *12.3.4 Long-term ageing (PAV) 42*
- *12.3.5 Long-term ageing (3 x RTFO) 42*

12.4 Experimental procedures 42
- *12.4.1 Penetration test 43*
- *12.4.2 Viscosity tests 44*
- *12.4.3 Softening point 44*
- *12.4.4 Dynamic shear rheometry 44*
- *12.4.5 Strain sweep 47*
- *12.4.6 Multiple stress creep recovery test 48*
- *12.4.7 SARA determination by column chromatography 49*
- *12.4.8 Microstructural observations 49*

12.5 Master Curves 55
- *12.5.1 Introduction 55*
- *12.5.2 Shift factor 55*
- *12.5.3 Master curve construction 56*

12.6 Black Diagrams 57

13 RESULTS AND DISCUSSION 59

13.1 Penetration test 59

13.2 Softening Point 60

13.3 Viscosity 60

13.4 RTFO Weight Loss 62

13.5 Strain Sweep 62

13.6 Master Curves of Complex Modulus 62
13.6.1 Dry mixes 63
13.6.2 Wet mixes 63

13.7 Rutting or Durability 64

13.8 Creep compliance 64

13.9 Fatigue Cracking Resistance 67

13.10 Black Diagrams 68

13.11 Chemical Analysis of C320 69

13.12 SEM images 69
13.12.1 Equipment 69
13.12.2 Observations 69

13.13 Ageing tests by FTIR 71

14 CONCLUSIONS 74

REFERENCES 76

APPENDIX A MRWA WA 716.1 2018, BITUMEN DURABILITY: DYNAMIC SHEAR RHEOMETER METHOD.TYPICAL OUTPUTS FROM SWEEP TESTS .. 82
APPENDIX B MASTER CURVES 91
APPENDIX C SUMMARY OF RHEOLOGY 134
APPENDIX D TYPICAL OUTPUTS FROM MSCR TESTS 154
APPENDIX E BLACK DIAGRAMS 157
APPENDIX F IMAGING 175

TABLES

Table 5.1: Summary of nanomodifications for asphalt mixtures 14
Table 7.1: Mixing details in the literature 16
Table 8.1: Observation techniques for nanomodified binders 18
Table 8.2: Methods for asphalt fractioning 20
Table 10.1: Summary of NS application in asphalt mixtures 29
Table 10.2: Summary of results obtained for NS effects (indicative %) 30
Table 10.3: Summary of test methods utilised during NS effects investigations 31
Table 12.1: Silicon oxide nanopowder SiO_2 certificate of analysis 33
Table 12.2: Physical properties of silicon oxide nanopowder SiO_2 34
Table 12.3: Mixture details for dry mixes 34
Table 12.4: Mixture details for wet mixes 35
Table 12.5: Penetration result for validity 43
Table 12.6: Target limits of $G^*/\sin(\delta)$ 47
Table 12.7: Solvents for SARA fractioning 49
Table 13.1: Penetration test 59
Table 13.2: Softening point (°C) 60
Table 13.3: Viscosity for unaged samples 61
Table 13.4: Viscosity for RTFO samples 61
Table 13.5: Weight loss for RTFO samples 62
Table 13.6: J_{nr} values for unaged bitumen 64
Table 13.7: J_{nr} values for RTFO aged bitumen 65
Table 13.8: J_{nr} values for PAV aged bitumen 65
Table 13.9: J_{nr} values for wet mixed unaged condition 66
Table 13.10: J_{nr} values for the 3 x RTFO condition 66
Table 13.11: Summary of DSR tests in the 3 x RTFO condition 68
Table 13.12: SARA fractions 69

FIGURES

Figure 2.1: Typical example of SARA fractions in bitumen 4
Figure 2.2: Maltene fractions 4
Figure 2.3: Sol model of bitumen 5
Figure 3.1: Concept for colloidal model 6
Figure 3.2: Microstructure of bitumen 7
Figure 3.3: Modified Yen model 7
Figure 3.4: Aggregation of asphaltenes leads to the formation of micelles with a lower solubility parameter 8
Figure 4.1: Sample preparation: (a) binder droplets (b) contact angle measurements 11
Figure 5.1: Schematic of nanoclay interactions with hydrocarbon molecules 13
Figure 6.1: Molecular structure of branch and linear styrene-butadiene-styrene (SBS) 15
Figure 8.1: Sample bitumen FTIR spectrum 19
Figure 8.2: Sample GPC spectrum 21
Figure 8.3: Sample NMR spectrum 22
Figure 8.4: Sample X-ray fluorescence spectroscopy spectrum 23
Figure 8.5: Interaction volume and various emissions 24
Figure 8.6: Elements of a scanning electron microscope 24
Figure 8.7: Interactions of the electron beam with atoms in the sample 25
Figure 8.8: Backscattered electrons 25

Figure 8.9: Sample AFM image ... 26
Figure 12.1: Silverson high-shear mixer ... 36
Figure 12.2: Wet mixes with 20% solvent ... 37
Figure 12.3: 20% solvent loss within C320 bitumen ... 37
Figure 12.4: NS60 nm and C320 bitumen master batch ... 38
Figure 12.5: NS 60 nm master batch sample ... 39
Figure 12.6: Virgin bitumen (75 mg) in commercial kerosene at 25 °C (t = 0.0 min.) ... 39
Figure 12.7: Complete dissolution of virgin bitumen in commercial kerosene at 25 °C (t = 12.0 min.) ... 40
Figure 12.8: Compatibility of nanosilica samples with kerosene ... 40
Figure 12.9: Nanosilica-turpentine gel – in dried condition ... 41
Figure 12.10: Rolling thin film oven (RTFO) ... 41
Figure 12.11: Rotating bottle carriage of RTFO ... 42
Figure 12.12: Penetrometer ... 43
Figure 12.13: Dynamic shear rheometer ... 45
Figure 12.14: DSR test ... 46
Figure 12.15: Creep concept ... 48
Figure 12.16: Soxhlet extraction facility ... 50
Figure 12.17: Asphaltene particles with NS particles ... 51
Figure 12.18: SEM equipped with a cryogenic stage (Zeiss 1555 VP-FESEM) ... 52
Figure 12.19: Rivets plunged in sample ... 52
Figure 12.20: Sample preparation for freezing ... 53
Figure 12.21: Fractured bitumen sample in the SEM ... 53
Figure 12.22: Distribution of elements in EDS layered image ... 54
Figure 12.23: X-ray spectrum of elements measured by EDS ... 54
Figure 12.24: X-ray imaging sample preparation ... 55
Figure 13.1: FTIR test results of unaged or RTFO aged (sample BTD4) nanosilica-modified bitumen ... 72
Figure 13.2: FTIR test results on RTFO and PAV aged nanosilica-modified binders ... 73

1 INTRODUCTION

1.1 Background

Nanotechnology is paving the way for innovative approaches in science and engineering. Its application covers different fields, including material improvement, drug delivery systems, biotechnology, food packaging and computer microchips. Nanotechnology is applicable where nanosized particles can be developed and utilised to create or manipulate the existing or new properties of materials.

Nanomaterials lead to development in understanding, characterisation and optimisation of engineering products. They support material science with the identification and managing of factors which are effective in chemical, physical and mechanical interactions at the molecular level. As a result, it would be possible to control the product fabrication or production steps more intelligently. It is possible they could improve the key properties of engineered materials.

In pavement engineering, application of this technology typically involves the following:

- self-sensing concrete pavement with piezoresistive multi-walled carbon nanotubes (MWNTs) for traffic monitoring (Han & Ou 2007)
- luminescent concrete pavements for safe roads by nanophosphors (Steyn 2008)
- air purifying pavements with titanium dioxide (TiO_2) (Murata et al. 1998)
- sustainable and perpetual asphalt pavements by minimising the usage of natural resources and increasing durability (Maher et al. 2006).

The last item consists of multiple nanoparticles such as carbon nanotubes (CNT), silica, alumina, magnesium, calcium, iron oxide and TiO_2 which have been the subject of research in recent years (Yang & Tighe 2013). These nanoparticles are applied to improve properties such as rutting, fatigue, ageing and storage stability of bitumen binder blends. The reasons for these changes are attributed to high functional density, high sensitivity, special surface effects, large surface area, high strain resistance, and catalytic effects of nanoparticles. These all influence directly or indirectly the nano-scale chemical interactions (Teizer et al. 2011). In other words, the alteration of the engineering properties of the material can occur as the particle size reduces, which results in the change in surface energies and interaction between the particle matrixes (Enieb & Diab 2017).

1.2 Scope and Objectives

This stage of the study aimed to evaluate the effect of nanosilica (NS) on the characteristics of bitumen typically used in Western Australia.

The scope and objectives of the study included:

- an extensive review of literature to understand bitumen binder and critical properties of bitumen binder
- an extensive review of literature to understand NS and methods to incorporate it into bitumen binder
- laboratory testing of bitumen binder blended with various proportions of NS, to characterise the blend's properties.

1.3 Structure of the Report

Section 1 is an introduction to the work detailed in the report. It sets out the scope and objectives of the work and describes the structure of the report.

Section 2 discusses bitumen and its chemical composition.

Section 3 sets out the microstructure of bitumen and the various models used to describe it.

Section 4 looks at the properties of bitumen that make it important in asphalt for pavement applications.

Section 5 describes the features of NS.

Section 6 discusses the use of couplants to help dispersion of nanoparticles.

Section 7 outlines the mixing methods that can be applied to disperse NS within bitumen.

Section 8 describes the advanced observational techniques that can be used to characterise NS-modified binders.

Section 9 discusses the microstructural interaction between NS and bitumen.

Section 10 summarises the findings from previous research involving NS-modified bitumen and asphalt.

Section 11 gives the important lessons learned from the literature survey.

Section 12 outlines the methodology used in the laboratory study of NS-modified bitumen.

Section 13 details the results and findings from the study and also discusses the implications.

Section 14 gives the conclusions from the findings of the work.

Note: Need to mention what is in the appendices.

2 BITUMEN COMPOSITION

Bitumen is a black viscous mixture formed by a large number of different molecules. These different molecules are mainly hydrogen and carbon, along with a small amount of oxygen, nitrogen, sulphur and trace metals (Austroads 2017).

Bitumen is classified as a viscoelastic material as it can exhibit both viscous and elastic properties, and a combination of both, depending on the temperature and the rate of loading. At a temperature above 100 °C, bitumen can behave completely as a viscous liquid, while at a temperature below -10 °C bitumen it can become an elastic solid and thus brittle.

Due to the complex structures in bitumen, a comprehensive analysis of the composition of bitumen would be impracticable as broad ranges of heavy hydrocarbon molecules are left in bitumen. Therefore, bitumen is usually characterised into different chemical families based on their size and solubility in the different solvents.

The first attempts for characterisation of bitumen and separating it into fractions were made based on the solubility of bitumen in solvents, which relates to the polarity of molecules in bitumen. For this purpose, a non-polar solvent like n-heptane is used to separate the fractions. The solved part is referred to as maltenes and the precipitated fraction is called asphaltenes. After extracting the solvent, the asphaltenes remain as black frangible solid particles, whereas maltenes turn to a very thick viscous liquid.

In the 1940s Hubbard and Stanfield (1948) used a set of solvents with different polarities and separated maltenes into resins and oils. Finally, in the late 1960s, Corbett (1969) separated maltenes into three fractions using liquid chromatography and different solvents.

The four fractions are saturates (S), aromatics (A), resins (polar aromatics) (R) and asphaltenes (A), referred to as SARA fractions (LeBaron et al. 1999). The polarity of these four fractions increases according to their respective order. In other words, saturates are the least polar part whereas the asphaltenes, which are made of several fused aromatic rings in a stack-like structure, are the most polar. In a typical bitumen the composition is as follows: saturates 5–15%, aromatics 30–45%, resins 30–45% and asphaltenes 5–20% as shown in Figure 2.1.

Resins are soluble in n-heptane and act as a stabiliser for asphaltenes. Asphaltenes are polar in nature and appear as brown solids or semi-solids (Choi 2017). Saturates usually contain aliphatic compounds and form light-coloured viscous liquid. Aromatics consist of aromatic groups with aliphatic side chains (Akmaz et al. 2011).

Figure 2.1: Typical example of SARA fractions in bitumen

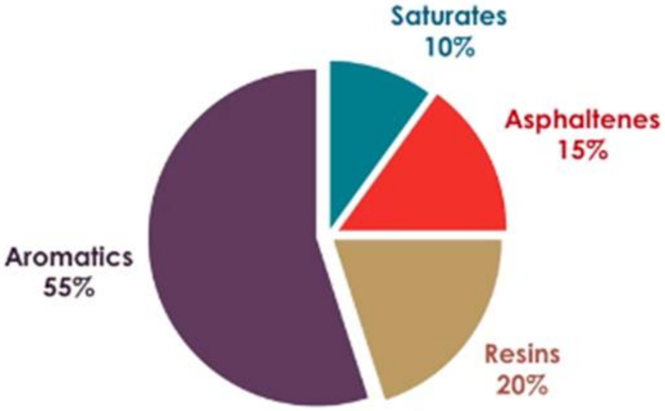

Source: Lang'at (2018)

The proportions of SARA fractions are important as they play a vital role in determining the chemical and physical properties of bitumen. These SARA fractions normally depend on the crude oil origin, manufacturing process and grade of the analysed bitumen. Figure 2.2 shows the colour and molecular arrangement of each part.

Figure 2.2: Maltene fractions

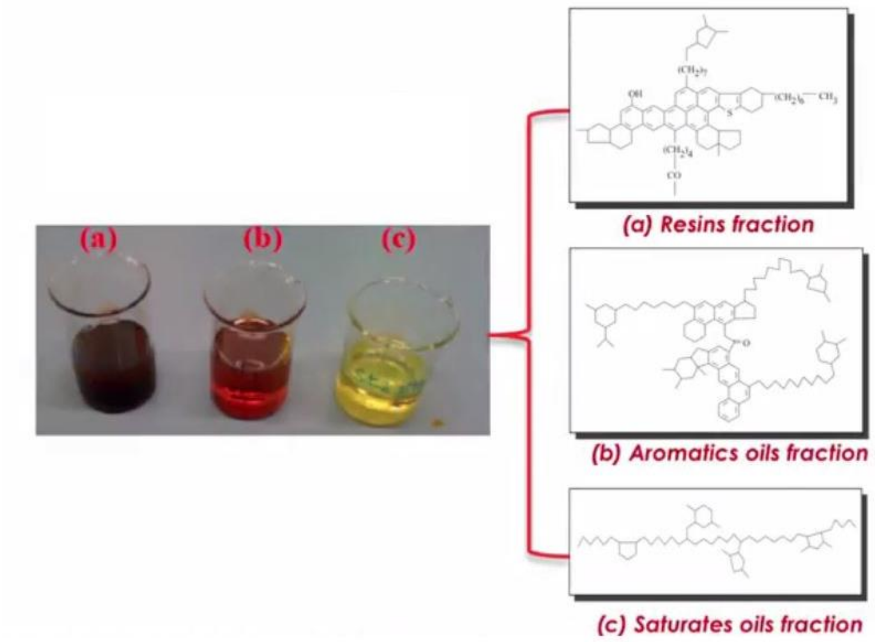

Source: Lang'at (2018)

In Australia, bitumen is classified based on its viscosity at 60 °C. There are five conventional classes of bitumen: Class 170, Class 240, Class 320, Class 450 and Class 600. Among all these classes of bitumen, Class 320 is the most suitable for use in road construction under hot, moderate and cold climates. Typically, only one main binder is stored at many plants and therefore due to its general suitability C320 is most likely to be the chosen binder.

The interaction between the molecules in bitumen also helps to define its physical properties or performance properties. The main molecular interactions in bitumen are dispersive interactions, polar and hydrogen bonding interactions and Pi-Pi interactions (Redelius & Soenen 2005). The dispersion forces are normally due to temporary dipoles caused by the movement of electrons around the hydrocarbon molecules. As electrons are mobile, they can react with other molecules causing the molecules present to be short of electrons and become unstable. The change in the number of electrons will cause an attraction force in all directions between the molecules to form a stable condition. This interaction results in a change in the physical properties of bitumen. Although these dispersion forces between molecules are considered to be very weak forces, they are certainly the most important in non-polar hydrocarbons and the most important interaction for the physical properties of bitumen (Redelius & Soenen, 2005). The polar and hydrogen bonding interactions are due to permanent dipoles from an imbalance in the distribution of electrons between molecules where atoms with different electronegativity are connected. This polar and hydrogen bonding happens when the hydrogen molecules react with nitrogen and oxygen. These interactions are considered much stronger than the dispersive interactions (Redelius & Soenen, 2005). However, with only 0–2% content of nitrogen and oxygen in bitumen, the dispersive interactions dominate in bitumen. However, this polar and hydrogen bonding interaction is still shown to correlate with the elastic part of the complex modulus of bitumen (Redelius & Soenen, 2005). Other interactions that could be expected in bitumen are pi-pi interactions, which occur between delocalised pi electrons in molecules. As asphaltenes contain many condensed aromatic rings, they can associate with full pi-pi bonding to form graphite-like stacks from planar molecules.

Asphaltenes are usually present as micelles that dissolve in the oily maltenes fraction as shown in Figure 2.3. Asphaltenes can associate in an aggregation process to create a gel structure when the aromatic/resin fraction is insufficient which results in the basic structure of the colloidal structure of bitumen (Austroads 2017). This colloidal structure of bitumen tends to have poor field performance as the micelle structure can be easily broken down.

Figure 2.3: Sol model of bitumen

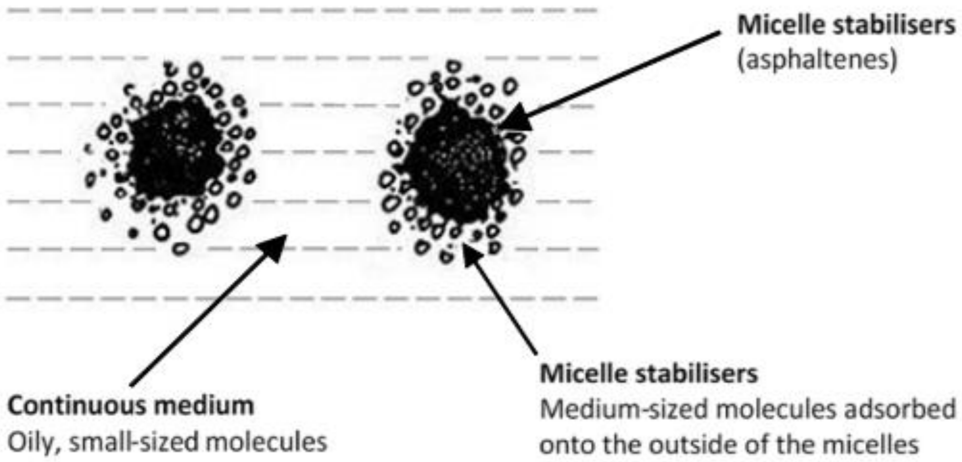

Source: Austroads (2017)

3 MICROSTRUCTURE OF BITUMEN

Knowing the spatial arrangements of bitumen molecules is helpful to identify the properties of bitumen. It is also important to investigate the chemical interactions induced by additives for the improvement of binder performance.

Efforts to model the microstructure of bitumen have been in place since the 1930s (Traxler 1936). Based on the polarity, size and chemical structure of molecules present in bitumen, two main microstructures have been suggested by researchers, which are the colloidal model and the dispersed fluid model.

3.1 Colloidal model

The colloidal model considers bitumen as a colloidal structure in which the different component groups with different polarities (SARA) collocate within the mass to create clear structural zones as depicted in Figure 3.1.

Figure 3.1: Concept for colloidal model

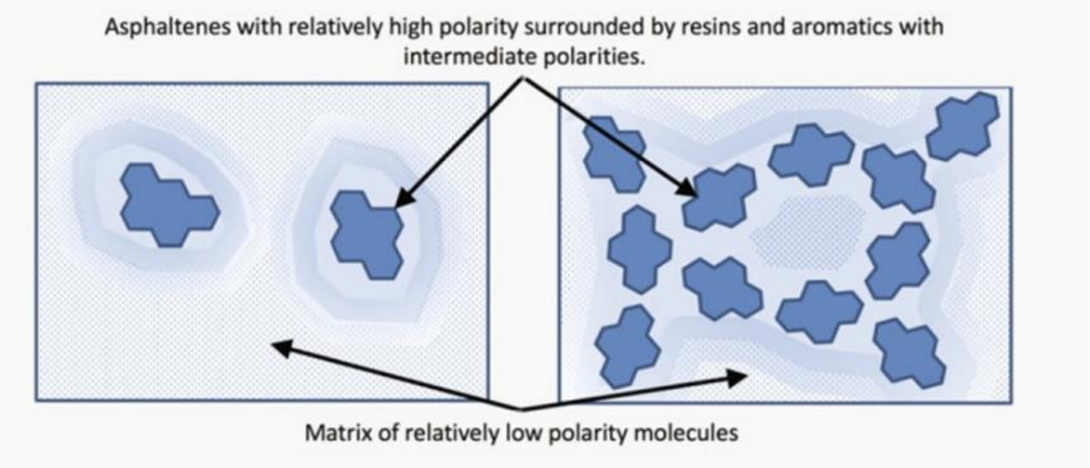

Source: Read and Whiteoak (2003).

The most famous model of the colloidal structure was proposed by Yen, when he and Dickie tried to measure the molecular weight of bitumen and its fractions with different techniques. In Yen’s model, crystallites, chain bundle particles and micelles are considered as illustrated in Figure 3.2.

Figure 3.2: Microstructure of bitumen

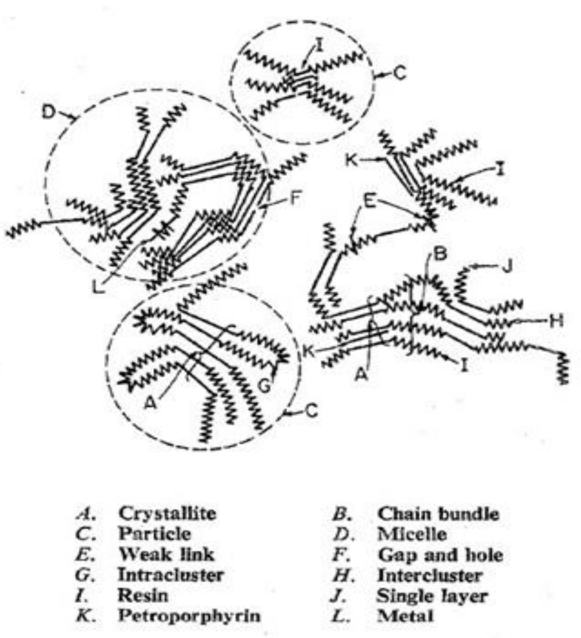

Source: Dickie and Yen (1967).

Mullins in 2009 suggested a modified model after Yen's model, in which new advancements delivered a better picture of bitumen. In the modified model, asphaltenes, as the most important part of bitumen, are duly considered and their interfacial properties are foreseen in the model according to Figure 3.3.

Figure 3.3: Modified Yen model

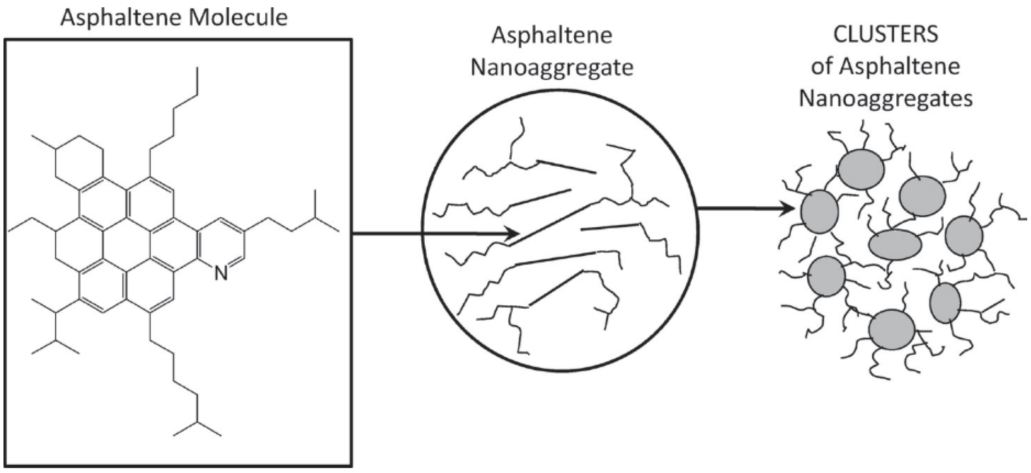

Note: (Left) The asphaltene molecular architecture. (Center) Asphaltene molecules. (Right) Asphaltene nanoaggregates.

Source: Mullins (2010).

As noted earlier, the aggregation of asphaltenes or clusters lead to the formation of micelles which have low solubility. As illustrated in Figure 3.4, condensed aromatic rings are stacked through pi-pi bonds and form planar asphaltene molecules like graphite.

Figure 3.4: Aggregation of asphaltenes leads to the formation of micelles with a lower solubility parameter

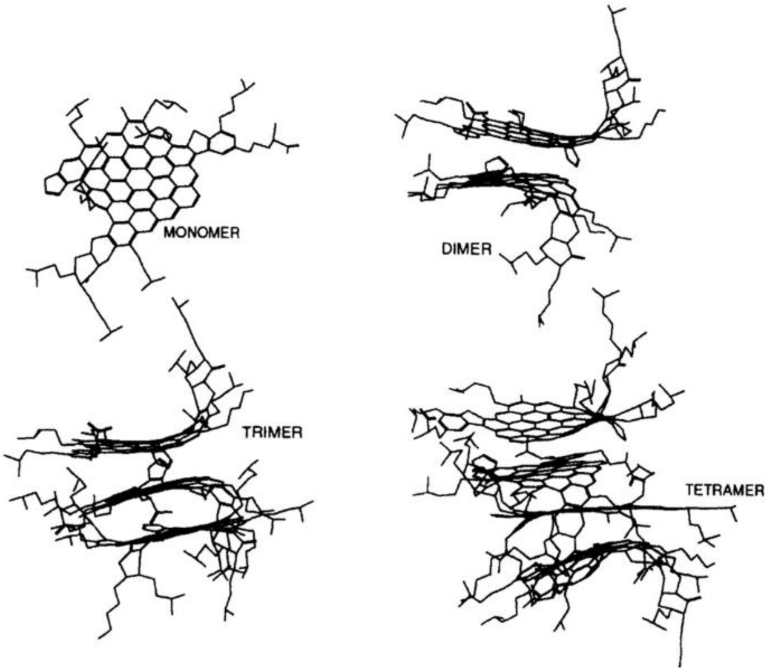

Source: Lesueur (2009).

3.2 Dispersed fluid model

Redelius (2011) argued that since the asphaltenes are mainly soluble in the maltenes, no colloidal dispersion can exist. This claim has been based on evidence and results of tests. As such the most likely model for bitumen is a thermodynamic solubility model where all molecules in bitumen are kept in solution by their mutual solubility.

4 BITUMEN PROPERTIES

4.1 Ageing

Ageing of bitumen can happen when it is exposed to air, UV light, heat and water. The main mechanism of ageing of bitumen is the oxidative reaction to the bitumen molecules. Oxidative hardening involves the reaction of atmospheric oxygen with hydrocarbon molecules in bitumen. Free radicals or molecular processes can be controlled by antioxidant additives; however, their influence is limited for high-viscosity bitumen. The most prevalent signs of ageing are described by the evolution of sulfoxide and carbonyl compounds. This results in the change in SARA fractions of bitumen where the percentage of saturates and asphaltenes increases and the percentage of aromatics and resins decreases.

Ageing of asphalt binder also occurs during hot mixing and construction through the volatilisation of the lighter components of the binder. This ageing process also known as short-term ageing is usually simulated in the laboratory using the rolling thin film oven (RTFO) test. However, ageing continues after the pavement is constructed due to environmental conditions. This ageing is a long-term or in-service ageing and it is simulated in the laboratory using the pressure ageing vessel (PAV).

Ageing of bitumen is a major concern in asphalt pavements because it negatively affects asphalt properties and performance.

4.2 Rutting and fatigue

Bitumen plays a vital role in road construction typically as a binder mixed with aggregate particles to create asphalt. Hence, it is important to study bitumen's properties in order to create better asphalt mixes. The primary distresses that affect the performance of asphalt pavements during their service life is rutting and fatigue cracking (Zou et al. 2017).

In this study, rutting and fatigue cracking are evaluated based on the complex modulus (G*) and phase angle (δ) derived from dynamic shear rheometer (DSR) tests (Asphalt Institute 2003; Bahia & Anderson 1995; Brown et al. 2009; Goh et al. 2011).

Since rutting and fatigue cracking are the two most common forms of asphalt distress, these two properties will be investigated through DSR tests to understand how the addition of NS particles is likely to affect asphalt mixture performance.

The work of each loading cycle can be divided into two parts. The first part is relevant to elastic deformation, which reflects the energy from rebounding actions. However, the second part is absorbed by means of rutting as permanent damage or crack dissipations as fatigue. Therefore, less work absorbed would mean better performance of asphalt. The work resulting from the two parts can be expressed as in Equations 1 and 2:

$$Rutting\colon\ W_c = \pi\sigma_o^2\left(\frac{1}{G^*/_{\sin\delta}}\right) \tag{1}$$

$$Fatigue\ cracking\colon\ W_c = \varepsilon_o^2(G^*\ \sin\delta) \tag{2}$$

where

Wc = work absorbed per load cycle

σ_o = stress applied during load cycle

ε_o = strain during load cycle

G^* = complex shear modulus

δ = phase angle

Equation 1 shows that an increase of $G^*/_{\sin\delta}$ is equivalent to more rutting resistance, which can be achieved either by a high G^* or a low δ when the stress-control mode is applied. On the other hand, low G* and δ will be ideal when the strain-controlled mode is used.

4.3 Adhesion and cohesion

The coating ability of a bitumen is an indicator of whether aggregates are coated uniformly. Stripping potential of asphalt or the tensile strength ratio is indicative of the coating's resistance to the stripping effect of water. Another approach is to evaluate coating at the microscale level, which is important in the control of ravelling as well.

The surface energy (SE) of chemical interactions between aggregate and bitumen or bitumen itself is a measure to evaluate the above properties. Work of debonding W_{wet} is an index of binder and aggregate compatibility according to Equations 3 and 4:

$$W_{AB} = \gamma^A + \gamma^B - \gamma^{AB} \quad 3$$

$$W_{wet} = \gamma^{Aw} + \gamma^{Bw} - \gamma^{AB} \quad 4$$

where

W_{AB} = the work of binder and aggregate adhesion

γ^A = the total SE of aggregate

γ^B = the total SE of binder

γ^{AB} = the total SE of binder-aggregate

W_{wet} = the work of debonding

γ^{Aw} = the total SE of aggregate in presence of water

γ^{Bw} = the total SE of binder in presence of water

Source: Little and Bhasin (2006).

These parameters can be assessed by a goniometer (sessile drop method) where contact angles of bitumen on different surfaces can be measured, as shown in Figure 4.1.

Figure 4.1: Sample preparation: (a) binder droplets (b) contact angle measurements

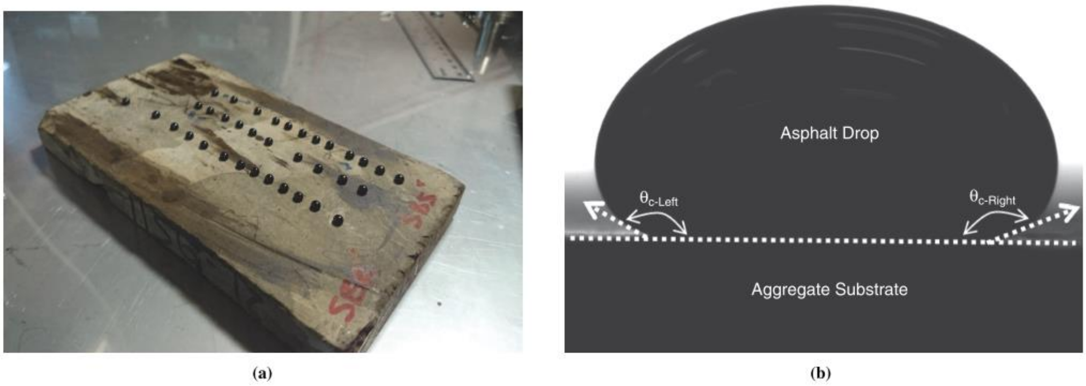

Source: Aguiar-Moya et al. (2015).

The energy ratio (ER) can indicate how high-moisture-resistant bonds are generated between aggregates and binder as adhesion (Equations 5 and 6):

$$ER = \frac{W_{AB}}{W_{wet}} \quad 5$$

$$W_{BB} = 2\gamma^{B} \quad 6$$

where

ER = the energy ratio

W_{AB} = the work of binder and aggregate adhesion

W_{wet} = the work of debonding

W_{BB} = the work of cohesion of the binder

γ^{B} = the total SE of binder

Source: Little and Bhasin (2006).

On the other hand, the work by cohesion of binder (W_{BB}), as binding interactions of bitumen molecules, will indicate the mechanical resistance of the binder itself.

5 FEATURES OF NANOSILICA

Multiple types of nanoparticles have been incorporated into asphalt mixtures to improve performance. Available records indicate NS, nanoclay (raw nanoclays, such as montmorillonite and bentonite), polysiloxanemodified montmorillonite and organophilic montmorillonite (organo-modified montmorillonite) all have been examined as listed in Table 10.1. In general, nanoclays and NS have been found to be more suitable and recommended for further studies and developments (Crucho et al. 2018).

The main problem of nanoclay particles is the difficulty in exfoliation or intercalation of nanolayered silicate in the complex macromolecular structures of bitumen as presented in Figure 5.1. This is mainly due to electrostatic coalescence forces formed by a large number of charges on the 2D interlayer silicate sheets, which make it difficult to disperse uniformly (Sun et al. 2017). NS, with semi-spherical shape, is not associated with this difficulty.

Figure 5.1: Schematic of nanoclay interactions with hydrocarbon molecules

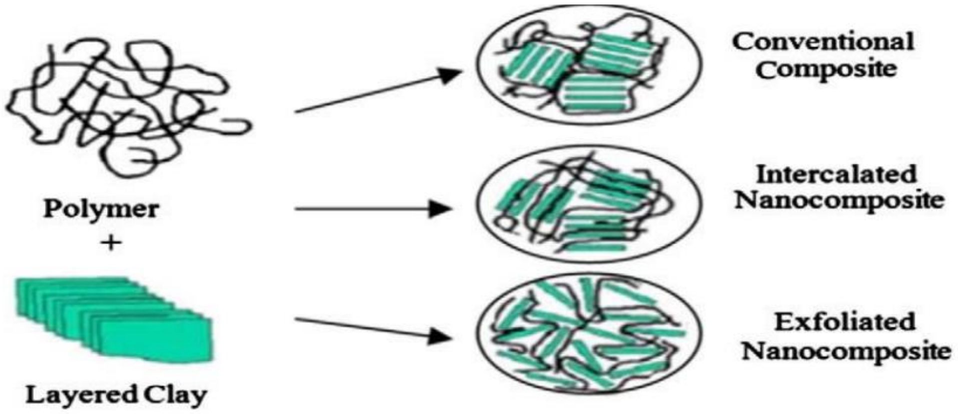

Source: Golestani et al. (2012).

It is well known that as the size of a particle decreases, a greater portion of atoms is exposed to the surface. In turn, NS particles would be more reactive with a larger surface area per unit mass compared to nanoclays (Sun et al. 2017).

NS is a relatively new inorganic material and has been broadly applied in polymeric and bituminous products (Hu et al. 2004; Zhou et al., 1999). The main functions of using NS as an additive include being a catalyst carrier, rubber strength agent, and plastic filler amongst others in various industries. NS has some features which make it distinct from other nanoparticles irrespective of its mechanical impacts on materials (Lazzara & Milioto 2010; Yao et al. 2013). These can be listed as:

- a high surface area which makes it high performance
- excellent stability
- low cost of production
- strong adsorption
- good dispersal ability
- high chemical purity
- inorganic filler.

Different filler types have their own particle size distributions (PSD). However, too little attention has been paid to PSD effects so far, although the size of particles will influence the quality of dispersion in a binder (Partl et al. 2004). However, NS is highly reactive compared to conventional fillers. The dispersal ability of NS particles into binder can lead to polymeric nanocomposites with desirable performance (LeBaron et al. 1999; Ray & Okamoto 2003). Table 5.1 lists some of the research on nanoparticles in asphalt.

Table 5.1: Summary of nanomodifications for asphalt mixtures

Nanomodification		Binder type	Effects on performance	
Nanoparticle	Percentage		Positive	Negative
Nanosilica	4%	35/50	Marshall stability	–
	4%	PG 76	Water sensitivity; permanent deformation; stiffness	–
	4%; 6%	PG 58–34 with ABS	Permanent deformation; stiffness	–
	2%	60/70 with 5% SBS	Marshall stability; Water sensitivity; stiffness	–
Nanoclay	1%; 3%; 5%	PG 58–28; PG64–28	Permanent deformation	–
	2%; 4%	PG 58–34	Permanent deformation; stiffness	Water sensitivity
Polysiloxane-modified montmorillonite	2%	PG 58–28	Water sensitivity	Indirect tensile strength (dry)
	2%; 4%	PG 58–34	Permanent deformation; stiffness	Water sensitivity
Organophilic montmorillonite	2%; 4%; 7%	60/70	Water sensitivity; stiffness	–
	6%	40/60	Water sensitivity; permanent deformation; stiffness	Fatigue life
	3%	PG 58–22	Water sensitivity; Stiffness; Fatigue life; Permanent deformation	–
	1.50%	PG 58–10 with 6% SBS	Water sensitivity; stiffness	–
	2%; 3.5%; 5%	50/70	Marshall stability; permanent deformation; indirect tensile strength (dry) at 25 °C	Indirect tensile strength (dry) at 15 °C
	Type A			
	2%; 3.5%; 5%	50/70	Marshall stability; permanent deformation; indirect tensile strength (dry) at 25 °C	Indirect tensile strength (dry) at 15 °C
	Type B			
	2%; 3.5%; 5%	50/70	Permanent deformation	Indirect tensile strength (dry) at 15 °C and 25 °C
	Type C			

Source: Crucho et al. (2018).

6 EFFECTS OF COUPLANT

Silicon dioxide (SiO_2) nanoparticles are hydrophilic, like nanoclays, which is due to the interaction of silicon and hydroxyl groups. In an organic matrix, this might compromise the wettability and compatibility of mixtures with different surfaces (Crucho et al. 2018; Ding et al. 2009; Sugimoto 2000; Sun et al. 2017).

It should be considered that bitumen is mainly composed of heavy hydrocarbons which are generally non-polar molecules. As such they interact with each other by dispersive forces. NS is non-polar but reacts with hydroxyl groups of silane coupling agents, which can assist its bonds with hyrdocarbon molecules. The oxygen atom in the hydroxyl groups is more electronegative than the hydrogen and promotes hydrogen bonds with aromatic sheets in polar aromatics. Likewise, the interaction of hydroxyl groups of NS with both polar aromatics and asphaltene molecules is effective in the reduction of the overall oxidation of asphalt (Fini et al. 2015).

Changing the hydrophilicity of NS to hydrophobicity can to some extent improve the nanoparticles' compatibility with bitumen. Together, these functions of silane couplant imply that NS could disperse more effectively with less agglomerations, which ultimately benefit the interfacial compatibility of nanoparticles in asphalt (Sun et al. 2017). Figure 6.1 demonstrates how couplant interacts with different molecules.

Figure 6.1: Molecular structure of branch and linear styrene-butadiene-styrene (SBS)

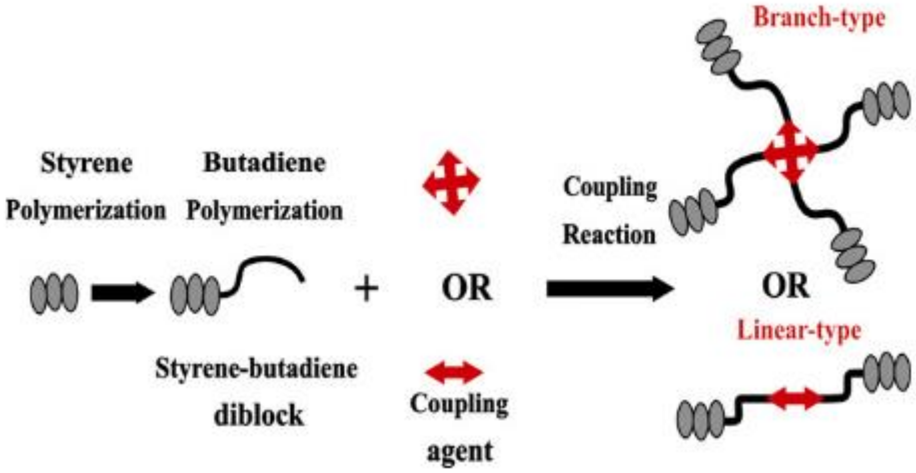

Source: Golestani et al. (2012).

7 MIXING CONDITION

7.1 Dry or wet

As noted earlier, good dispersion of nanoparticles in an organic matrix such as bitumen is very important. Otherwise the presence of the nanocomposites will not be as effective as expected and they might behave similarly to microscale additives.

The question that might arise is how blending of nanoparticles within a binder could be more efficient. Obviously in this case the objective is to achieve high dispersions of particles. In the literature, two methods of dry blending or wet blending with a solvent method are used (Crucho et al. 2018).

Dry blending is the most commonly used and has some advantages such as simplicity, low cost and is quick and easy to apply. It also might be environmentally friendly in the sense that it does not have a chemical solvent. The time and rate of blending from the reviewed articles are noted in Table 7.1.

Table 7.1: Mixing details in the literature

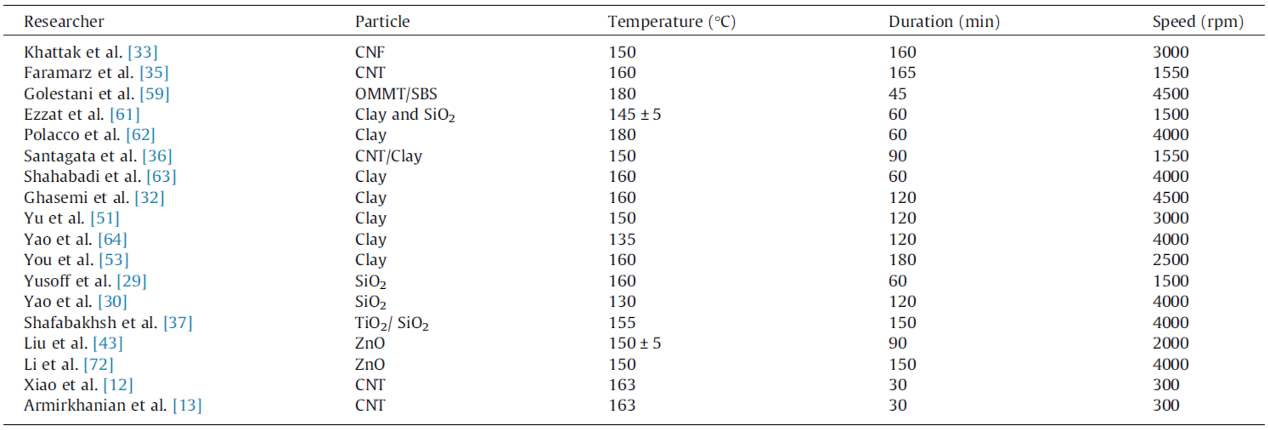

Researcher	Particle	Temperature (°C)	Duration (min)	Speed (rpm)
Khattak et al. [33]	CNF	150	160	3000
Faramarz et al. [35]	CNT	160	165	1550
Golestani et al. [59]	OMMT/SBS	180	45	4500
Ezzat et al. [61]	Clay and SiO_2	145 ± 5	60	1500
Polacco et al. [62]	Clay	180	60	4000
Santagata et al. [36]	CNT/Clay	150	90	1550
Shahabadi et al. [63]	Clay	160	60	4000
Ghasemi et al. [32]	Clay	160	120	4500
Yu et al. [51]	Clay	150	120	3000
Yao et al. [64]	Clay	135	120	4000
You et al. [53]	Clay	160	180	2500
Yusoff et al. [29]	SiO_2	160	60	1500
Yao et al. [30]	SiO_2	130	120	4000
Shafabakhsh et al. [37]	TiO_2/ SiO_2	155	150	4000
Liu et al. [43]	ZnO	150 ± 5	90	2000
Li et al. [72]	ZnO	150	150	4000
Xiao et al. [12]	CNT	163	30	300
Armirkhanian et al. [13]	CNT	163	30	300

Source: Li et al. (2017).

Almost all of the researchers used high shear mixers. It is also noted that air bubbles in the binder should be avoided. Any air entrapment can cause accelerated oxidation which is undesirable. This phenomenon may occur through vortex currents during high-speed stirring. Thus, the rate of blending can be adjusted during preparation works.

Wet mixing or the so-called ‘solvent melting process’ has also been applied in some of the literature. In this method, the solvent is expected to be an intermediate medium facilitating the introduction of nanoparticles into bitumen. In addition, it would be ideal to let the solvent evaporate using a low-shear mixer with a medium-to-high temperature. However, selection of an appropriate solvent will require special attention to its attributes, namely:

- not adversely impacting the physical or mechanical properties of the binder
- good dissolution capability in binder at room temperature
- volatile with low viscosity not compromising mixing quality.

Examples of solvent types used are kerosene, varsol, turpentine and acetone for carbon nanotubes-modified asphalts (Faramarzi et al. 2015; Khattak et al. 2012; Li et al. 2017). In the case of NS, Sun et al. (2017) examined K-1, K-2, and K-3 solvents which acted as coupling agents as well. All three types of coupling agents are used for composite materials and have chemical formulas, namely $NH_2CH_2CH_2CH_2Si(OC_2H_5)_3$, $CH_3(CH_2)_{16}COOH$, and $(CH_2CH_2NH)_n$. However, these had adverse effects on the physical properties of bitumen. Therefore, these couplants will not be considered in this study.

7.2 Temperature and speed of stirring

Generally, high temperatures assist in lowering the viscosity of bitumen for better dispersion; similarly, higher temperatures allow nanoparticles to diffuse more effectively. However, high temperature would accelerate the ageing or deteriorate the durability of bitumen. Thus, achieving a balance between temperature and stirring rate and time is essential. Mixing time is directly related to energy consumption and production costs (Li et al. 2017). Table 7.1 represents the mixing details considered by different authors in their work.

8 ADVANCED OBSERVATION TECHNIQUES

Nano to microstructural changes occur in bitumen during the ageing process, i.e. when it is exposed to air, UV light, heat and water. These nano to microstructural changes can be investigated through using various observation techniques. In this study the aim was to compare unaged, aged and NS-dispersed bitumen samples.

This section summarises commonly used and more advanced observation techniques.

8.1 Commonly used

Commonly used observation techniques include scanning electron microscopy (SEM), X-ray and/or different spectroscopy techniques such as infrared (IR) or fourier-transform infrared spectroscopy (FTIR).

These methods are carried out to evaluate mixing efficiency to ensure that all particles can effectively influence the desired properties of a modified binder. For example, during mixing, likely agglomerations should be avoided which can be monitored with the SEM in secondary electron (SE) mode. In most related articles, SEM has been used to monitor dispersion quality while exploring the microstructural changes (Table 8.1).

Table 8.1: Observation techniques for nanomodified binders

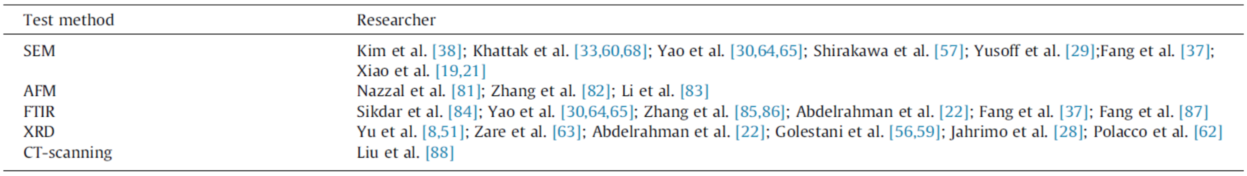

Test method	Researcher
SEM	Kim et al. [38]; Khattak et al. [33,60,68]; Yao et al. [30,64,65]; Shirakawa et al. [57]; Yusoff et al. [29];Fang et al. [37]; Xiao et al. [19,21]
AFM	Nazzal et al. [81]; Zhang et al. [82]; Li et al. [83]
FTIR	Sikdar et al. [84]; Yao et al. [30,64,65]; Zhang et al. [85,86]; Abdelrahman et al. [22]; Fang et al. [37]; Fang et al. [87]
XRD	Yu et al. [8,51]; Zare et al. [63]; Abdelrahman et al. [22]; Golestani et al. [56,59]; Jahrimo et al. [28]; Polacco et al. [62]
CT-scanning	Liu et al. [88]

Source: Li et al. (2017).

FTIR is a molecular spectroscopy which is used to characterise both organic and inorganic species. In this method, the sample is bombarded with infrared radiation. When the frequency of the infrared radiation matches with the natural frequency of the molecular bond, the amplitude of the vibration increases, and the infrared radiation is absorbed.

Carbonyl groups (esters, ketones etc.) and sulfoxides are the major functional groups formed during oxidative ageing (Petersen 2009). They are characterised by C=O and S=O double bonds, respectively. It is generally observed that sulfoxides tend to form at a faster rate and at higher temperatures than carbonyl groups. Various methods are used to quantify the ageing-related evolution of the bitumen spectrums at the sulfoxide (~1,030 cm^{-1}) and carbonyl (~1,700 cm^{-1}) wavenumbers specifically. The infrared spectra can help to understand how ageing resistance of modified binder has been changed by evaluating the level of carbonyl and sulfoxide groups generated during age conditioning (Marsac et al. 2014).

The FTIR test is also used to evaluate functional group characteristics of asphalt binders after chemical interactions during oxidation or inclusion of a couplant (Xu et al. 2010a, 2010b).

Figure 8.1 shows an example result for a sample of bitumen using FTIR.

Figure 8.1: Sample bitumen FTIR spectrum

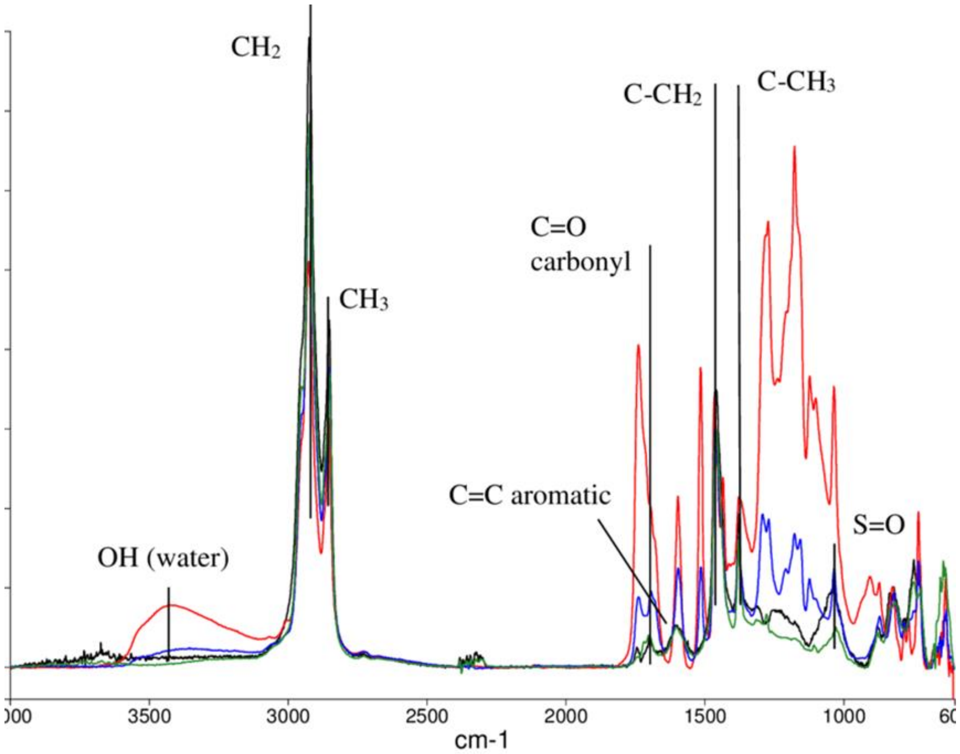

Source: Mikhailenko (2015).

Other methods mainly characterise the bitumen by providing data about the physical and chemical composition of a given sample. Fractioning is one such method. In fractioning methods, the bitumen composition is broken down in a solution based on the polarity and adsorption characteristics of the different molecules in the sample (Masson et al. 2001). Table 8.2 demonstrates common fractioning methods beside chromatography approaches which are applied to delineate bitumen compositions.

Table 8.2: Methods for asphalt fractioning

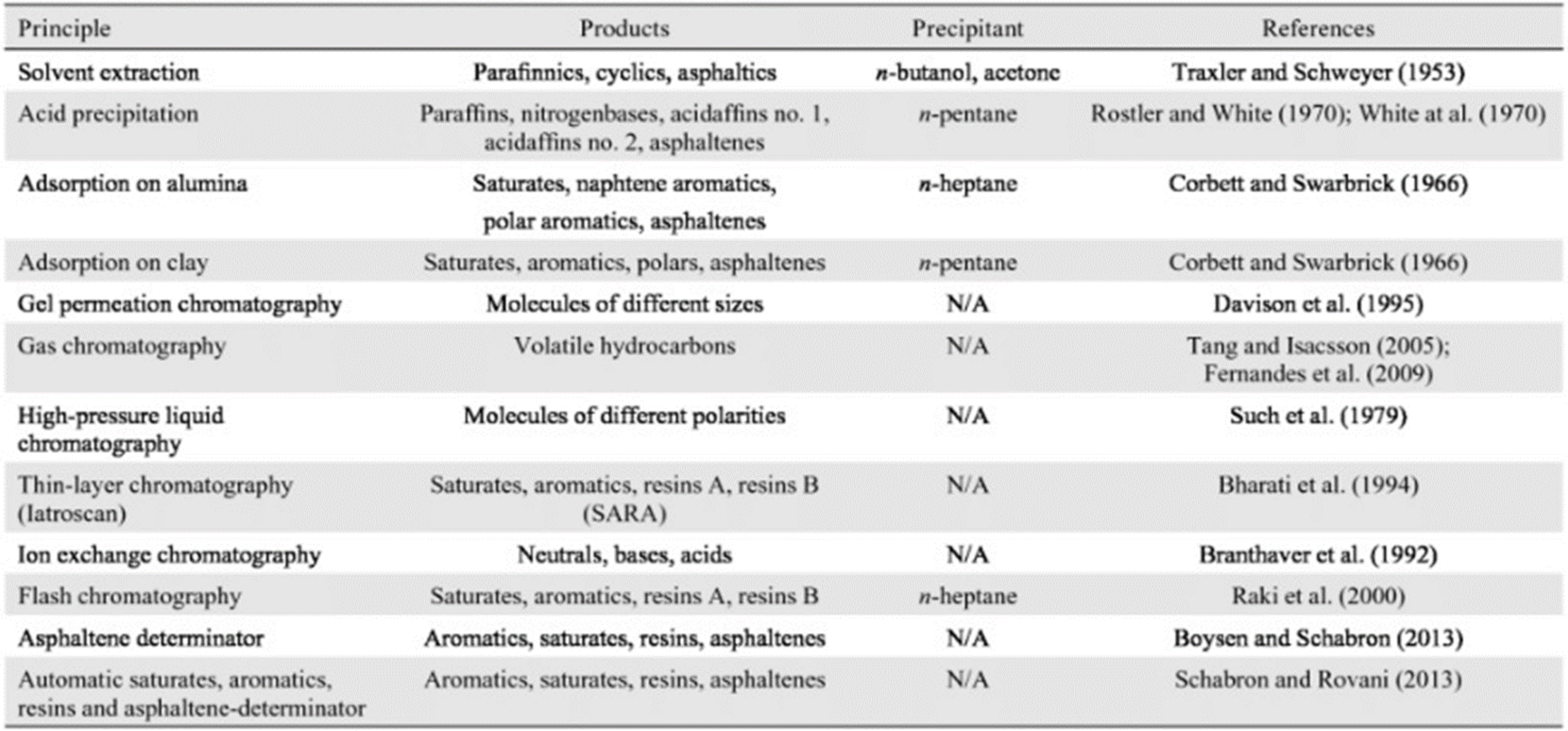

Principle	Products	Precipitant	References
Solvent extraction	Parafinnics, cyclics, asphaltics	*n*-butanol, acetone	Traxler and Schweyer (1953)
Acid precipitation	Paraffins, nitrogenbases, acidaffins no. 1, acidaffins no. 2, asphaltenes	*n*-pentane	Rostler and White (1970); White at al. (1970)
Adsorption on alumina	Saturates, naphtene aromatics, polar aromatics, asphaltenes	*n*-heptane	Corbett and Swarbrick (1966)
Adsorption on clay	Saturates, aromatics, polars, asphaltenes	*n*-pentane	Corbett and Swarbrick (1966)
Gel permeation chromatography	Molecules of different sizes	N/A	Davison et al. (1995)
Gas chromatography	Volatile hydrocarbons	N/A	Tang and Isacsson (2005); Fernandes et al. (2009)
High-pressure liquid chromatography	Molecules of different polarities	N/A	Such et al. (1979)
Thin-layer chromatography (Iatroscan)	Saturates, aromatics, resins A, resins B (SARA)	N/A	Bharati et al. (1994)
Ion exchange chromatography	Neutrals, bases, acids	N/A	Branthaver et al. (1992)
Flash chromatography	Saturates, aromatics, resins A, resins B	*n*-heptane	Raki et al. (2000)
Asphaltene determinator	Aromatics, saturates, resins, asphaltenes	N/A	Boysen and Schabron (2013)
Automatic saturates, aromatics, resins and asphaltene-determinator	Aromatics, saturates, resins, asphaltenes	N/A	Schabron and Rovani (2013)

Source: Masson et al. (2001).

8.2 Thermogravimetric analysis (TGA)

In this method the mass of the sample is measured while heating from room temperature up to high temperatures. Different groups of hydrocarbon molecules evaporate or decompose at different temperatures, therefore TGA can be used for the identification of bitumen components, especially when considering volatile components. Some information about residual solvents, overall thermal stability, as well as the influence of the different additives on the thermal stability of bitumen can also be measured by TGA.

8.3 Differential scanning calorimetry (DSC)

In this method, the crystalline components that exist in aged or oxidised bitumen are identified. The difference in the amount of heat needed for elevating the temperature of the sample is compared with a reference curve as a function of temperature. Other parameters can be picked up such as phase changes and melting point.

8.4 Gel permeation chromatography (GPC)

In this method, a solution of bitumen passes through a porous column. Depending on the size of molecules (their hydrodynamic volume) the duration of their transition through the column varies. Therefore, it will be separated based on its molecular size. This information is used to understand the quantitative distribution of all species existing in a binder including maltenes, asphaltenes, and polymers. Typical results are shown in Figure 8.2.

Figure 8.2: Sample GPC spectrum

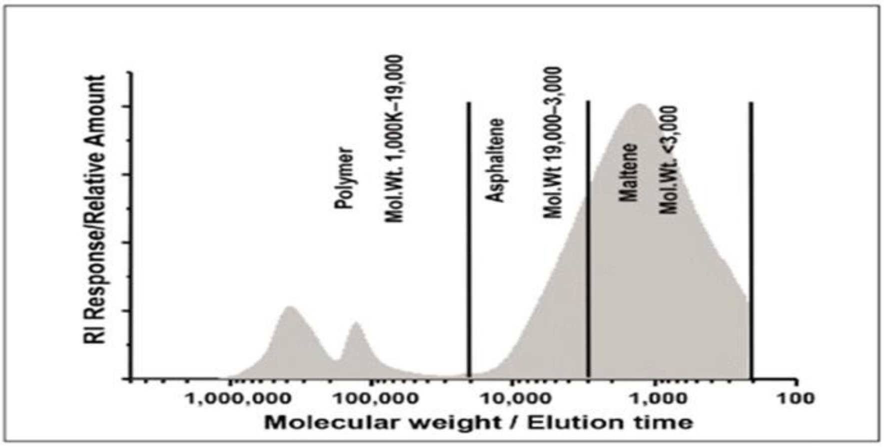

Source: Daly and Negulescu (2013)

8.5 Nuclear magnetic resonance analysis (NMR)

Samples are subjected to a very strong static magnetic field in which nuclei of H are perturbed and react by producing an electromagnetic signal with a specific frequency. The radiated signals are detected and recorded as NMR spectra. The frequency of signals is governed by chemical bonds, elements and chemical groups.

There is an option to use C13 NMR, in which the nuclei of carbon atoms are targeted. C13 NMR gives information about different carbon-based molecules in the sample such as aromatic carbon, aliphatic carbon, bridged carbons, methyl carbons, ring carbons, naphtenic carbons, parrafinic chain lengths, and some other parameters. Elemental analysis (C, H, O, S, etc.), SARA composition, additives and their quantities, information on ageing and its mechanisms can all be investigated with this tool. Typical results are shown in Figure 8.3.

Figure 8.3: Sample NMR spectrum

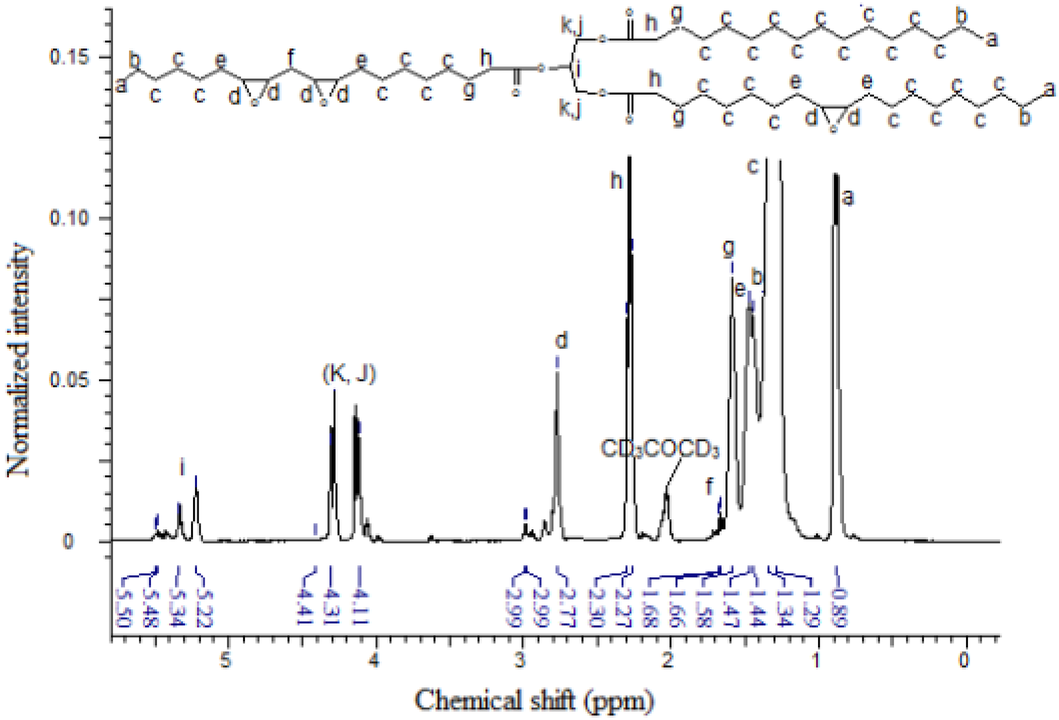

Source: Salih (2015).

8.6 X-ray fluorescence spectroscopy

In summary, spectrometry is based on the emission of fluorescent X-rays from a sample which is excited by a bombardment of high-energy X-rays or gamma rays. It can be used for elemental analysis, quantification of bitumen (presence of heavy metals, sulphur, etc.) and type of additives. A typical result is shown in Figure 8.4.

Figure 8.4: Sample X-ray fluorescence spectroscopy spectrum

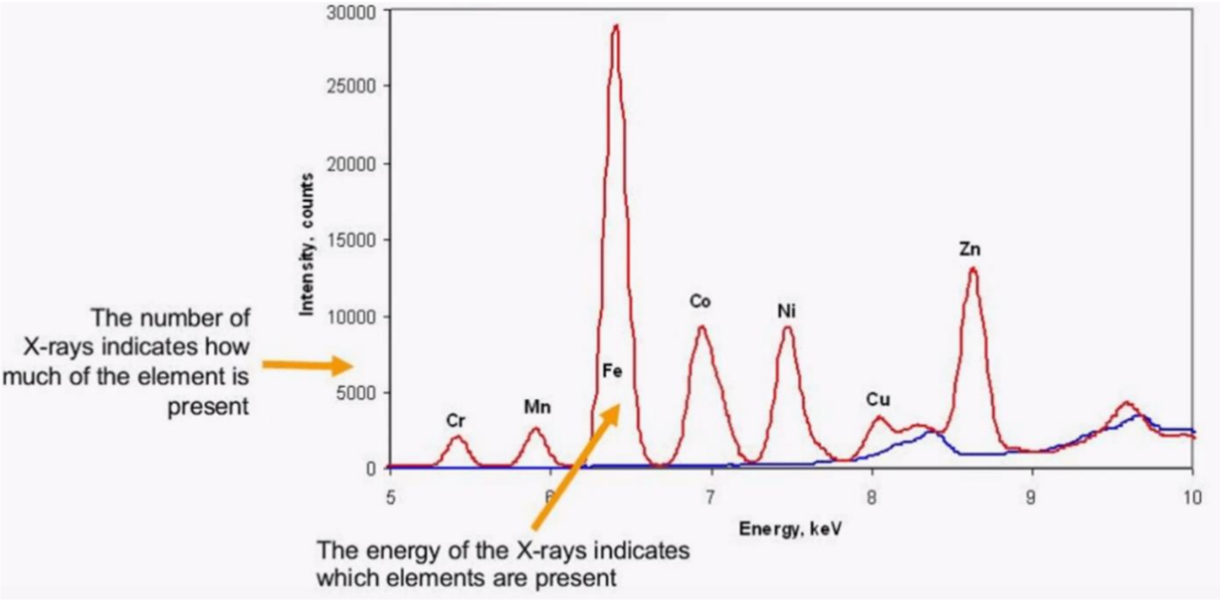

Source: Michaud (2011)

8.7 Scanning electron microscopy

Advanced observation techniques such as SEM imaging can assist in investigations at the nanoscale level.

An SEM captures atomic-resolution images through electron irradiation from a surface by analysing the electromagnetic responses received. A concentrated beam of electrons with energies around 1–40 keV does a raster-scan across the surface. The bombarded electrons penetrate the surface and decelerate by collisions with the sample's atoms. The interaction volume in the sample is pear-shaped in the case of a low atomic number target, which changes to hemi-spherical form when high atomic number materials are imaged as shown in Figure 8.5. The interaction volume is around one or two micrometres in dimension and affects the diffraction pattern or dissipation energy.

Figure 8.5: Interaction volume and various emissions

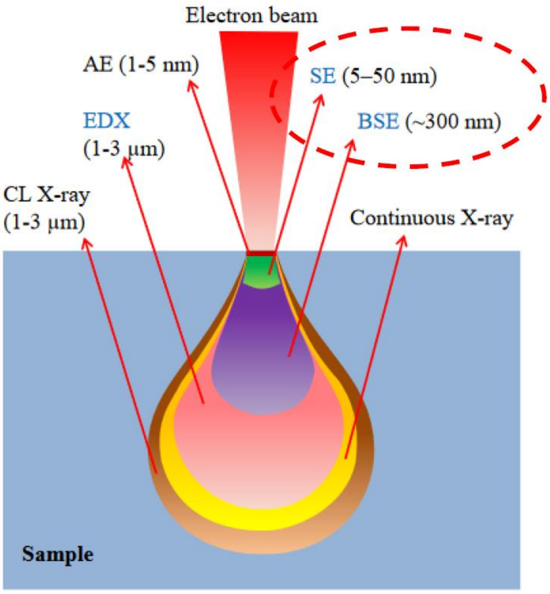

Source: Abbott (n.d.)

Various detectors in the SEM chamber collect the whole range of escaped or reflected electrons from the surface. Their location is shown in a general assembly of an SEM in Figure 8.6. The final results are often greyscale micrographs which are categorised as backscattered electron (BSE) or secondary electron (SE) images.

Figure 8.6: Elements of a scanning electron microscope

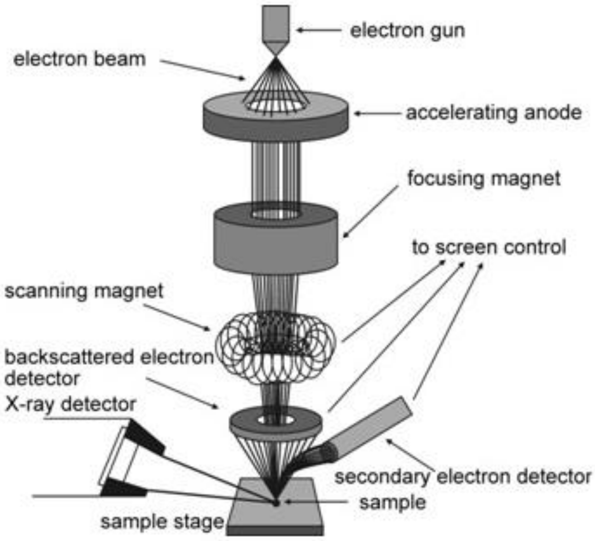

Source: Havancsák,(n.d.)

Some of the high-energy electrons of the beam (> 50 eV) interact with the target sample without significant change in their kinetic energy as shown in Figure 8.7.

Figure 8.7: Interactions of the electron beam with atoms in the sample

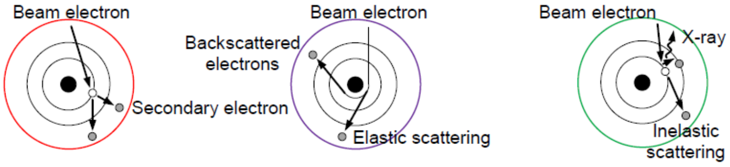

Source: Poulikakos et al. (2012).

In this case, elastic scattering occurs during collisions with large particles (atoms). Large atoms with greater cross-sectional area have higher probability of producing elastic collisions because of their greater atomic number (Z) as illustrated in Figure 8.8.

Figure 8.8: Backscattered electrons

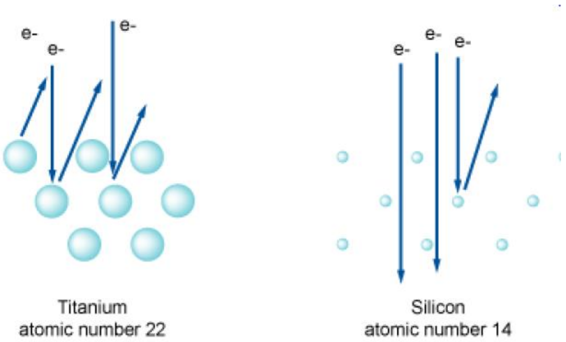

Source: Abbott (n.d.)

Therefore, the number of electrons reaching the BSE detector is proportional to the mean atomic number of the sample. In other words, the brighter areas in BSE images represent greater average Z in the sample. BSE images often are used as high-resolution compositional maps of a typical sample and a quick check for heavy elements or phases.

The inelastic collision of electrons with sample atoms causes the ejection of secondary electrons from the sample. These electrons escape from the upper 10 nanometres of the specimen due to their low energy, which is of the order of 5 eV. Thus, the intensity of the SE signals is more relevant to surface topography which is essential for high-resolution images of a fine surface texture.

8.8 Atomic force microscopy

An atomic force microscope (AFM) has a nanometre-sized probe at the end of a cantilever that scans the surface of the asphalt sample and records the topography of the surface and changes in the probe-surface interaction. It can map the roughness and stiffness of the sample surface at a nanoscale (Figure 8.9).

Figure 8.9: Sample AFM image

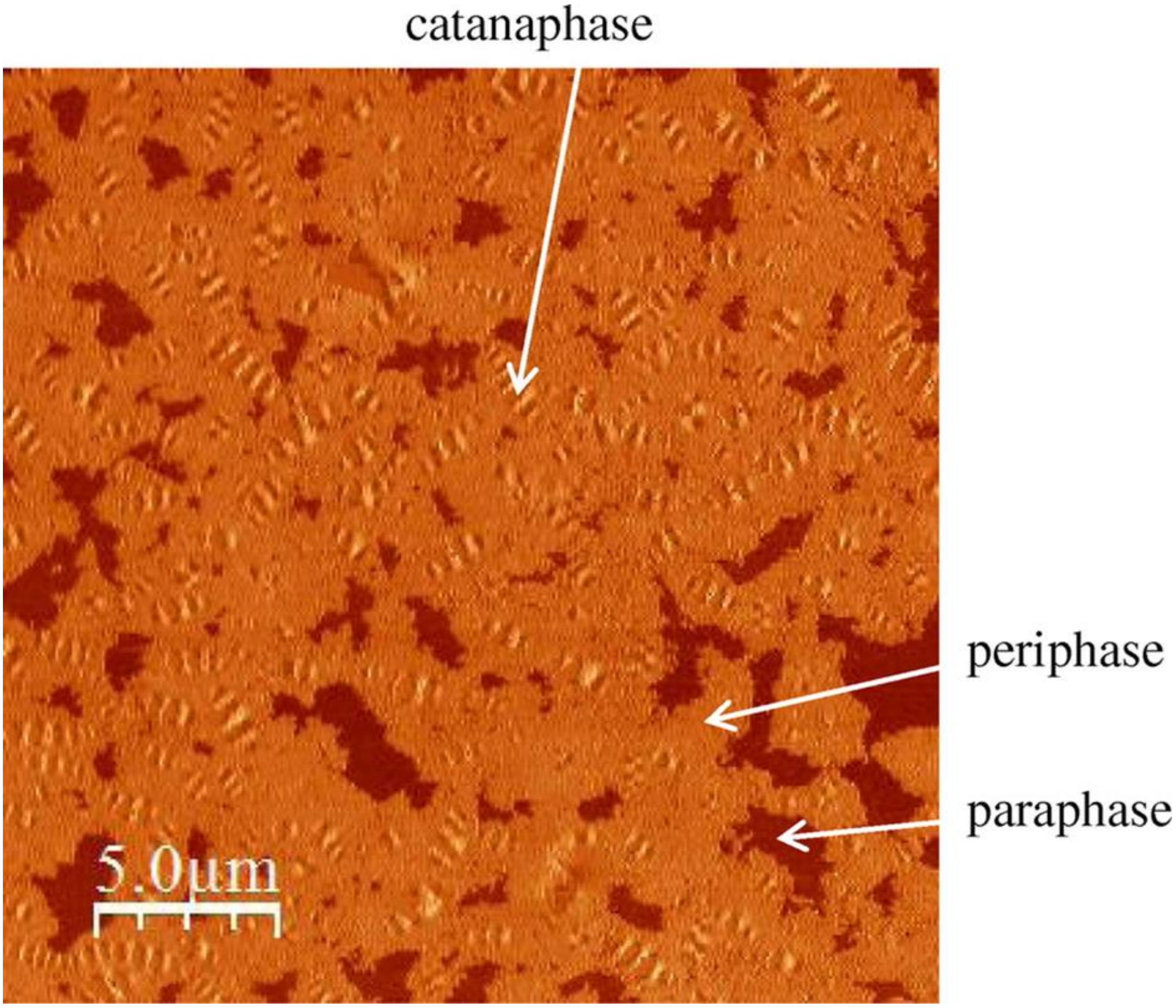

Source: Veytskin et al. (2016).

Variations of the bee-like structure or so-called catana phase have previously been attributed to asphaltenes. However, recent works have suggested that the bee structures are related to wax or the composition of asphaltenes with other maltene phases in the binder. Any bitumen treatment can affect the formation or reduction of the bee-shape network (De Moraes et al. 2010; Loeber et al. 1998).

9 MICROSTRUCTURAL INTERACTION OF NANOSILICA AND BITUMEN

The molecules of silicon dioxide (SiO_2) are non-polar in their structural arrangement. However, the angstrom-sized molecules are agglomerated into NS particles. In the agglomerated condition, they might have minor polarity due to their spatial shape. Likewise, some coatings such as silane couplant, can alter the surface polarity of the NS particles and make them more compatible with the polar environment that exists within bitumen.

Considering the colloidal model as a basis, silane coated NS is supposed to act as a compatibility agent and reinforce the bonds between the polar and non-polar zones. In addition, NS particles can fill the micropores in the asphaltene stacks and improve their surface interaction with aromatics and resins.

Silane coated NS is expected to interact more effectively with both polar and non-polar entities of bitumen which in turn contribute to the improvement of the properties. Providing high dispersion is essential so that particles can establish a strong interfacial attraction with the polar molecules and create a nanocomposite structure.

10 SUMMARY OF RESULTS FOR NS-MODIFIED BITUMINOUS MIXES

The review of literature shows that there have been about 13 articles regarding NS inclusion in bituminous mixtures. Each has concentrated on a series of examinations, which cover multiple methodologies. This is due to different materials (aggregate type, bitumen source, mixture designs), testing methods or standards. Some of the information about blends and testing methods is summarised in Table 10.1. This diversity makes it difficult to make meaningful comparisons. Nonetheless, these have been very helpful to optimise or improve the further steps of this study. As shown in Table 10.2, in most of the cases rutting, ageing and fatigue resistance are improved in some way.

Other properties such as storage stability have been improved after NS introduction to mixes. Storage stability is defined as the difference between the softening point of samples taken from the top and the bottom of the specimens (Alhamali et al. 2016; Fini et al. 2015; Zafari et al. 2014). This difference should be less than 2.5 °C (ASTM D5976-00).

Moisture-induced damage also is evaluated by means of adhesion, cohesion and tensile strength ratio (TSR) experiments. All imply that stripping of binder and ravelling of aggregates is reduced (Baldi-Sevilla et al. 2016; Yang & Tighe 2013).

The different test methods or approaches that have been implemented indicates careful attention should be given to further laboratory work. Reviewing Table 10.3 and comparing it with the testing plan of this study provides enough certainty that the applicable test methods have been considered in this study.

Table 10.1: Summary of NS application in asphalt mixtures

Author	Nano particles	NS Source	Nano percentages	Bitumen type	Asphalt testing	Chemical tests	Rheological test	Morphological study	Mixing method
Yao (2013)	NS	MTI Corporation (U.S.A.)	4% and 6%	PG 58-34	YES	FTIR	Rotational viscosity (RV), DSR, bending beam rheometer (BBR), RTFO, PAV	SEM	High shear rate machine (Silverson L4RT-A) at 130°C and blended using a shear rate of 4,000 (rpm) for two hours
Zafari (2014)	NS	Neutrino Corporation	2%, 4% and 6%	60/70	NO	FTIR	RTFO - Storage Stability - MSCR (creep) test at 50°C after RTFO	SEM	IKA®bench top high shear mixer at 4000 rpm for 2 hours
Yusoff (2014)	NS			PG-76	YES				
Zhang (2015)	NS, Nanozinc oxide and nanotitanium dioxide	Zhoushan		60/80		FTIR	RTFO, PAV	SEM	150°C at a rate of 5,000 rpm for 1h
Fini (2015)	NS	Neutrino Corporation		60/70	YES	FTIR			180°C at a rate of 4,000 rpm with a high-shear mixer for 2h
Sadeghpour (2015)	NS	Sigma-Aldrich, USA		60/70					
Ezzat (2016)	NS							TEM/XRD	
Baldi (2016)	NS, Diatomite		2%, 4% and 6%		NO	SFE , IR spectra	DSR , MSCR , PAV		Low shear stirrer at 175°C for 1.5 h
Alhamali (2016)	NS-PMB		2%, 4% and 6%	PG-76	NO		RV, DSR, storage stability test	SEM, BSE, EDS	163°C at rate of 3000rpm for 1h
Sun (2017)	NS, CaCO3, montmorillonite, TiO2, ferric oxide (Fe2O3), ZnO, and bentonite. Their particle sizes are 15, 30, 25, 35, 20, 30, and 25 nm, respectively.				YES	FTIR, gel permeation chromatography (GPC), differential scanning calorimetry (DSC)	DSR, BBR, softening point (SP), ductility at 10°C, and Brookfield viscosity at 60°C, Zero Shear Viscosity Test (ZSV)	SEM	170°C; 5,000 rpm; 30 min
Enieb (2017)	NS		2%, 4% and 6%	60/70	YES	FTIR	RV , SP and Penetration Index (PI)	TEM	160°C at a rate of 2000 rpm for 1 h
Crucho (2018)	NS, zero-valent iron and bentonite			35/50					160°C at a rate of 2000 rpm for 1h

Table 10.2: Summary of results obtained for NS effects (indicative %)

Author	Nano particles	Nano percentages	Bitumen type	Penetration	Softening Point	Viscosity	Ductility	Rutting	Ageing	Fatigue
Yao (2013)	NS	4% and 6%	PG 58-34			- 4%		+ 50%	+ 12%	+ 20 to 30%
Sarsam (2013)	NS	1%, 2%, 3%, 4%	40/50	-19%	+14%	+37%				
Zafari (2014)	NS	2%, 4% and 6%	60/70	-26%	+23%	+	-82%	+25%	+30 to 40%	
Yusoff (2014)	NS	2%, 4%	PG-76					+ 50% to 60%	+ 50%	+
Zhang (2015)	NS, Nanozinc oxide and nanotitanium dioxide	1.86-1.98%	60/80	- 6%	+4%	%14%	-15%		+	
Fini (2015)	NS	2%, 4% and 6%	60/70	-25%	+23%		-82%	+40%	+25 to 35%	+30%
Sadeghpour (2015)	NS	2%, 4% and 6%	60/70	-20%	+14%		-19%	+40%		+
Baldi (2016)	NS, Diatomite	2%, 4% and 6%							+	
Ezzat (2016)	NS	3%, 5% and 7%		-20%	+17%	+25%		+30 to 35%	+50%	
Alhamali (2016)	NS-PMB	2%, 4% and 6%	PG-76	-	+20%	+35%	-	+50%		+45%
Sun (2017)	NS, CaCO3, montmorillonite, TiO2, ferric oxide (Fe2O3), ZnO, and bentonite.	3%, 5% and 7%	AH-70	-6%	+12%	+37%	-	+40%		
Enieb (2017)	Ns	2%, 4% and 6%	60/70	-50%	+20%	+33%	-	+25%	+	+42%
Crucho (2018)	NS, zero-valent iron and bentonite	4%	35/50	-39%	+7%	+51%		+42%	+	

Table 10.3: Summary of test methods utilised during NS effects investigations

Author	NS (%)	Bitumen type	Viscosity	Rutting	Ageing	Fatigue	Other
Yao (2013)	4% and 6%	PG 58-34	RV	DSR/Wheel Track	RTFO/PAV/FTIR	DSR	AMPT
Sarsam (2013)	1%, 2%, 3%, 4%	40/50	BK				AMPT
Zafari (2014)	2%, 4% and 6%	60/70		DSR	RTFO/FTIR	DSR	Storage stability
Yusoff (2014)	2%, 4%	PG-76		DSR	RTFO/PAV		TSR/AMPT
Zhang (2015)	1.86-1.98%	60/80	RV		FTIR		
Fini (2015)	2%, 4% and 6%	60/70		DSR	RTFO/FTIR	DSR	
Sadeghpour (2015)	2%, 4% and 6%	60/70		DSR/Wheel Track		DSR	AMPT/IDT
Baldi (2016)	2%, 4% and 6%				FTIR	DSR	SE/MSCR
Ezzat (2016)	3%, 5% and 7%		RV	DSR	RTFO	DSR	
Alhamali (2016)	2%, 4% and 6%	PG-76		DSR		DSR	Storage stability
Sun (2017)	3%, 5% and 7%	AH-70		DSR	FTIR/GPC/DSC/BBR	DSR	ZSV
Enieb (2017)	2%, 4% and 6%	60/70	RV		FTIR		TSR/AMPT/IDT
Crucho (2018)	4%	35/50		DSR/Wheel Track		4PB	TSR/IDT

11 IMPORTANT LESSONS FROM THE LITERATURE REVIEW

The following remarks summarise the findings taken to the binder-level program of the study from the literature reviewed:

- The experimental data reviewed does not show any controversial results, and there is general agreement when performance parameters are evaluated.
- Achieving a balance between cohesion and adhesion of aggregate and bitumen is a good approach to determine the optimal NS content. However, asphalt mix performance tests are the main criteria to indicate the optimal NS content.
- Details of mixing methods indicate that the best method depends upon achieving a balance between dispersion qualities and ageing, which may occur during mixing.

12 METHODOLOGY

12.1 Introduction

This study aims to provide insights about NS modified batches of bitumen with respect to bitumen classes commonly used in practice in WA, namely C320, A15E and C600. The types of NS particles considered are 20–30 nm, 60–70 nm and 20–30 nm NS particles coated with silane. Characteristics such as rutting, fatigue performance and ageing resistance are expected to be improved, which can be reflected partly in conventional properties such as viscosity, penetration value and softening point.

All these properties are dependent upon the quality of mixing. As such, various SEM imaging techniques are employed to capture the status of the nanoparticles in different batches after dry and wet mixing.

The dry mixing method seems to be simpler than the wet method. However, efficiency and safety are the key indicators in selecting the best option. Therefore, a brief investigation into the chemical compatibility of dispersed NS in bitumen and different solvents was conducted before selecting a wet mixing method.

12.2 Materials

12.2.1 Bitumen

The C320 bitumen was sourced from Puma Bitumen. C600 and A15E binders were sourced from SAMI Bitumen Technologies. Its conventional properties and rheological behaviour were analysed. It is produced according to AS 2008-2013 (Standards Australia 2008). It is the most versatile and widely used bitumen for hot mix asphalt (HMA) in a wide range of applications (Austroads 2017).

12.2.2 Nanosilica

Two size ranges, 20–30 nm and 60–70 nm, of NS particles were used in this study to investigate the effects on the bitumen under the mixing conditions. The material was purchased from US Research Nanomaterials Inc., the main producer of all NS sizes with and without couplant, who are based in Houston, Texas, USA. In Australia 60 nm size NS can be purchased from Sigma Aldrich. The NS contents evaluated were 2%, 4% and 6% by weight of the bitumen as suggested by Farhad et al. (2014). Table 12.1 and Table 12.2 list the compositional analysis and physical characteristics of the NS particles in this study.

Table 12.1: Silicon oxide nanopowder SiO_2 certificate of analysis

Size	**SiO2**	**Ti**	**Ca**	**Na**	**Fe**
60-70 nm	> 98%	< 220 ppm	< 130ppm	< 80ppm	< 40ppm
20-30 nm	99.50%	120ppm	70ppm	30ppm	20ppm
20-30 nm	96.3+wt%: 3-4wt% (SiO_2: KH550)	< 120ppm	< 20ppm	< 50ppm	< 200ppm

Table 12.2: Physical properties of silicon oxide nanopowder SiO_2

Asymmetric particles (APS)	60-70 nm	20-30 nm	20-30 nm (with 3-4wt% KH550 couplant)
Purity	98+%	99.50%	96.3+%
SSA	160-600 m^2/g	180-600 m^2/g	130-600 m^2/g
Colour	White	White	White
Bulk density	< 0.10 g/cm^3	< 0.10 g/cm^3	< 0.10 g/cm^3
True density	2.4 g/cm^3	2.4 g/cm^3	2.4 g/cm^3
Manufacturing method	High-temperature combustion	High-temperature combustion	

The silane coupling agent KH-550 is aminopropyltriethoxysilane (formula: $C_9H_{23}N_2O_3Si$, CAS:919-30-2), which is colourless or a slightly yellow transparent liquid, soluble in benzene, ethyl acetate and reactive with water. It is super oleophilic, hydrophilic and easily dispersed, suitable for oily and waterborne systems.

12.2.3 Details of batches

The percentages of NS in bitumen mixtures are selected to replicate the prominent mixes in the literature. This study deviates from those in the literature by evaluating multiple NS sizes, and different mixing conditions with C320 bitumen. Table 12.3 shows that all the NS-modified mixtures range between 2% and 6%.

Table 12.3: Mixture details for dry mixes

Mix ID	Ns type	Ns (%)
BTD2	20-30 nm with 3-4% KH550	2
BTD4		4
BTD6		6
20BRD2	20-30 nm	2
20BRD4		4
20BRD6		6
60BRD2	60-70 nm	2
60BRD4		4
60BRD6		6

All the tests conducted in this study were on virgin C320 bitumen to establish a baseline for modification. Thereafter, virgin C600 bitumen and polymer modified A15E binder was also tested, to explore the differences in their characteristics. C600 and polymer modified A15E is used in WA in wearing or intermediate course asphalt mixes.

Since the NS mixing method also influences the results, some DSR tests were undertaken on wet mixes. The details of the mixing methods are explained in the next sections. Table 12.4 lists the batches tested using the wet method. The concentration of NS was increased to 8% for the wet mixes.

Table 12.4: Mixture details for wet mixes

Mix ID	Ns type	Ns (%)
20CW2	20-30 nm with 3-4% KH550	2
20CW4		4
20CW6		6
20CW8		8
20W2	20-30 nm	2
20W4		4
20W6		6
20W8		8
60W2	60-70 nm	2
60W4		4
60W6		6
60W8		8

12.3 Sample Preparation

12.3.1 Dry mixing method

The sample preparation of bitumen is referred to in Australia Standard AS 2341.21-2015. The preparation of bitumen must be done carefully because heating of bitumen in the presence of water may foam excessively and spatter or overflow the sample containers. Before heating the bitumen, physical inspection was done to ensure that no water or layer of condensate exists on the surface of the bitumen. In general, the two different preparation methods are called the hotplate method and the oven method.

In this research, both the hotplate and oven facilities are used for the preparation of NS-bitumen samples. Initially, around 20 litres of bitumen in a metal pail were placed in the oven and heated up to a temperature of 130 °C. This takes around 1 to 2 hours. The required time depends on the temperature and weight of bitumen. When the temperature of the heated sample reaches 130 °C, the bitumen is stirred with a spatula to disperse any unmelted bitumen and to remove additional air bubbles. Then about 2 litres of hot bitumen were poured into a smaller container and placed on the hotplate. The NS was then added into the bitumen at 2%, 4% and 6% (by weight of the bitumen).

NS is lighter than bitumen and therefore floats on top. The NS is introduced slowly into the container on the hotplate to avoid spillage or dispersion into the air. In this case, nearly 20 minutes were needed for full absorption of the dry and fluffy NS particles while blending with a Silverson mixer as shown in Figure 12.1. The mixer is set to a rotational speed of 4000 rpm for 2 hours while the temperature was maintained at 130 °C for all samples (after Yao et al. 2013). After mixing was completed, the hot sample was transferred and split into 150 ml containers for further testing.

Figure 12.1: Silverson high-shear mixer

12.3.2 *Wet mixing method*

The wet mixing method consists of using a chemical solvent to better disperse the NS particles within the bitumen. The solvent can be utilised in two ways, namely simple wet mixing and in master batches.

Simple wet mixing

In this method, NS was simply added to the solvent to make a gel-like mix before introducing it to the bitumen. The solvent was expected to evaporate during mechanical mixing. The solvent used was required to have the following characteristics:

- bitumen solubility in solvent
- compatibility with NS
- impregnation (volatility).

Among a broad range of solvents, kerosene, unleaded fuel 91 (petrol) and mineral turpentine, which are petroleum-based solvents, were selected. These seem to be more compatible with bitumen in their molecular shape. Acetone and similar solvents or diluents may have elements which do not interact well with bitumen.

As a trial, 6% by weight of bitumen of 60 nm NS was mixed with kerosene (Diggers kerosene) and petrol (unleaded 91 research octane number (RON)). Petrol and kerosene of 10 and 20 % (by weight of bitumen) were mixed with NS before adding to C320 bitumen. Figure 12.2 shows the morphology of NS and 20% solvent, which resembled ice-shake-like pastes.

Figure 12.2: Wet mixes with 20% solvent

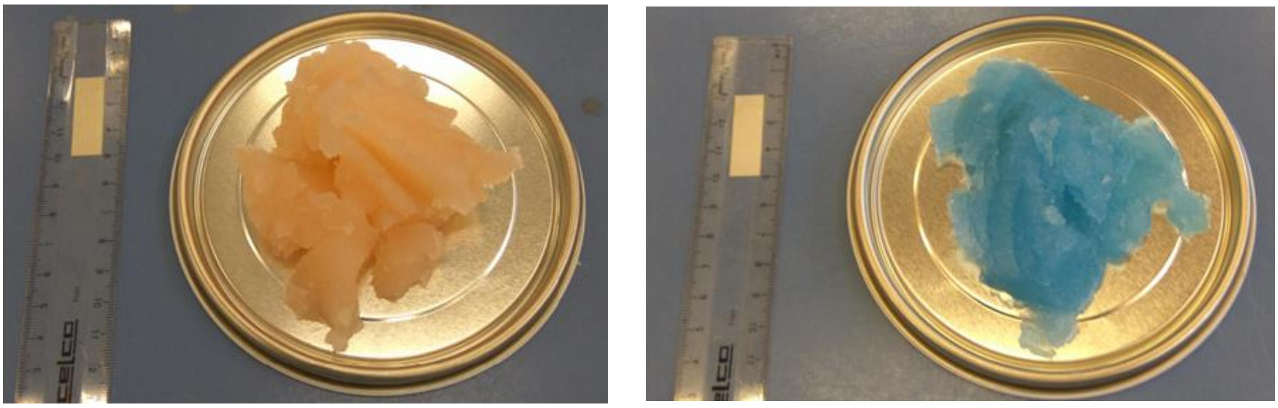

(I) Unleaded 91

(II) Kerosene

Figure 12.3 shows the evaporation rate of NS solvent during blending with bitumen using a Silverson mixer for 120 minutes at 130 °C and 4000 rpm for unleaded petrol and kerosene respectively.

Figure 12.3: 20% solvent loss within C320 bitumen

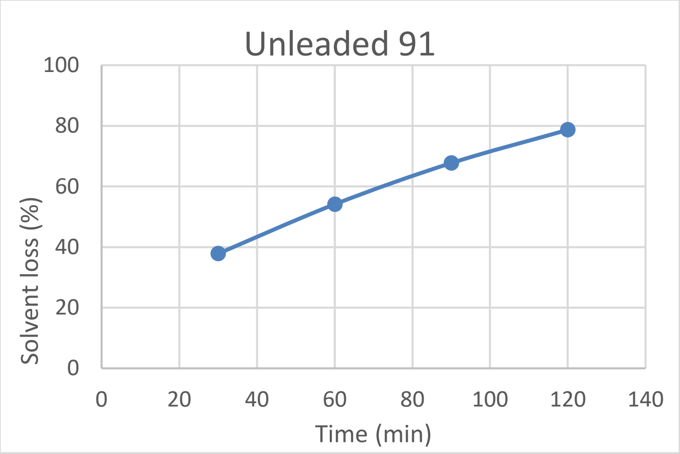

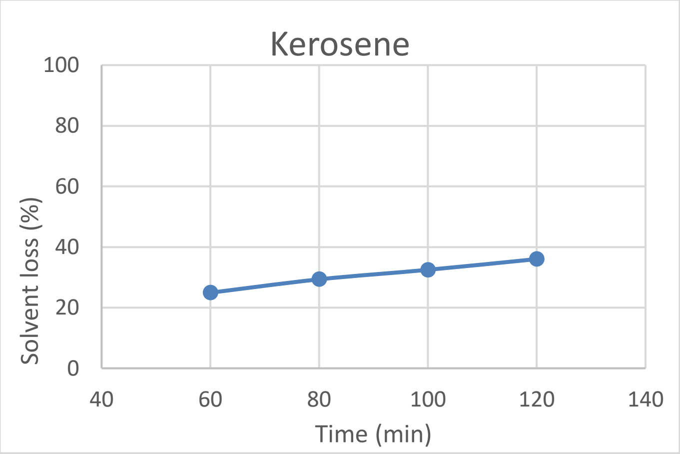

This figure shows that kerosene does not fully evaporate during mixing. The weight loss trend indicates that 6 to 8 hours is required for kerosene to fully evaporate, which will result in excessive ageing of the bitumen.

Master batches

An alternative approach to wet mixing is to make master batches. Typical master batches include dissolution of 40% 60 nm NS with 60% C320 bitumen within turpentine. The solution is kept at 60 °C in an oven which accommodated an ultrasonic mixer. The solution is agitated for 24 hours. At the end, semi-solid particles of bitumen mixed with NS remain. The solvent must be fully evaporated in this method. Then, these particles can be easily mixed with the virgin bitumen. Figure 12.4 shows the methodology in this approach. Figure 12.5 shows a resultant master batch sample.

Figure 12.4: NS60 nm and C320 bitumen master batch

Note: Ultrasonic mixing.

Figure 12.5: NS 60 nm master batch sample

Note: Semisolid particles.

In this case NS was easily added to a dilution of solvent (typically turpentine) to give a potentially higher dispersion quality binder. This approach has been carried out for all the wet sample combinations considered in the study.

Solubility

Some solvents, such as commercial kerosene, commercial turpentine and pure n-heptane were investigated for solubility. The solution kinetics of bitumen in a given solvent depend on temperature, the intensity of the agitation, the contact surface or the shape and size of the particles in the solvent, the bitumen and the solvent composition. Typically, 5% (by weight) of bitumen in the above solvents was prepared in the study. The bitumen was dissolved completely in all three solvents as shown in Figure 12.6 and Figure 12.7. Asphaltene precipitation occurred in n-heptane.

Figure 12.6: Virgin bitumen (75 mg) in commercial kerosene at 25 °C (t = 0.0 min.)

Figure 12.7: Complete dissolution of virgin bitumen in commercial kerosene at 25 °C (t = 12.0 min.)

Compatibility

The NS samples were impregnated with solvents in a dropwise manner. All NS samples were compatible with the solvents and formed a gel as shown in Figure 12.8.

Figure 12.8: Compatibility of nanosilica samples with kerosene

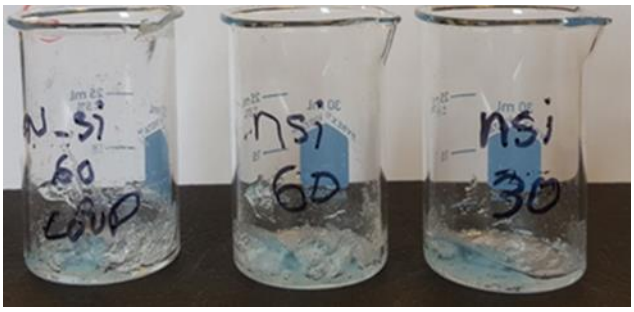

Impregnation

A sample of NS (60 nm) in turpentine (17% wt) gel was prepared, weighed and placed in an oven at 70 °C for 24 hours. After this period, less than 1% of turpentine remained and the NS was almost dry as shown in Figure 12.9. This was done to make sure that the solvent can evaporate fully.

Figure 12.9: Nanosilica-turpentine gel – in dried condition

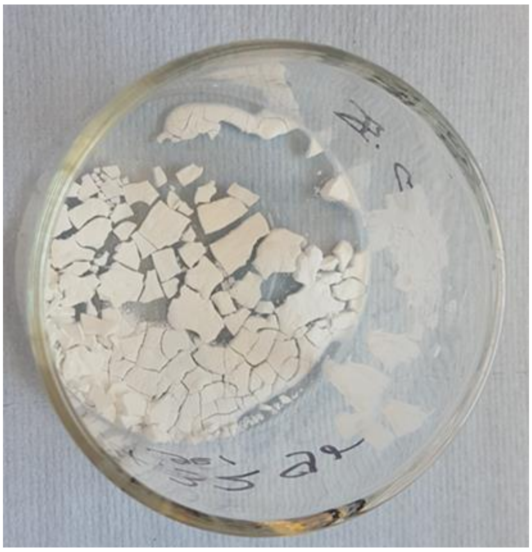

12.3.3 Short-term ageing (RTFO)

The rolling thin film oven (RTFO) test (Figure 12.10) was conducted to simulate the short-term ageing, similar to the ageing during asphalt production. A detailed procedure for the RTFO test can be found in Australian Standard AS 2341.10-2015. Bitumen samples of 35 ± 0.5 g are poured into each glass bottle. Then, the bottles are loaded carefully into the carriage (see Figure 12.11). The RTFO oven is preheated to 163 ± 0.5 °C for 30 minutes without rotating the carriage and no air-flow supply, to ensure a stable sample condition. The glass bottles are then rotated for 60 minutes at 163 ± 0.5 °C while air is blown through the nozzles into the bottles at a rate of 4.0 ± 0.5 L/min. At the end of the ageing process, the bottles are drained into containers until the bitumen has stopped dripping.

Figure 12.10: Rolling thin film oven (RTFO)

Figure 12.11: Rotating bottle carriage of RTFO

12.3.4 *Long-term ageing (PAV)*

Long-term ageing generally occurs when pavements are exposed to atmospheric conditions during road operation. In the laboratory, the pressure ageing vessel (PAV) uses heated, pressurised air to simulate the long-term oxidative ageing of asphalt binders. Testing can be done according to AASHTO R28, ASTM D6521 or EN 14769 requirements. The Austroads test method AGPT/T194 describes the PAV and associated DSR test methods. According to this method, 15.6 ± 0.5 g of bitumen is poured into pans to provide a nominal 1.0 mm film after heating and evenly spreading in the pans of the vessel. A temperature of 100 ± 0.5 °C and air pressure of 2.1 MPa is maintained within the vessel for 72 hours ± 30 minutes. Afterwards, the residue should be collected from the pans. Heating to 163 °C has been found to be suitable to allow pouring of the aged binder into a container.

12.3.5 *Long-term ageing (3 x RTFO)*

In Europe, there are other ageing protocols available which have not yet been standardised (Besamusca et al. 2012). For instance, 3 x RTFO ageing is suggested to be equivalent to PAV ageing. Since PAV is carried out at a lower temperature (90–100 °C) compared with RTFO (163 °C), it is considered to be more representative of field ageing.

The correlation of PAV ageing with 3 x RTFO performed at 163 °C has been criticised because at temperatures higher than 100 °C the chemical mechanisms of ageing are different, while the temperature of long-term ageing on the road network can be in the region of 40–70 °C.

This study undertook 3 x RTFO only on NS-modified samples with couplant in the dry mixed condition. This was to see whether PAV ageing can be replaced by 3 x RTFO for the purpose of understanding the ageing process with rheology tests.

12.4 Experimental procedures

In this study, the dry mixing method was the main procedure to incorporate NS. Likewise, most of the experimental tests were carried out on dry mixed NS-modified batches. However, wet mixed samples (by the masterbatch technique) were also tested using the DSR to evaluate the differences in properties compared with dry mixed samples.

12.4.1 Penetration test

The penetration test was used to characterise the hardness or consistency of bitumen. The vertical penetration of a standard needle into the bituminous material under specific conditions of load, time and temperature is measured in tenths of a millimetre (dm) and reported in penetration units (1 penetration unit (pu) = 0.1 mm). The needle falls under a 100 g mass loading at a constant temperature of 25 °C for 5 seconds. The needle used in the penetration test should comply with Australia Standard AS 2341.12-1993. The equipment used for the test is a penetrometer as shown in Figure 12.12.

Figure 12.12: Penetrometer

The test procedure involves pouring bitumen into a cylindrical metallic container, which is 55 mm in diameter and 35 mm in depth. This is then allowed to cool down to ambient temperature on a non-conductive surface for 60 ± 5 minutes. Then, the sample container is submerged into a water bath at a temperature 25 ± 0.1 °C for another 60 ± 5 minutes. The tip of the needle should just be in contact with the bitumen sample surface before releasing it under load for 5 seconds and recording the penetration result. Three values are recorded from positions more than 10 mm apart and more than 10 mm from the side of the container. The result is only valid when three results obtained are close enough to each other based on Table 12.5. Otherwise, the sample should be discarded and the test repeated. For a complete procedure of the penetration test, refer to Australian Standard AS 2341.12-1993.

Table 12.5: Penetration result for validity

Penetration (pu)	Maximum difference between highest and lowest determination
0 to 49	2
50 to 149	4
150 to 249	6
Above 250	8

12.4.2 Viscosity tests

Viscosity tests measure the viscosity of bitumen at the specified temperature and inform the fluidity of bitumen for proper pumping, aggregate coating, mixing and laying of asphalt material. Common standard test methods are:

- AS 2341.2 *Determination of dynamic viscosity by flow through a capillary tube*; Austroads Test Method AG-PT/T161
- AS 2341.3 *Determination of kinematic viscosity by flow through a capillary tube*
- AS 2341.4 *Determination of dynamic viscosity by a rotational viscometer*.

In the capillary tube method, the time required for bitumen to flow between two marks is defined as viscosity at 135 °C or 60 °C. Rotational viscometers work on the basis of required torque to rotate the spindle at the specified shear rate in an annular space between two concentric cylinders. Test results are expressed as 1 Pa.s = 10 P (poise) for the dynamic case. In the kinematic case, viscosity is denoted in mm^2/s ($1\ mm^2/s$ = 1 centistokes) which can be converted to Pa.s by multiplying by the density of the bitumen.

In this research, a Cannon-Manning vacuum capillary viscometer for kinematic viscosity at 60 °C and a Brookfield thermosel for dynamic at viscosity 135 °C measurements were utilised.

12.4.3 Softening point

Softening point is defined as the temperature at which a bitumen sample can no longer support the weight of a 3.5 g steel ball. The steel ball is placed on top of a bitumen film in a brass ring. The whole assembly is suspended in a water bath (when the softening point is over 80 °C) or a glycerine bath (when the softening point is under 80 °C). According to Australian Standard AS 2341.18 (1992), the temperature of the bath is increased by 5 °C per minute increments until the steel ball goes through the ring. The softening point is the temperature of the bath when the ball touches the base plate, which is 25 mm below the ring.

12.4.4 Dynamic shear rheometry

The dynamic shear rheometer (DSR) (Figure 12.13) and the rotational viscometer are used to measure the viscoelastic properties of bituminous binder. It is important to demonstrate the changes in engineering properties and viscosity at high and low in-service temperatures. DSR testing can determine the acceptable range of temperatures at which a binder should be used in the American performance grade (PG) binder classification system.

In addition, the DSR is an ideal instrument to conduct experimental tests and examine changes in the level of micromechanical properties of a binder under different conditions such as temperature, loading regimes and chemical compositions.

Multiple test procedures using this equipment measure the rheological properties such as complex shear modulus $|G^*|$, complex shear compliance (J_{nr}), and phase angle (δ) at low to high temperatures.

Figure 12.13: Dynamic shear rheometer

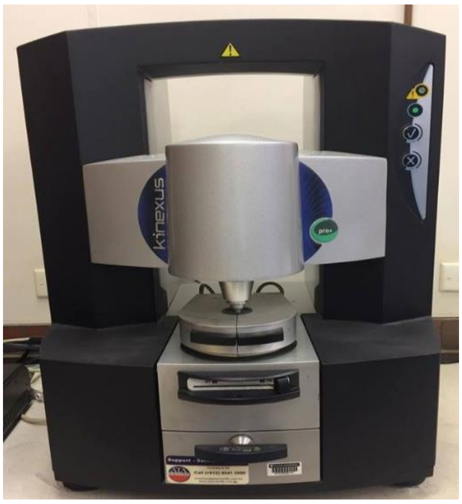

The DSR used in this research was a Kinexus Pro+ from Malvern. It was controlled by rSpace software. This machine has a torque capacity of 2.0 nNm to 200 mNm. The machine is equipped with cartridge environmental controllers to provide a temperature range of 40 °C to 200 °C (active hood cartridges).

The details of standard testing procedures for bitumen rheology are given in Austroads standard AGPT-T192-15, MRWA test method WA716.1-2018 and ASTM D7175-15. A film of bituminous binder is sandwiched between two parallel plates, which is called the testing geometry. The diameter of the specimen or size of the spindle plate depends on the torque of the DSR motor.

The DSR specimen size, thickness and other factors such as the smoothness of the contact surface, and the uniformity of the bulge at the side of the specimen all have an influence on the results. Therefore, selection of a larger plate size is preferred as it can reduce likely defects.

Usually a circular, flat geometry 25 mm diameter plate and a bitumen film thickness of 1 mm is used for unaged samples at intermediate to high temperatures. Silicone moulds are used to ensure the correct geometry and proper placement between the plates as shown in Figure 12.14. However, direct pouring was also used for testing of soft binder samples. For aged samples or low to intermediate temperatures an 8 mm plate diameter with a 2 mm bitumen film thickness can be used. During the test, a defined oscillating strain or torque with frequency of 10 rad/sec (1.59 Hz) is applied on the upper plate while the lower plate remains fixed and the angular resistance or rotation is measured. Recording the deformation or torque provides the initial data for the interpretation of the material response.

Figure 12.14: DSR test

25 mm sample 8 mm sample

Ultimately some judgment on the potential rutting and fatigue resistance of asphalt mixes can be made from the rheology results of the constituent binder for early and long-life performance of the pavement during its service life. The DSR tests are conducted on unaged, short-term aged and long-term aged samples.

The complex shear modulus (G*) is defined as the summation of the elastic or storage modulus (G’) and the viscous or loss modulus (G”) as per Equations 7, 8 and 9 (Schramm 1994).

$$G^* = G' + iG'' \tag{7}$$

$$G' = G^*.\cos(\delta) \tag{8}$$

$$G'' = G^*.\sin(\delta) \tag{9}$$

where

G^* = complex shear modulus

G' = storage modulus

G'' = viscous or loss modulus

δ = phase angle

The phase angle (δ) is the time lag between the applied shear stress and observed shear strain during oscillatory loading.

The rutting parameter or G*/sin(δ) is determined by DSR testing on a binder at 60 °C and a frequency of 10 rad/s. Kandhal and Foo (1997) found G*/sin(δ) to be a parameter to assess the rutting resistance of an asphalt mixture based on the work-energy principle. Lower values may imply higher vulnerability of the resultant mixture made from the binder to rutting.

In the USA the G*/sin(δ) values need to meet specific limits according to Strategic Highway Research Program (SHRP) binder specifications or ASTM D7175-15 as shown in Table 12.6.

Table 12.6: Target limits of G*/sin(δ)

Original binder	≥ 1.0 kPa
RTFO residue	≥ 2.20 kPa
PAV residue	≤ 5000.0 kPa

Note: Source ASTM D7175-08 15

The DSR test is performed at temperature of 40 °C to 70 °C at 6 °C intervals. After selection of the desired test sequence in the rSpace software, all test details are checked, and the loading of the sample is conducted automatically. This software collects all the rheological outputs in real time and reports results for each frequency. Output files include η* as complex viscosity. The complex viscosity (η*) at 60 °C, 1 rad/s and 10% strain is assumed to be equal to capillary viscosity of bitumen at 60 °C (Austroads AGPT/T192). Equation 10 is used to calculate complex viscosity.

$$\eta^* = \frac{G^*}{i\omega} \tag{10}$$

where

η^* = complex viscosity (Pa.s)

G^* = complex shear modulus (Pa)

i = complex number ($x^2 = -1$)

ω = angular frequency (rads^{-1})

As noted earlier, 3 x RTFO aged samples were also considered in this research. However, due to their higher stiffness, the 8 mm diameter plate geometry and 2 mm bitumen film thickness were chosen for testing this material.

12.4.5 Strain sweep

DSR testing can be undertaken at different temperatures, typically from 40 °C to 70 °C, to evaluate the rutting resistance at high temperatures. This can be done by coding a sequence within the rSpace software to facilitate the testing procedure.

Assuming linear viscoelastic conditions of the binder mixes, the responses of the DSR tests can be extended for a wide range of temperatures and frequencies in terms of complex shear modulus (G*) or phase angle (δ). The time-temperature superposition principle can be applied to generate new data from the data measured in the laboratory experiments. The linear viscoelastic region is assessed through the application of a range of strain levels and the measurement of complex modulus. G* should be constant over applied strain levels (ASTM D7175-08 15).

Superposition is the underlying principle for developing master curves and being in the linear viscoelastic region is important which should be checked while reviewing results. This will be explained in the following sections.

12.4.6 Multiple stress creep recovery test

The main objective of the MSCR test is to determine the creep compliance. In fact, it is the inverse of the binder stiffness which is determined though creep tests. In MSCR, the stress and strain of samples are recorded every 0.1 s, while these are measured every 0.25 s in a frequency sweep test.

MSCR tests here are conducted on unaged samples and RTFO aged samples using the DSR. The test is often conducted according to AASHTO T 350-14 specification at 64 °C, the temperature at which RTFO samples are recommended for MSCR testing. The samples are tested in creep and recovery at two stress levels of 0.1 kPa and 3.2 kPa. The non-recoverable creep compliance (J_{nr}) and percent recovery (%R) are the main parameters that are derived from analysing the MSCR test results. As noted earlier, the non-recoverable creep compliance (J_{nr}) is determined by dividing non-recoverable shear strain by the shear stress and better evaluates the rutting potential of a binder.

Creep is defined as strain increase with time at a constant stress. Under a constant stress, bitumen as a viscous material has instantaneous elastic deformation and with time continuous and steady creep deformation. As shown in Figure 12.15, stress removal results in partial recovery of strain with time. However, there will be some residual deformation that can be indicative of rutting in bituminous materials.

Figure 12.15: Creep concept

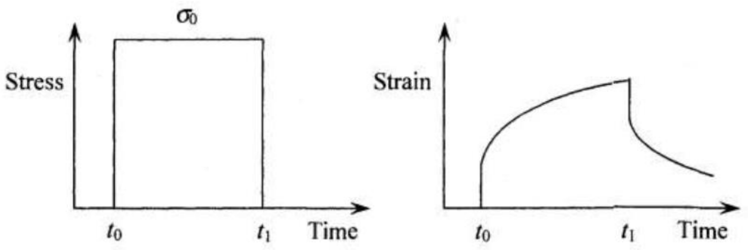

The MSCR test provides insight into the behaviour of bitumen at high temperatures. It more accurately indicates the rutting performance of the asphalt, since creep deformations are also recorded. Research by the Federal Highway Administration (FHWA) using the accelerated loading facility (ALF), has shown better correlations between rutting performance and J_{nr} from the MSCR tests compared to G*/sinδ from DSR tests. This MSCR test protocol aligns with the rutting definition as a progressive accumulation of longitudinal depressions in a wheel path under repetitive loading.

The MSCR test is based on the creep and recovery concept utilising multiple pulse loads to assess the permanent deformation of binder using a DSR. AASHTO T 350 describes the test procedure on RTFO aged bitumen samples.

In the early stages, a one-second creep load at a low stress (0.1 kPa) level is applied to the bitumen sample. After removing the one-second load, the sample is allowed to recover for 9 seconds. Then creep-recovery cycles are repeated 10 times. Following this, the stress level is raised to 3.2 kPa, and a similar loading pattern is repeated. In this research, the test is carried out on RTFO aged samples at a temperature of 64 °C.

The main parameter that is obtained from the MSCR test is the value of J_{nr}, which is the non-recoverable creep compliance (Equations 11 and 12) (D'Angelo et al. 2007). The sample size in the MSCR test is the same as in the conventional DSR test. A test plate of 25 mm diameter and a bitumen film thickness of 1 mm are used.

$$J_{nr}(0.1, N) = \frac{\varepsilon_{10}}{0.1} \qquad 11$$

$$J_{nr\ 0.1} = \frac{Sum[J_{nr(0.1,N)}]}{0.1} \text{ for N = 1 to 10} \qquad 12$$

J_{nr} = non-recoverable creep compliance (kPa^{-1})

ε_{10} = strain after 10 cycles

12.4.7 SARA determination by column chromatography

SARA fractioning was determined by using 20 to 35 mg of each bitumen sample. The bitumen sample was poured into a glass vial and dissolved with a known volume of dichloromethane. An aliquot of each solution was taken, containing ~ 8 mg of bitumen, and absorbed onto a small amount of silica gel (activated overnight at 160 °C). The dichloromethane was left to evaporate, and the dry silica containing the bitumen sample was transferred into a small column of activated silica gel with a Pasteur pipette (5.5 cm height, 0.5 cm internal diameter, pre-rinsed with hexane). Fractions were eluted into weighed glass vials using the solvent mixtures shown in Table 12.7. The asphaltene fraction remained in the column after the other fractions were eluted.

Table 12.7: Solvents for SARA fractioning

Saturates	100% hexane	3 mL
Aromatics	30% dichloromethane in hexane	4 mL
Resins	1:1 dichloromethane in methanol	4 mL

The three fractions were dried by evaporation under a gentle stream of nitrogen gas, and weighed to calculate the mass of saturates, aromatics and resins. These masses were subtracted from the mass of bitumen that was separated to determine the mass of asphaltenes that remained in the column.

12.4.8 Microstructural observations

Binder properties at different levels from the nano- to the micro-level have a critical role in the responses of bitumen to different loadings. Scanning electron microscopy (SEM) is a tool that can help to observe micro- to nanostructural changes in C320 bitumen after NS addition. There are a range of sample preparation methods and imaging techniques that can be used with the SEM. The key objectives are to have clear images with high resolution while the sample remains intact. However, some trades-off should always be made between image quality and the clarity of the object searched for.

Poor sample preparation can lead to erroneous diagnoses. Generally, SEM samples need to be conductive to carry high electron charges formed on the surface to earth. For unconducive samples, platinum, carbon or gold coating can render a thin conductive layer over the sample to help transit the electrons.

Discharge of electrons on a small area can heat up the sample to such an extent that any water or oil in the sample is evaporated. This may cause contamination of detectors in the SEM, which are costly and tedious to clean. As such, samples need to be oil free and dry for imaging within ordinary SEM equipment.

Loeber (1996) suggested five sample preparation methods for bituminous samples based on the standard method of ČSN 65 6073 in the Czech Republic. In these methods, the oily phase of bitumen is washed out by different solvents to get the asphaltene residue. These methods all involve the removal of oily compositions in bitumen, with dissolution in a solvent and filtration through paper.

A Soxhlet extractor was used in this study (Figure 12.16) to obtain the solid or asphaltene fraction of bitumen as a dry sample for SEM imaging. According to the method prescribed by ASTM D-3279-19, the sample of the bitumen was firstly dissolved in n-heptane as the solvent for at least 48 hours. That continued until no discolouration was observed in the reflux. Next, the extraction was performed by replacing n-heptane with toluene as the solvent for a further period of at least 8 hours until no further discolouration.

Figure 12.16: Soxhlet extraction facility

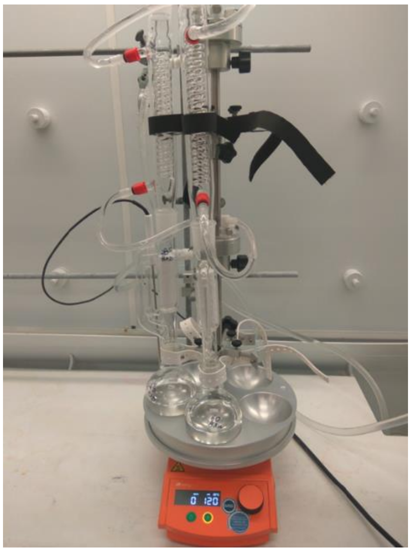

Finally, the extract was filtered and further dried at 100 °C under vacuum in an oven. The NS-asphaltene samples were sealed and stored in containers for further analysis (Figure 12.17).

Figure 12.17: Asphaltene particles with NS particles

In this approach the binder microstructure is disturbed and only asphaltenes and NS bundles are left for observation. The benefit of this method is that the size of the agglomerated NS clusters can be examined by the SEM. As explained in the literature review section, asphaltenes are more polar than aromatics and resins and are expected to interact with NS more. Thus, poor distribution of NS can be accompanied with a larger size of NS and asphaltene micelles.

In a second approach, the SEM is equipped with a cryogenic stage (Figure 12.18). In this case, the virgin binder sample is flash frozen using liquid nitrogen and then placed in the SEM chamber at around −150 °C at a pressure of 2.5 x 10^{-4} Pa. This approach helps to reduce changes in the binder structure although a high voltage 20 kV electron beam is applied (Yao et al. 2013).

Figure 12.18: SEM equipped with a cryogenic stage (Zeiss 1555 VP-FESEM)

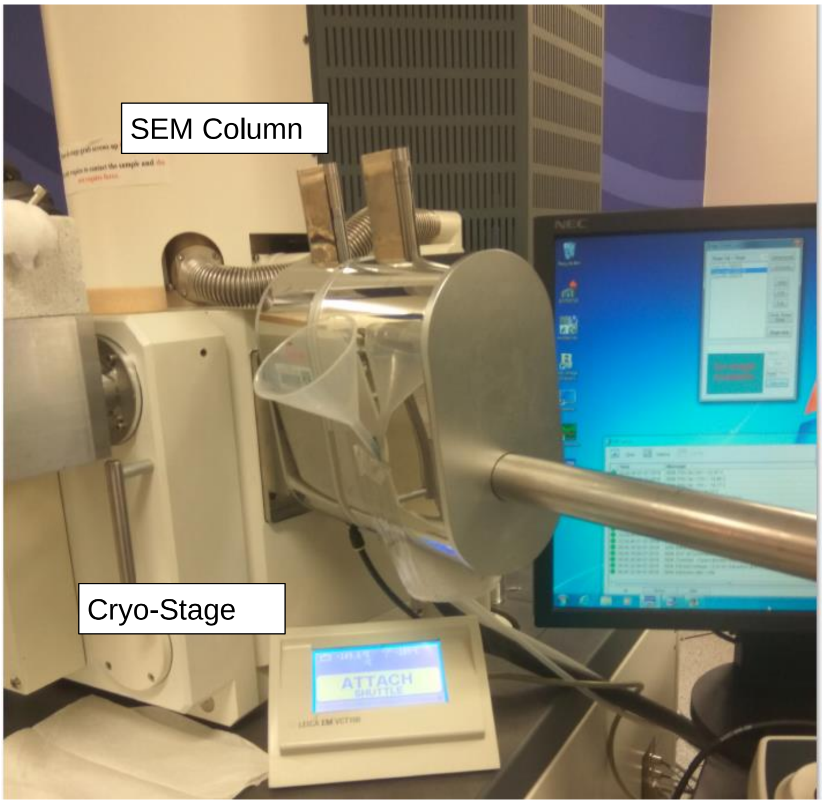

There is no need for special procedures for sample preparation. When the cryogenic-SEM sample holder is plunged into liquid nitrogen at -150 °C, the sample is frozen immediately and a thin layer of ice with some small crystals form on the surface. This influences the surface quality before conductive coating is applied and can induce some charging in the SEM images. Figure 12.19 shows rivets which have been plunged into bitumen to obtain thin coatings. These rivets are secured in the holes of the sample holder.

Figure 12.19: Rivets plunged in sample

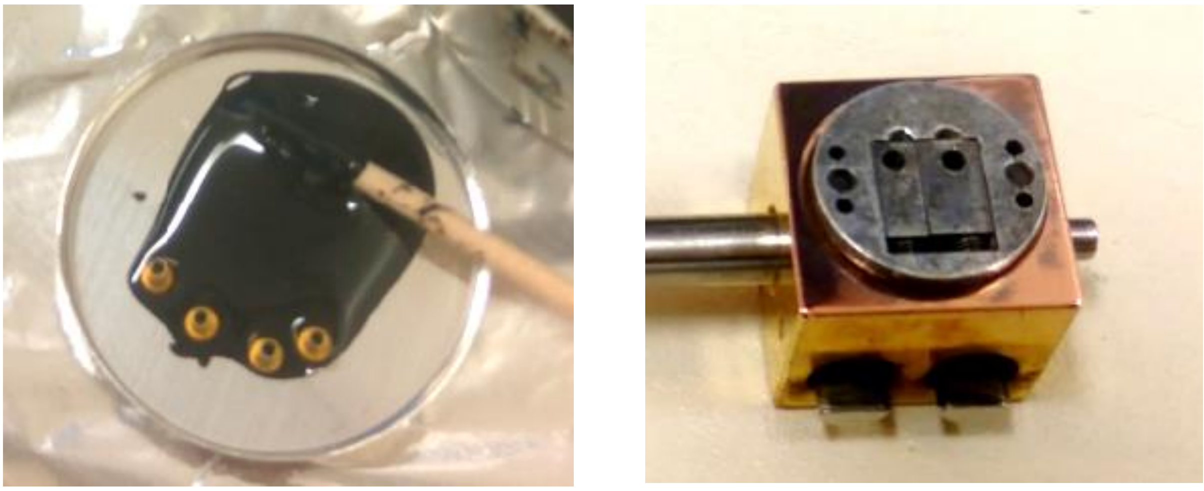

Bitumen

Sample holder in cryo-stage

This technique is used to make a fresh surface after freezing. Rivets are placed on top of the liquid bitumen (Figure 12.20). Then the sample is transferred to the sample preparation chamber filled with liquid nitrogen. After freezing, the rivets are displaced with a cool knife to expose the fresh bitumen surface.

Figure 12.20: Sample preparation for freezing

Bitumen between two rivets and the mount

Sample preparation chamber

This technique is called fracturing of samples as it induces some cracks on the surface as shown in Figure 12.21.

Figure 12.21: Fractured bitumen sample in the SEM

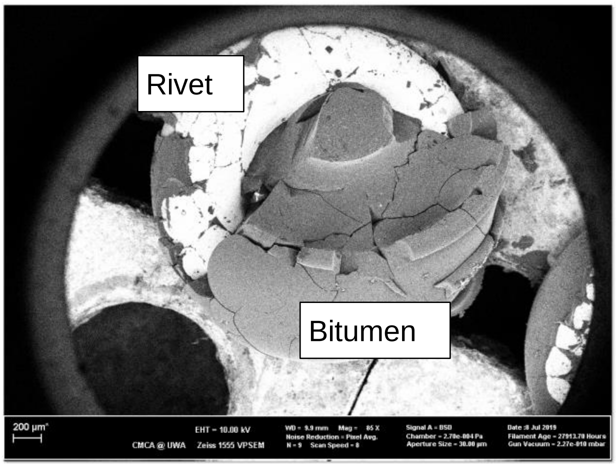

The quality of images from the first method without the cryogenic system was expected to be higher than with the cryogenic stage, as the SEM chamber operates at a higher vacuum condition. This is highly dependent upon the various capabilities of the SEM instruments used. However, the findings reflected in this report indicate that images of bitumen from the cryogenic-stage-equipped SEM at the University of Western Australia are clearer than the high-resolution SEM facility at Curtin University.

The composition of any area or particle in the SEM images can be determined by energy dispersive X-ray spectrometer (EDS) analysis. After bombarding samples with high-energy electrons, the ejected inner-shell electrons are replaced by outer-shell electrons. This replacement produces X-rays which are characterised to determine the chemical elements in the targeted point of the sample (Figure 12.22).

Figure 12.22: Distribution of elements in EDS layered image

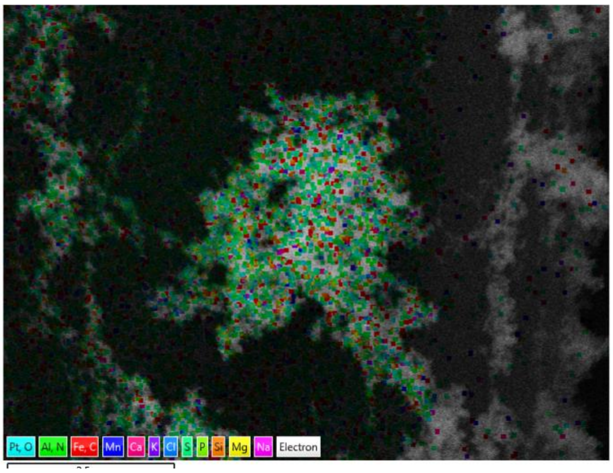

The spectrum of X-ray energy level versus the number of counts at each energy interval is the output as shown in Figure 12.23. The amplitude and location of the peaks in the spectrum are representative of the elements in the sample.

Figure 12.23: X-ray spectrum of elements measured by EDS

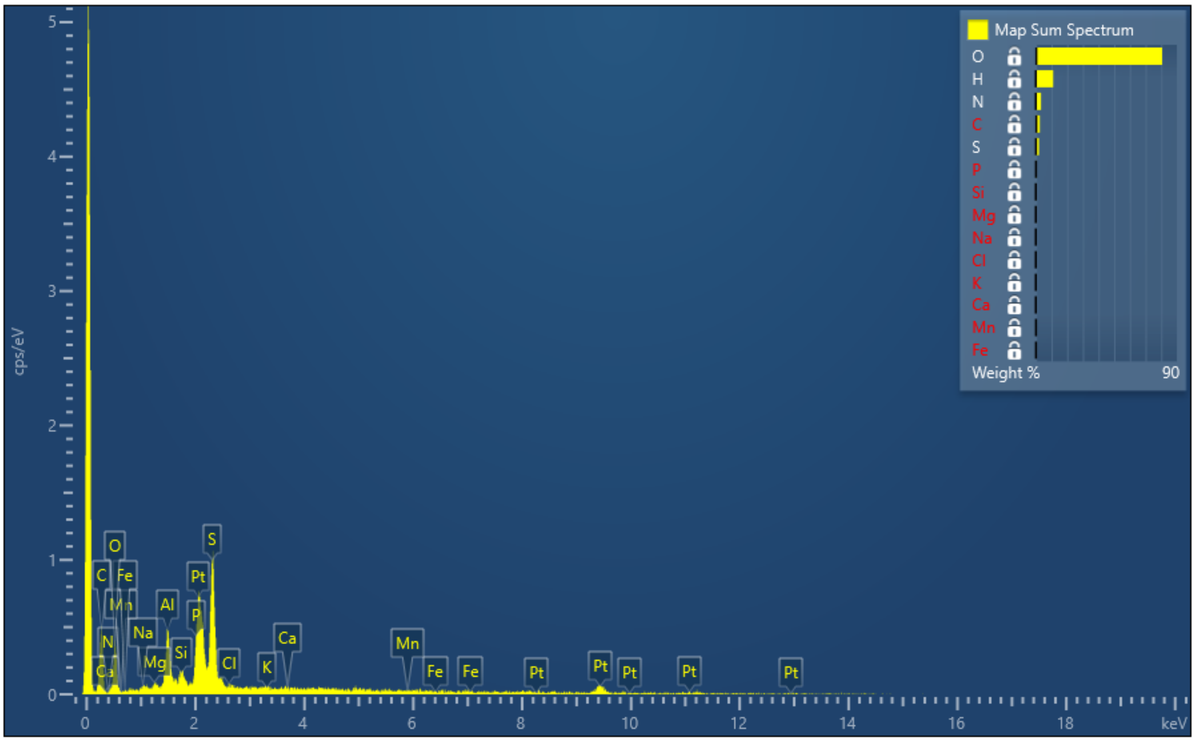

Surface roughness may inhibit X-rays from reaching detectors due to absorption in the dry samples of bitumen in the SEM. Thus, resin-impregnated and polished samples will deliver the best X-rays to the detector. The filtrated or dried bitumen samples in this study had high roughness on aluminium studs and therefore all of the samples are prepared with resin impregnation and polished with delicate tools as shown in Figure 12.24.

Figure 12.24: X-ray imaging sample preparation

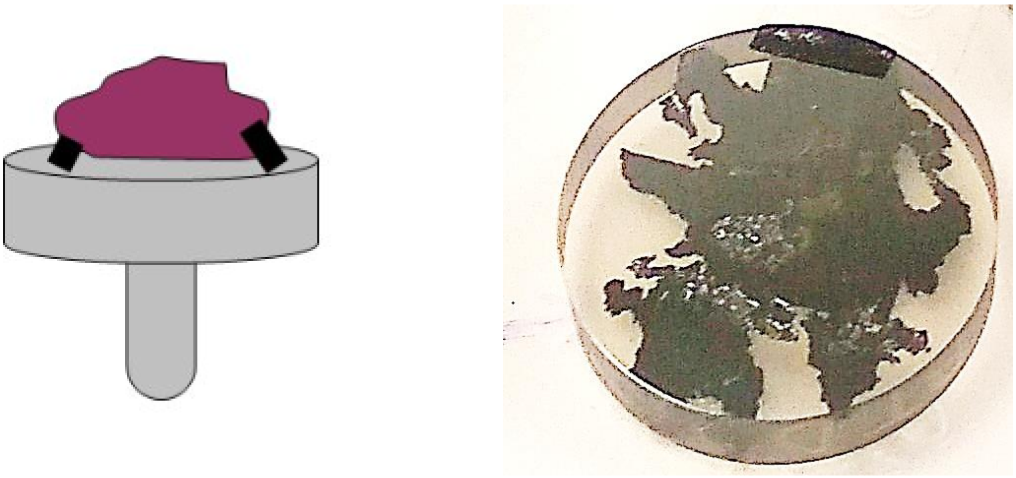

Metal stub and sample

Polished resin impregnated dry bitumen

12.5 Master Curves

12.5.1 Introduction

The rheological properties of bitumen can theoretically be characterised over a broad range of loading frequencies and various temperatures. The full range cannot be measured in the laboratory due to the operational limitations of the testing device (DSR). Master curves are constructed by horizontal shifting of the isothermal data from frequency sweep measurements. The required data inputs are storage modulus G′, loss modulus G″ and the phase angle (δ) at temperatures such as 40 °C, 50 °C, 60 °C and 70 °C (Alhaddad 2015). The loading is varied over a range of frequencies (0.1, 0.1259, 0.1585, 0.1995, 0.2512, 0.3162, 0.3981, 0.5012, 0.631, 0.7943, 1.0, 1.259, 1.585, 1.995, 2.512, 3.162, 3.981, 5.012, 6.31, 7.943 and 10 Hz). The test is performed with the DSR, with a 25 mm diameter plate using a 1 mm gap for the binder.

12.5.2 Shift factor

The shift factor is a parameter that governs the time-temperature superposition results. It is defined in Equation 13 as:

$$a_T = \frac{\omega_r}{\omega} \tag{13}$$

where

ω_r = reduced frequency at the reference temperature

ω = the testing frequency in the DSR test

Source: Yusoff et al. (2011).

Multiple models are proposed for the determination of shift factors. They include the log-polynomial, the Arrhenius and the Williams-Landel-Ferry models. The log-polynomial model is defined by Equation 14:

$$\log a_T\,[T] = \; b_0 + b_1 T + b_2\,T^2 \tag{14}$$

where

$a_T\,[T]$ = the shift factor at temperature T

b_0, b_1 and b_2 = the constants for the polynomial function model

The Arrhenius model is expressed in Equation 15:

$$\log a_T\,[T] = \frac{-E_a}{2.303R}\left[\frac{1}{T} - \frac{1}{T_R}\right] \tag{15}$$

where

$a_T\,[T]$ = the shift factor at temperature T

E_a = activation energy (J/mol)

R = gas constant [J/mol/K]

T_R = reference temperature in (K)

12.5.3 Master curve construction

After obtaining the shift factor, the process of developing a master curve can be started. To construct a master curve, a shifting method is applied to produce the best fit between measured and modelled data. The master curve describes the complex modulus over a range of temperatures and frequencies, and it can be defined by a sigmoidal function which is noted in the NCHRP report 547 (Witczak 2005) as Equation 16:

$$\log|G^*| \; = \lambda + \frac{\alpha}{1 + e^{\beta + \gamma(log\omega_r)}} \tag{16}$$

where

G^* = the complex modulus of the binder in kPa

ω_r = the reduced frequency in Hz

λ = the minimum value of the complex modulus in kPa

α = the difference between the maximum and minimum value of the complex modulus in kPa

β, γ = the parameters describing the shape of the sigmoidal function

The maximum value of G* corresponds to the glassy modulus of the bituminous binder and is around 1 GPa (Bonaquist 2008). In bitumen, the transformation from the glassy to the liquid state occurs at temperatures between -40 °C and 0 °C and depends on the asphaltene content (Cheung & Cebon 1997). At ambient temperatures, bitumen turns to viscoelastic behaviour and thus time-dependent relationships between stress and strain are required.

There are several parameters in the above equation that are required to be determined. Adjustment of the master curve model to determine the best fit is often accomplished by an optimisation process. The aim will be to have minimum error between the data from the experiment and the master curve model. This can be achieved by a minimisation of the summation of square errors (SSE) in an iterative process (Equation 17).

$$SSE = \sum \frac{(log|G_e^*| - log|G_m^*|)^2}{(log|G_e^*|)^2} \qquad 17$$

where

G_e^* = the measured complex modulus

G_m^* = its corresponding value at the same temperature and frequency condition from the arbitrary master curve model

Microsoft Excel Solver was used for optimisation by assessing a range of each of the parameters to achieve the lowest SSE value.

Important frequencies in typical master curves are 10 rad/s (1.59 Hz), 5 rad/s (0.8 Hz) and 1 rad/s (0.159 Hz). These correspond to traffic speeds of 100 km/h, 50 km/h and 10 km/h. These frequencies are used when comparing different master curves.

12.6 Black Diagrams

A black diagram is basically a graph of complex modulus (G*) versus the phase angle (δ) which is measured during a DSR test. A smooth curve indicates the equivalency between time and temperature, which is important for the applicability of the superposition principle for the development of master curves.

Discrepancies in the black diagram can be due to non-linearity effects, which in turn undermine the shifting concept for rheological data. Linearity in viscoelastic responses allows the rheological properties to be extended over a wide range of temperatures and frequencies.

Non-smooth master curves can be caused by several factors including non-linear viscoelasticity at strain levels beyond the linear region, compliance errors of the selected DSR geometry, operation errors, and structural changes with temperature in the binder (e.g. wax crystallisation).

Black diagrams can assist in understanding the inconsistencies in rheological data induced by ageing, binder modification additives, non-linearity and improper selection of geometries.

During oxidative ageing, G* increases while the δ decreases. This phenomenon is reflected in the black diagram curves by a shift to the left or towards lower phase angles.

13 RESULTS AND DISCUSSION

The detailed results for each test are provided in the appendices.

13.1 Penetration test

The penetration test was performed three times for each prepared sample according to the method prescribed in Australian Standard AS 2341.12-1993. The average results obtained from the tests are listed in Table 13.1.

Table 13.1: Penetration test

Sample	Penetration values (0.1 mm)		
	Unaged	1 X RTFO	3 X RTFO
C320	50	36	25
BTD2	45	33	23
BTD4	42	29	20
BTD6	39	27	19
20BRD2	50	37	
20BRD4	46	40	
20BRD6	42	36	
60BRD2	42	38	
60BRD4	44	44	
60BRD6	43	32	
C600	29	21	

The reported C320 results are acceptable as the penetration value meets the minimum requirement of 40 (0.1 mm) as specified in AS 2008-2013 for unaged bitumen.

Results indicate that as the concentration of NS in the bitumen increases, the penetration values decrease for NS samples with couplant. This can be attributed to an increased stiffness with the addition of NS, which in turn reduces the penetration value. However, this trend does not show a uniformly decreasing trend when the NS type is uncoupled 20 or 60 nm size. The 20 nm NS-modified bitumen seems to be softer than the 60 nm NS-modified bitumen samples.

A similar situation exists for post-RTFO samples, though they have Pu values lower than unaged specimens. The aged specimens demonstrate higher penetration of about 10 to 30% more than the unaged condition.

Only NS with couplant results for 3 x RTFO are reported. If 3 x RTFO is assumed to be equal to PAV, then a 50% reduction in penetration depths would be expected based on the results above. As noted earlier, this is due to the loss of volatile oils and the increase in asphaltene content during ageing (Kumbargeri & Biligiri 2016). As the asphaltene content increases, the bitumen becomes stiffer and harder to penetrate. In general, the modified bitumen will have a better ability to resist permanent deformation since it is stiffer than the base bitumen.

13.2 Softening Point

Table 13.2 lists the softening point results for various compositions. There is not a significant variation in the softening point values among mixes. However, the highest values (57 °C) are for 4.0% NS with couplant, whereas other samples are around 50 °C. The softening point of A15E is considerably higher than all other samples by almost 100%.

Table 13.2: Softening point (°C)

Sample	Softening point ˚C
C320	51.0
BTD2	51.0
BTD4	57.0
BTD6	51.0
20BRD2	49.0
20BRD4	50.0
20BRD6	50.5
60BRD2	50.5
60BRD4	49.5
60BRD6	48.5
A15E	92.5
C600	52.0

Table 13.2 indicates that there is no clear relation between softening point and NS irrespective of its type. Bitumen samples modified with 20 nm NS have an almost constant SP, very close to 50 °C. The SP of samples modified with 60 nm NS exhibits a decreasing trend. Nevertheless, the trend for samples modified with 20 nm NS and couplant is non-uniform with a peak for the 4% sample (BTD4). The next sections show that the stiffness (G*) of BTD4 is more that BTD2 and BTD6 as well.

13.3 Viscosity

The aim of viscosity tests is to assess the changes in viscosity induced by NS addition at various temperatures and to compare the resulting viscosity with the base bitumen results. The expectation was to have an increase in viscosity with NS inclusion as observed in the literature.

Results in Table 13.3 indicate that 4% NS will give the highest viscosity when its size is 60 nm. Similarly, the second highest viscosity corresponds to 6% of 20 nm Ns with couplant. These results are also shown in Figure C 2 where viscosity changes are shown for each type of NS sample.

Some of the trends in the results are difficult to explain. For example, for the 20BRD samples, the viscosity at 60 °C for 20BRD4 is lower than that of 20BRD2 and it is higher for 60BRD4 than 60BRD6. These trends are unexpected. The only explanation for this can be due to the poor quality of the dry-mixing method. These inconsistencies were not seen after wet mixing. See Figure C 25 to Figure C 30.

It should be noted that the viscosity of the C600 bitumen had high viscosity and could be said to be non-conforming.

Table 13.3: Viscosity for unaged samples

Sample	Viscosity Pa.s	
	135 ˚C	60 ˚C
C320	0.500	334.10
BTD2	0.638	408.55
BTD4	0.680	432.25
BTD6	0.786	504.25
20BRD2	0.610	408.87
20BRD4	0.730	390.25
20BRD6	0.750	457.05
60BRD2	0.702	370.20
60BRD4	0.730	519.90
60BRD6	0.739	424.25
C600	-	1051.00
C600 (alternative)	0.670	763.60
A15E	0.78 (165 °C)	1548.00

Evaluating the results summarised in Table 13.4, it appears that viscosity is almost double after RTFO ageing. A graph illustrating the viscosity changes is shown in Figure C10. It is interesting to note that some NS-modified samples such as BTD4 (4% 20 nm NS with couplant) have a very high viscosity, nearly double that of virgin C320. It should be kept in mind that this is just for two samples with couplant (BTD4 and BTD6) and the rest of the samples are in a limited range after RTFO ageing.

Table 13.4: Viscosity for RTFO samples

Sample	Viscosity (Pa.s) @ 60 °C
C320	708.90
BTD2	999.70
BTD4	1366.80
BTD6	1181.00
20BRD2	799.30
20BRD4	748.80
20BRD6	952.60
60BRD2	687.00
60BRD4	844.40
60BRD6	838.70
C600	1966.00
A15E	1694.00

13.4 RTFO Weight Loss

The mass loss during the RTFO test is generally less than 1% according to the results summarised in Table 13.5. A maximum allowable mass loss has not been noted in AS 2008-2013, but Austroads (2017) recommends a maximum of 0.5% and AGPT/T190-19 stipulates a maximum of 0.6%. ASTM D2872-19 and some American sources allow up to 1%.

Table 13.5: Weight loss for RTFO samples

Sample	Weight loss (%)
C320	0.07
BTD2	0.10
BTD4	0.09
BTD6	0.17
20BRD2	0.08
20BRD4	0.50
20BRD6	0.64
60BRD2	0.10
60BRD4	0.08
60BRD6	0.20
A15E	0.79
C600	0.45

13.5 Strain Sweep

The DSR testing involved strain sweep tests to verify results. Typical outputs for some samples are shown in Figure A 1 to Figure A 9 . Figure A 1 indicates that G* is nearly constant over a broad range of strain levels. Therefore, G* is independent of the level of strain and the material behaviour is in a linear region from 40 °C to 70 °C.

13.6 Master Curves of Complex Modulus

As noted earlier, the main objective of a master curve is to predict the complex modulus of the bitumen over a wide range of frequencies and temperatures which cannot be experimentally obtained. The master curves are developed at a reference temperature of 60 °C, based on the Arrhenius model and the procedure is explained in Section 12.5. Results of duplicate specimens for each sample are individually interpreted to study the likely variabilities of results.

Detailed master curves are shown in Figure B 1 to Figure B 42 for each specimen . These figures cover both unaged, RTFO and PAV conditions. However, for wet samples the DSR tests were undertaken only in the unaged condition.

In some cases, results have shown discrepancies, which were indicative of an error during the testing. Those tests were repeated, and the results of the repeated tests replaced the erroneous results.

For better visualisation of the amount of data generated, the rheological results at 60 °C are summarised in Figure C 1 to Figure C 30 . Important findings from the dry mixes are listed below.

13.6.1 Dry mixes

(a) The 60 nm NS has a higher G*. However, couplant is highly effective at offsetting this trend by increasing G* even more than 60 nm NS. This is only observed for the unaged or RTFO aged condition; 60 nm NS is stiffer with couplant added to 20 nm NS in the PAV aged condition.

(b) In terms of viscosity, NS-modified batches do not differ markedly in the unaged condition. However, NS with couplant has a higher viscosity in the RTFO aged condition, but this is similar to 60 nm NS in the PAV aged condition.

(c) The increases in G* vary from 10% (for 6% NS 20 nm) to 45% (for 6% NS 20 nm with couplant) in the unaged condition with respect to virgin C320 as shown in Figure C 23. This is the same for RTFO aged as well, but the G* increase is between 20 to 25% in the PAV aged condition, except for 2% NS content.

(d) The enhancements in viscosity vary from 15% (for 2% NS 60 nm) to 55% (for 6% NS 60 nm) in the unaged condition with respect to virgin C320 as shown in Figure C 4. This range extends to 80% (for 4% NS 20 nm with couplant) in the RTFO aged condition as shown in Figure C 12. However, the viscosity increase is limited to a maximum of 25% for the PAV aged condition as shown in Figure C 20.

(e) There are no uniform trends in rheological properties after dry mixing. Thus, the observed steady trends reported in the literature could not be verified even after multiple repeated testing.

A detailed look at the master curves from Figure B 37 to Figure B 39 can give additional findings:

(f) NS modified batches have improved G* in the range of frequencies from 0.159 Hz to 1.59 Hz (i.e. 1.3 km/h to 13 km/h). However, the significant improvement is for frequencies either higher than 100 Hz (800 km/h) or lower than 0.01 Hz (0.08 km/h).

(g) NS-modified batches generally have lower G* than C600 or A15E. However, the NS-modified batches are considerably stiffer when the PAV aged condition is considered.

(h) Considering only G* for the best NS content, the optimum percentage of NS is between 4 to 6% considering all the ageing conditions. The most suitable size is 60 nm, however questions remain about 60 nm with couplant, which was not tested here. Initially, it was thought that the 20 nm NS particles would perform the best, so as just one size with couplant was planned to be tested, the 20 nm NS seemed the preferred option.

13.6.2 Wet mixes

A wet preparation method was performed to prepare master batch samples. These could be prepared more accurately than the dry mixes. Findings from this work are shown below.

(a) The largest size of NS (i.e. 60 nm) has the highest G*. The increases of G* in the case of NS 60 are around 40% (2% wt) to 105% (8% wt). See Figure C 27.

(b) The viscosity of all the NS-modified batches changes in a similar way. However, 60 nm NS or NS modified with couplant exhibit higher viscosities at higher NS contents.

The viscosity increases are between 20% (for 2% NS 20 nm with couplant) and 140% (for 8% NS 20 nm with couplant), depending on the NS content. See Figure C 28.

(c) Assuming viscosity as a binder classification criterion, NS can easily raise the viscosity of bitumen at 60 °C from 300 to 450 Pa.s, i.e. a change from C300 to C450 or one grade in Australian terminology. However, an increase from 300 to 600 Pa.s is achievable when 6% NS is used, i.e. a change from C300 to C600 or two grades in Australian terminology.

(d) There is a direct or linear trend in rheological properties with the increase of NS for these mixes.

(e) Evaluating Figure B 40 to Figure B 42 indicates that 4 to 6% NS 60 nm can easily compete with C600 over a broad range of frequencies representative of normal traffic speed conditions (60–100 km/h).

13.7 Rutting or Durability

In the case of unaged bitumen, the G*/sinδ or rutting parameter should be more than 1.0 kPa. Figure C 5 shows the G*/sinδ values at 60 °C which are higher than 3.0 kPa, corresponding to a C320 bitumen.

Figure C 7 indicates a rutting resistance improvement with respect to C320 bitumen. In this figure, the rutting resistance has improved up to 50% when 20 nm NS with couplant has been added.

However, it is difficult to select the optimum NS content for each NS size; 4% NS seems to be the best for 60 nm NS, while the rutting improvement is the lowest at this percentage for 20 nm NS. This non-uniformity is considerably decreased in the RTFO and PAV aged conditions.

In the literature, rutting trends have a direct relationship with increasing NS content, however this is not the case for dry mixes, especially for the unaged condition. Results of the wet samples better support the trends in the literature and Figure C 29 shows a steadily improving rut resistance with NS content.

Important things to note are:

(a) All batches meet the limit of G*/sinδ > 1.0 kPa for the unaged condition and G*/sinδ > 2.2 kPa for RTFO aged conditions.

(b) In the RTFO aged condition, the 20 nm with couplant performs better than NS without couplant.

(c) In the PAV aged condition, the advantage of the couplant is lost and 60 nm NS performs the best.

(d) The rutting resistance of NS mixes is similar to C600, but not as good as A15E when tested in the PAV aged condition.

13.8 Creep compliance

Figure D 1 and Figure D 2 show the typical results of the MSCR test for C320 bitumen.

Summaries of all results are contained in Table 13.6 to Table 13.10. These tables show the variation of creep compliance at a 3.2 kPa stress level, the percentage difference of creep compliance and the percentage recovery of the RTFO aged binders with and without NS additive at 64 °C.

Table 13.6: J_{nr} values for unaged bitumen

Mix	J_{nr} (0.1) kPa^{-1}	J_{nr} (3.2) kPa^{-1}	R (3.2)	$J_{nr\ diff}$ < 75
C320	5.709	6.109	-0.77	7.0
BTD2	3.351	3.705	-0.25	10.6
BTD4	3.672	4.082	-0.62	11.2

Mix	J_{nr} (0.1) kPa^{-1}	J_{nr} (3.2) kPa^{-1}	R (3.2)	$J_{nr\ diff} < 75$
BTD6	3.089	3.443	-0.64	11.5
20BRD2	4.06	4.474	-0.56	10.2
20BRD4	4.362	4.725	-0.80	8.3
20BRD6	3.765	4.182	-0.53	11.1
60BRD2	4.334	4.674	-0.54	7.8
60BRD4	4.094	4.522	-0.56	10.5
60BRD6	4.104	4.446	-0.78	8.3
C600	1.762	2.098	1.60	19.1
A15E	-0.03	-0.03	102.42	-9.71

Table 13.7: J_{nr} values for RTFO aged bitumen

Mix	J_{nr} (0.1) kPa^{-1}	J_{nr} (3.2) kPa^{-1}	R (3.2)	$J_{nr\ diff} < 75$
C320	2.805	3.066	-0.07	9.30
BTD2	1.897	2.109	0.5	11.18
BTD4	1.909	2.112	0.3	10.63
BTD6	-	-	-	-
20BRD2	2.196	2.508	0.3	14.21
20BRD4	2.102	2.271	-0.1	8.04
20BRD6	2.137	2.352	-0.4	10.06
60BRD2	2.327	2.547	0.1	9.45
60BRD4	1.836	2.274	0.3	23.86
60BRD6	1.994	2.313	0.0	16.00
C600	0.792	0.906	7.6	14.40
A15E	-0.0153	0.0128	98.5	-183.66

Table 13.8: J_{nr} values for PAV aged bitumen

Mix	J_{nr} (0.1) kPa^{-1}	J_{nr} (3.2) kPa^{-1}	R (3.2)	$J_{nr\ diff} < 75$
C320	0.140	0.147	22.90	5.10
BTD2	0.177	0.187	18.50	4.65
BTD4	0.172	0.178	16.35	3.95
BTD6	0.213	0.220	12.50	2.95
20BRD2	0.243	0.264	14.25	7.75

Mix	J_{nr} (0.1) kPa^{-1}	J_{nr} (3.2) kPa^{-1}	R (3.2)	$J_{nr\ diff}$ < 75
20BRD4	0.132	0.142	21.85	7.65
20BRD6	0.133	0.139	20.85	4.45
60BRD2	0.129	0.139	23.40	8.15
60BRD4	0.130	0.135	20.85	4.10
60BRD6	0.152	0.157	17.15	4.00
C600	0.123	0.137	32.60	11.30
A15E	0.042	0.087	77.90	105.80

Table 13.9: J_{nr} values for wet mixed unaged condition

Mix	J_{nr} (0.1) kPa^{-1}	J_{nr} (3.2) kPa^{-1}	R (3.2)	$J_{nr\ diff}$ < 75
C320	5.709	6.109	-0.77	7.0
BTD2	5.558	6.082	-0.70	9.4
BTD4	4.045	4.594	-0.40	13.6
BTD6	4.055	4.894	-0.60	20.7
BTD8	3.406	4.297	-0.50	26.2
20BRD2	4.395	4.844	-0.50	10.2
20BRD4	4.278	4.773	0.00	4.6
20BRD6	3.916	4.339	-0.40	10.8
20BRD8	3.499	3.838	-0.60	9.7
C600	1.762	2.098	1.60	19.1
A15E	-0.03	-0.03	102.42	-9.71

Table 13.10: J_{nr} values for the 3 x RTFO condition

Mix	J_{nr} (0.1) kPa^{-1}	J_{nr} (3.2) kPa^{-1}	R (3.2)	$J_{nr\ diff}$ < 75
BTD2	0.770	0.864	3.50	12.2
BTD4	1.003	1.122	2.30	11.9
BTD6	0.711	0.800	2.30	12.4

*Jnr 3.2 of C600 after RTFO is 0.906 – similar to NS-modified mixes after 3 x RTFO.

Table 13.7 shows that the addition of NS will cause the J_{nr} value to decrease. In other words, the rutting resistance of bitumen improves by 25% (4% wt of 20 nm NS) to 45% (6% wt of 20 nm NS with couplant) for different combinations of NS-modified binders. The comparison of these results with the corresponding DSR tests in Figure C 7 indicates that the MSCR test shows a similar range of rutting improvement. The trend is uniform without any fluctuation. This trend is repeated for wet samples according to Table 13.9.

When considering J_{nr} values of unaged binders, the NS-modified binders perform better than the C320 bitumen, however, not as well as C600 bitumen, which would appear to be more resistant to permanent deformation. So, although NS-modified bitumens have a significant deformation improvement over C320 bitumen, they are not able to achieve the increases in permanent deformation resistance to reach the level of a C600, which is likely to be the binder used in heavy traffic applications.

The general trend for J_{nr} of the unaged modified binders is for the NS with couplant to have the best resistance to rutting, whereas there seems little difference between the 20 and 60 nm sized uncoupled NS. There is a general trend for improved rutting resistance with increasing NS content, but there are some inconsistencies. These could be related to the dry blending process. These inconsistencies seem to have been reduced when considering wet blending as shown in Table 13.9.

In the RTFO aged condition, the J_{nr} of the modified binders still shows an increased resistance to rutting over the base C320 bitumen. Again, this improvement does not match that of a C600 bitumen. In the dry blended mixtures, there seem to be some inconsistencies in the results. The 20 nm NS size with couplant performs better than without couplant and the 60 nm NS size performs best of all. There is little difference between 2, 4 and 6% NS addition, however.

The J_{nr} value of 20 nm NS with couplant is again lower than similar mixes with 20 nm or 60 nm NS and bitumen. This is the case for the unaged condition; however, Table 13.8 shows that the couplant effect is diminished in the PAV aged condition (i.e. 60 nm NS works better than 20 nm NS with couplant).

After PAV ageing, it seems there is little difference between the J_{nr} of all binder conditions. There is even little difference between C320 and C600 bitumen after PAV ageing, which must be due to the severity of the ageing protocol.

A comparison of the results between 3 x RTFO and PAV aged conditions according to Table 13.8 and Table 13.10 shows that the 3 x RTFO aged condition is not as severe as PAV ageing. This is discussed in more detail in the next section. According to the grading criteria in AASHTO TP 70, all the NS-modified bitumen mixes fall in the same grade as ‘heavy traffic’ or $J_{nr} < 2.0$ kPa^{-1}, which is higher than ‘standard traffic’ or $J_{nr} < 4.0$kPa^{-1}. Thus, it can be inferred that NS has the potential to enhance bitumen quality from 10 million equivalent standard axle loads (ESALs) (and $V > 70$ km/h) to one level higher, 10 to 30 million ESALs (or $20 < V < 70$ km/h). The results show that all the modified bitumens have a PAV aged J_{nr} (3.2) less than 0.5 kPa, which means they all meet the heavy traffic E class specification.

The $J_{nr\ diff}$ indicates that the strain responses of mixes are linear and results of the MSCR tests are not sensitive to the stress level. In all cases, except for A15E which is a polymer modified bitumen, the recorded values are less than 75% which indicates that NS-modified bitumen is not stress sensitive like PMB bitumen.

13.9 Fatigue Cracking Resistance

The G*sinδ value should be less than 5000 kPa for the PAV aged condition as suggested in ASTM D7175-15. This parameter is used to predict the performance of bitumen against fatigue cracking. The G*sinδ values were evaluated for unaged bitumen, RTFO, 3 x RTFO and PAV aged conditions. Appendix C shows this information in more detail. The results of limited tests on 3 x RTFO aged condition are presented in Table 13.11.

Table 13.11: Summary of DSR tests in the 3 x RTFO condition

Binder	Viscosity (Pa.s)	G* (kPa)	Phase angle δ (degree)	G*/Sin (δ)	G*.Sin (δ)
C320	1778	14.8	80.12	15.0	14.5
BTD2	2053	17.1	80.1	17.3	16.8
BTD4	2004	16.9	81.1	17.1	16.7
BTD6	2386	20.2	80.91	20.4	19.9

Figure C 6 shows the variation of this parameter with respect to C320 bitumen at 60 °C. The results are converted to percentages (by dividing the result with the corresponding value of the C320 bitumen) as shown in Figure C 8, Figure C 16 and Figure C 24.

The findings from the fatigue parameter study can be listed as follows:

(a) All batches meet the limit of G*.sinδ < 5000 kPa for PAV or 3 x RTFO aged conditions.
(b) In theory, it is ideal to have lower G*sinδ values or more fatigue resistance. NS-modified bitumens show lower fatigue resistance. However, G*sinδ has not been validated for all ageing conditions. Thus, the validity of the DSR test for fatigue is not confirmed and the NS effects should be tested in real asphalt mixture samples.
(c) The 20 nm NS with couplant shows better fatigue performance in the PAV aged condition.
(d) In the unaged or RTFO aged condition, the modified C320 with 6% of 20 nm NS performs better than other combinations.
(e) A 4% addition of 20 nm NS with couplant seems to be the best option for fatigue.

Results of 3 x RTFO aged samples are summarised in Table 13.11. Comparisons of 3 x RTFO and PAV results in terms of rutting and fatigue parameters indicate that ageing is approximately 15 to 20% lower for 3 x RTFO than for the PAV aged condition. In other words, ageing by 3 x RTFO is less severe than that for PAV conditioning.

13.10 Black Diagrams

The isochronal (temperature independent) black diagrams corresponding to each batch of binders are shown in Appendix E. The curves are mostly smooth in all unaged, RTFO or PAV aged conditions which confirms the observations made based on the amplitude sweep tests at the two temperatures of 40 °C and 70 °C during DSR testing as noted earlier.

Time-temperature equivalency can be assumed even when slightly disjointed curves are seen in many figures in this appendix. A 15E has abnormal trends specifically in the PAV aged condition that mostly relates to the presence of polymers in this binder.

These results also demonstrate that the 25 mm geometry works well for all binders studied. There are no compliance errors associated with the use of inappropriate sample (spindle) geometries causing significant scattering in the data.

With ageing, all the curves shift to the left as expected, with an increasing slope of the curves, which indicates higher G*.

More importantly, the comparison of NS-modified binders with virgin C320 shows that NS particles are enhancing, to different extents, the slope of the curves in the unaged, RTFO or PAV aged conditions. Moreover, NS is compatible with bitumen and does not cause formation of any crystal structures within bitumen.

13.11 Chemical Analysis of C320

Understanding of macrostructural changes depends on the physicochemical interactions between bitumen and aggregates, which in turn impacts on the durability and performance of the resultant mixes. This provides motivation to study individually or jointly the influence of the saturate, aromatic, resin and asphaltene (SARA) components within bitumen (Table 13.12).

Table 13.12: SARA fractions

SARA fractions	Sample 1 (6% 20 nm NS with couplant)	Sample 2 (C320)	Sample 3 (6% 20 nm NS)	Sample 4 (6% 60 nm NS with petrol)
Saturates	6.35	6.50	11.9	6.45
Aromatics	42.6	38.4	31.2	16.8
Resins	23.0	29.0	34.6	19.6
Asphaltenes	28.1	26.1	22.2	57.1

The results in Table 13.12 indicate that there are no significant fluctuations in the asphaltene content of the selected mixes. As noted earlier, NS targets asphaltene particles mostly due to their polarity.

13.12 SEM images

13.12.1 Equipment

A Zeiss Neon 40EsB FIBSEM (field emission/focussed ion beam SEM) at Curtin University was used in this study. It included focused (gallium) ion beam imaging and milling, SE (secondary electron) detector, in-lens SE detector, a BSE (back-scattered electron) detector, an In-lens BSE detector, an Oxford Inca EDS (energy dispersive spectrometer) x-ray detector and an HKL Channel 5 EBSD (electron back-scattered detector).

In addition, a cryo-stage equipped SEM facility at the University of Western Australia was also used in the study. This was a Zeiss 1555 VP-FESEM high-resolution, field-emission variable-pressure (VP) scanning electron microscope (SEM). The cryo-samples were frozen before imaging at temperatures as low as -150 °C. X-ray microanalysis can also be performed using an Oxford Instruments X-Max 80 silicon drift EDS system with AZtec and INCA software.

13.12.2 Observations

Pure NS particles are imaged as shown in Figure F 1 to Figure F 6 . Clusters of dry NS particles can be observed in these figures. As can be seen, the cluster sizes are bigger with couplant for the same size of NS particles (20 nm). However, the number of clusters is higher for NS without couplant. Figure F 3 illustrates situations where plenty of uniformly sized clusters are seen close together. Another finding is that the size of cluster has a direct relation with the NS size i.e. bigger clusters for 60 nm NS particles. Figure F 5 and Figure F 6 show the aggregation of NS particles to be larger for 60 nm NS particles. This implies that 60 nm NS particles have lower efficiency as they cannot disperse in the same way as the 20 nm NS particles when the dispersion effort is kept the same.

The next step was to check the NS dispersion quality in bitumen mixes. As noted earlier, this examination was carried out for both the dry and wet mixed samples.

No solvent was used during dry mixing of NS particles. However, the wet mixing method was based on the dispersion of NS particles in a solvent prior to introduction into bitumen. The procedure was expected to be more efficient. Thus, both mixing methods were examined in this study. Figure F 7 to Figure F 25 show images taken from dry mixed samples. However, some samples were extracts of asphaltenes and NS particles, since oily samples are not allowed in SEM facilities unless they are frozen first on the cryo-stage.

Figure F 7 and Figure F 8 show the approximate sizes for the clusters of NS. The composition of the clusters was also verified through X-ray mapping with the EDS detector. In a typical case, Figure F 10 shows the presence of heavy Si elements, which is representative of NS particles. These kinds of maps could potentially indicate the approximate dispersion quality by distribution or scattering of points across the surface. Figure F 11 and Figure F 12 show the energy of waves emanating from the sample surface, which can distinguish NS accumulation within the clusters. On the other hand, the BSE images in Figure F 14 and Figure F 15 reveal more features of clusters embedded deeper in the surface of the sample. This shows how each cluster is made up from multiple smaller clusters that should be broken through the mixing process.

Similar observations with more clarity and transparency were made from frozen modified bitumen as shown in Figure F 16 to Figure F 25. These figures show the small nanosized clusters being well dispersed within micro-sized clusters. These images are unique in that there are no similar reliable observations available in the literature.

The most interesting finding is that the bitumen surface seems to be concealed by an interface of icy crystals which look like NS clusters as shown Figure F 18. They have previously been mistaken in some of the literature, which has used freezing techniques, for bitumen.

The information reported in the study removes the concerns regarding the reliability of dry mixing methods. Comparison of Figure F 17 to Figure F 25 with Figure F 26 to Figure F 30 indicates that cluster sizes are smaller when the wet mixing method is used. This size of the clusters is difficult to find at the microscale as they are mostly smaller than a couple of hundred nanometres.

However, it should be kept in mind that SE images mostly represent the surface features of samples. The morphology of samples is clearer with SE imaging than the BSE images as shown in Figure F 29 and Figure F 30. The rough surface texture of hydrocarbon molecules in bitumen is visible in Figure F 28 and Figure F 29.

As noted earlier, the BSE images include different greyscale levels. These are related to the atomic number of the elements being imaged. Brighter areas are representative of heavy elements, beyond the atomic weight of hydrocarbons. The undulating surface texture in bitumen causes inhomogeneous volume contractions and interferes with the image quality as observed in Figure F 30. Nevertheless, EDS maps cover this weakness and reveal the NS particles in the sample.

Results from EDS spectrometry are shown in Figure F 10, Figure F 16, Figure F 17 and Figure F 30. The distribution of Si and O elements in a fuzzy pattern indicates that NS particles could exist anywhere in the NS-modified samples as X-rays come from deeper within the sample compared to SE or BSE images. The limitation is that EDS maps cannot be made at the nanoscale level. X-rays are emitted from an interaction volume that in general has dimensions in the microscale size. Nonetheless, they can confirm the presence and distribution of specific elements at a large scale. For instance, the presence of sulphur, S, which is an important element in bitumen is obvious from these images.

Another important finding from these images is shown in Figure F 26 and Figure F 27 and comparison of them with other images from wet samples. As explained before, wet samples here were made from master batches, which were made to maximise dispersion. Figure F 26 and Figure F 27 are for bitumen simply mixed with the NS diluted in unleaded petrol. The size of clusters indicates that their dispersion is between dry mixed samples and wet mixed by the master batch technique. The frequency of the micro-sized clusters is low compared with the dry mixed samples; however, the clusters are larger than shown in Figure F 28 to Figure F 30.

An important finding is that the sizes of the clusters is greatly reduced after wet mixing. This indicates the benefits of wet mixing, as seen in Figure F 28 to Figure F 30. The distribution of the clusters is nearly uniform in terms of their size and location across the whole surface of the sample. This point indicates that there is no significant difference between wet mixing and dry mixing at the microstructural level. However, results indicate that wet samples will be more homogeneous.

13.13 Ageing tests by FTIR

A Nicolet iS50 FTIR spectrometer was used to understand the ageing process of NS-modified bitumen subjected to age conditioning. The results of the FITR tests on C320 bitumen modified with 4% 20 nm NS with couplant (BTD4) are described in this section.

The spectra of the unaged sample (labelled as BTDO) which is the base binder of the BTD4 mix sample, is a typical bitumen spectrum except that it has a very low sulfoxide content (which indicates its good quality). There is no peak at 1700cm^{-1}, which is the absorption wavelength of the carbonyl groups that are often considered to be a product of ageing.

As shown in Figure 13.1 the spectrum for the RTFO aged (labelled as BTDF) sample is like that of the unaged condition. The sharp peaks at 1100 and 465 cm^{-1} are typical of NS and related to the presence of silica (SiO_2).

The spectra of the 3 x RTFO aged (BTD-3*RTFO) sample show a weak absorption at 1700cm^{-1}, which means some ageing has occurred, but it is not significant. A spectrum of an aged bitumen sample is also shown for comparison. In the unaged or slightly aged condition, like RTFO, it can be inferred that the benefits of NS cannot be distinguished properly. This topic will be further investigated by FTIR testing on PAV aged samples.

In another trial, the representative batches of the 6% NS-modified binders (dry mixed) were evaluated in the FTIR device. As shown in Figure 13.2 , all four samples show strong peaks at 1700cm^{-1}, which is due to the existence of the carbonyl groups. This means that all samples have been oxidised. All the spectra include peaks at 1030cm^{-1}, which is a sign of sulfoxide content, another ageing product of bitumen. The results in this figure show considerable ageing after PAV conditioning.

Figure 13.2 indicates that NS enhances the presence of multiple functional groups, which are related to different physical properties. The 60 nm NS-modified bitumen has the most absorption peaks, which could indicate better interaction with C320 binder. This agreed with the observations in the rheological tests.

Figure 13.1: FTIR test results of unaged or RTFO aged (sample BTD4) nanosilica-modified bitumen

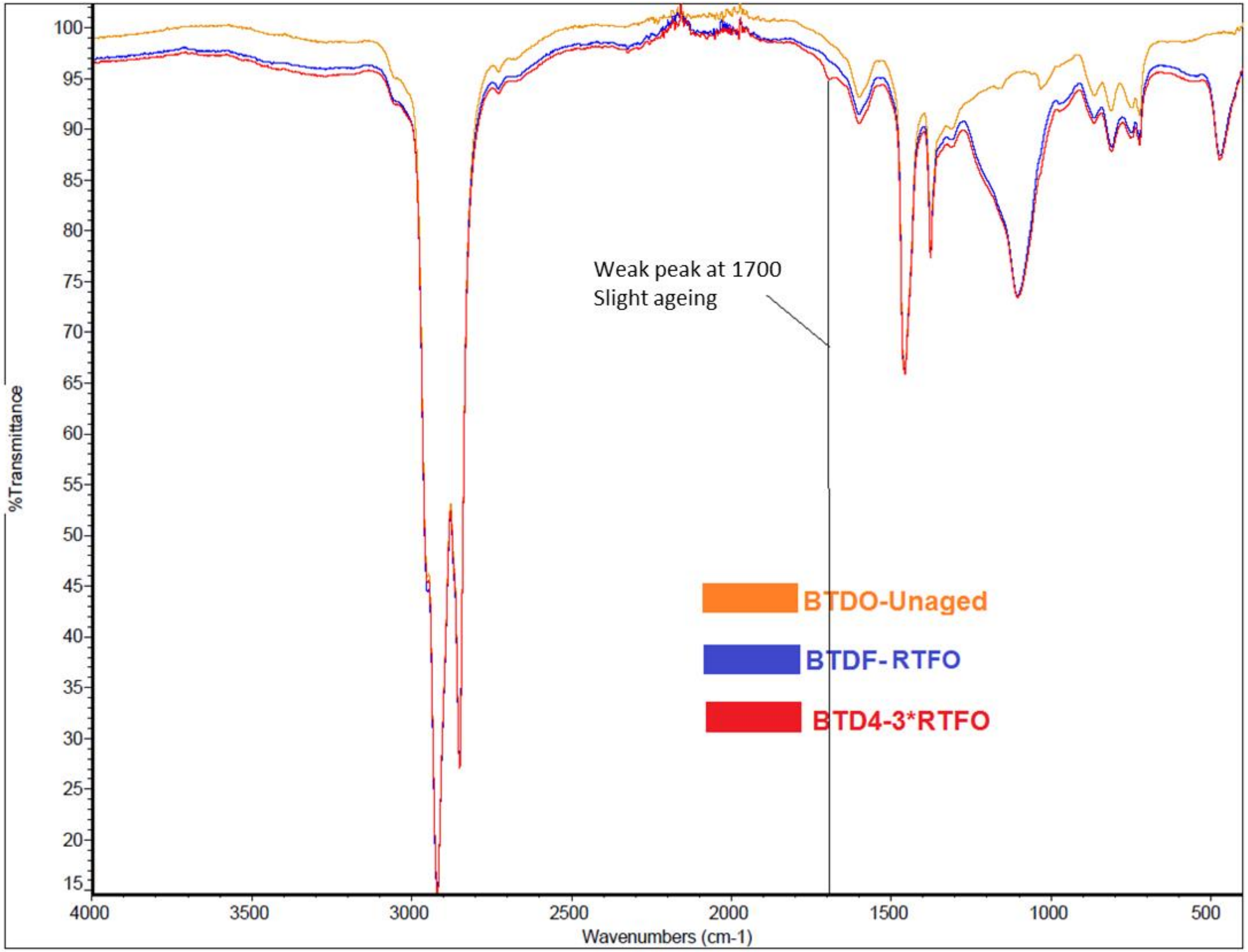

Figure 13.2: FTIR test results on RTFO and PAV aged nanosilica-modified binders

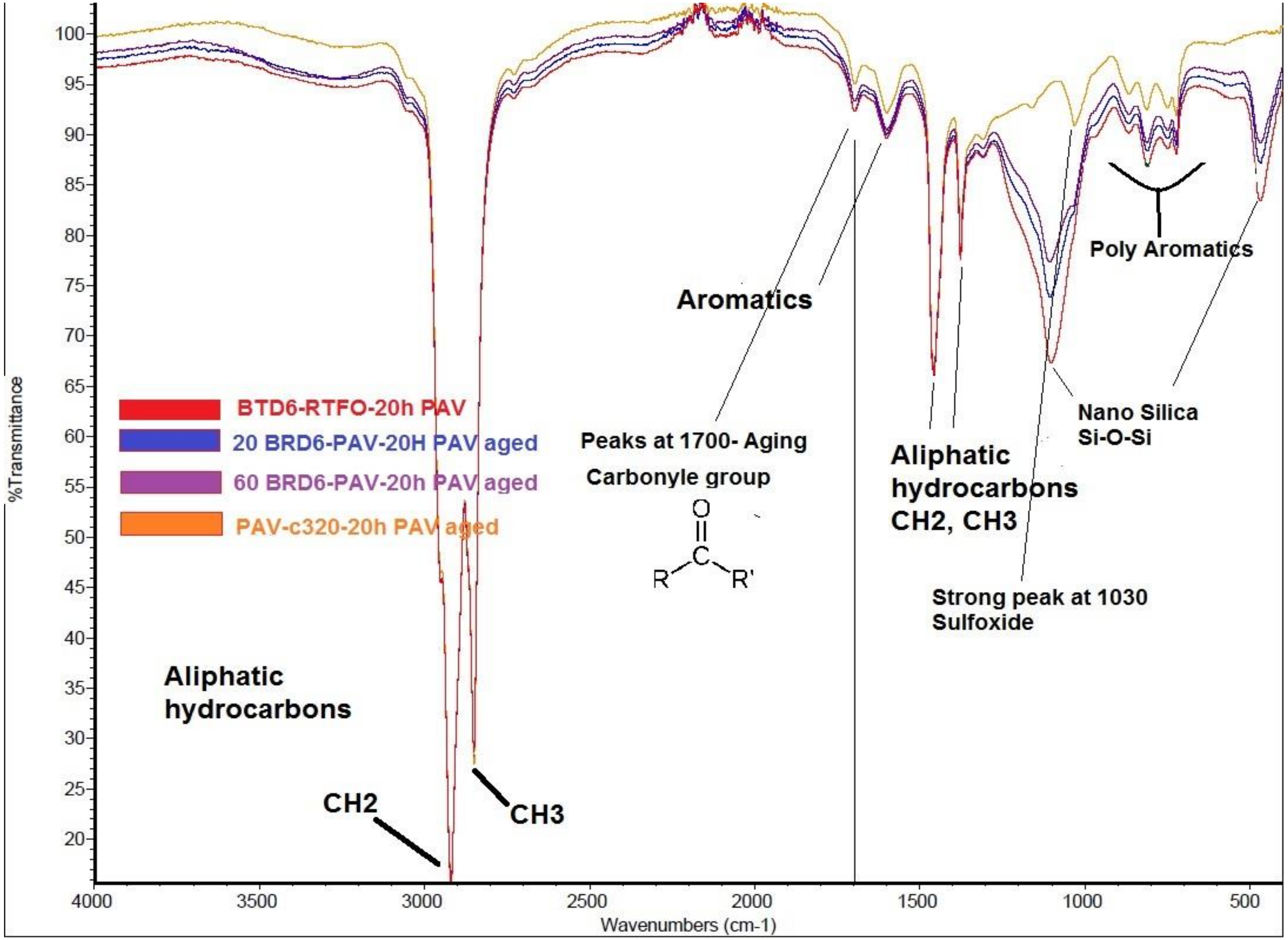

14 CONCLUSIONS

The effects of NS on the properties of Class 320 bitumen from Western Australia were investigated in this study. The bitumen mastics considered contained 2%, 4% and 6% of NS by weight of the total bitumen. Primarily, dry mixing was used to undertake the first phase of fundamental or rheology tests. However, results from samples produced by the wet mix process are also reported. Properties such as penetration values, softening points, rutting resistance and fatigue resistance of all samples including virgin C320, C600 and polymer modified A15E bitumen were investigated in four ageing conditions, namely unaged, short-term RTFO aged, 3 x RTFO aged (as a proxy to long-term ageing) and PAV aged conditions. The ageing of bitumen was initially carried out in the laboratory using the RTFO oven, thereafter, exposing all samples to PAV ageing.

The key conclusions which can be drawn are:

- The addition of NS causes bitumen to become stiffer and more viscous. The results obtained from penetration tests for all samples before ageing, after standard RTFO ageing and after 3 x RTFO ageing show a similar decreasing trend.
- The enhancements in viscosity vary from 15% (for 2% NS 60 nm) to 55 % (for 6% NS 60 nm) in the unaged condition with respect to virgin C320. For wet mixed samples, the viscosity increases are typically between 20% and 140% (for 2% NS 20 nm with couplant), depending on the NS content. The larger the NS particle size, the higher the viscosity for the NS-modified C320.
- The larger size of NS (i.e. 60 nm) gives a bigger increase for G*. However, the use of the couplant with the 20 nm NS is highly effective to offset the size effect by increasing G* even more than the 60 nm NS without couplant. This effect is only observed for the unaged or the RTFO aged condition. In the PAV aged condition, the 60 nm NS is superior to the 20 nm NS with couplant.
- The increases in G* vary from 10% (for 6% NS 20 nm) to 45 % (for 6% NS 20 nm with couplant) in the unaged condition with respect to virgin C320. Significant increases of G* are seen for frequencies either higher than 100 Hz or lower than 0.01 Hz.
- NS modified C320 batches generally have lower G* than C600 or A15E. However, after PAV ageing, NS-modified batches exhibit a higher G* than C600 or A15E.
- Considering only G*, the optimum dosage of NS is between 4 to 6% considering all ageing conditions. The wet mixing method shows the biggest increase in G* at 6%.
- The most suitable NS size is 60 nm. However, the use of a couplant is likely to increase its performance even more.
- These results support the claim that wet mixed samples are better for dispersion efficiency, which is inherently poor for nanoparticles that tend to agglomerate. This finding is based on evidence from both mechanical tests and SEM observations.
- Dry mixed samples do not show consistent trends during rheological testing. Thus, the findings in the literature involving uniform trends for dry mixes cannot be verified. This can be attributed to the efficiency of different mixers or the quality of the dry mixing process and agglomeration of particles. Note that a Silverson mixer is used in this testing to ensure the highest quality mixes.
- A field emission gun scanning electron microscope (FEGSEM) with a cryogenic stage was shown to be a good tool to directly monitor the binders under different conditions. The observation of the dispersion quality of NS within the modified binders was a unique aspect of this research.

- All the batches investigated met the SHRP criteria for rutting and fatigue resistance.
- The DSR results for binders blended with NS showed an increase in the G*/Sin(δ) parameter, which is indicative of an increased resistance to rutting.
- The increase of G*/Sin(δ) or decrease in J_{nr} value in the MSCR test indicates that NS particles can reduce rutting by about 25% to 45%.
- The fatigue parameter (G*.sinδ) has a direct relationship with NS content. NS seems to make the binder more rigid. However, this finding cannot be confirmed without fatigue tests on asphalt mixtures.
- The 3 x RTFO ageing method is not a direct equivalent to PAV ageing. It is a less severe ageing protocol. It was not chosen as a direct comparison to PAV, but as a method that could simulate what might happen under long-term ageing as a PAV was not available for use during this work.
- Limited investigations with FTIR have shown that there is better ageing resistance in bitumen containing NS. The most suitable type of NS was found to be the 60 nm size. The effects of the couplant could no longer be seen after PAV ageing.
- According to the grading criteria in the USA or Australia, suitable NS-modified bitumen has the potential to bump the grade of bitumen by at least one class, taking into account any of the parameters considered in the study when considering PAV ageing.
- Despite improving the rutting resistance of C320 bitumen, NS-modified bitumen cannot reach the stiffness of C600 bitumen.
- In the PAV aged condition, NS modified bitumen is significantly stiffer than common bitumen types in practice.

REFERENCES

Abbott, T n.d., SEM match maker: selecting the right SEM for imaging your samples, NUANCE, Northwestern University Atomic and Nanoscale Characterization Experimental Center, Evanston, IL, USA, viewed 6 March 2020, <http://www.nuance.northwestern.edu/docs/tech-talks/techtalk-tirzah-presentation.pdf>.

Aguiar-Moya, J, Salazar-Delgado, JA, Baldi Sevilla, A, Leiva-Villacorta, F & Loria-Salazar, L 2015, ‘Effect of aging on adhesion properties of asphalt mixtures with the use of bitumen bond strength and surface energy measurement tests’, Transportation Research Record, no. 2505, pp. 57-65.

Akmaz, S, Iscan, O, Gurkaynak, MA & Yasar, M 2011, ‘The structural characterization of saturate, aromatic, resin, and asphaltene fractions of Batiraman crude oil’, Petroleum Science and Technology, vol. 29, no. 2, pp. 160-71.

Alhaddad, AHA, 2015, ‘Predicting complex shear modulus using artificial neural networks’, Journal of Civil Engineering and Construction Technology, vol. 6, no. 3, pp. 15-26.

Alhamali, DI, Wu, JT, Liu, Q, Hassan, NA, Yusoff, NIM & Ali, SIA 2016, ‘Physical and rheological characteristics of polymer modified bitumen with nanosilica particles’, Arabian Journal for Science and Engineering, vol. 41, no. 4, pp. 1521-30.

Asphalt Institute 2003, Superpave performance graded asphalt binder specification and testing, Asphalt Institute, Lexington, KY, USA.

Austroads 2017, Guide to pavement technology part 4F: bituminous binders, AGPT04F-17, Austroads Sydney, NSW.

Bahia, H & Anderson, D 1995, The new proposed rheological properties of asphalt binders: why are they required and how do they compare to conventional properties, STP1241, ASTM International, West Conshohocken, PA, USA.

Baldi-Sevilla, A, Montero, ML, Aguiar, JP & Loría, LG 2016, ‘Influence of nanosilica and diatomite on the physicochemical and mechanical properties of binder at unaged and oxidized conditions’, Construction and Building Materials, vol. 127, pp. 176-82.

Besamusca, J, Volkers, A, vd Water, J & Gaarkeuken, B 2012, ‘Simulating ageing of EN 12591 70/100 bitumen at laboratory conditioning compared to porous asphalt’, 5th Eurasphalt & Eurobitume congress, 13-15th June 2012, Istanbul, Turkey.

Bonaquist, R 2008, Refining the simple performance tester for use in routine practice, National Cooperative Highway Research Program (NCHRP) report 614, Transportation Research Board, Washington, DC, USA.

Brown, E, Kandhal, PS, Roberts, FL, Kim, YR, Lee, D-Y & Kennedy, TW 2009, Hot mix asphalt materials, mixture design and construction, 3rd edn, NAPA Research and Education Foundation, Lanham, MD, USA.

Cheung, CY & Cebon, D 1997, ‘Deformation mechanisms of pure bitumen’, Journal of Materials in Civil Engineering, vol. 9, no. 3, pp. 117-29.

Corbett, LW 1969, ‘Composition of asphalt based on generic fractionation, using solvent deasphaltening, elution-adsorption chromatography, and densimetric characterization’, Analytical Chemistry, vol. 41, no. 4, pp. 576-9.

Crucho, JML, das Neves, JMC, Capitão, SD & de Picado-Santos, LG 2018, ‘Mechanical performance of asphalt concrete modified with nanoparticles: nanosilica, zero-valent iron and nanoclay’, Construction and Building Materials, vol. 181, pp. 309-18.

Daly, WH & Negulescu, I 2013, Implementation of GPC characterization of asphalt binders at Louisiana Materials Laboratory, LTRC report 505, Louisiana Transportation Research Center, Baton Rouge, LA, USA, viewed 6 March 2020, <https://www.ltrc.lsu.edu/pdf/2013/ts_505.pdf>.

D'Angelo, J, Kluttz, R, Dongre, RN, Stephens, K & Zanzotto, L 2007, ‘Revision of the Superpave high temperature binder specification: the multiple stress creep recovery test (with discussion)’, Journal of the Association of Asphalt Paving Technologists, vol. 76, pp. 123-62.

De Moraes, M, Pereira, R, Simão, R & Leite, L 2010, ‘High temperature AFM study of CAP 30/45 pen grade bitumen’, Journal of Microscopy, vol. 239, no. 1, pp. 46-53.

Dickie, JP & Yen, TF 1967, ‘Macrostructures of the asphaltic fractions by various instrumental methods’, Analytical Chemistry, vol. 39, no. 14, pp. 1847-52.

Ding, P, Orwa, M & Pacek, A 2009, ‘De-agglomeration of hydrophobic and hydrophilic silica nano-powders in a high shear mixer’, Powder Technology, vol. 195, no. 3, pp. 221-6.

Enieb, M & Diab, A 2017, ‘Characteristics of asphalt binder and mixture containing nanosilica’, International Journal of Pavement Research and Technology, vol. 10, no. 2, pp. 148-57.

Faramarzi, M, Arabani, M, Haghi, A & Mottaghitalab, V 2015, ‘Carbon nanotubes-modified asphalt binder: preparation and characterization’, International Journal of Pavement Research and Technology, vol. 8, no. 1, pp. 29-37.

Farhad, YR, Sefidmazgi, NR & Bahia, H 2014, ‘Application of diffusion mechanism: degree of blending between fresh and recycled asphalt pavement binder in dynamic shear rheometer’, Transportation Research Record, no. 2444, pp. 71-7.

Fini, EH, Hajikarimi, P, Rahi, M & Nejad, FM 2015, ‘Physiochemical, rheological, and oxidative aging characteristics of asphalt binder in the presence of mesoporous silica nanoparticles’, Journal of Materials in Civil Engineering, vol. 28, no. 2.

Goh, S, You, Z, Wang, H, Mills-Beale, J & Ji, J 2011, ‘Determination of flow number in asphalt mixtures from deformation rate during secondary state’, Transportation Research Record, no. 2210, pp. 106-12.

Golestani, B, Nejad, FM & Galooyak, SS 2012, ‘Performance evaluation of linear and nonlinear nanocomposite modified asphalts’, Construction and Building Materials, vol. 35, pp. 197-203.

Han, B & Ou, J 2007, ‘Embedded piezoresistive cement-based stress/strain sensor’, Sensors and Actuators A: Physical, vol. 138, no. 2, pp. 294-8.

Havancsák, K n.d., High-resolution scanning electron microscopy, webpage, Technoorg Linda, Eötvös Loránd University, Budapest, Hungary, viewed 6 March 2020, <http://www.technoorg.hu/news-and-events/articles/high-resolution-scanning-electron-microscopy-1/>.

Hu, Y-H, Chen, C-Y & Wang, C-C 2004, ‘Viscoelastic properties and thermal degradation kinetics of silica/PMMA nanocomposites’, Polymer Degradation and Stability, vol. 84, no. 3, pp. 545-53.

Hubbard, RL & Stanfield, KE 1948, ‘Determination of asphaltenes, oils, and resins in asphalt’, Analytical Chemistry, vol. 20, no. 5, pp. 460-5.

Kandhal, PS & Foo, KY 1997, Designing recycled hot mix asphalt mixtures using Superpave technology, NCAT report 96-5, National Center for Asphalt Technology, Auburn University, Auburn, AL, USA.

Khattak, MJ, Khattab, A, Rizvi, HR & Zhang, P 2012, 'The impact of carbon nano-fiber modification on asphalt binder rheology', Construction and Building Materials, vol. 30, pp. 257-64.

Kumbargeri, Y & Biligiri, KP 2016, 'Rational performance indicators to evaluate asphalt materials aging characteristics', Journal of Materials in Civil Engineering, vol. 28, no. 12.

Lang'at, C 2018, 'Experience of polymer modified bitumen and emulsion on pavement construction in Kenya', 2nd International Transport and Road Research Conference (iTRARR), Mombasa, Kenya.

Lazzara, G & Milioto, S 2010, 'Dispersions of nanosilica in biocompatible copolymers', Polymer Degradation and Stability, vol. 95, no. 4, pp. 610-7.

LeBaron, PC, Wang, Z & Pinnavaia, TJ 1999, 'Polymer-layered silicate nanocomposites: an overview', Applied Clay Science, vol. 15, no. 1-2, pp. 11-29.

Lesueur, D 2008, 'The colloidal structure of bitumen: consequences on the rheology and on the mechanisms of bitumen modification', Advances in Colloid and Interface Science, vol. 145, no. 1-2, pp. 42-82.

Li, R, Xiao, F, Amirkhanian, S, You, Z & Huang, J 2017, 'Developments of nano materials and technologies on asphalt materials: a review', Construction and Building Materials, vol. 143, pp. 633-48.

Little, DN & Bhasin, A 2006, Using surface energy measurements to select materials for asphalt pavement, Transportation Research Board, Washington, DC, USA.

Loeber, L, Sutton, O, Morel, J, Valleton, J-M & Muller, G 1996, 'New direct observations of asphalts and asphalt binders by scanning electron microscopy and atomic force microscopy,' Journal of Microscopy, vol. 182, no. 1, pp. 32-9.

Loeber, L, Muller, G, Morel, J & Sutton, O 1998, 'Bitumen in colloid science: a chemical, structural and rheological approach', Fuel, vol. 77, no. 13, pp. 1443-50.

Maher, M, Uzarowski, L, Moore, G & Aurilio, V 2006, 'Sustainable pavements-making the case for longer design lives for flexible pavements', Conference of the Canadian Technical Asphalt Association, 51st, 2006, Charlottetown, Prince Edward Island, CTAA, Victoria, BC, Canada.

Marsac, P, Piérard, N, Porot, L, Grenfell, J, Mouillet, V & Pouget, S 2014, 'Potential and limits of FTIR methods for reclaimed asphalt characterization', Materials and Structures, vol. 47, no. 8, pp. 1273-86.

Masson, J, Price, T & Collins, P 2001, 'Dynamics of bitumen fractions by thin-layer chromatography/flame ionization detection', Energy & Fuels, vol. 15, no. 4, pp. 955-60.

Michaud, D 2015, XRF sample preparation methods/procedure, webpage, 911 Metallurgist, viewed 6 March 2020, <https://www.911metallurgist.com/blog/sample-preparation-methods-for-xrf-analysis>.

Mikhailenko, P 2015, 'Valorization of by-products and products from agro-industry for the development of release and rejuvenating agents for bituminous materials', PhD Thesis, University Paul Sabatier, Toulouse, France.

Mullins, OC 2010 'The Modified Yen model', Energy & Fuels, vol. 24, pp. 2179–07.

Murata, Y, Kamitani, K, Tawara, H & Takeuchi, K 1998, ‘Air purifying pavement: development of photocatalytic concrete blocks’, Journal of the Mining and Materials Processing Institute of Japan, vol. 114, pp. 381-6.

Partl, M, Gubler, R & Hugener, M 2004, 'Nano-science and-technology for asphalt pavements’, Special Publication: Royal Society of Chemistry, vol. 292, pp. 343-56.

Petersen, JC 2009, ‘A review of the fundamentals of asphalt oxidation: chemical, physicochemical, physical property, and durability relationships’, Transportation Research Circular, no. E-C140, 78 pp.

Poulikakos, L, Partl, MJC & Materials, B 2012, ‘A multi-scale fundamental investigation of moisture induced deterioration of porous asphalt concrete’, Construction and Building Materials, vol. 36, pp. 1025-35.

Ray, SS & Okamoto, M 2003, ‘Polymer/layered silicate nanocomposites: a review from preparation to processing’, Progress in Polymer Science, vol. 28, no. 11, pp. 1539-1641.

Read, J & Whiteoak, D 2003, The Shell bitumen handbook, 5th edn, Thomas Telford, London, UK.

Redelius, P 2009, ‘Asphaltenes in bitumen, what they are and what they are not’, Road Materials and Pavement Design, vol. 10, supp. 1, pp. 25-43.

Redelius, P & Soenen, H 2005, ‘Correlation between bitumen polarity and rheology’, Road Materials and Pavement Design, vol. 6, no. 3, pp. 385-405.

Salih, AM, Ahmad, MB, Ibrahim, NA, Dahlan, KZ, Tajau, R, Mahmood, MH & Yunus, WM 2015, ‘Synthesis of radiation curable palm oil–based epoxy acrylate: NMR and FTIR spectroscopic investigations’, Molecules, vol. 20, no. 8, pp. 14191-211.

Schramm, G 1994, A practical approach to rheology and rheometry, 2nd edn, ThermoHaake Rheology, Gebrueder HAAKE GmbH, Karlsruhe, Germany.

Sugimoto, T 2000, Fine particles: synthesis, characterization, and mechanisms of growth, CRC Press, Boca Raton, FL, USA.

Sun, L, Xin, X & Ren, J 2017, ‘Inorganic nanoparticle-modified asphalt with enhanced performance at high temperature’, Journal of Materials in Civil Engineering, vol. 29, no. 3.

Steyn, WJM 2008, ‘Development of autoluminescent surfacings for concrete pavements’, Transportation Research Record, no. 2070, pp. 22-31.

Teizer, J, Venugopal, M, Teizer, W & Felkl, J 2011, ‘Nanotechnology and its impact on construction: bridging the gap between researchers and industry professionals’, Journal of Construction Engineering and Management, vol. 138, no. 5, pp. 594-604.

Traxler, RN 1936, ‘The physical chemistry of asphaltic bitumen’, Chemical Reviews, vol. 19, no. 2, pp. 119-43.

Veytskin, Y, Bobko, C & Castorena, C 2016, ‘Nanoindentation and atomic force microscopy investigations of asphalt binder and mastic’, Journal of Materials in Civil Engineering, vol. 28, no. 6.

Witczak, M 2005, Simple performance tests: summary of recommended methods and database, National Cooperative Highway Research Program (NCHRP) report 547, Transportation Research Board, Washington, DC, USA.

Xu, T & Huang, X 2010a, ‘Study on combustion mechanism of asphalt binder by using TG–FTIR technique’, Fuel, vol. 89, no. 9, pp. 2185-90.

Xu, T & Huang, X 2010b, ‘A TG-FTIR investigation into smoke suppression mechanism of magnesium hydroxide in asphalt combustion process’, Journal of Analytical and Applied Pyrolysis, vol. 87, no. 2, pp. 217-23.

Yang, J & Tighe, S 2013, ‘A review of advances of nanotechnology in asphalt mixtures’, Procedia: Social and Behavioral Sciences, vol. 96, pp. 1269-76.

Yao, H, You, ZP, Li, L, Lee, CH, Wingard, D, Yap, YK & Goh, SW 2013, ‘Rheological properties and chemical bonding of asphalt modified with nanosilica’, Journal of Materials in Civil Engineering, vol. 25, no. 11, pp. 1619-30.

Yusoff, NIM, Shaw, MT & Airey, GD 2011, ‘Modelling the linear viscoelastic rheological properties of bituminous binders’, Construction and Building Materials, vol. 25, no. 5, pp. 2171-89.

Zafari, F, Rahi, M, Moshtagh, N & Nazockdast, H 2014, ‘The improvement of bitumen properties by adding nanosilica’, Study of Civil Engineering and Architecture, vol. 3, pp. 62-9.

Zhou, Z, Xu, Z, Masliyah, JH & Czarnecki, J 1999, ‘Coagulation of bitumen with fine silica in model systems’, Colloids and Surfaces A: Physicochemical and Engineering Aspects, vol. 148, no. 3, pp. 199-211.

Zou, G, Xu, J & Wu, C 2017, ‘Evaluation of factors that affect rutting resistance of asphalt mixes by orthogonal experiment design’, International Journal of Pavement Research and Technology, vol. 10, no. 3, pp. 282-8.

Standards

AASHTO R 28 2012 (2016), Standard practice for accelerated aging of asphalt binder using a pressurized aging vessel (PAV).

AASHTO T 350 2014, Standard method of test for multiple stress creep recovery (MSCR) test of asphalt binder using a dynamic shear rheometer (DSR).

AASHTO TP 70 (2013), Standard method of test for multiple stress creep recovery (MSCR) test of asphalt binder using a Dynamic Shear Rheometer (DSR).

AGPT/T190 2019, Specification framework for polymer modified binders.

AGPT/T192 2015, Characterisation of the viscosity of reclaimed asphalt pavement (RAP) binder using the Dynamic Shear Rheometer (DSR).

AGPT/T194 2017, Long-term ageing resistance of bitumen using the Pressure Ageing Vessel (PAV) and the Dynamic Shear Rheometer (DSR).

AS 2008-2013, Bitumen for pavements.

AS 2341.12-1993, Methods of testing bitumen and related roadmaking products: determination of penetration.

AS 2341.18-1992, Methods of testing bituminous and related roadmaking products: determination of softening point (ring and ball method).

AS/NZS 2341.10:2015, Methods of testing bitumen and related roadmaking products: determination of the effect of heat and air on a moving film of bitumen (rolling thin film oven (RTFO) test).

AS/NZS 2341.21:2015, Methods of testing bitumen and related roadmaking products: sample preparation.

ASTM D6521-19A, Standard practice for accelerated aging of asphalt binder using a Pressurized Aging Vessel (PAV).

ASTM D7175-15, Standard test method for determining the rheological properties of asphalt binder using a Dynamic Shear Rheometer.

ASTM D3279-19, Standard test method for n-Heptane insolubles.

ASTM D2872-19, Standard test method for effect of heat and air on a moving film of asphalt (Rolling Thin-Film Oven Test).

ASTM D5976-00, Standard specification for type 1 polymer modified asphalt cement for use in pavement construction, (withdrawn 2005).

ČSN 65 6073 (656073) 2008, Ropné výrobky: stanovení obsahu asfaltenů heptanem.

EN 14769 2012, Bitumen and bituminous binders: accelerated long-term ageing conditioning by a Pressure Ageing Vessel (PAV).

APPENDIX A MRWA WA 716.1 2018, BITUMEN DURABILITY: DYNAMIC SHEAR RHEOMETER METHOD.TYPICAL OUTPUTS FROM SWEEP TESTS

Figure A 1: Strain amplitude sweep test at 70 °C, f = 10 rad/s for unaged C320 sample: (I) graph, (II) data

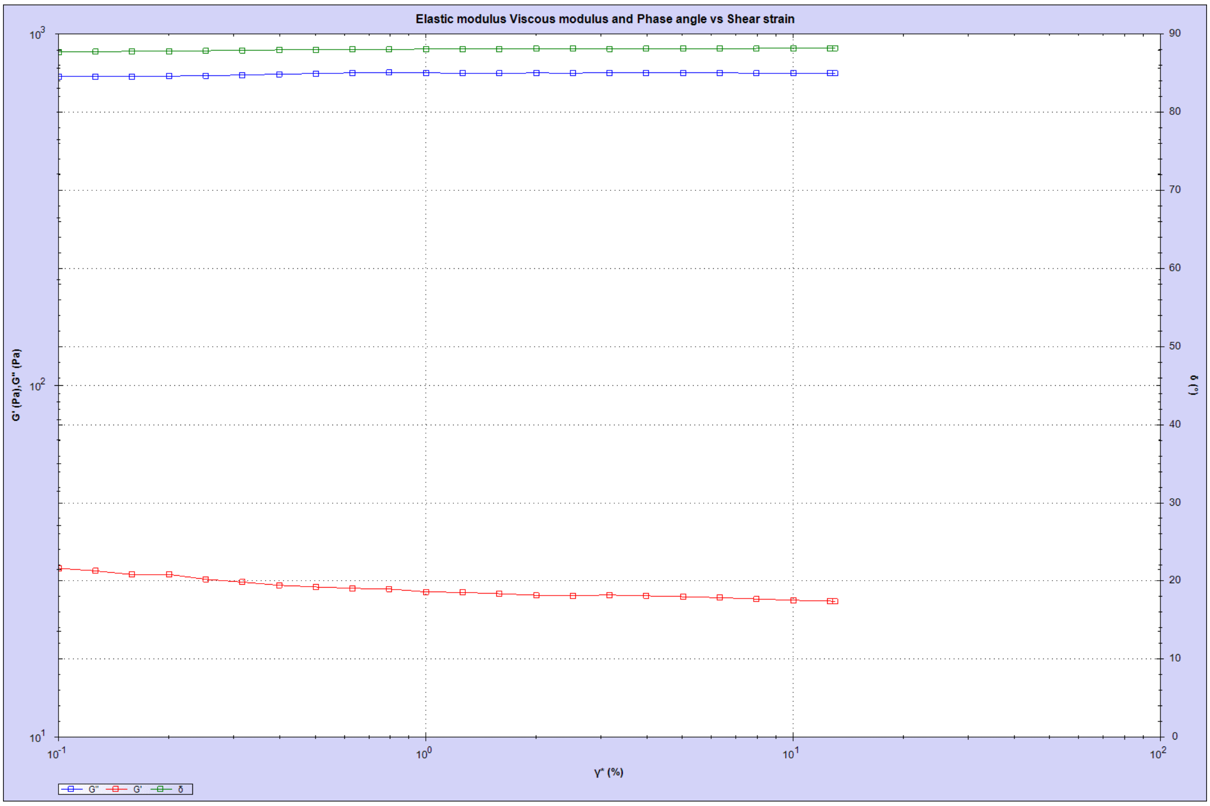

(I)

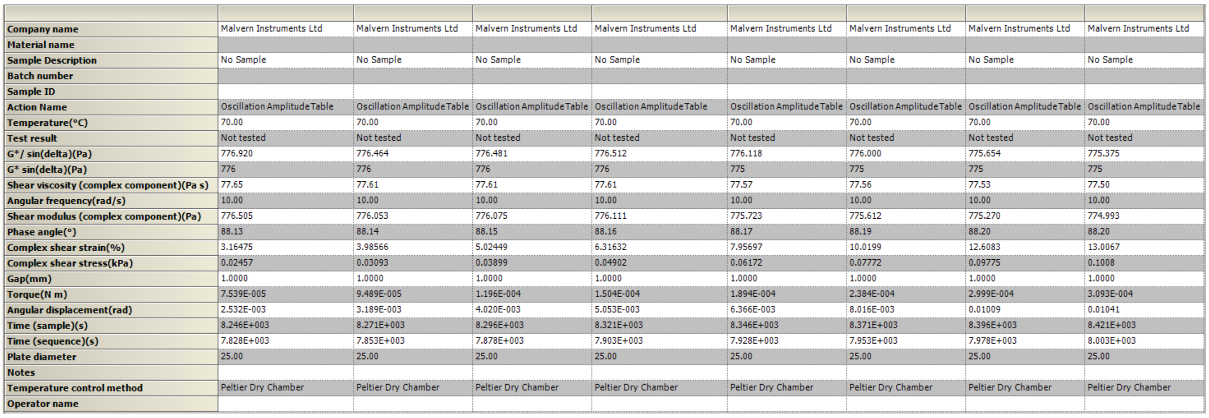

Company name	Malvern Instruments Ltd	Malvern Instruments Ltd	Malvern Instruments Ltd	Malvern Instruments Ltd	Malvern Instruments Ltd	Malvern Instruments Ltd	Malvern Instruments Ltd	Malvern Instruments Ltd
Material name								
Sample Description	No Sample	No Sample	No Sample	No Sample	No Sample	No Sample	No Sample	No Sample
Batch number								
Sample ID								
Action Name	Oscillation Amplitude Table	Oscillation Amplitude Table	Oscillation Amplitude Table	Oscillation Amplitude Table	Oscillation Amplitude Table	Oscillation Amplitude Table	Oscillation Amplitude Table	Oscillation Amplitude Table
Temperature(°C)	70.00	70.00	70.00	70.00	70.00	70.00	70.00	70.00
Test result	Not tested	Not tested	Not tested	Not tested	Not tested	Not tested	Not tested	Not tested
G*/ sin(delta)(Pa)	776.920	776.464	776.481	776.512	776.118	776.000	775.654	775.375
G* sin(delta)(Pa)	776	776	776	776	775	775	775	775
Shear viscosity (complex component)(Pa s)	77.65	77.61	77.61	77.61	77.57	77.56	77.53	77.50
Angular frequency(rad/s)	10.00	10.00	10.00	10.00	10.00	10.00	10.00	10.00
Shear modulus (complex component)(Pa)	776.505	776.053	776.075	776.111	775.723	775.612	775.270	774.993
Phase angle(°)	88.13	88.14	88.15	88.16	88.17	88.19	88.20	88.20
Complex shear strain(%)	3.16475	3.98566	5.02449	6.31632	7.95697	10.0199	12.6083	13.0067
Complex shear stress(kPa)	0.02457	0.03093	0.03899	0.04902	0.06172	0.07772	0.09775	0.1008
Gap(mm)	1.0000	1.0000	1.0000	1.0000	1.0000	1.0000	1.0000	1.0000
Torque(N m)	7.539E-005	9.489E-005	1.196E-004	1.504E-004	1.894E-004	2.384E-004	2.999E-004	3.093E-004
Angular displacement(rad)	2.532E-003	3.189E-003	4.020E-003	5.053E-003	6.366E-003	8.016E-003	0.01009	0.01041
Time (sample)(s)	8.246E+003	8.271E+003	8.296E+003	8.321E+003	8.346E+003	8.371E+003	8.396E+003	8.421E+003
Time (sequence)(s)	7.828E+003	7.853E+003	7.878E+003	7.903E+003	7.928E+003	7.953E+003	7.978E+003	8.003E+003
Plate diameter	25.00	25.00	25.00	25.00	25.00	25.00	25.00	25.00
Notes								
Temperature control method	Peltier Dry Chamber	Peltier Dry Chamber	Peltier Dry Chamber	Peltier Dry Chamber	Peltier Dry Chamber	Peltier Dry Chamber	Peltier Dry Chamber	Peltier Dry Chamber
Operator name								

(II)

Figure A 2: Strain amplitude sweep Test at 40 °C, f = 10 rad/s for unaged C320 sample: (I) graph, II data

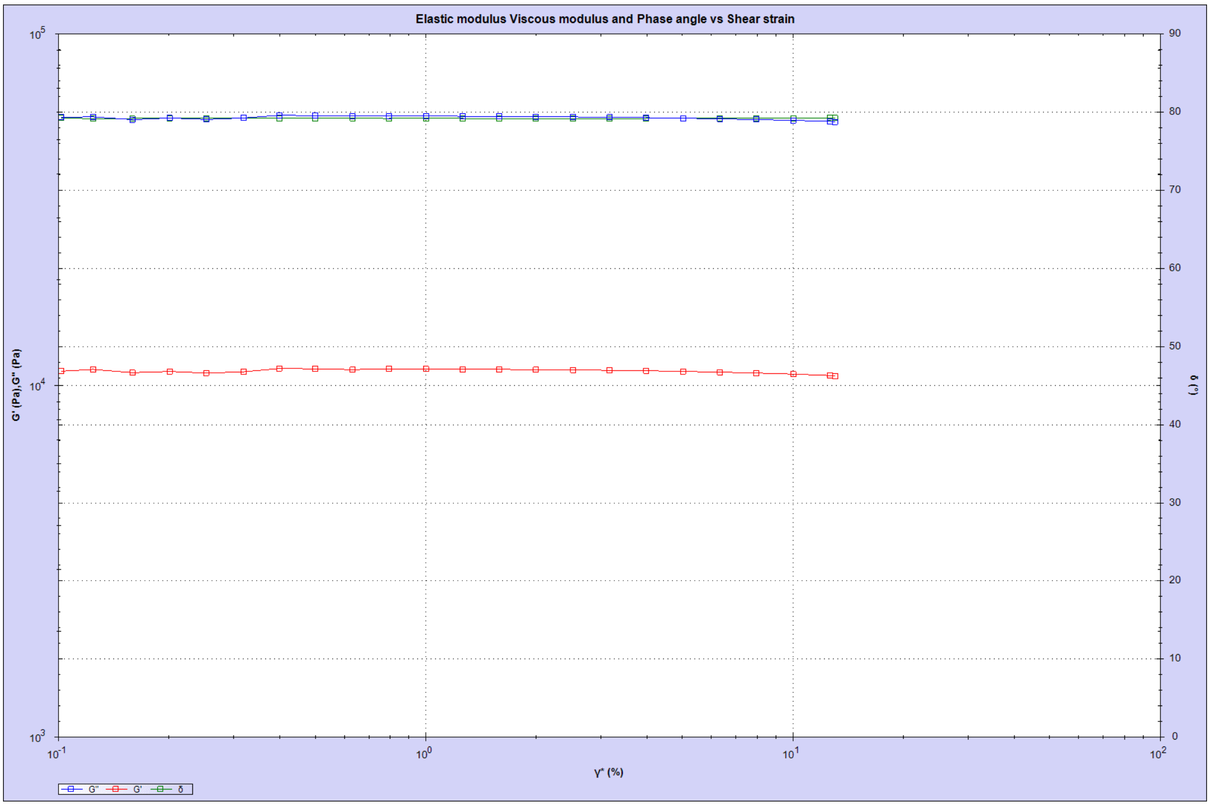

(I)

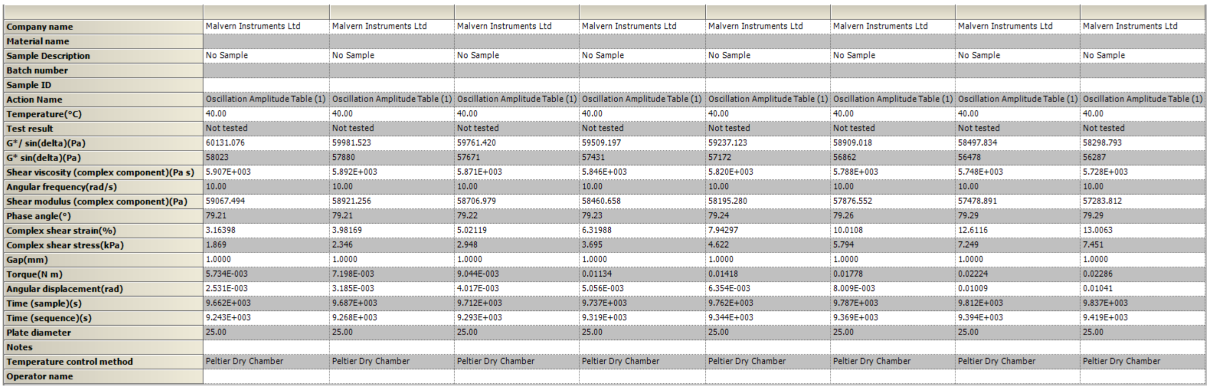

Company name	Malvern Instruments Ltd	Malvern Instruments Ltd	Malvern Instruments Ltd	Malvern Instruments Ltd	Malvern Instruments Ltd	Malvern Instruments Ltd	Malvern Instruments Ltd	Malvern Instruments Ltd
Material name								
Sample Description	No Sample	No Sample	No Sample	No Sample	No Sample	No Sample	No Sample	No Sample
Batch number								
Sample ID								
Action Name	Oscillation Amplitude Table (1)	Oscillation Amplitude Table (1)	Oscillation Amplitude Table (1)	Oscillation Amplitude Table (1)	Oscillation Amplitude Table (1)	Oscillation Amplitude Table (1)	Oscillation Amplitude Table (1)	Oscillation Amplitude Table (1)
Temperature(°C)	40.00	40.00	40.00	40.00	40.00	40.00	40.00	40.00
Test result	Not tested	Not tested	Not tested	Not tested	Not tested	Not tested	Not tested	Not tested
G*/ sin(delta)(Pa)	60131.076	59981.523	59761.420	59509.197	59237.123	58909.018	58497.834	58298.793
G* sin(delta)(Pa)	58023	57880	57671	57431	57172	56862	56478	56287
Shear viscosity (complex component)(Pa s)	5.907E+003	5.892E+003	5.871E+003	5.846E+003	5.820E+003	5.788E+003	5.748E+003	5.728E+003
Angular frequency(rad/s)	10.00	10.00	10.00	10.00	10.00	10.00	10.00	10.00
Shear modulus (complex component)(Pa)	59067.494	58921.256	58706.979	58460.658	58195.280	57876.552	57478.891	57283.812
Phase angle(°)	79.21	79.21	79.22	79.23	79.24	79.26	79.29	79.29
Complex shear strain(%)	3.16398	3.98169	5.02119	6.31988	7.94297	10.0108	12.6116	13.0063
Complex shear stress(kPa)	1.869	2.346	2.948	3.695	4.622	5.794	7.249	7.451
Gap(mm)	1.0000	1.0000	1.0000	1.0000	1.0000	1.0000	1.0000	1.0000
Torque(N m)	5.734E-003	7.198E-003	9.044E-003	0.01134	0.01418	0.01778	0.02224	0.02286
Angular displacement(rad)	2.531E-003	3.185E-003	4.017E-003	5.056E-003	6.354E-003	8.009E-003	0.01009	0.01041
Time (sample)(s)	9.662E+003	9.687E+003	9.712E+003	9.737E+003	9.762E+003	9.787E+003	9.812E+003	9.837E+003
Time (sequence)(s)	9.243E+003	9.268E+003	9.293E+003	9.319E+003	9.344E+003	9.369E+003	9.394E+003	9.419E+003
Plate diameter	25.00	25.00	25.00	25.00	25.00	25.00	25.00	25.00
Notes								
Temperature control method	Peltier Dry Chamber	Peltier Dry Chamber	Peltier Dry Chamber	Peltier Dry Chamber	Peltier Dry Chamber	Peltier Dry Chamber	Peltier Dry Chamber	Peltier Dry Chamber
Operator name								

(II)

Figure A 3: Frequency sweep test at 40 °C, complex shear strain = 1% for unaged C320 sample: (I) graph, II data

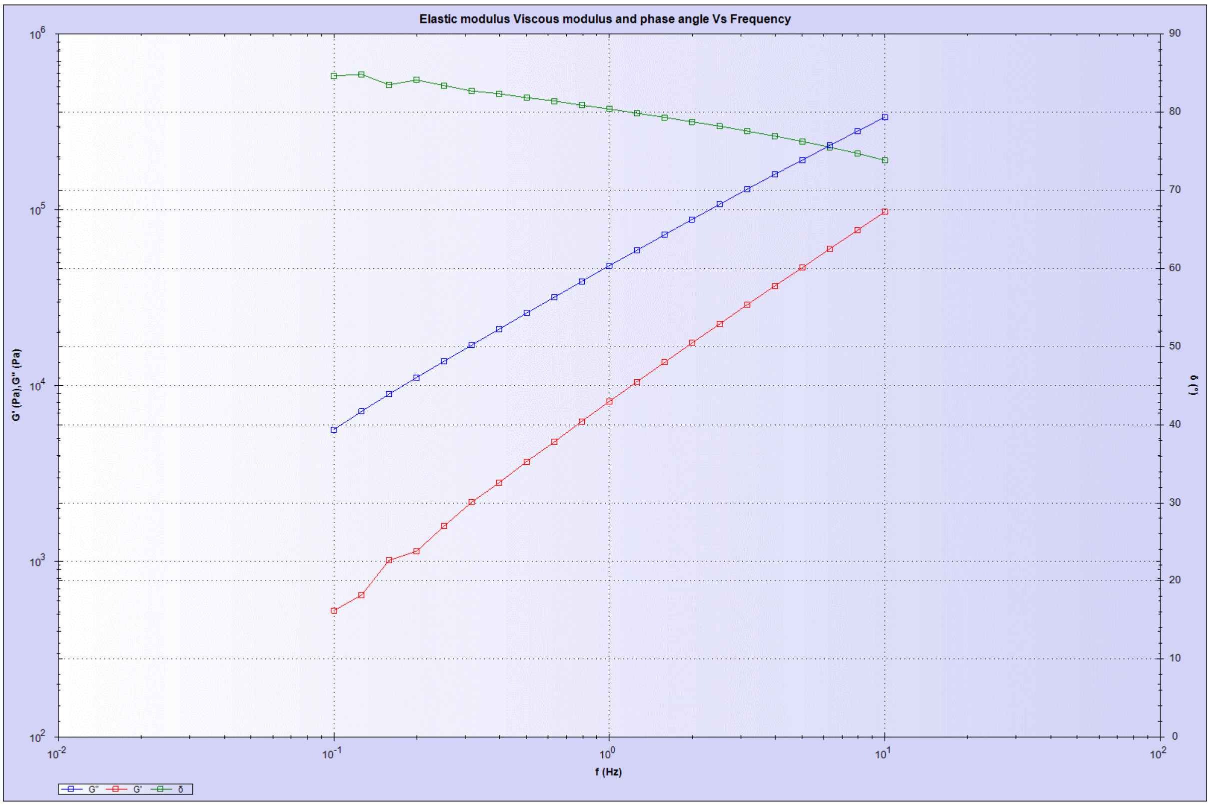

(I)

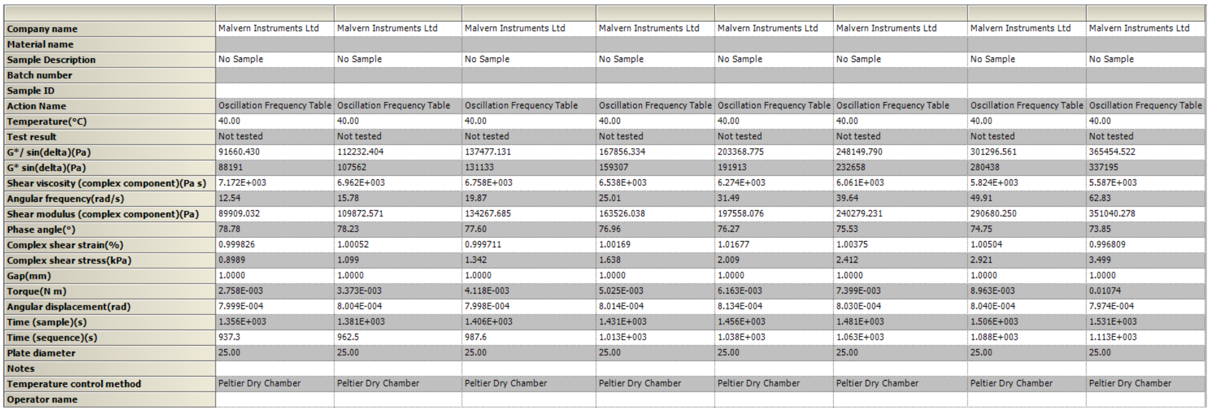

Company name	Malvern Instruments Ltd	Malvern Instruments Ltd	Malvern Instruments Ltd	Malvern Instruments Ltd	Malvern Instruments Ltd	Malvern Instruments Ltd	Malvern Instruments Ltd	Malvern Instruments Ltd
Material name								
Sample Description	No Sample	No Sample	No Sample	No Sample	No Sample	No Sample	No Sample	No Sample
Batch number								
Sample ID								
Action Name	Oscillation Frequency Table	Oscillation Frequency Table	Oscillation Frequency Table	Oscillation Frequency Table	Oscillation Frequency Table	Oscillation Frequency Table	Oscillation Frequency Table	Oscillation Frequency Table
Temperature(°C)	40.00	40.00	40.00	40.00	40.00	40.00	40.00	40.00
Test result	Not tested	Not tested	Not tested	Not tested	Not tested	Not tested	Not tested	Not tested
G*/ sin(delta)(Pa)	91660.430	112232.404	137477.131	167856.334	203368.775	248149.790	301296.561	365454.522
G* sin(delta)(Pa)	88191	107562	131133	159307	191913	232658	280438	337195
Shear viscosity (complex component)(Pa s)	7.172E+003	6.962E+003	6.758E+003	6.538E+003	6.274E+003	6.061E+003	5.824E+003	5.587E+003
Angular frequency(rad/s)	12.54	15.78	19.87	25.01	31.49	39.64	49.91	62.83
Shear modulus (complex component)(Pa)	89909.032	109872.571	134267.685	163526.038	197558.076	240279.231	290680.250	351040.278
Phase angle(°)	78.78	78.23	77.60	76.96	76.27	75.53	74.75	73.85
Complex shear strain(%)	0.999826	1.00052	0.999711	1.00169	1.01677	1.00375	1.00504	0.996809
Complex shear stress(kPa)	0.8989	1.099	1.342	1.638	2.009	2.412	2.921	3.499
Gap(mm)	1.0000	1.0000	1.0000	1.0000	1.0000	1.0000	1.0000	1.0000
Torque(N m)	2.758E-003	3.373E-003	4.118E-003	5.025E-003	6.163E-003	7.399E-003	8.963E-003	0.01074
Angular displacement(rad)	7.999E-004	8.004E-004	7.998E-004	8.014E-004	8.134E-004	8.030E-004	8.040E-004	7.974E-004
Time (sample)(s)	1.356E+003	1.381E+003	1.406E+003	1.431E+003	1.456E+003	1.481E+003	1.506E+003	1.531E+003
Time (sequence)(s)	937.3	962.5	987.6	1.013E+003	1.038E+003	1.063E+003	1.088E+003	1.113E+003
Plate diameter	25.00	25.00	25.00	25.00	25.00	25.00	25.00	25.00
Notes								
Temperature control method	Peltier Dry Chamber	Peltier Dry Chamber	Peltier Dry Chamber	Peltier Dry Chamber	Peltier Dry Chamber	Peltier Dry Chamber	Peltier Dry Chamber	Peltier Dry Chamber
Operator name								

(II)

Figure A 4: Frequency sweep test at 45 °C, complex shear strain = 1% for unaged C320 sample: (I) graph, II data

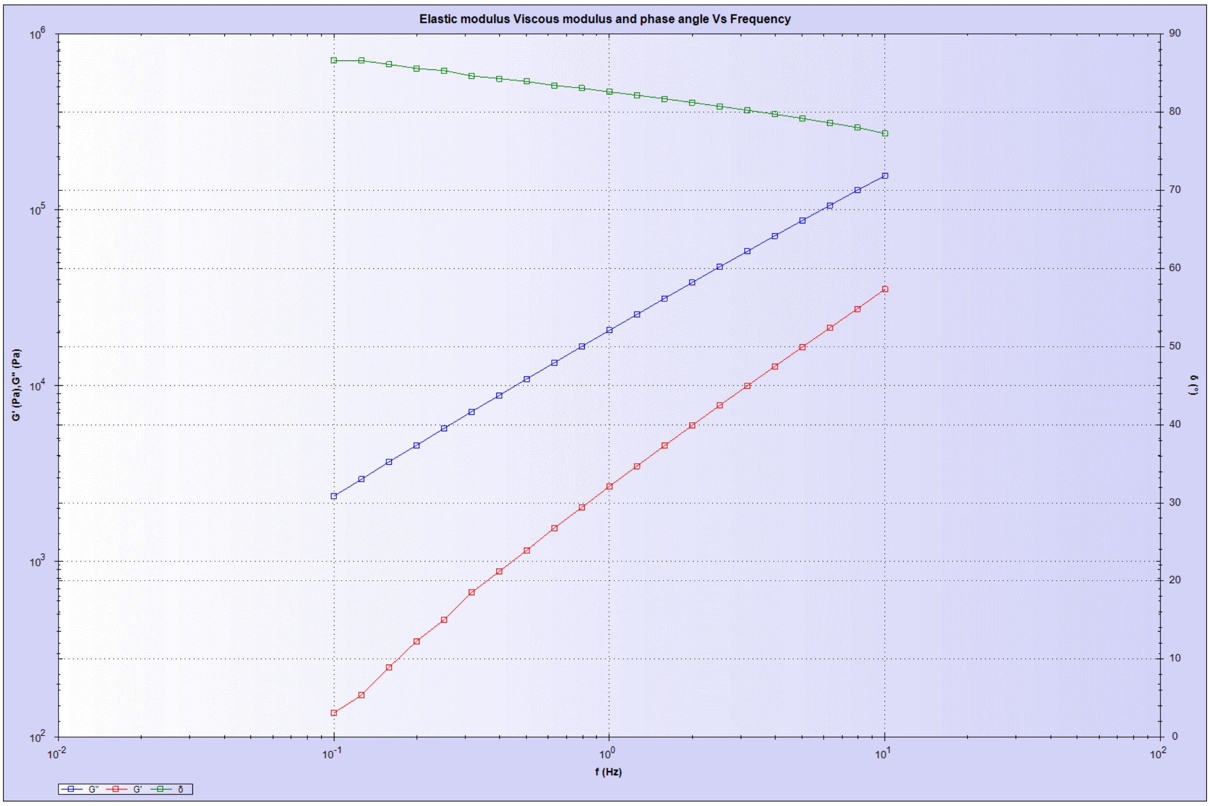

(I)

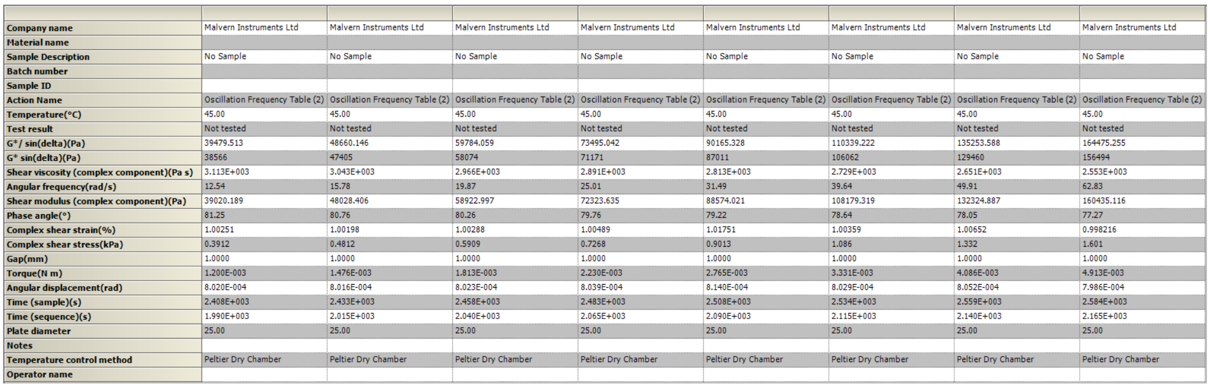

Company name	Malvern Instruments Ltd	Malvern Instruments Ltd	Malvern Instruments Ltd	Malvern Instruments Ltd	Malvern Instruments Ltd	Malvern Instruments Ltd	Malvern Instruments Ltd	Malvern Instruments Ltd
Material name								
Sample Description	No Sample	No Sample	No Sample	No Sample	No Sample	No Sample	No Sample	No Sample
Batch number								
Sample ID								
Action Name	Oscillation Frequency Table (2)	Oscillation Frequency Table (2)	Oscillation Frequency Table (2)	Oscillation Frequency Table (2)	Oscillation Frequency Table (2)	Oscillation Frequency Table (2)	Oscillation Frequency Table (2)	Oscillation Frequency Table (2)
Temperature(°C)	45.00	45.00	45.00	45.00	45.00	45.00	45.00	45.00
Test result	Not tested	Not tested	Not tested	Not tested	Not tested	Not tested	Not tested	Not tested
G*/ sin(delta)(Pa)	39479.513	48660.146	59784.059	73495.042	90165.328	110339.222	135253.588	164475.255
G* sin(delta)(Pa)	38566	47405	58074	71171	87011	106062	129460	156494
Shear viscosity (complex component)(Pa s)	3.113E+003	3.043E+003	2.966E+003	2.891E+003	2.813E+003	2.729E+003	2.651E+003	2.553E+003
Angular frequency(rad/s)	12.54	15.78	19.87	25.01	31.49	39.64	49.91	62.83
Shear modulus (complex component)(Pa)	39020.189	48028.406	58922.997	72323.635	88574.021	108179.319	132324.887	160435.116
Phase angle(°)	81.25	80.76	80.26	79.76	79.22	78.64	78.05	77.27
Complex shear strain(%)	1.00251	1.00198	1.00288	1.00489	1.01751	1.00359	1.00652	0.998216
Complex shear stress(kPa)	0.3912	0.4812	0.5909	0.7268	0.9013	1.086	1.332	1.601
Gap(mm)	1.0000	1.0000	1.0000	1.0000	1.0000	1.0000	1.0000	1.0000
Torque(N m)	1.200E-003	1.476E-003	1.813E-003	2.230E-003	2.765E-003	3.331E-003	4.086E-003	4.913E-003
Angular displacement(rad)	8.020E-004	8.016E-004	8.023E-004	8.039E-004	8.140E-004	8.029E-004	8.052E-004	7.986E-004
Time (sample)(s)	2.408E+003	2.433E+003	2.458E+003	2.483E+003	2.508E+003	2.534E+003	2.559E+003	2.584E+003
Time (sequence)(s)	1.990E+003	2.015E+003	2.040E+003	2.065E+003	2.090E+003	2.115E+003	2.140E+003	2.165E+003
Plate diameter	25.00	25.00	25.00	25.00	25.00	25.00	25.00	25.00
Notes								
Temperature control method	Peltier Dry Chamber	Peltier Dry Chamber	Peltier Dry Chamber	Peltier Dry Chamber	Peltier Dry Chamber	Peltier Dry Chamber	Peltier Dry Chamber	Peltier Dry Chamber
Operator name								

(II)

Figure A 5: Frequency sweep test at 50 °C, complex shear strain = 1% for unaged C320 sample: (I) graph, II data

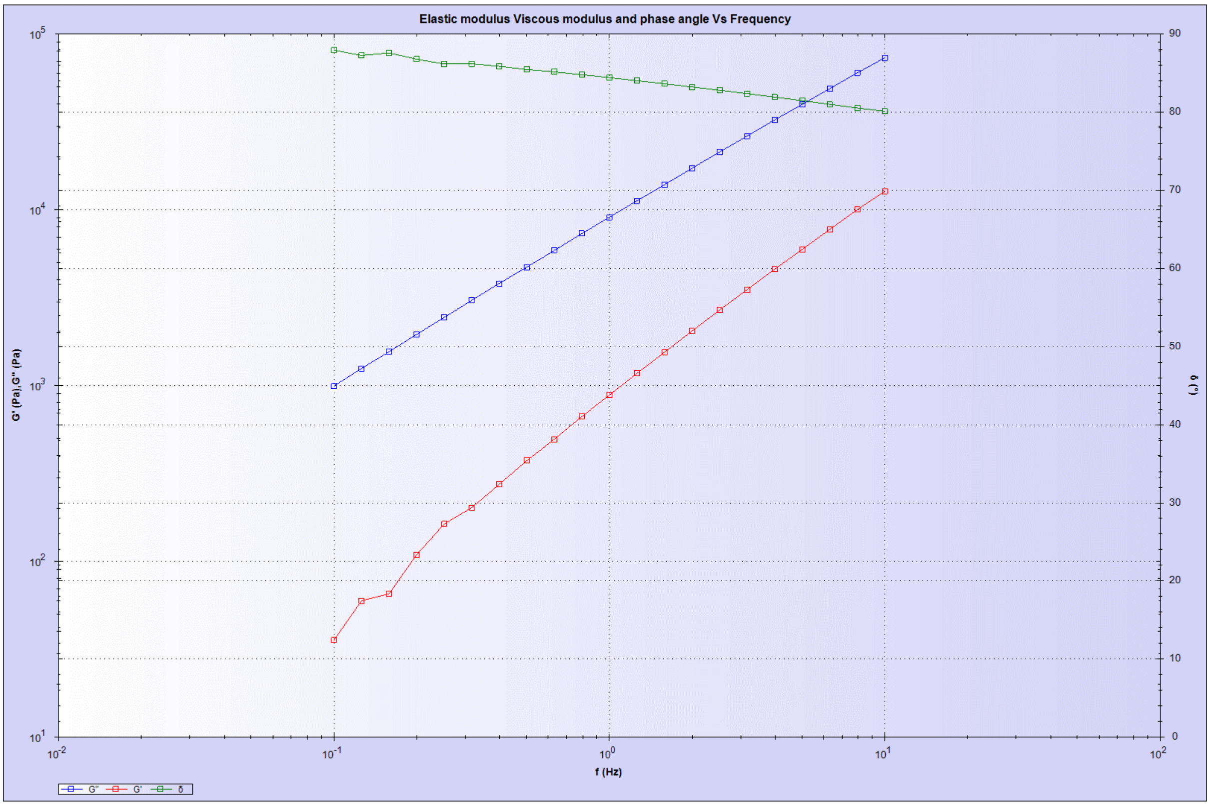

(I)

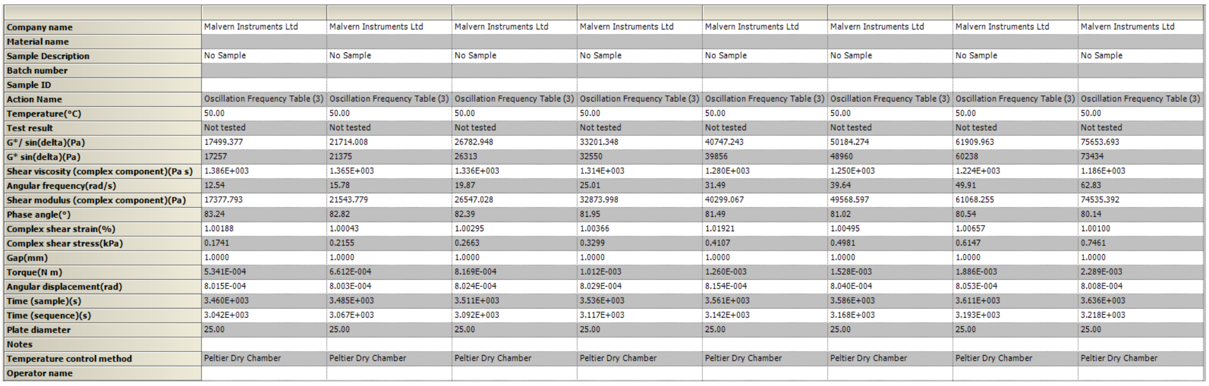

Company name	Malvern Instruments Ltd	Malvern Instruments Ltd	Malvern Instruments Ltd	Malvern Instruments Ltd	Malvern Instruments Ltd	Malvern Instruments Ltd	Malvern Instruments Ltd	Malvern Instruments Ltd
Material name								
Sample Description	No Sample	No Sample	No Sample	No Sample	No Sample	No Sample	No Sample	No Sample
Batch number								
Sample ID								
Action Name	Oscillation Frequency Table (3)	Oscillation Frequency Table (3)	Oscillation Frequency Table (3)	Oscillation Frequency Table (3)	Oscillation Frequency Table (3)	Oscillation Frequency Table (3)	Oscillation Frequency Table (3)	Oscillation Frequency Table (3)
Temperature(°C)	50.00	50.00	50.00	50.00	50.00	50.00	50.00	50.00
Test result	Not tested	Not tested	Not tested	Not tested	Not tested	Not tested	Not tested	Not tested
G*/ sin(delta)(Pa)	17499.377	21714.008	26782.948	33201.348	40747.243	50184.274	61909.963	75653.693
G* sin(delta)(Pa)	17257	21375	26313	32550	39856	48960	60238	73434
Shear viscosity (complex component)(Pa s)	1.386E+003	1.365E+003	1.336E+003	1.314E+003	1.280E+003	1.250E+003	1.224E+003	1.186E+003
Angular frequency(rad/s)	12.54	15.78	19.87	25.01	31.49	39.64	49.91	62.83
Shear modulus (complex component)(Pa)	17377.793	21543.779	26547.028	32873.998	40299.067	49568.597	61068.255	74535.392
Phase angle(°)	83.24	82.82	82.39	81.95	81.49	81.02	80.54	80.14
Complex shear strain(%)	1.00188	1.00043	1.00295	1.00366	1.01921	1.00495	1.00657	1.00100
Complex shear stress(kPa)	0.1741	0.2155	0.2663	0.3299	0.4107	0.4981	0.6147	0.7461
Gap(mm)	1.0000	1.0000	1.0000	1.0000	1.0000	1.0000	1.0000	1.0000
Torque(N m)	5.341E-004	6.612E-004	8.169E-004	1.012E-003	1.260E-003	1.528E-003	1.886E-003	2.289E-003
Angular displacement(rad)	8.015E-004	8.003E-004	8.024E-004	8.029E-004	8.154E-004	8.040E-004	8.053E-004	8.008E-004
Time (sample)(s)	3.460E+003	3.485E+003	3.511E+003	3.536E+003	3.561E+003	3.586E+003	3.611E+003	3.636E+003
Time (sequence)(s)	3.042E+003	3.067E+003	3.092E+003	3.117E+003	3.142E+003	3.168E+003	3.193E+003	3.218E+003
Plate diameter	25.00	25.00	25.00	25.00	25.00	25.00	25.00	25.00
Notes								
Temperature control method	Peltier Dry Chamber	Peltier Dry Chamber	Peltier Dry Chamber	Peltier Dry Chamber	Peltier Dry Chamber	Peltier Dry Chamber	Peltier Dry Chamber	Peltier Dry Chamber
Operator name								

(II)

Figure A 6: Frequency sweep test at 55 °C, complex shear strain = 1% for unaged C320 sample: (I) graph, II data

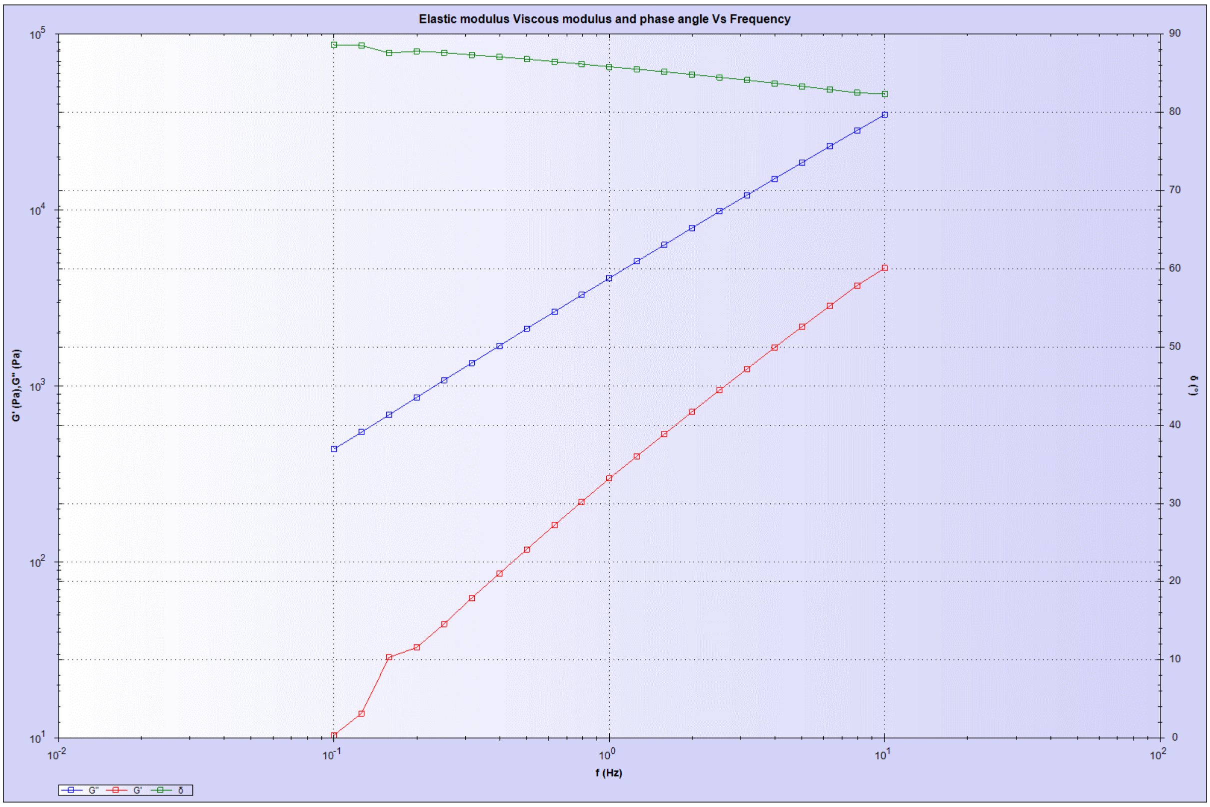

(I)

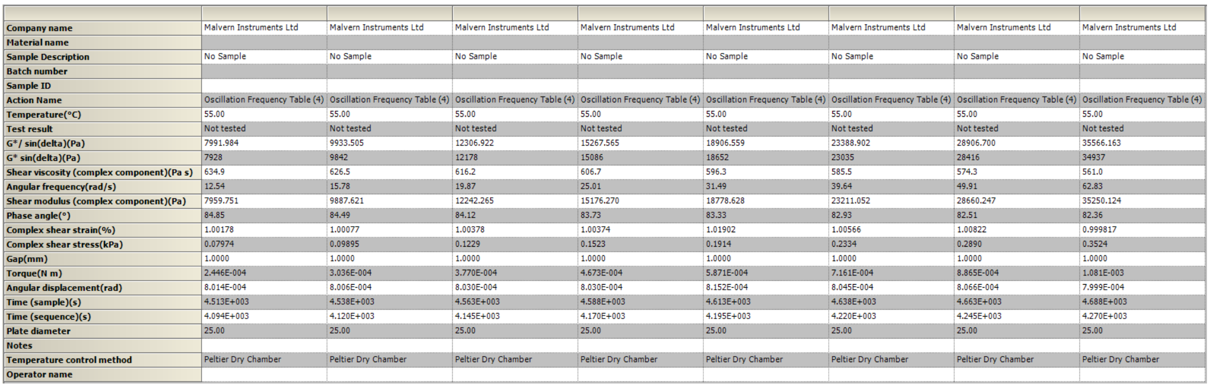

Company name	Malvern Instruments Ltd	Malvern Instruments Ltd	Malvern Instruments Ltd	Malvern Instruments Ltd	Malvern Instruments Ltd	Malvern Instruments Ltd	Malvern Instruments Ltd	Malvern Instruments Ltd
Material name								
Sample Description	No Sample	No Sample	No Sample	No Sample	No Sample	No Sample	No Sample	No Sample
Batch number								
Sample ID								
Action Name	Oscillation Frequency Table (4)	Oscillation Frequency Table (4)	Oscillation Frequency Table (4)	Oscillation Frequency Table (4)	Oscillation Frequency Table (4)	Oscillation Frequency Table (4)	Oscillation Frequency Table (4)	Oscillation Frequency Table (4)
Temperature(°C)	55.00	55.00	55.00	55.00	55.00	55.00	55.00	55.00
Test result	Not tested	Not tested	Not tested	Not tested	Not tested	Not tested	Not tested	Not tested
G*/ sin(delta)(Pa)	7991.984	9933.505	12306.922	15267.565	18906.559	23388.902	28906.700	35566.163
G* sin(delta)(Pa)	7928	9842	12178	15086	18652	23035	28416	34937
Shear viscosity (complex component)(Pa s)	634.9	626.5	616.2	606.7	596.3	585.5	574.3	561.0
Angular frequency(rad/s)	12.54	15.78	19.87	25.01	31.49	39.64	49.91	62.83
Shear modulus (complex component)(Pa)	7959.751	9887.621	12242.265	15176.270	18778.628	23211.052	28660.247	35250.124
Phase angle(°)	84.85	84.49	84.12	83.73	83.33	82.93	82.51	82.36
Complex shear strain(%)	1.00178	1.00077	1.00378	1.00374	1.01902	1.00566	1.00822	0.999817
Complex shear stress(kPa)	0.07974	0.09895	0.1229	0.1523	0.1914	0.2334	0.2890	0.3524
Gap(mm)	1.0000	1.0000	1.0000	1.0000	1.0000	1.0000	1.0000	1.0000
Torque(N m)	2.446E-004	3.036E-004	3.770E-004	4.673E-004	5.871E-004	7.161E-004	8.865E-004	1.081E-003
Angular displacement(rad)	8.014E-004	8.006E-004	8.030E-004	8.030E-004	8.152E-004	8.045E-004	8.066E-004	7.999E-004
Time (sample)(s)	4.513E+003	4.538E+003	4.563E+003	4.588E+003	4.613E+003	4.638E+003	4.663E+003	4.688E+003
Time (sequence)(s)	4.094E+003	4.120E+003	4.145E+003	4.170E+003	4.195E+003	4.220E+003	4.245E+003	4.270E+003
Plate diameter	25.00	25.00	25.00	25.00	25.00	25.00	25.00	25.00
Notes								
Temperature control method	Peltier Dry Chamber	Peltier Dry Chamber	Peltier Dry Chamber	Peltier Dry Chamber	Peltier Dry Chamber	Peltier Dry Chamber	Peltier Dry Chamber	Peltier Dry Chamber
Operator name								

(II)

Figure A 7: Frequency sweep test at 60 °C, complex shear strain = 1% for unaged C320 sample: (I) graph, II data

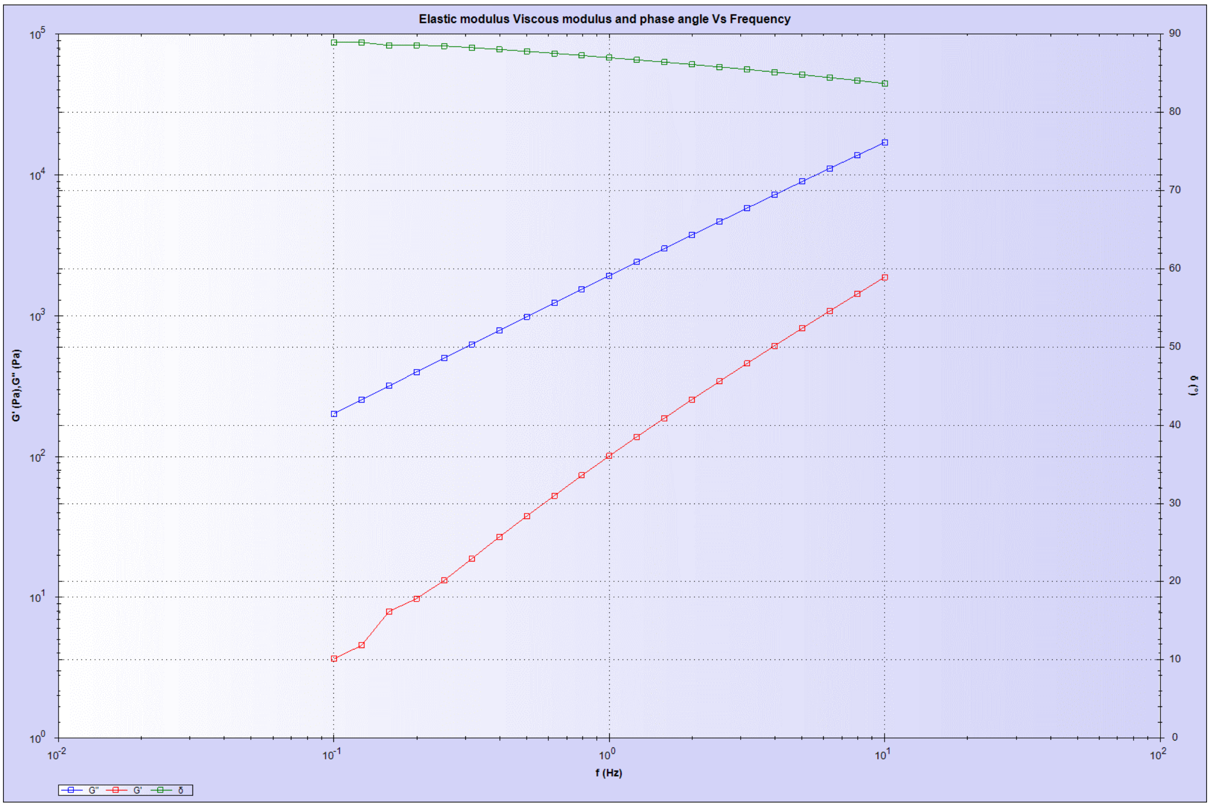

(I)

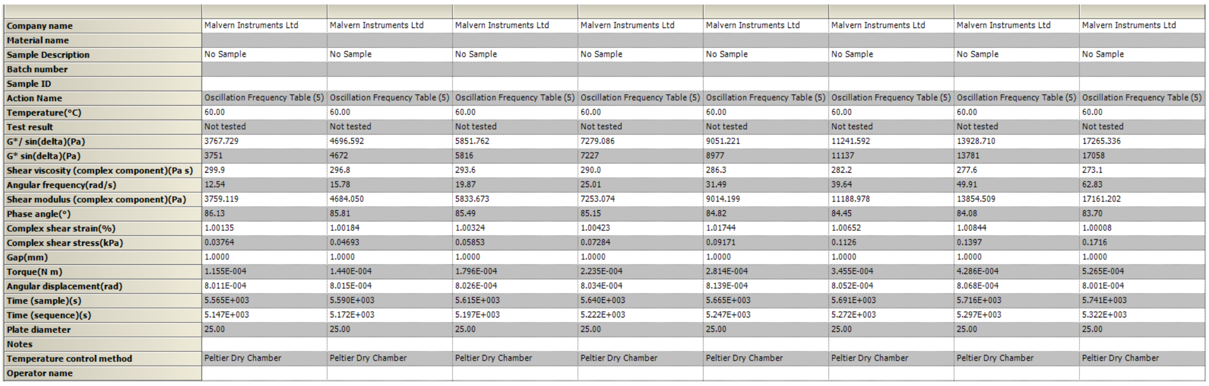

Company name	Malvern Instruments Ltd	Malvern Instruments Ltd	Malvern Instruments Ltd	Malvern Instruments Ltd	Malvern Instruments Ltd	Malvern Instruments Ltd	Malvern Instruments Ltd	Malvern Instruments Ltd
Material name								
Sample Description	No Sample	No Sample	No Sample	No Sample	No Sample	No Sample	No Sample	No Sample
Batch number								
Sample ID								
Action Name	Oscillation Frequency Table (5)	Oscillation Frequency Table (5)	Oscillation Frequency Table (5)	Oscillation Frequency Table (5)	Oscillation Frequency Table (5)	Oscillation Frequency Table (5)	Oscillation Frequency Table (5)	Oscillation Frequency Table (5)
Temperature(°C)	60.00	60.00	60.00	60.00	60.00	60.00	60.00	60.00
Test result	Not tested	Not tested	Not tested	Not tested	Not tested	Not tested	Not tested	Not tested
G*/ sin(delta)(Pa)	3767.729	4696.592	5851.762	7279.086	9051.221	11241.592	13928.710	17265.336
G* sin(delta)(Pa)	3751	4672	5816	7227	8977	11137	13781	17058
Shear viscosity (complex component)(Pa s)	299.9	296.8	293.6	290.0	286.3	282.2	277.6	273.1
Angular frequency(rad/s)	12.54	15.78	19.87	25.01	31.49	39.64	49.91	62.83
Shear modulus (complex component)(Pa)	3759.119	4684.050	5833.673	7253.074	9014.199	11188.978	13854.509	17161.202
Phase angle(°)	86.13	85.81	85.49	85.15	84.82	84.45	84.08	83.70
Complex shear strain(%)	1.00135	1.00184	1.00324	1.00423	1.01744	1.00652	1.00844	1.00008
Complex shear stress(kPa)	0.03764	0.04693	0.05853	0.07284	0.09171	0.1126	0.1397	0.1716
Gap(mm)	1.0000	1.0000	1.0000	1.0000	1.0000	1.0000	1.0000	1.0000
Torque(N m)	1.155E-004	1.440E-004	1.796E-004	2.235E-004	2.814E-004	3.455E-004	4.286E-004	5.265E-004
Angular displacement(rad)	8.011E-004	8.015E-004	8.026E-004	8.034E-004	8.139E-004	8.052E-004	8.068E-004	8.001E-004
Time (sample)(s)	5.565E+003	5.590E+003	5.615E+003	5.640E+003	5.665E+003	5.691E+003	5.716E+003	5.741E+003
Time (sequence)(s)	5.147E+003	5.172E+003	5.197E+003	5.222E+003	5.247E+003	5.272E+003	5.297E+003	5.322E+003
Plate diameter	25.00	25.00	25.00	25.00	25.00	25.00	25.00	25.00
Notes								
Temperature control method	Peltier Dry Chamber	Peltier Dry Chamber	Peltier Dry Chamber	Peltier Dry Chamber	Peltier Dry Chamber	Peltier Dry Chamber	Peltier Dry Chamber	Peltier Dry Chamber
Operator name								

(II)

Figure A 8: Frequency sweep test at 65 °C, complex shear strain = 1% for unaged C320 sample: (I) graph, II data

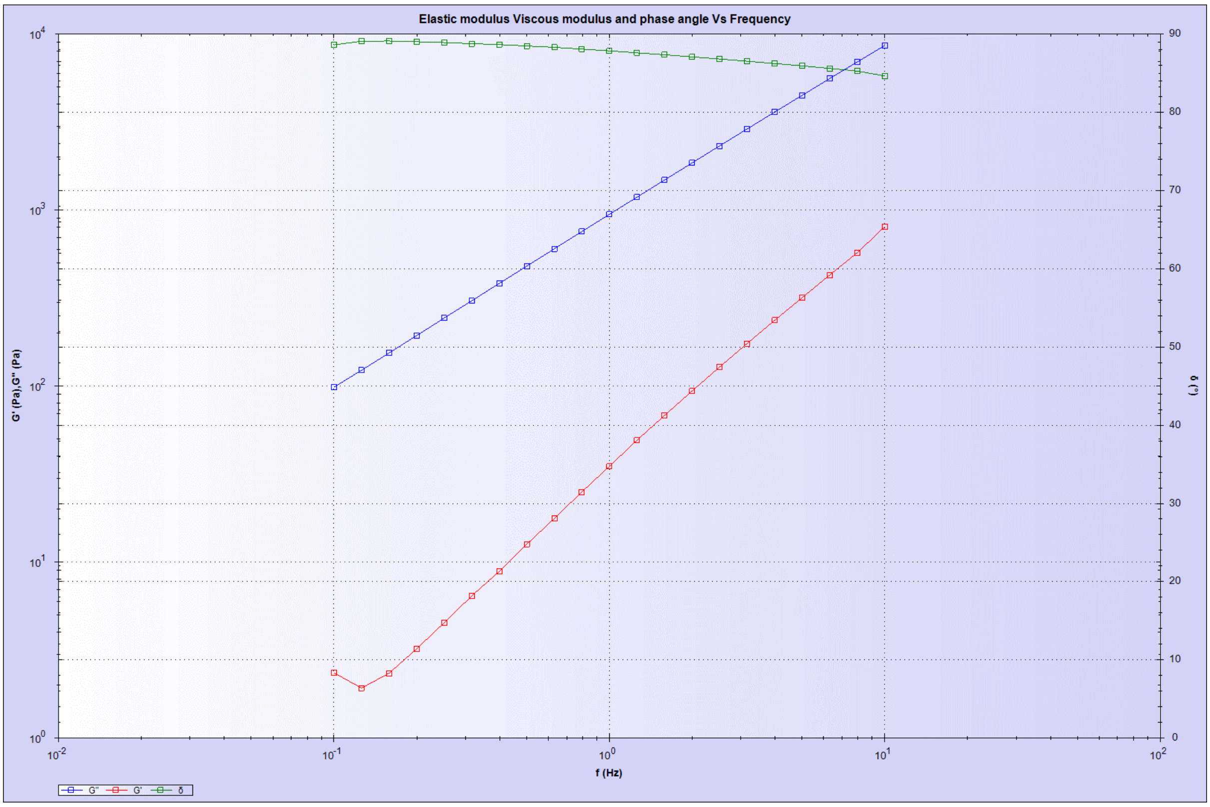

(I)

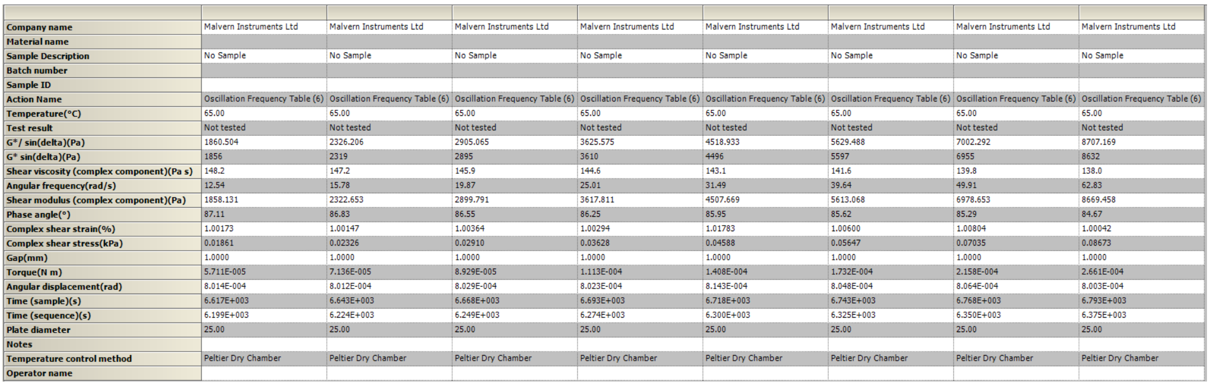

Company name	Malvern Instruments Ltd	Malvern Instruments Ltd	Malvern Instruments Ltd	Malvern Instruments Ltd	Malvern Instruments Ltd	Malvern Instruments Ltd	Malvern Instruments Ltd	Malvern Instruments Ltd
Material name								
Sample Description	No Sample	No Sample	No Sample	No Sample	No Sample	No Sample	No Sample	No Sample
Batch number								
Sample ID								
Action Name	Oscillation Frequency Table (6)	Oscillation Frequency Table (6)	Oscillation Frequency Table (6)	Oscillation Frequency Table (6)	Oscillation Frequency Table (6)	Oscillation Frequency Table (6)	Oscillation Frequency Table (6)	Oscillation Frequency Table (6)
Temperature(°C)	65.00	65.00	65.00	65.00	65.00	65.00	65.00	65.00
Test result	Not tested	Not tested	Not tested	Not tested	Not tested	Not tested	Not tested	Not tested
G*/ sin(delta)(Pa)	1860.504	2326.206	2905.065	3625.575	4518.933	5629.488	7002.292	8707.169
G* sin(delta)(Pa)	1856	2319	2895	3610	4496	5597	6955	8632
Shear viscosity (complex component)(Pa s)	148.2	147.2	145.9	144.6	143.1	141.6	139.8	138.0
Angular frequency(rad/s)	12.54	15.78	19.87	25.01	31.49	39.64	49.91	62.83
Shear modulus (complex component)(Pa)	1858.131	2322.653	2899.791	3617.811	4507.669	5613.068	6978.653	8669.458
Phase angle(°)	87.11	86.83	86.55	86.25	85.95	85.62	85.29	84.67
Complex shear strain(%)	1.00173	1.00147	1.00364	1.00294	1.01783	1.00600	1.00804	1.00042
Complex shear stress(kPa)	0.01861	0.02326	0.02910	0.03628	0.04588	0.05647	0.07035	0.08673
Gap(mm)	1.0000	1.0000	1.0000	1.0000	1.0000	1.0000	1.0000	1.0000
Torque(N m)	5.711E-005	7.136E-005	8.929E-005	1.113E-004	1.408E-004	1.732E-004	2.158E-004	2.661E-004
Angular displacement(rad)	8.014E-004	8.012E-004	8.029E-004	8.023E-004	8.143E-004	8.048E-004	8.064E-004	8.003E-004
Time (sample)(s)	6.617E+003	6.643E+003	6.668E+003	6.693E+003	6.718E+003	6.743E+003	6.768E+003	6.793E+003
Time (sequence)(s)	6.199E+003	6.224E+003	6.249E+003	6.274E+003	6.300E+003	6.325E+003	6.350E+003	6.375E+003
Plate diameter	25.00	25.00	25.00	25.00	25.00	25.00	25.00	25.00
Notes								
Temperature control method	Peltier Dry Chamber	Peltier Dry Chamber	Peltier Dry Chamber	Peltier Dry Chamber	Peltier Dry Chamber	Peltier Dry Chamber	Peltier Dry Chamber	Peltier Dry Chamber
Operator name								

(II)

Figure A 9: Frequency sweep test at 70 °C, complex shear strain = 1% for unaged C320 sample: (I) graph, II data

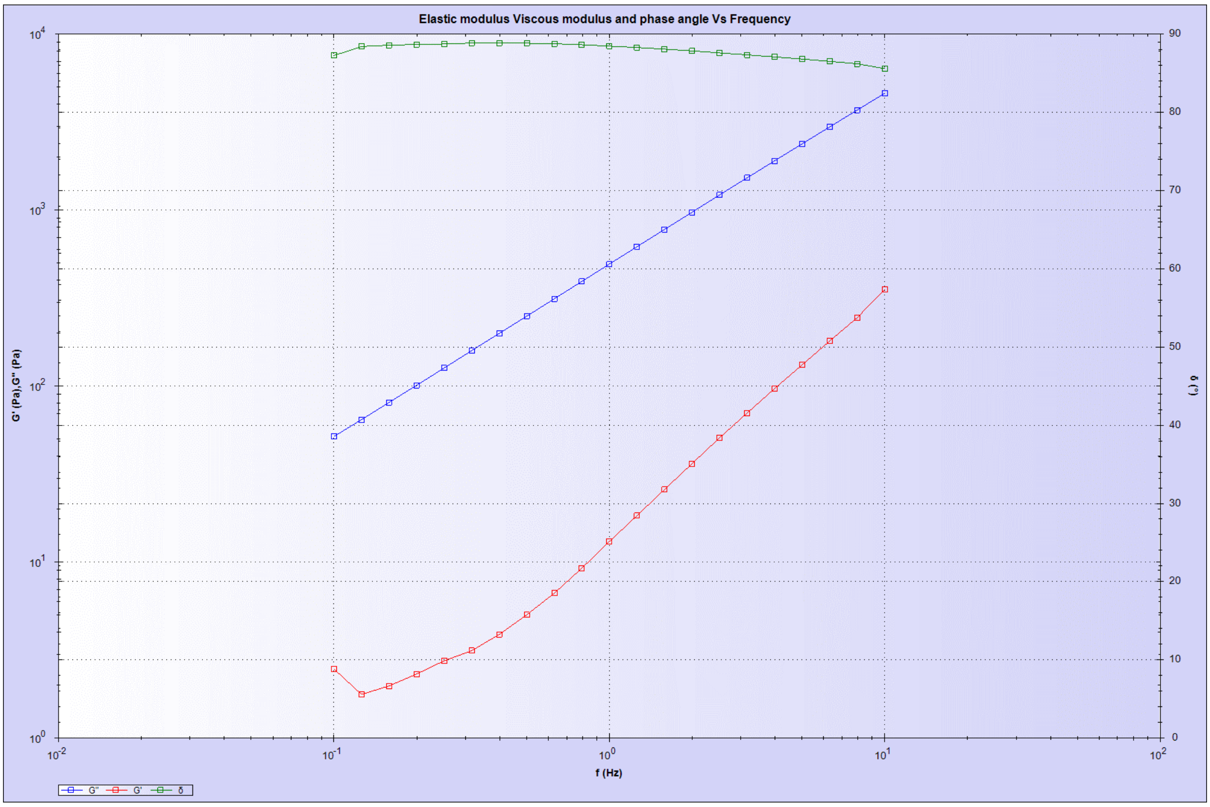

(I)

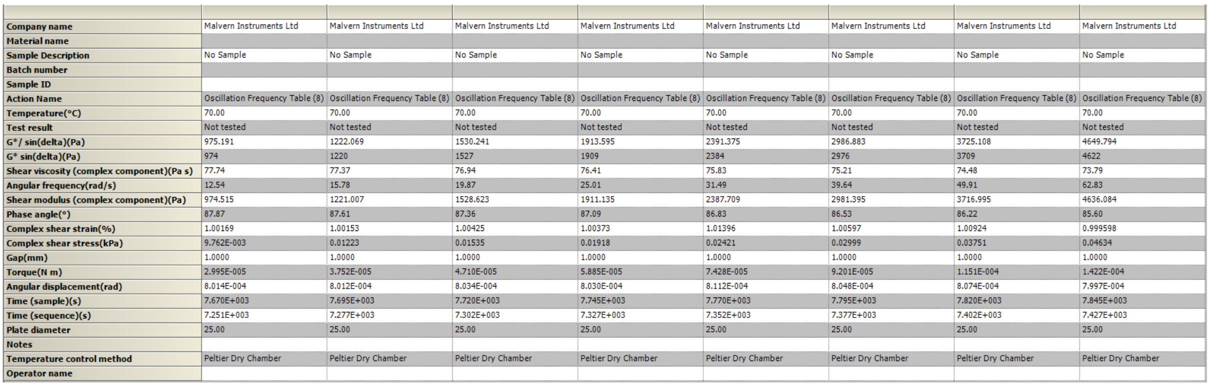

Company name	Malvern Instruments Ltd	Malvern Instruments Ltd	Malvern Instruments Ltd	Malvern Instruments Ltd	Malvern Instruments Ltd	Malvern Instruments Ltd	Malvern Instruments Ltd	Malvern Instruments Ltd
Material name								
Sample Description	No Sample	No Sample	No Sample	No Sample	No Sample	No Sample	No Sample	No Sample
Batch number								
Sample ID								
Action Name	Oscillation Frequency Table (8)	Oscillation Frequency Table (8)	Oscillation Frequency Table (8)	Oscillation Frequency Table (8)	Oscillation Frequency Table (8)	Oscillation Frequency Table (8)	Oscillation Frequency Table (8)	Oscillation Frequency Table (8)
Temperature(°C)	70.00	70.00	70.00	70.00	70.00	70.00	70.00	70.00
Test result	Not tested	Not tested	Not tested	Not tested	Not tested	Not tested	Not tested	Not tested
G*/ sin(delta)(Pa)	975.191	1222.069	1530.241	1913.595	2391.375	2986.883	3725.108	4649.794
G* sin(delta)(Pa)	974	1220	1527	1909	2384	2976	3709	4622
Shear viscosity (complex component)(Pa s)	77.74	77.37	76.94	76.41	75.83	75.21	74.48	73.79
Angular frequency(rad/s)	12.54	15.78	19.87	25.01	31.49	39.64	49.91	62.83
Shear modulus (complex component)(Pa)	974.515	1221.007	1528.623	1911.135	2387.709	2981.395	3716.995	4636.084
Phase angle(°)	87.87	87.61	87.36	87.09	86.83	86.53	86.22	85.60
Complex shear strain(%)	1.00169	1.00153	1.00425	1.00373	1.01396	1.00597	1.00924	0.999598
Complex shear stress(kPa)	9.762E-003	0.01223	0.01535	0.01918	0.02421	0.02999	0.03751	0.04634
Gap(mm)	1.0000	1.0000	1.0000	1.0000	1.0000	1.0000	1.0000	1.0000
Torque(N m)	2.995E-005	3.752E-005	4.710E-005	5.885E-005	7.428E-005	9.201E-005	1.151E-004	1.422E-004
Angular displacement(rad)	8.014E-004	8.012E-004	8.034E-004	8.030E-004	8.112E-004	8.048E-004	8.074E-004	7.997E-004
Time (sample)(s)	7.670E+003	7.695E+003	7.720E+003	7.745E+003	7.770E+003	7.795E+003	7.820E+003	7.845E+003
Time (sequence)(s)	7.251E+003	7.277E+003	7.302E+003	7.327E+003	7.352E+003	7.377E+003	7.402E+003	7.427E+003
Plate diameter	25.00	25.00	25.00	25.00	25.00	25.00	25.00	25.00
Notes								
Temperature control method	Peltier Dry Chamber	Peltier Dry Chamber	Peltier Dry Chamber	Peltier Dry Chamber	Peltier Dry Chamber	Peltier Dry Chamber	Peltier Dry Chamber	Peltier Dry Chamber
Operator name								

(II)

APPENDIX B MASTER CURVES

Figure B 1: Master curve of unaged C320 at 60 °C: (I) sample 1, (II) sample 2

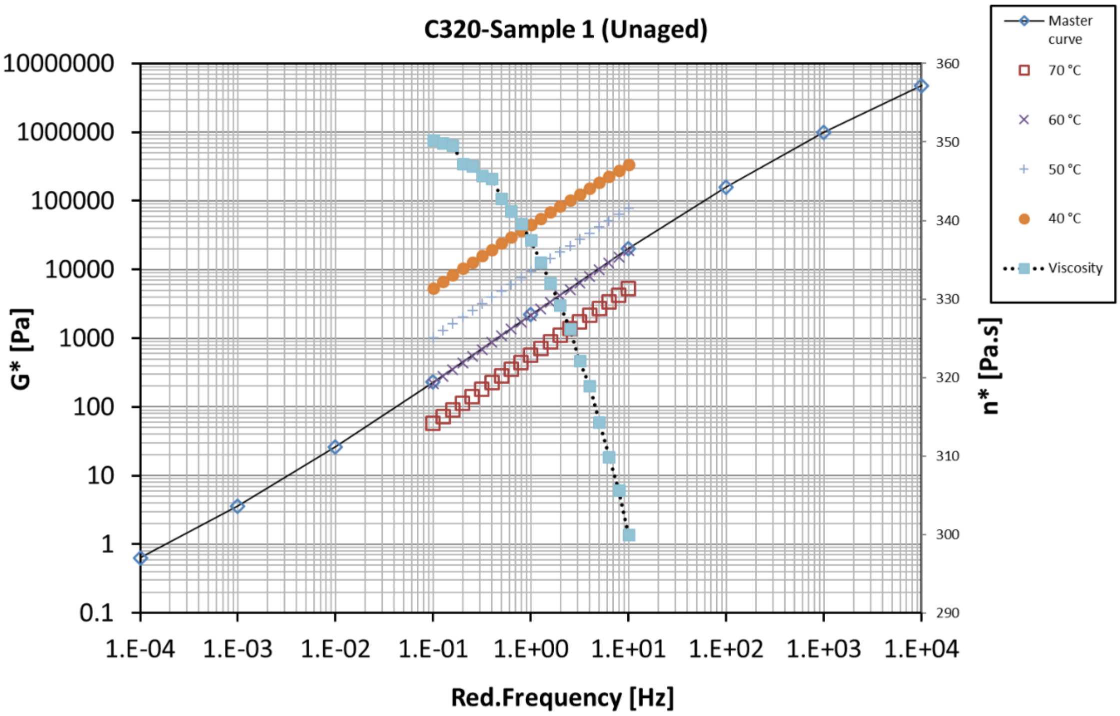

(I)

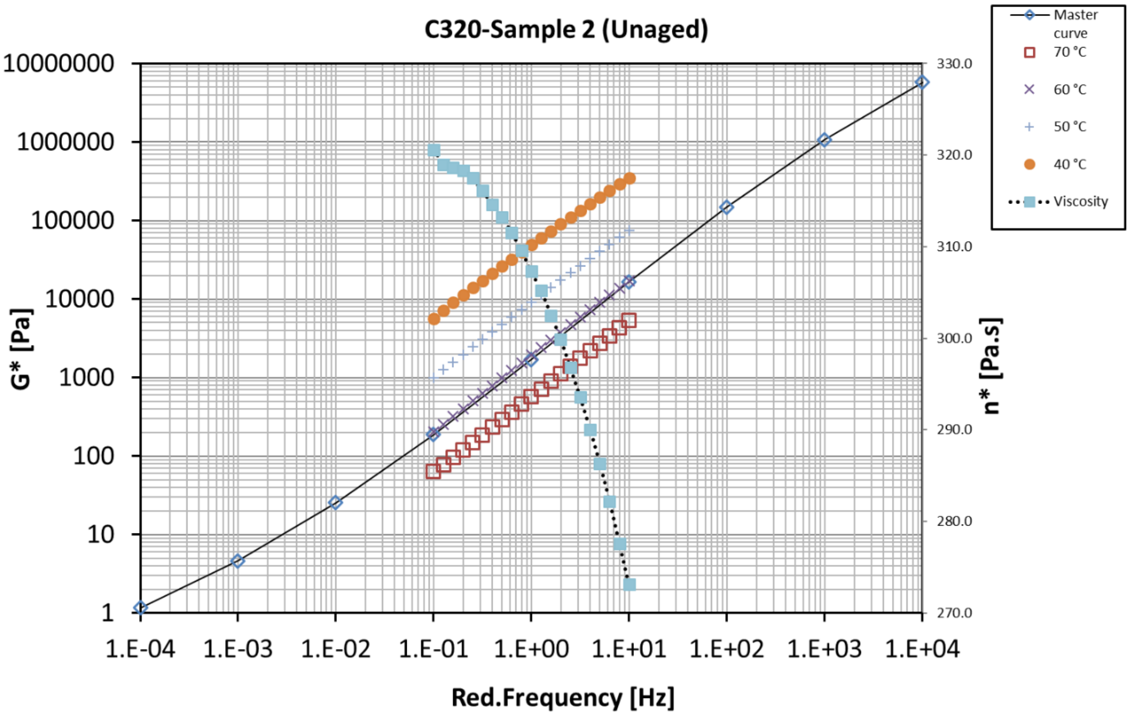

(II)

Figure B 2: Master curve of unaged C320 + 2% NS (20nm + KH550 couplant) at 60 °C: (I) sample 1, (II) sample 2

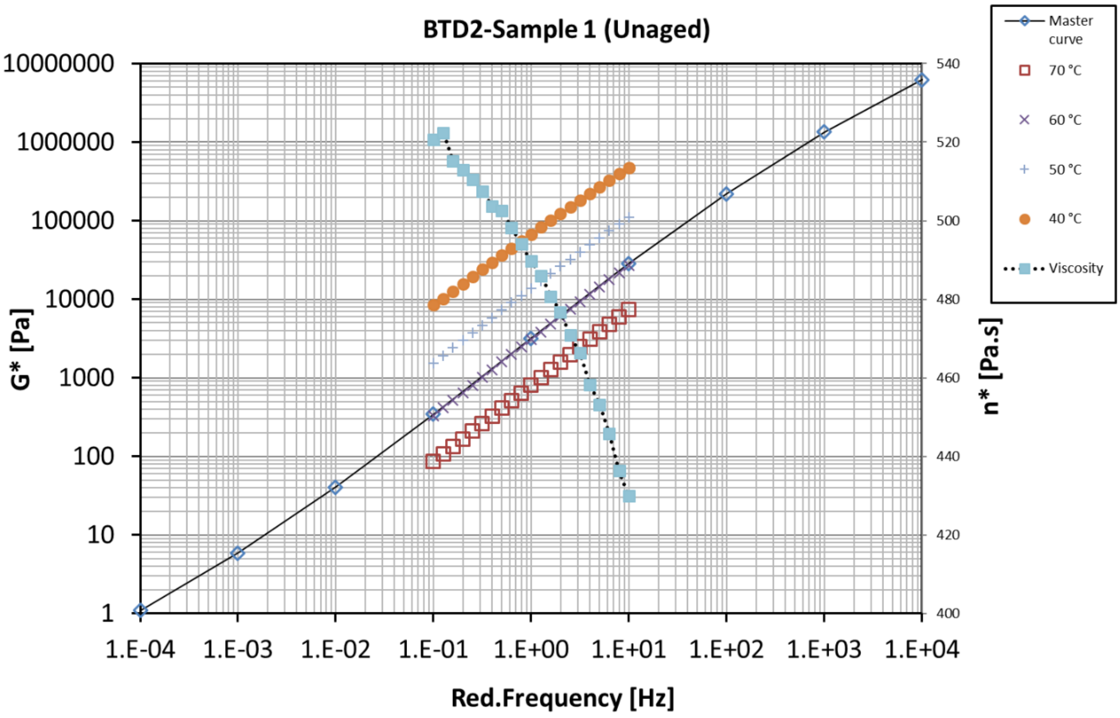

(I)

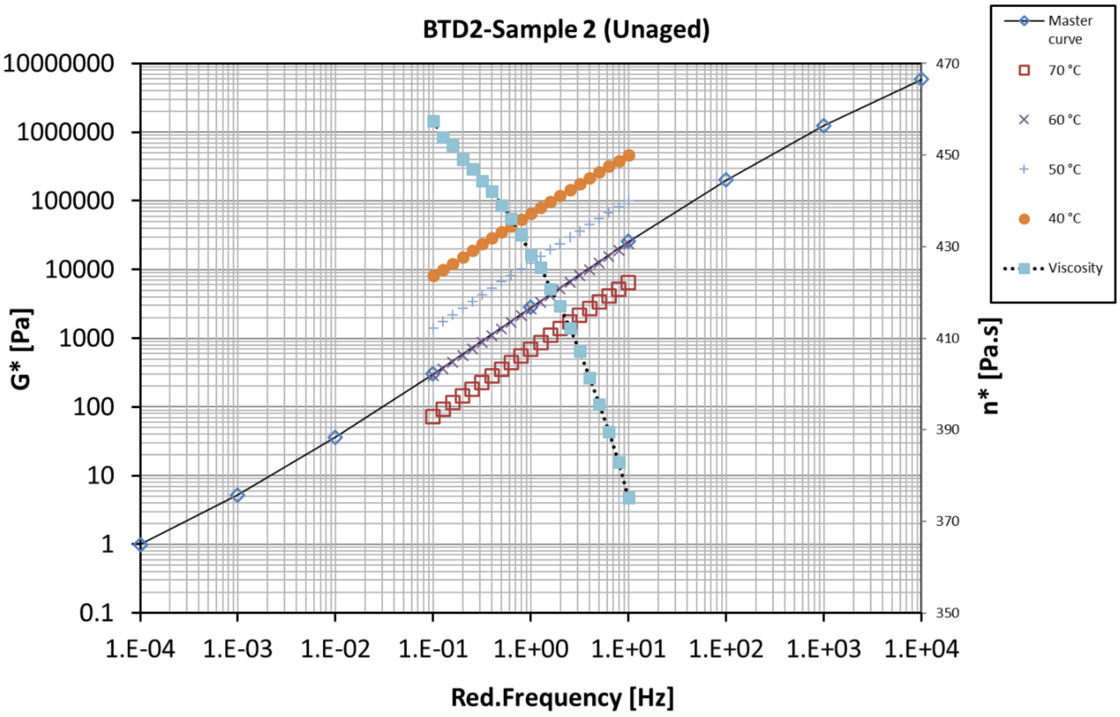

(II)

Figure B 3: Master curve of unaged C320 + 4% NS (20nm + KH550 couplant) at 60 °C: (I) sample 1, (II) sample 2

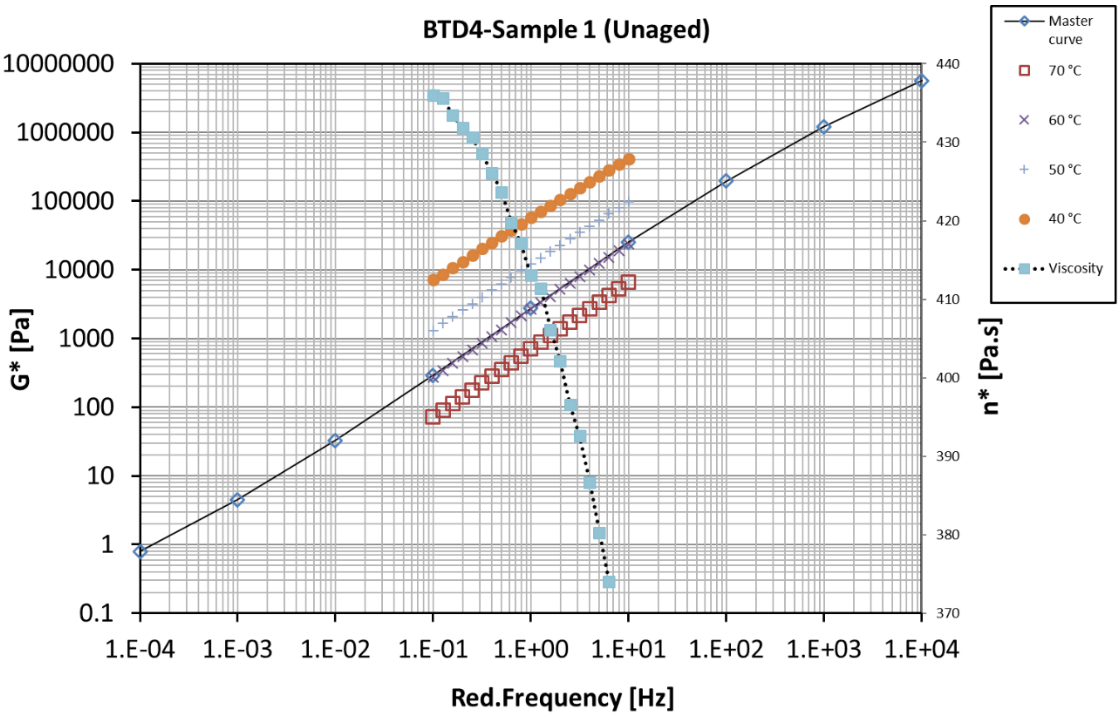

(I)

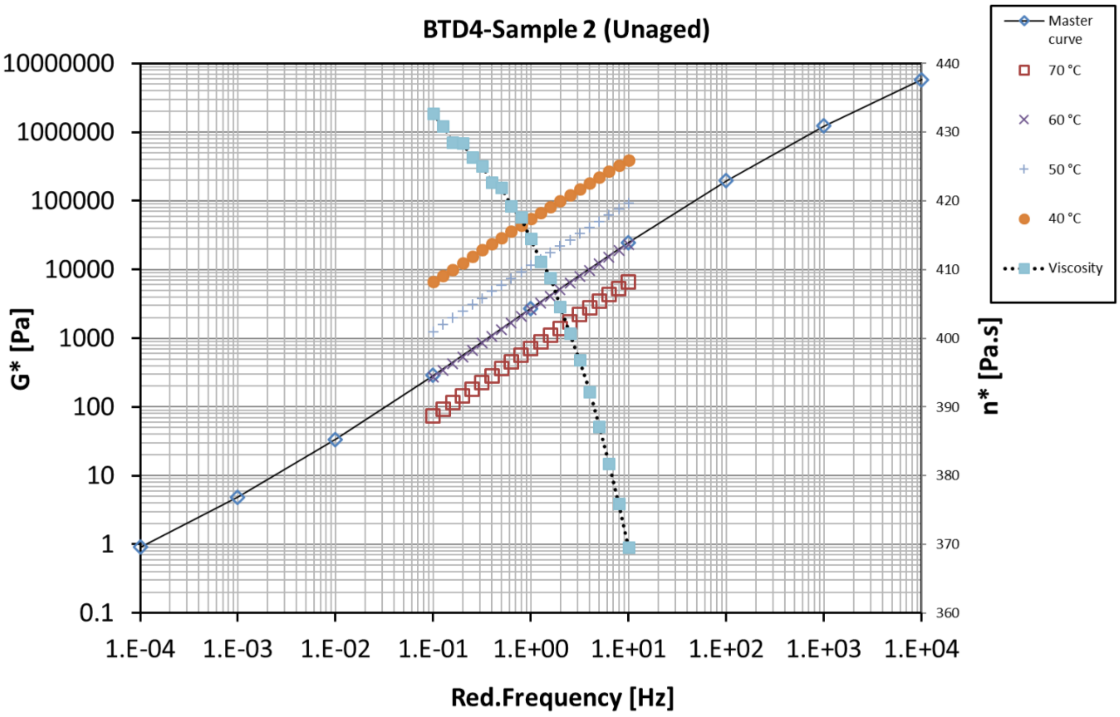

(II)

Figure B 4: Master curve of unaged C320 + 6% NS (20nm + KH550 couplant) at 60 °C: (I) sample 1, (II) sample 2

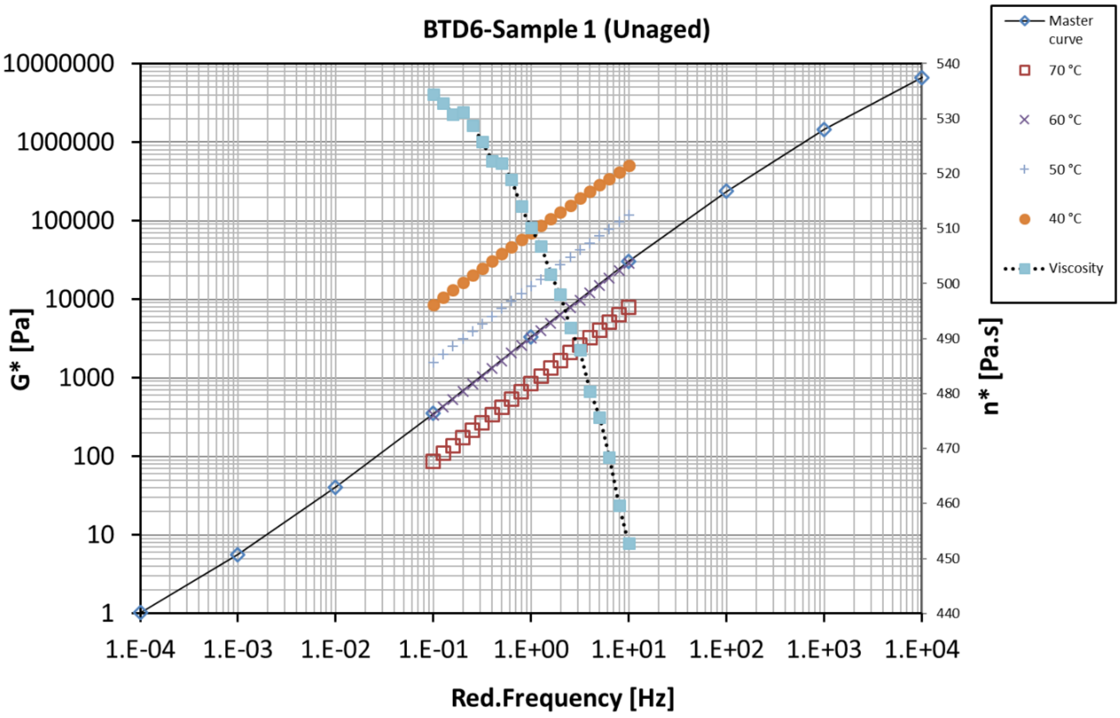

(I)

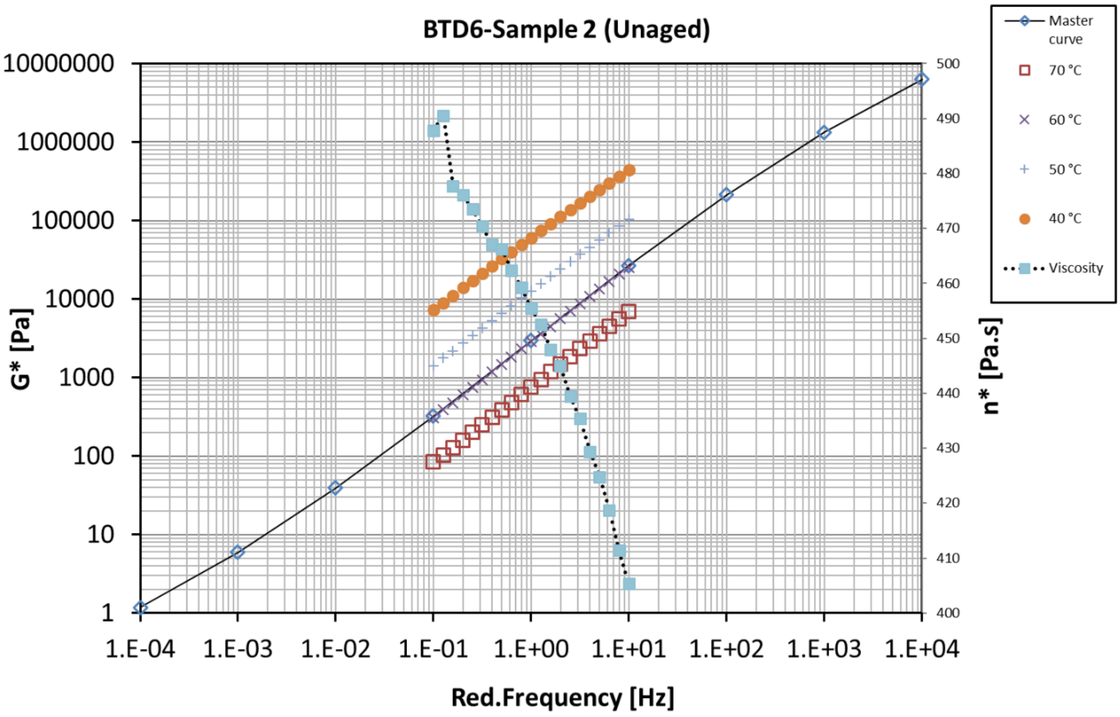

(II)

Figure B 5: Master curve of unaged C320 + 2% NS (20nm) at 60 °C: (I) sample 1, (II) sample 2

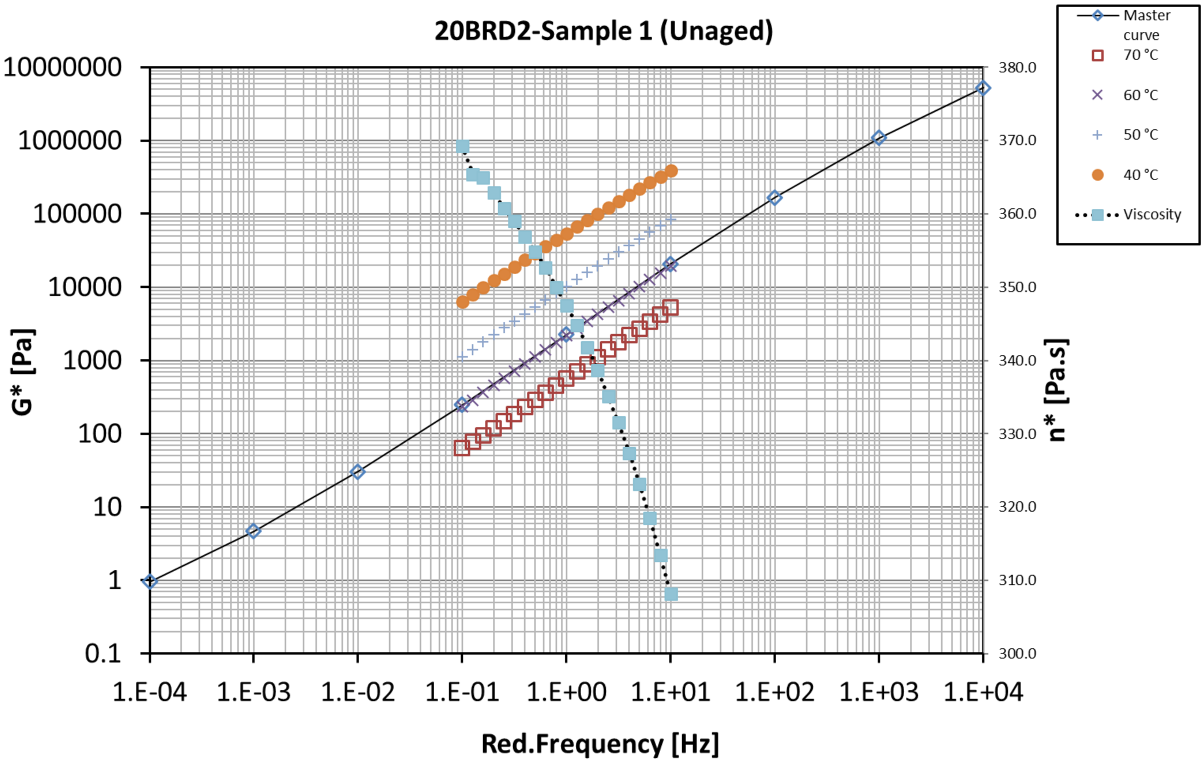

(I)

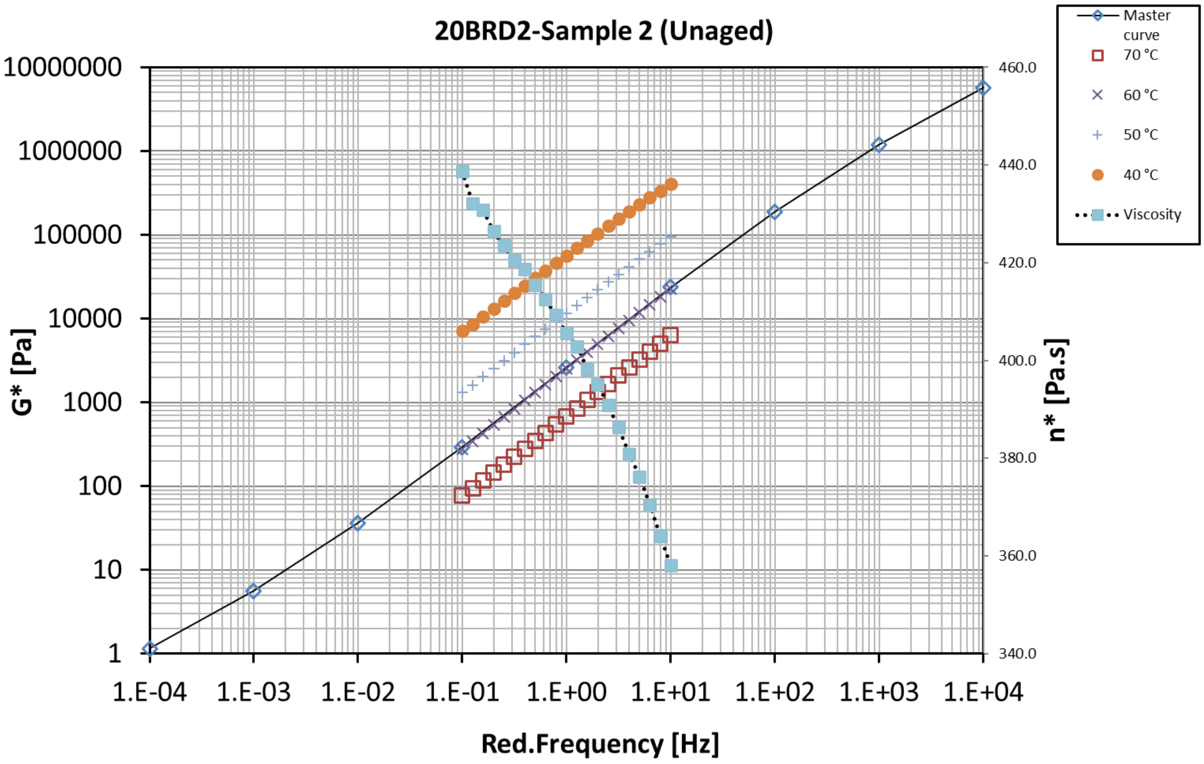

(II)

Figure B 6: Master curve of unaged C320 + 4% NS (20nm) at 60 °C: (I) sample 1, (II) sample 2

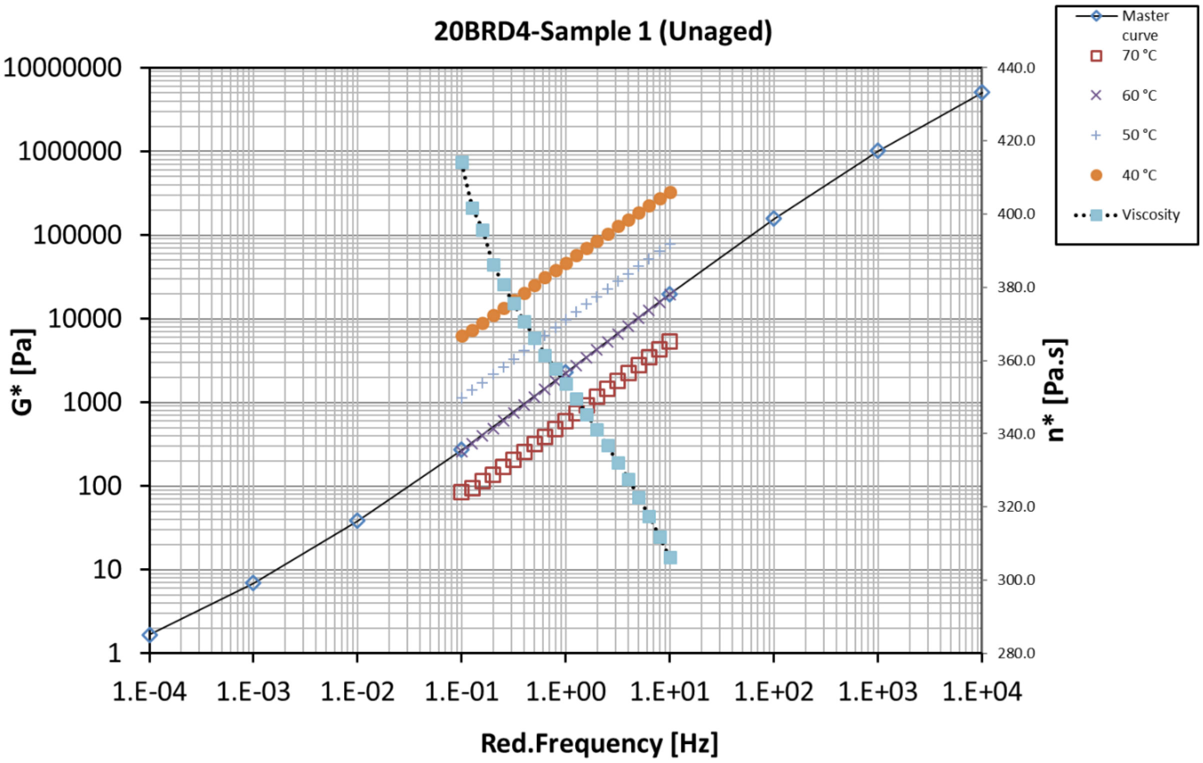

(I)

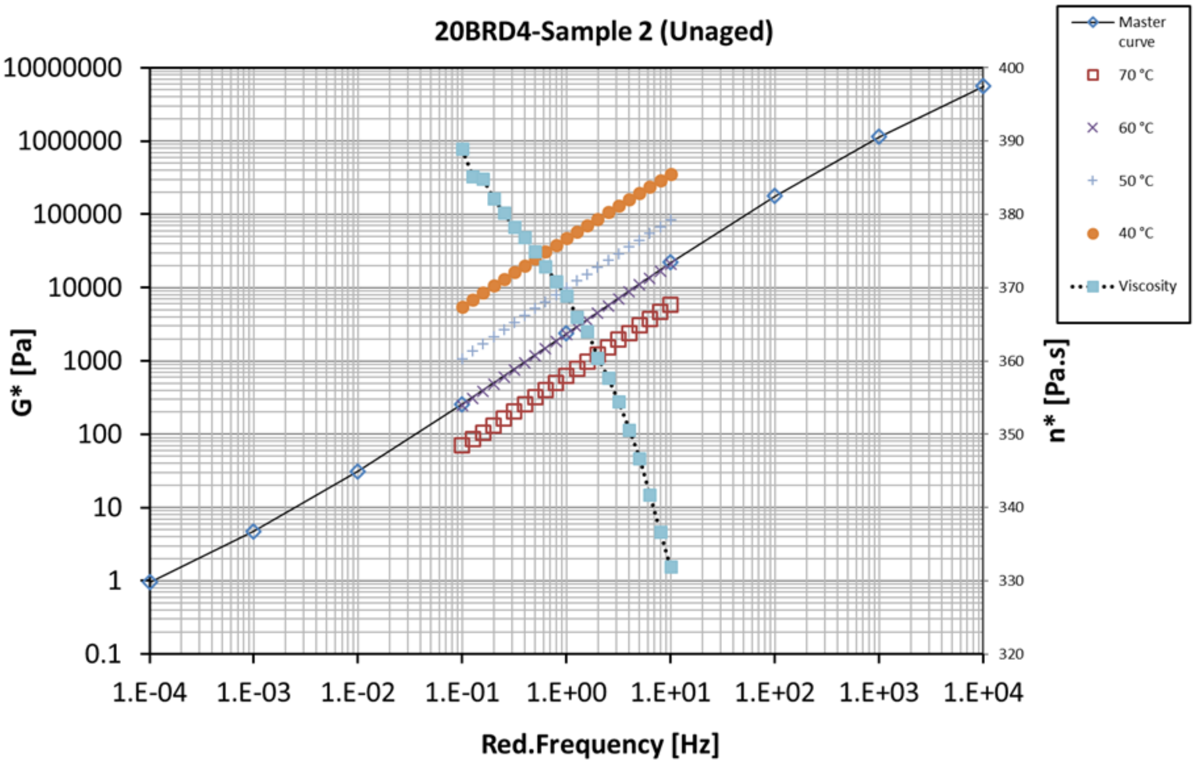

(II)

Figure B 7: Master curve of unaged C320 + 6% NS (20nm) at 60 °C.

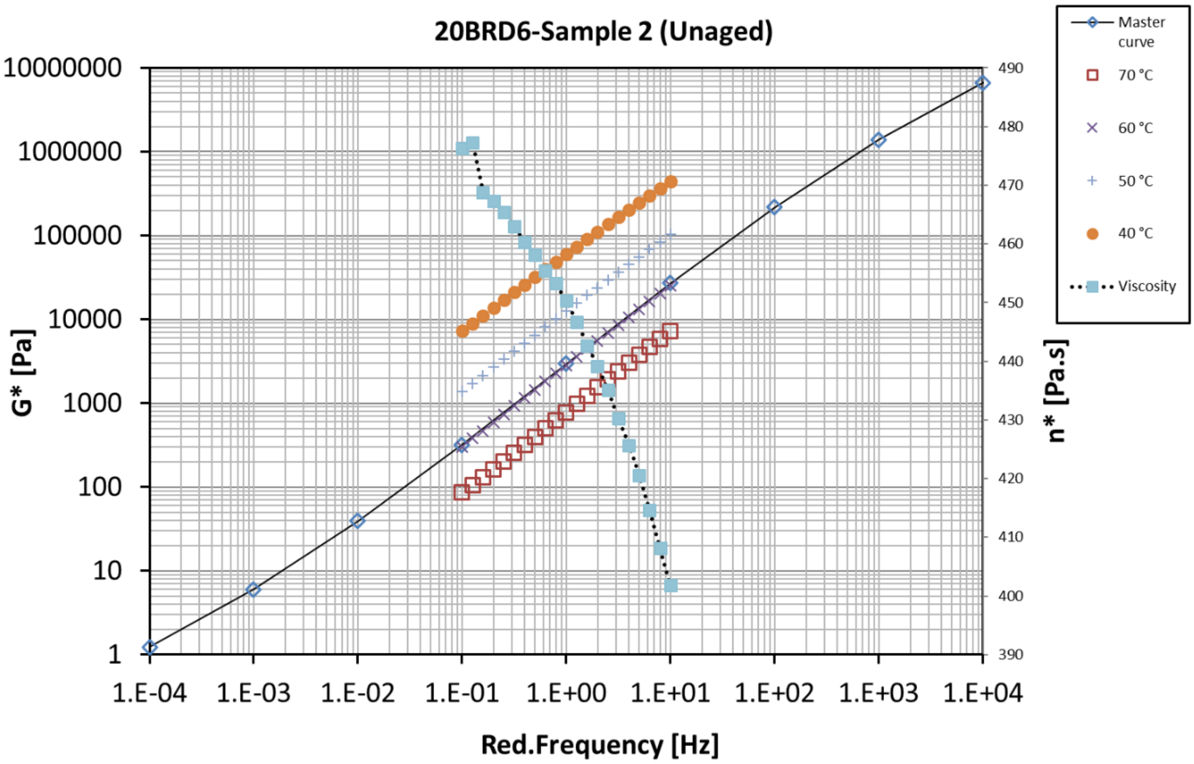

Figure B 8: Master curve of unaged C320 + 2% NS (60nm) at 60 °C: (I) sample 1, (II) sample 2

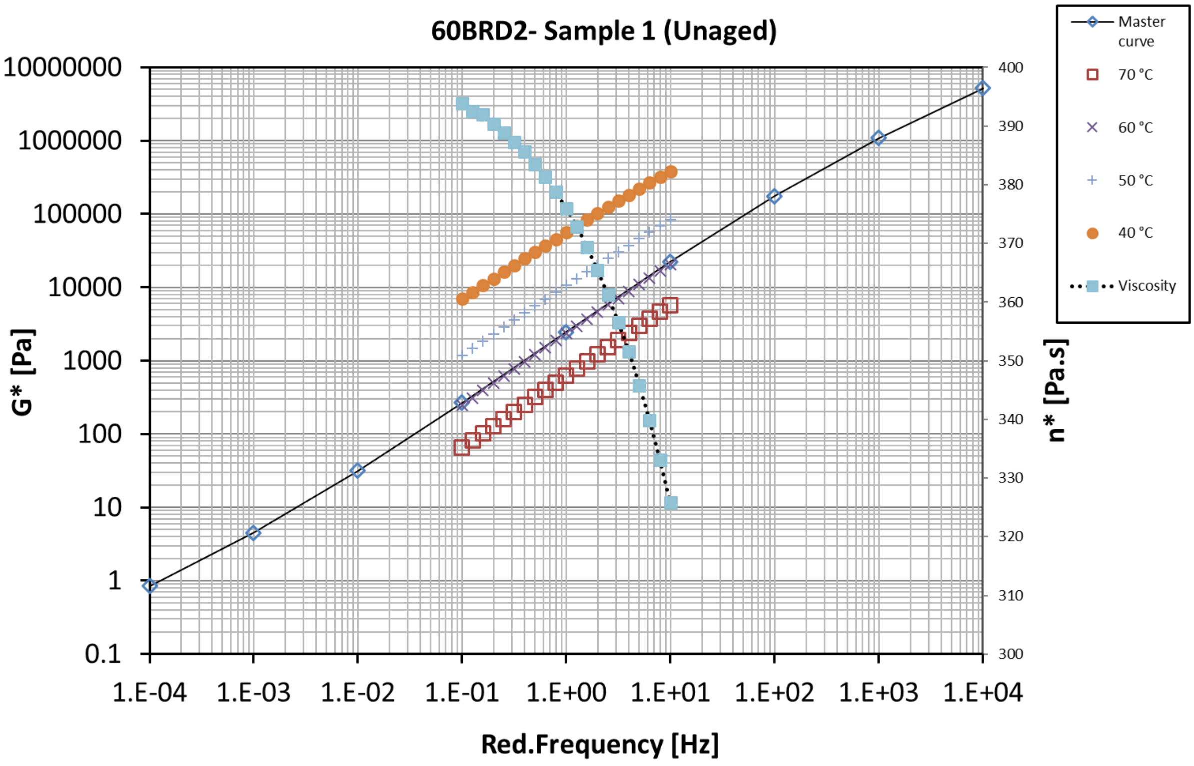

(I)

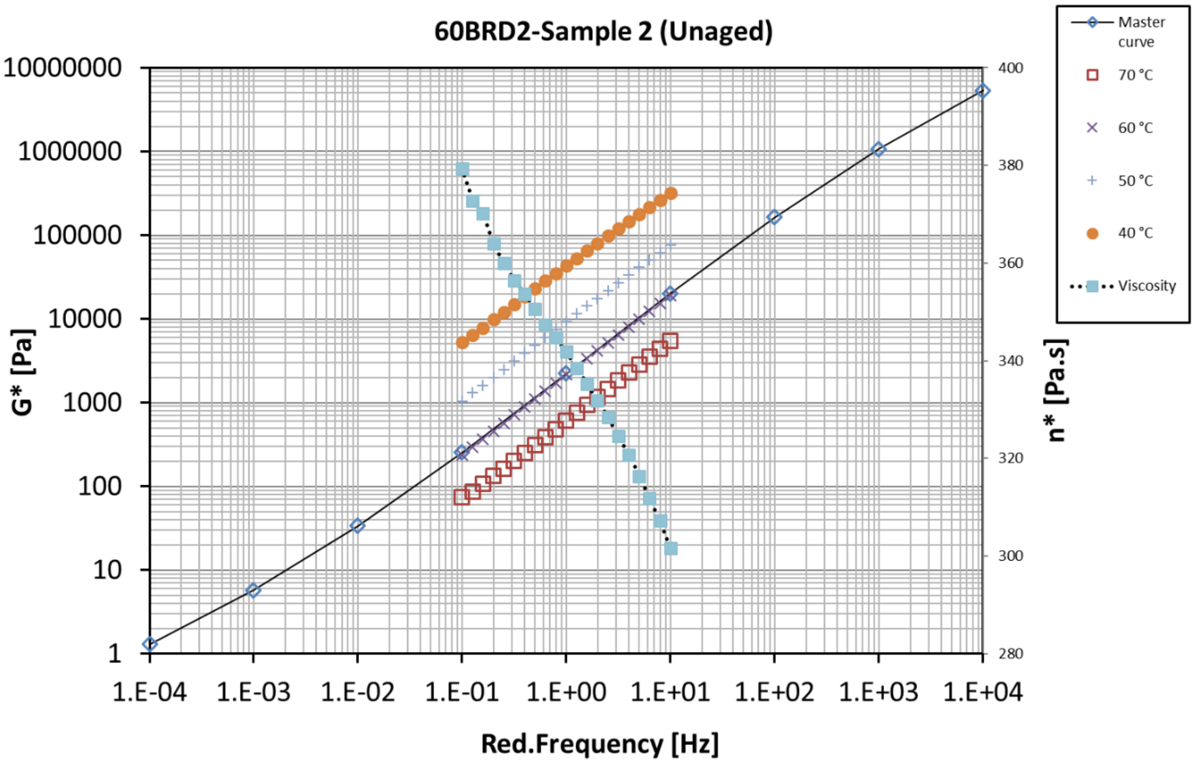

(II)

Figure B 9: Master curve of unaged C320 + 4% NS (60nm) at 60 °C.

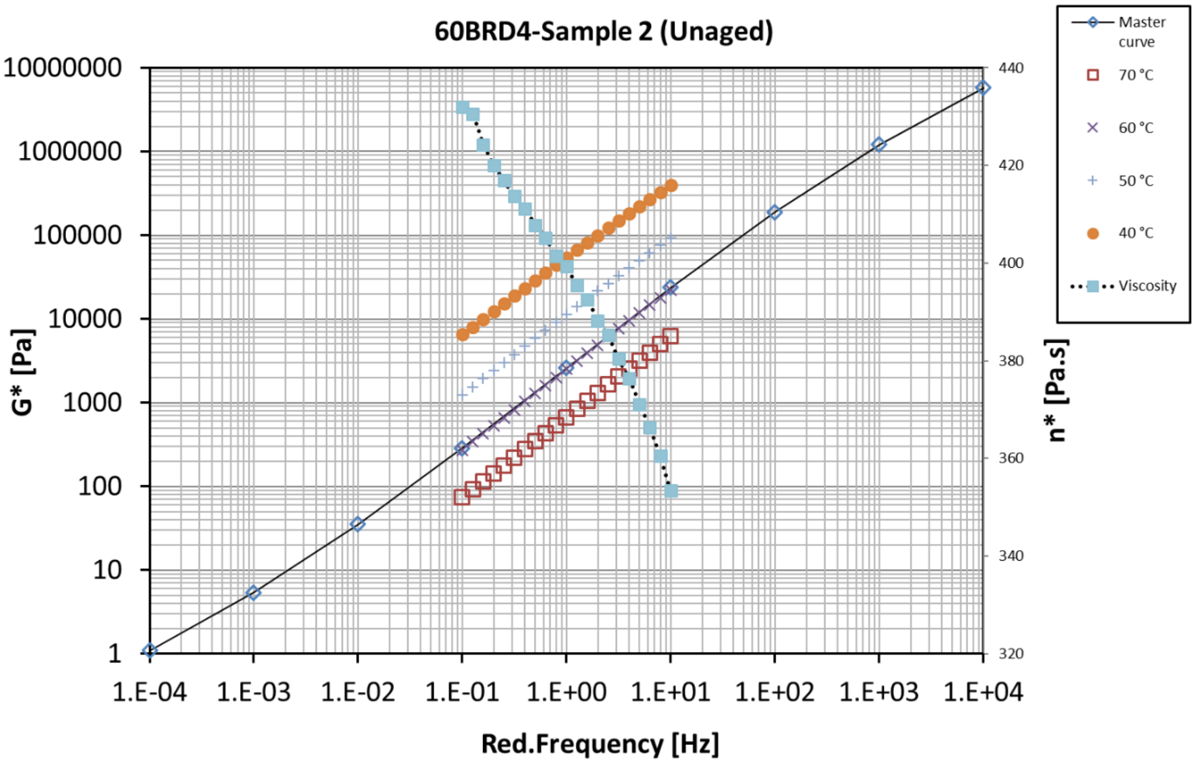

Figure B 10: Master curve of unaged C320 + 6% NS (60nm) at 60 °C: (I) sample 1, (II) sample 2

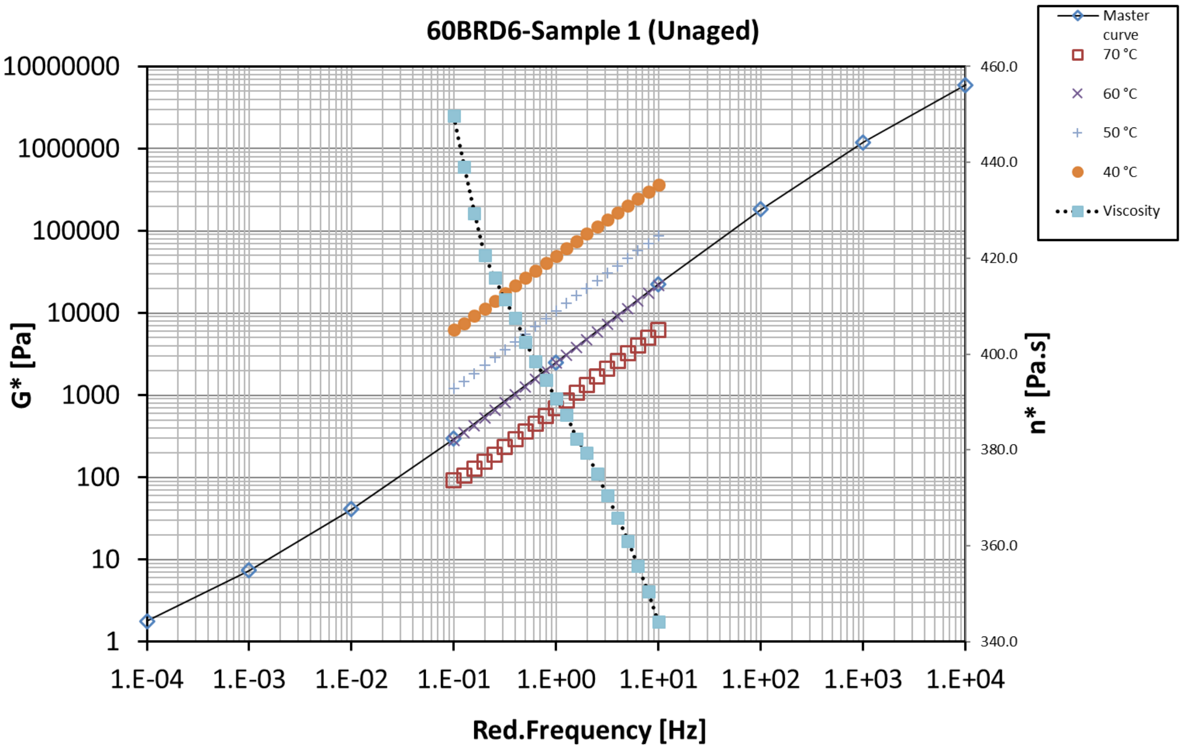

(I)

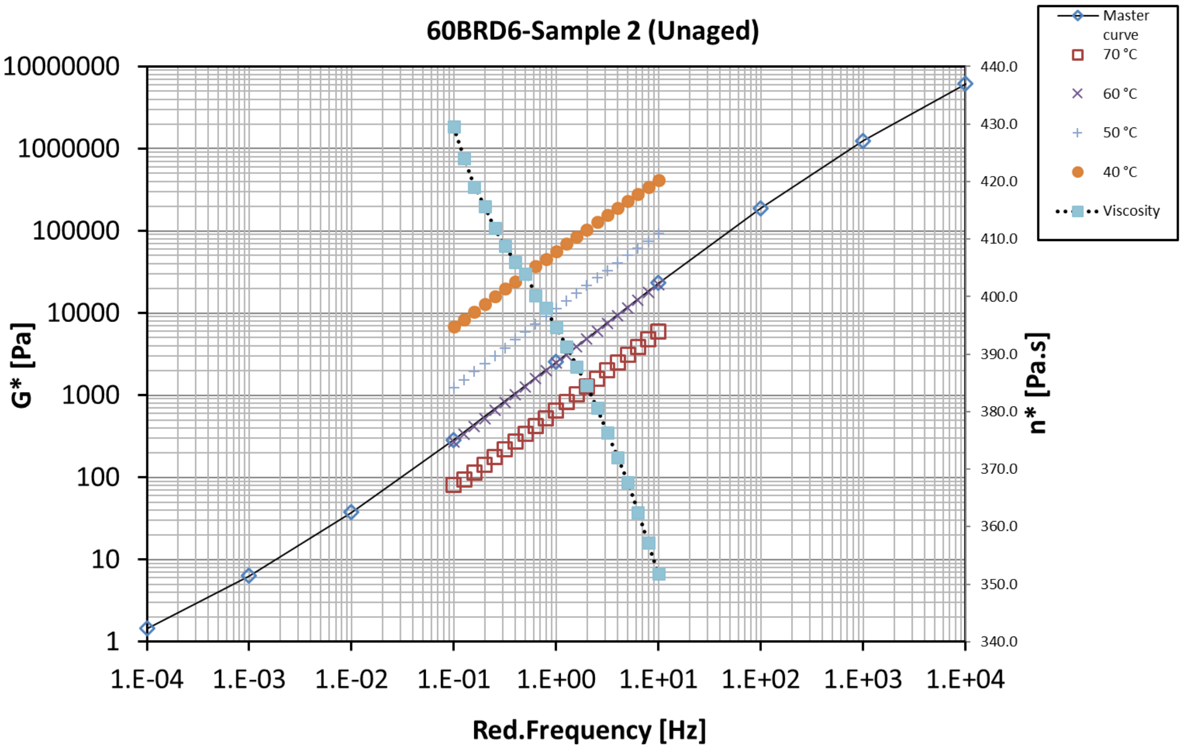

(II)

Figure B 11: Master curve of unaged C600 at 60 °C: (I) sample 1, (II) sample 2

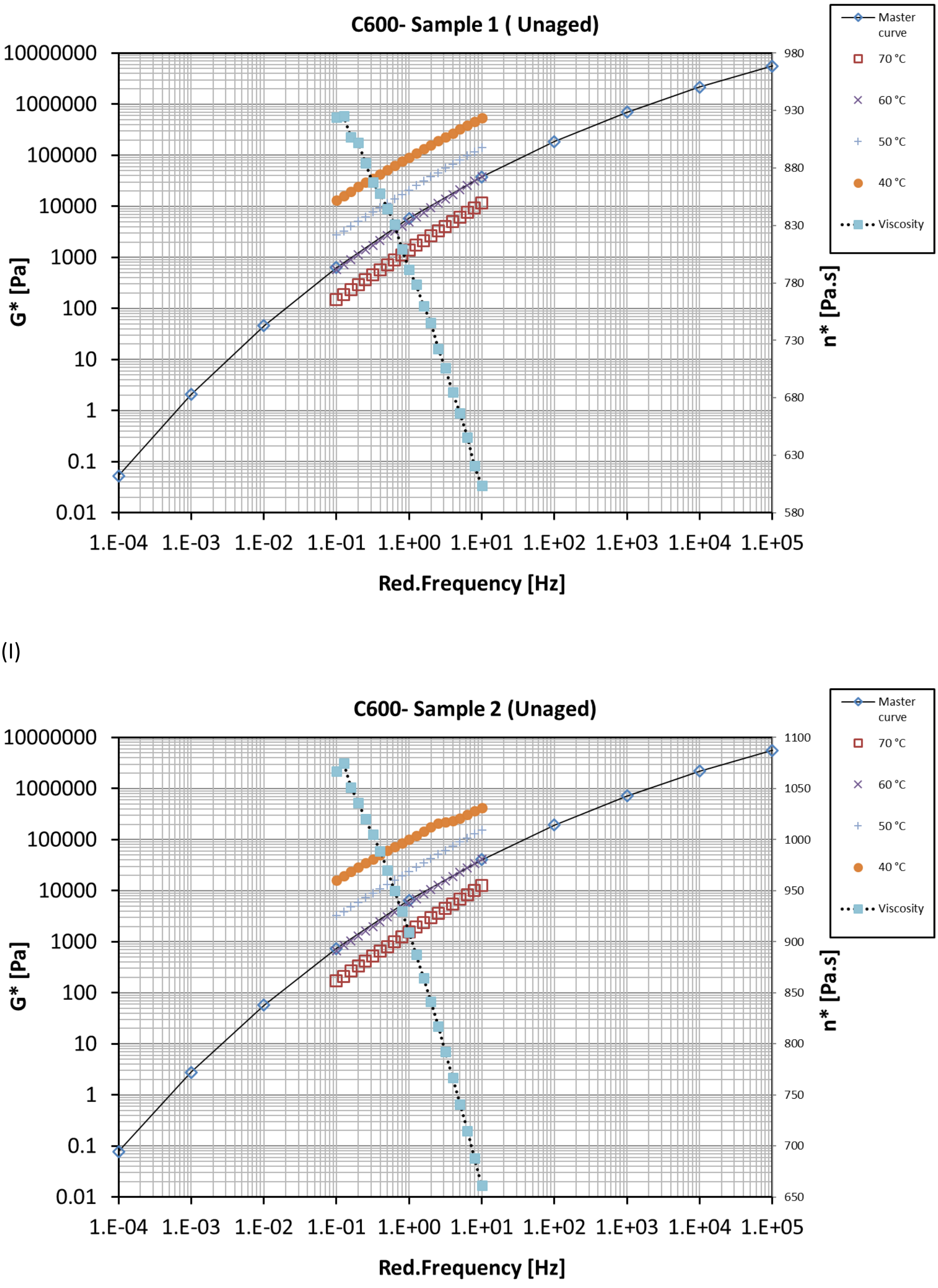

(I)

(II)

Figure B 12: Master curve of unaged A15E at 60 °C: (I) sample 1, (II) sample 2

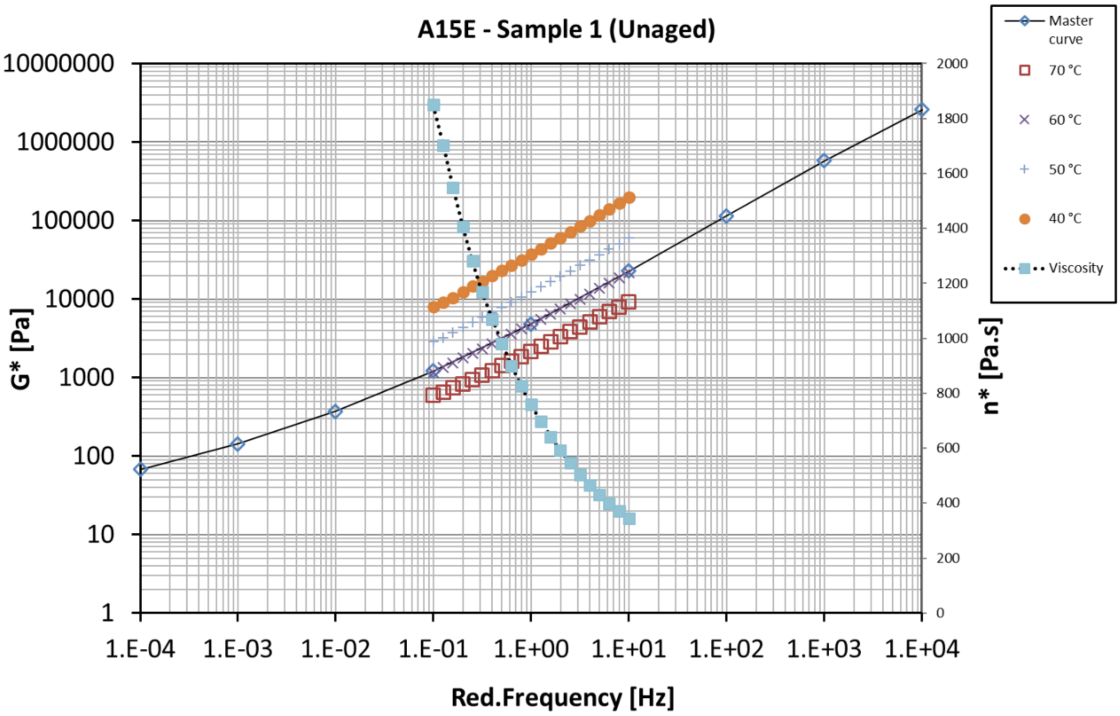

(I)

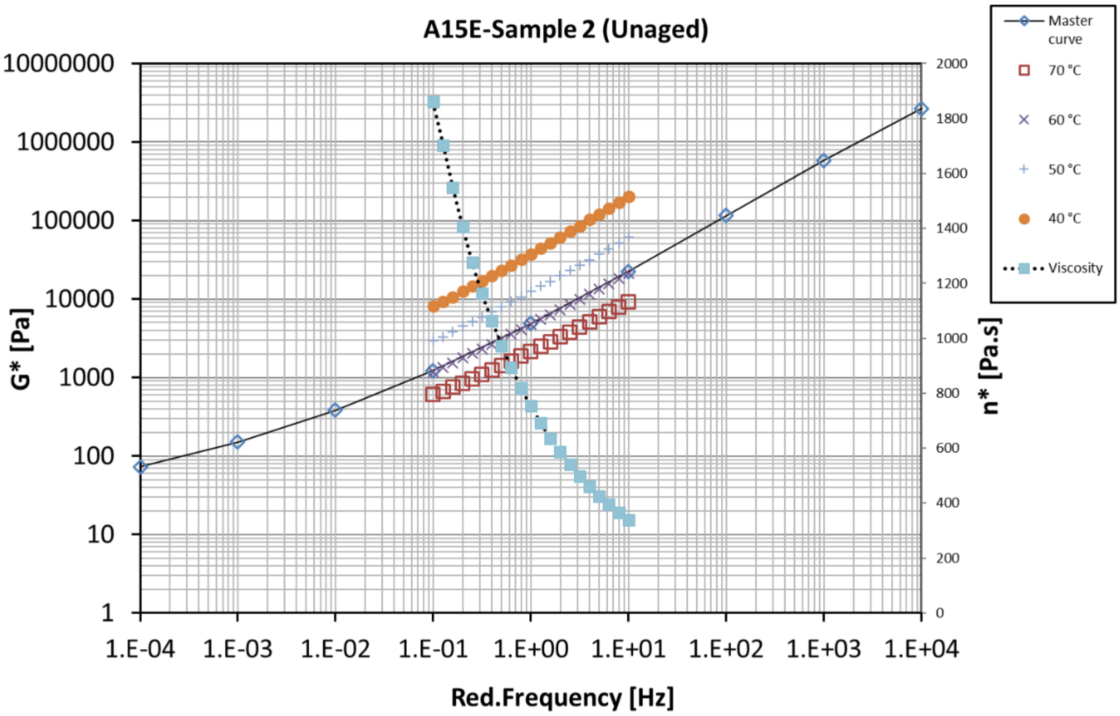

(II)

Figure B 13: Master curve of RTFO C320 at 60 °C: (I) sample 1, (II) sample 2

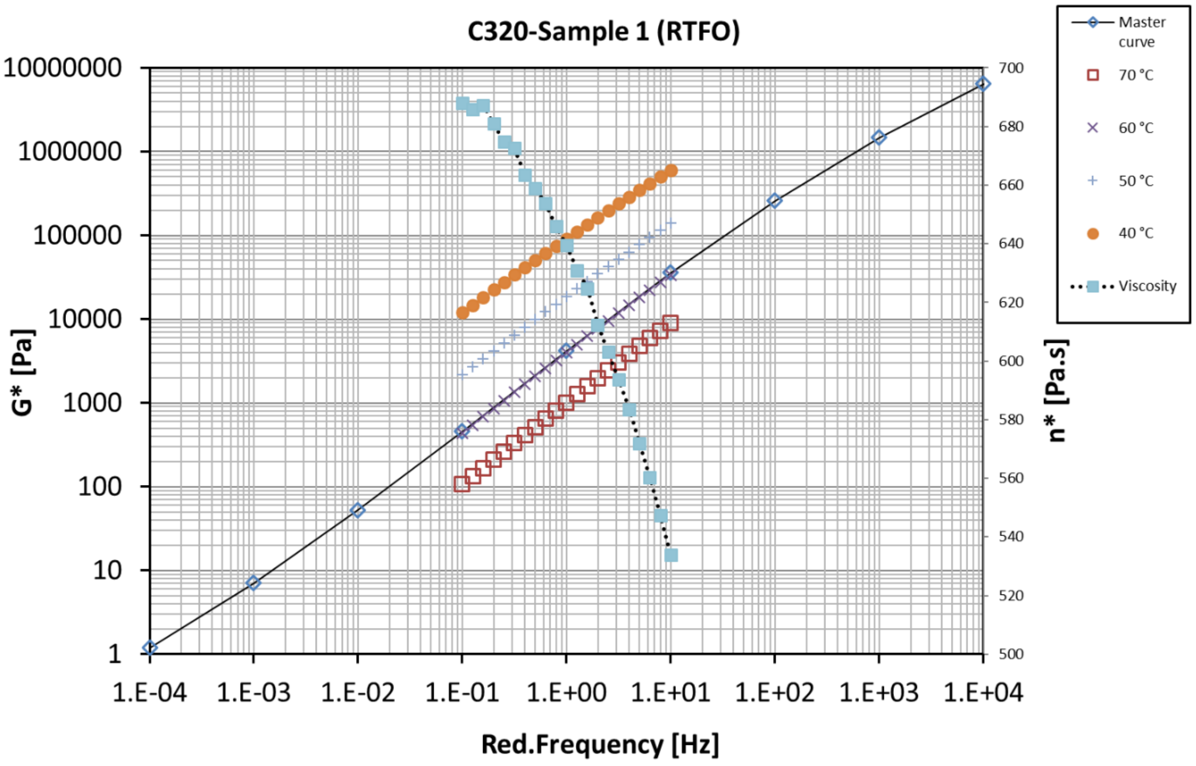

(I)

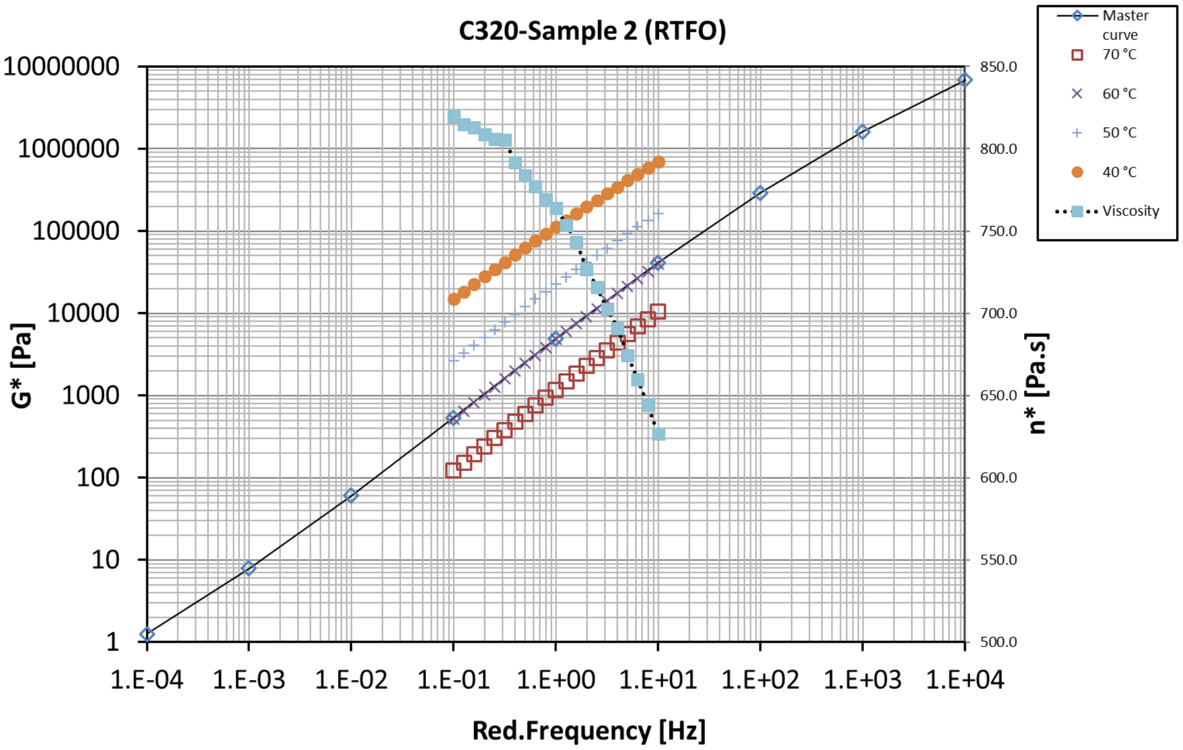

(II)

Figure B 14: Master curve of RTFO C320 + 2% NS (20nm + KH550 couplant) at 60 °C: (I) sample 1, (II) sample 2

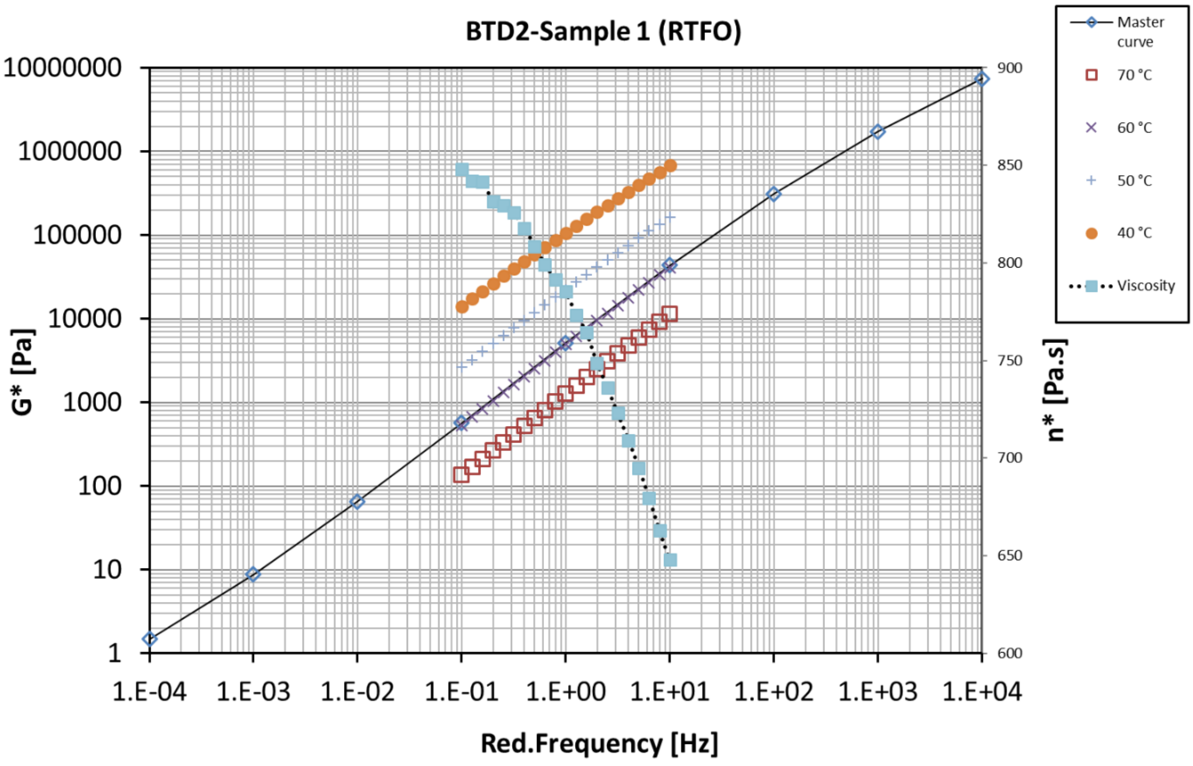

(I)

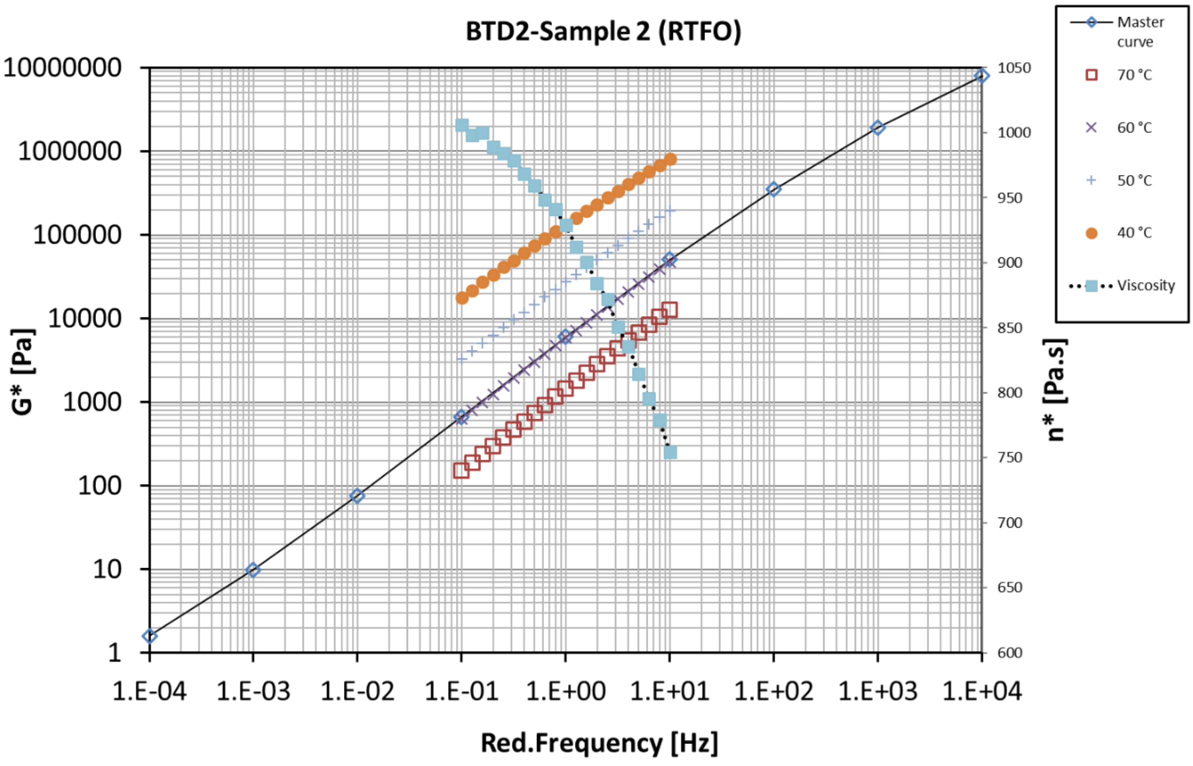

(II)

Figure B 15: Master curve of RTFO C320 + 4% NS (20nm + KH550 couplant) at 60 °C: (I) sample 1, (II) sample 2

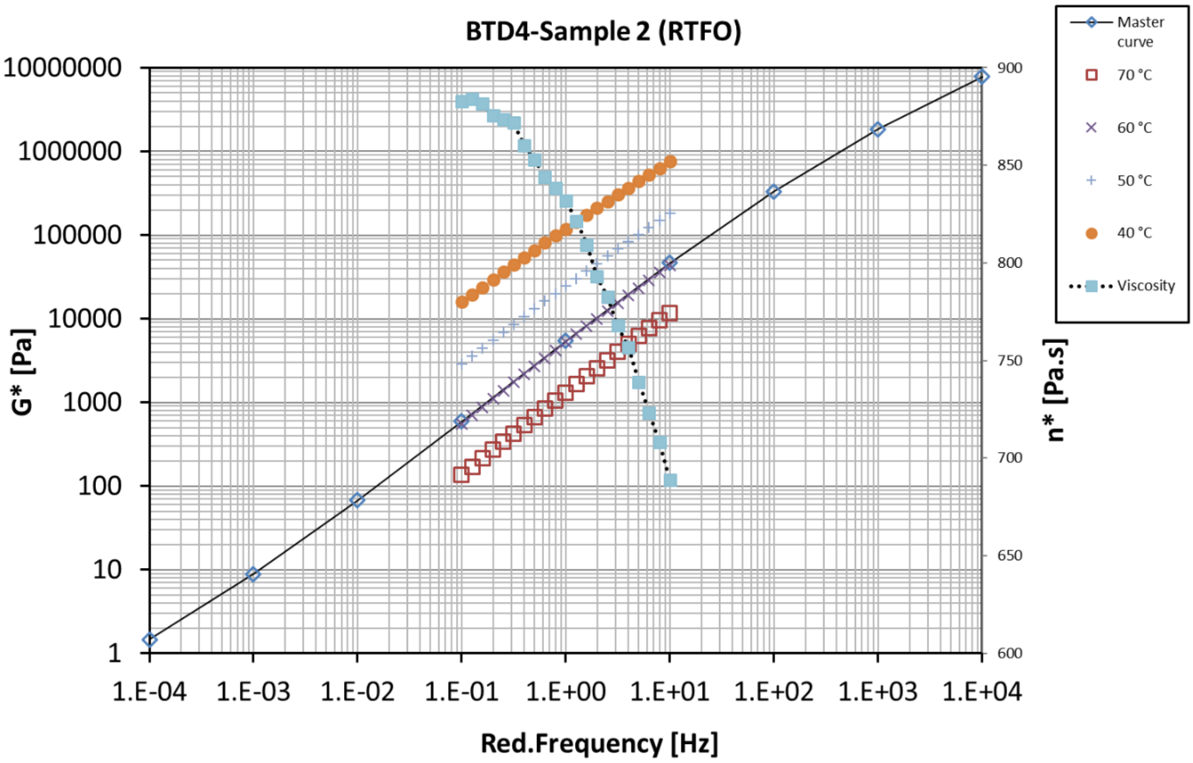

Figure B 16: Master curve of RTFO C320 + 6% NS (20nm + KH550 couplant) at 60°C: (I) sample 1, (II) sample 2

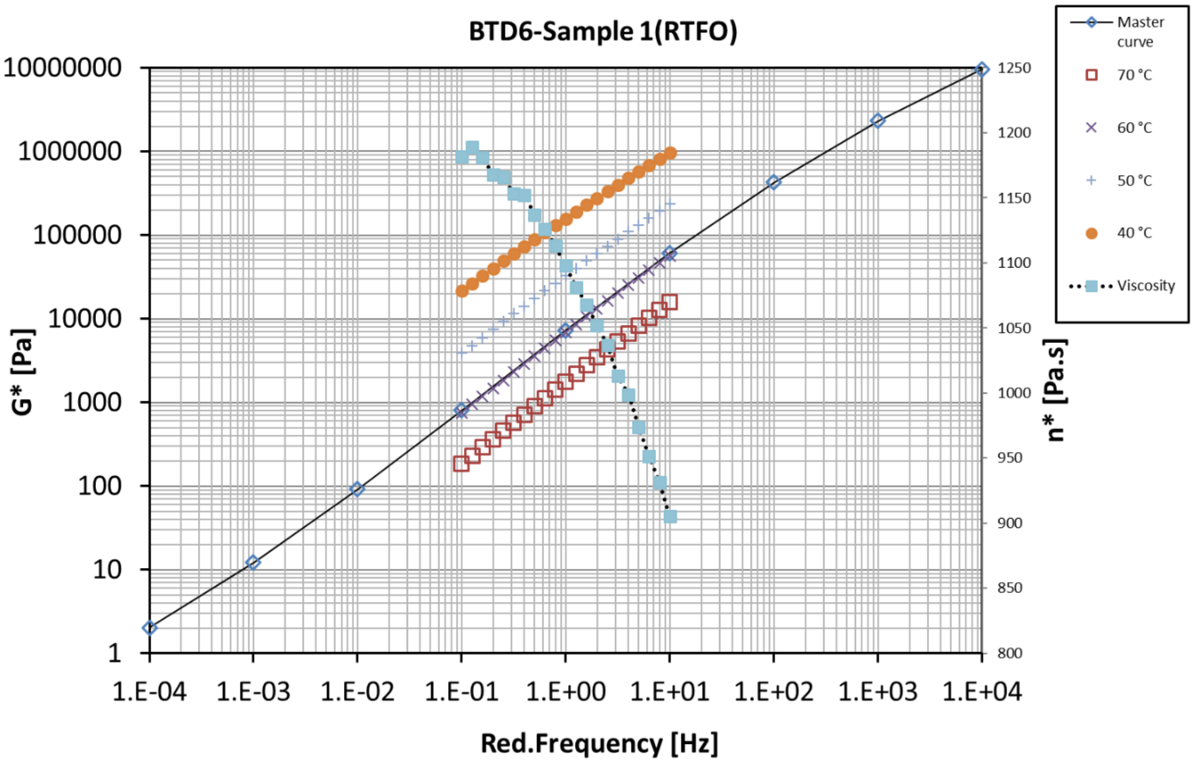

(I)

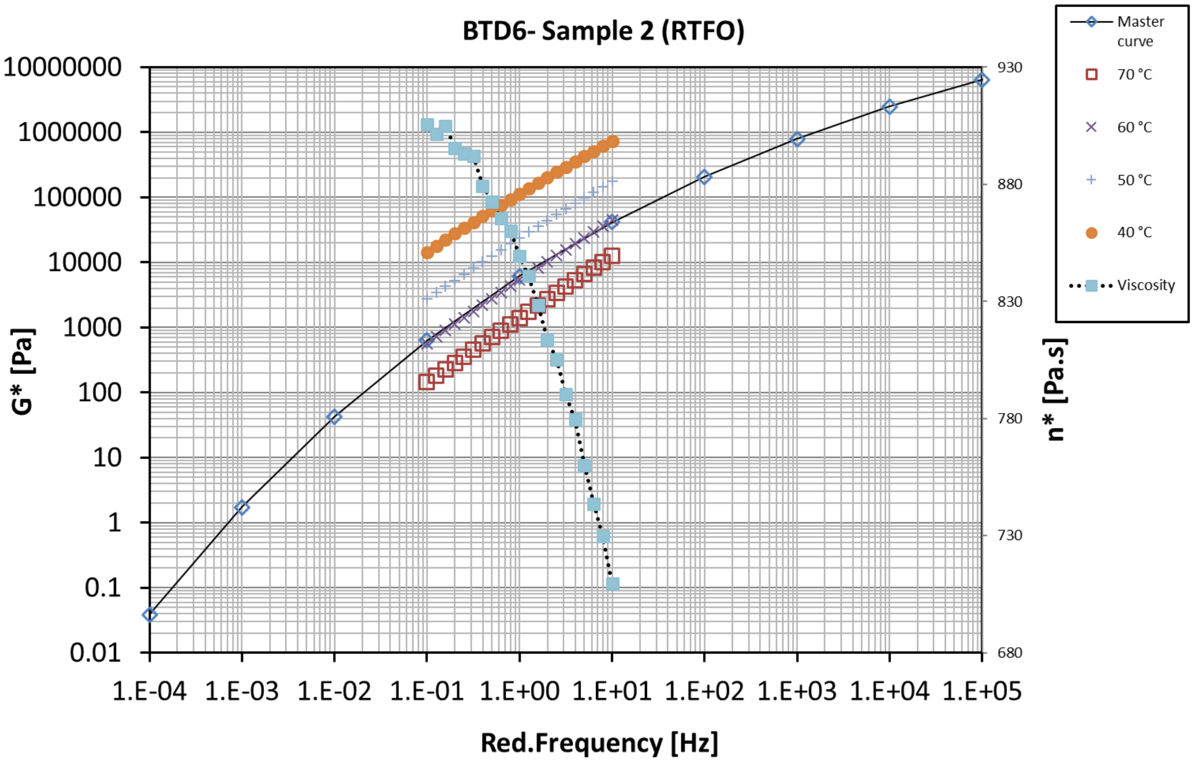

(II)

Figure B 17: Master curve of RTFO C320 + 2% NS (20nm) at 60 °C: (I) sample 1, (II) sample 2

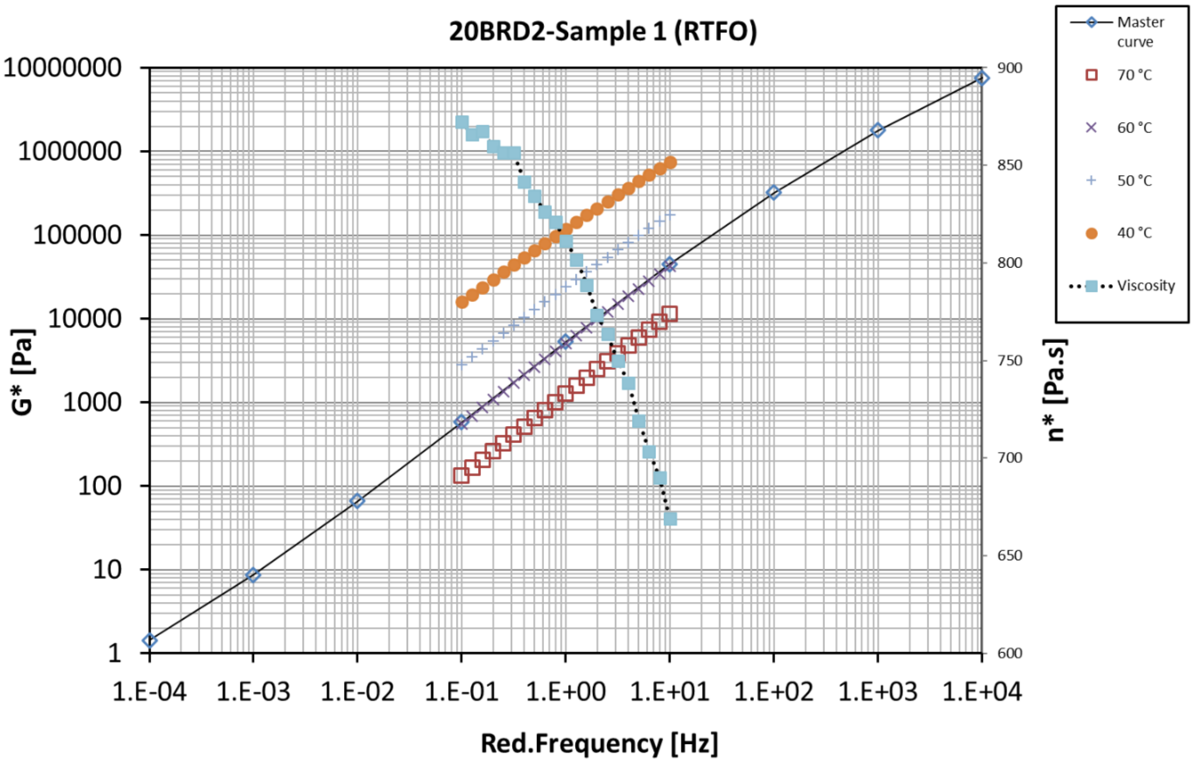

(II)

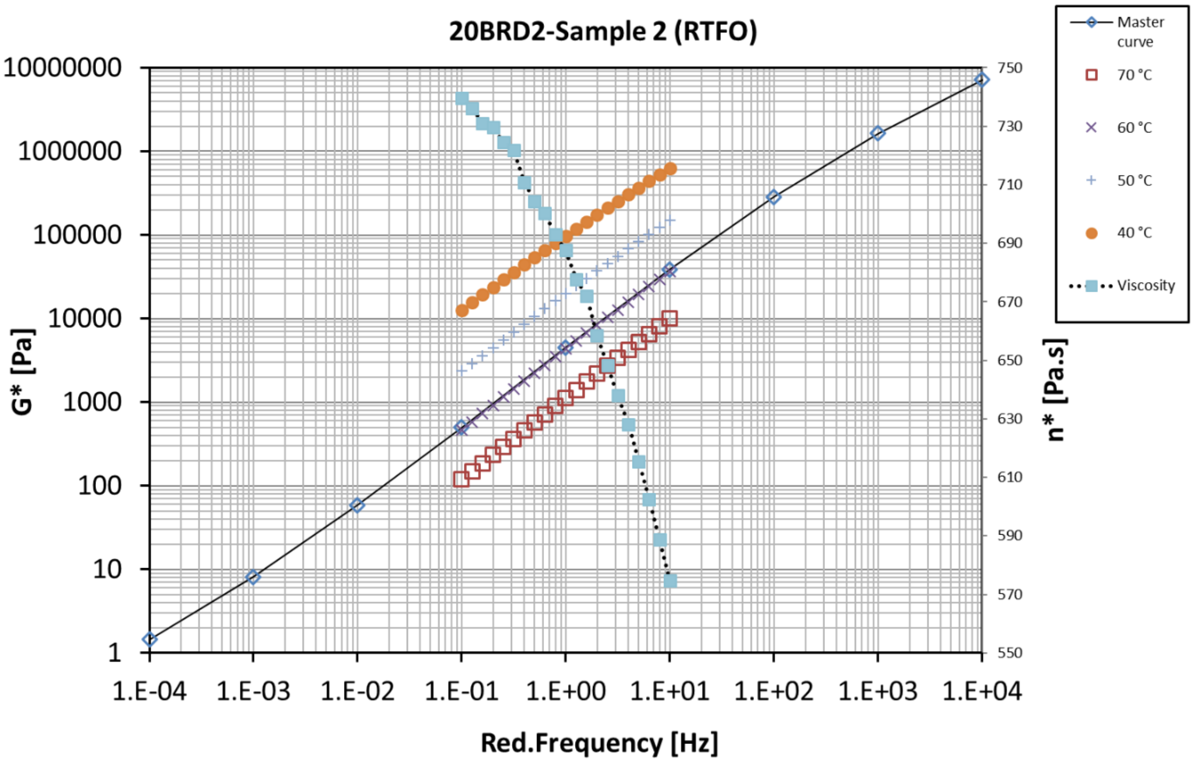

Figure B 18: Master curve of RTFO C320 + 4% NS (20nm) at 60 °C: (I) sample 1, (II) sample 2

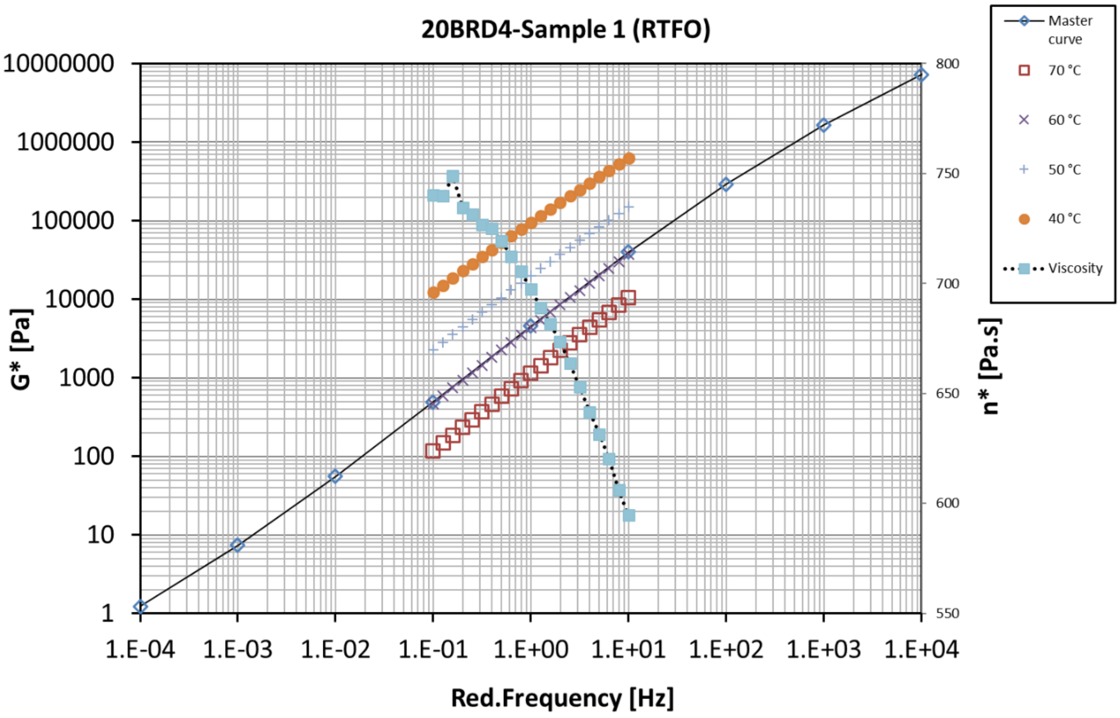

(I)

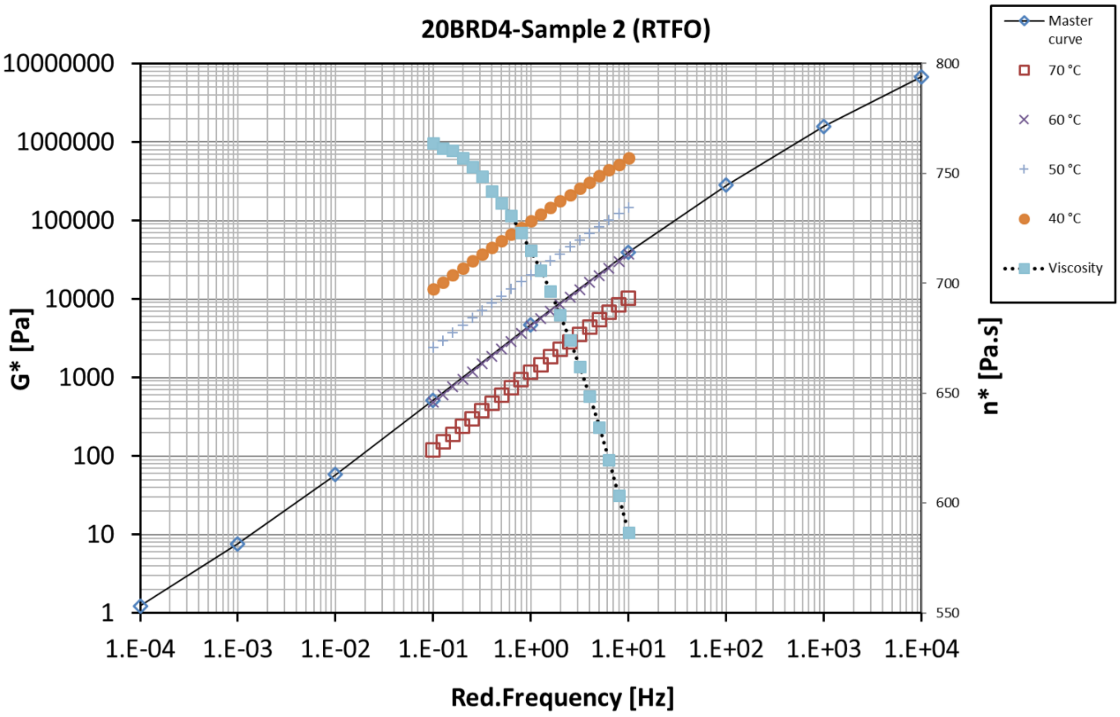

(II)

Figure B 19: Master curve of RTFO C320 + 6% NS (20nm) at 60 °C: (I) sample 1, (II) sample 2

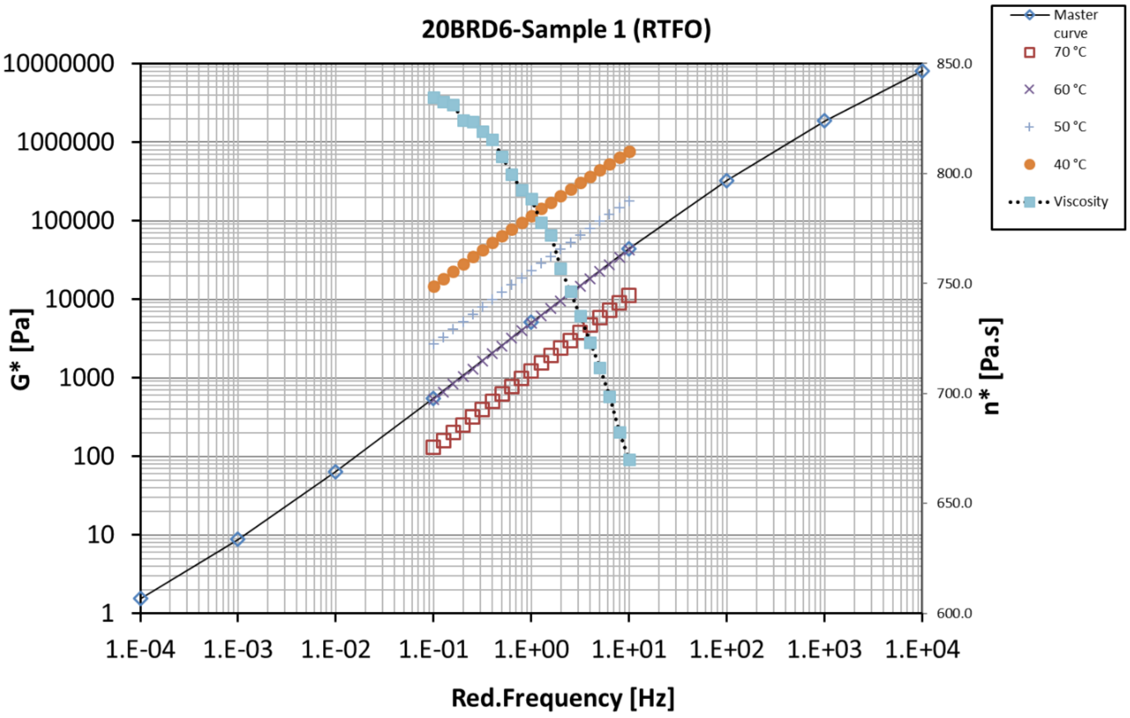

(I)

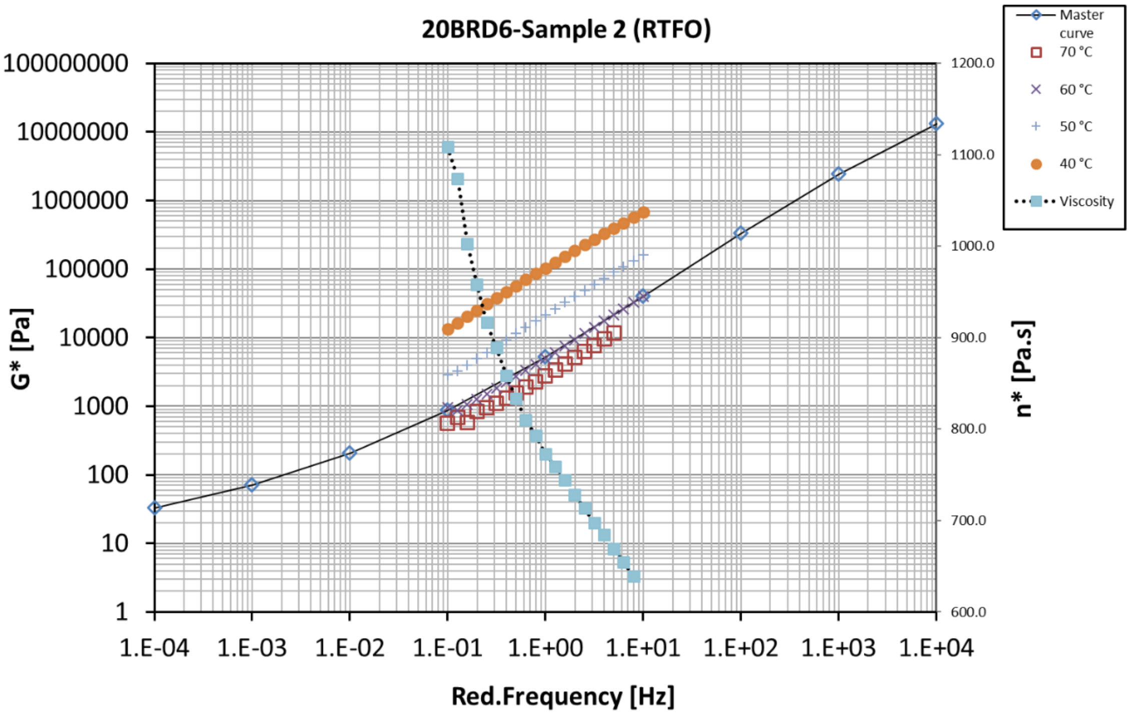

(II)

Figure B 20: Master curve of RTFO C320 + 2% NS (60nm) at 60 °C: (I) sample 1, (II) sample 2

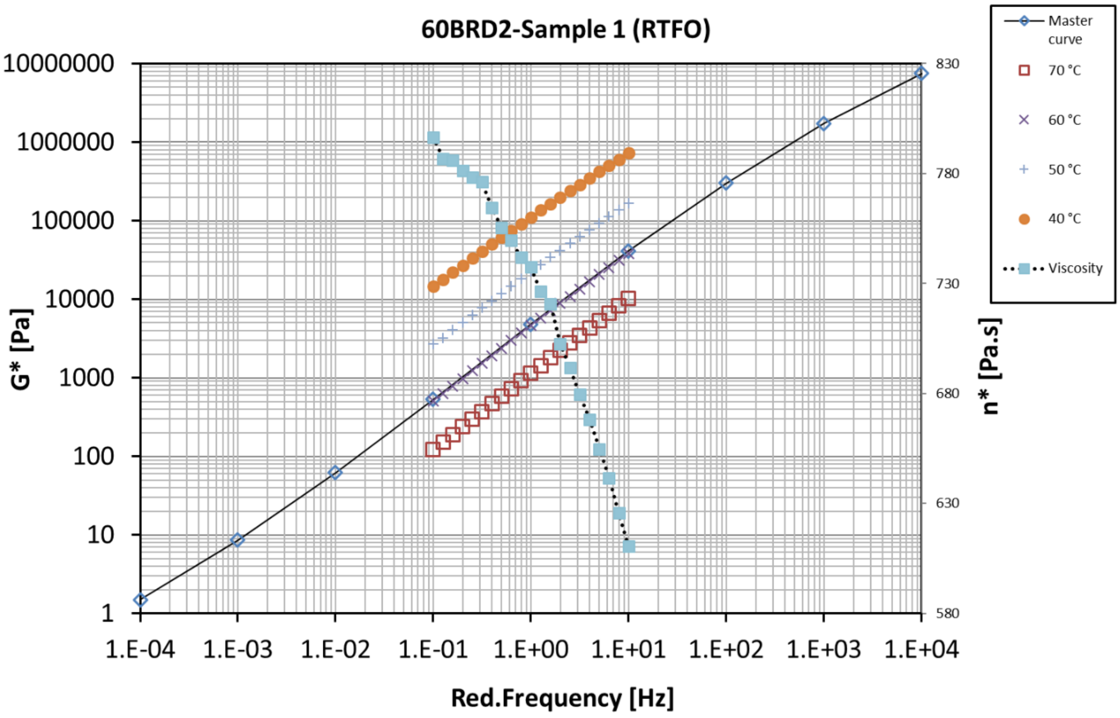

(I)

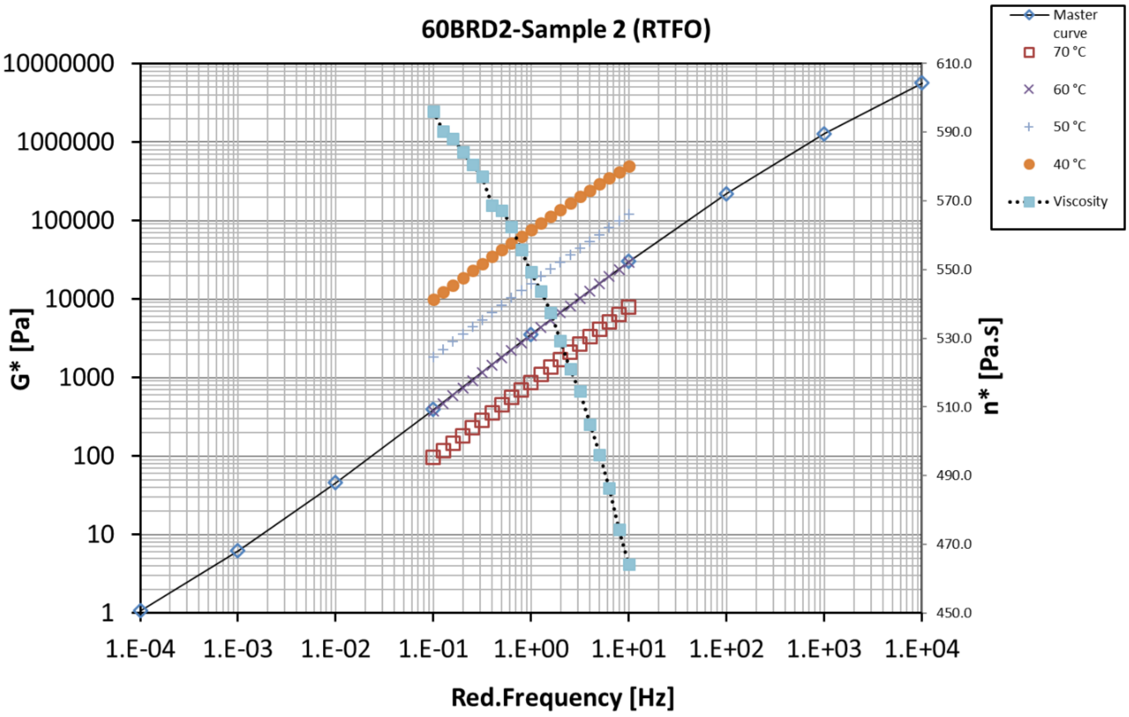

(II)

Figure B 21: Master curve of RTFO C320 + 4% NS (60nm) at 60 °C: (I) sample 1, (II) sample 2

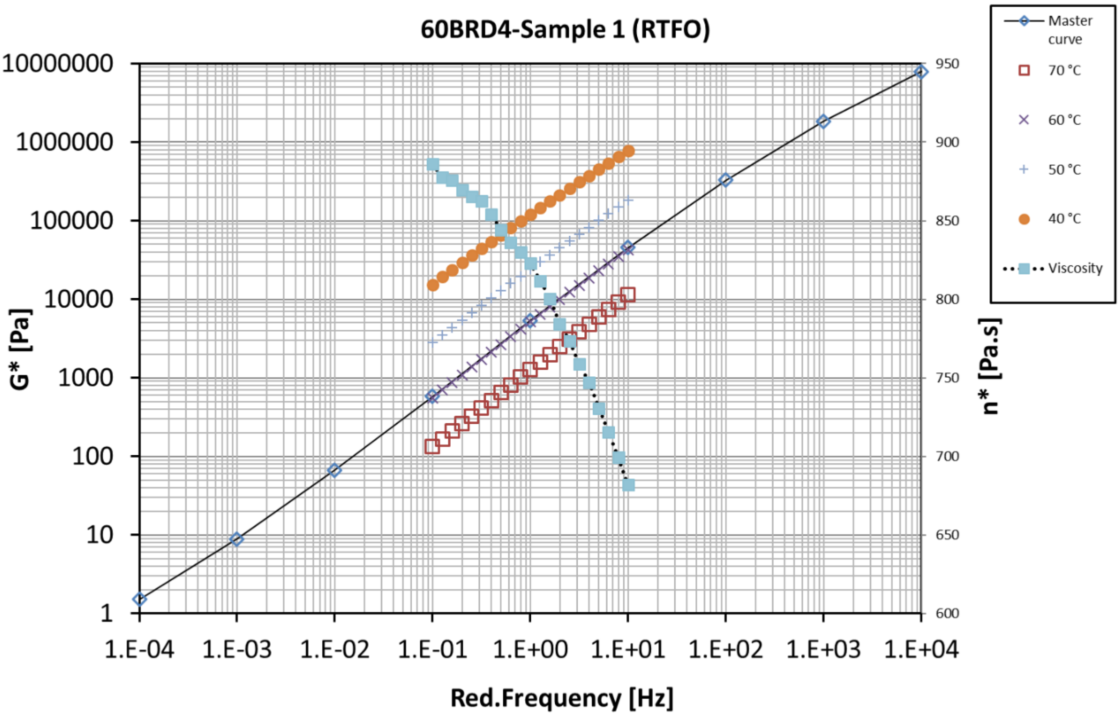

(I)

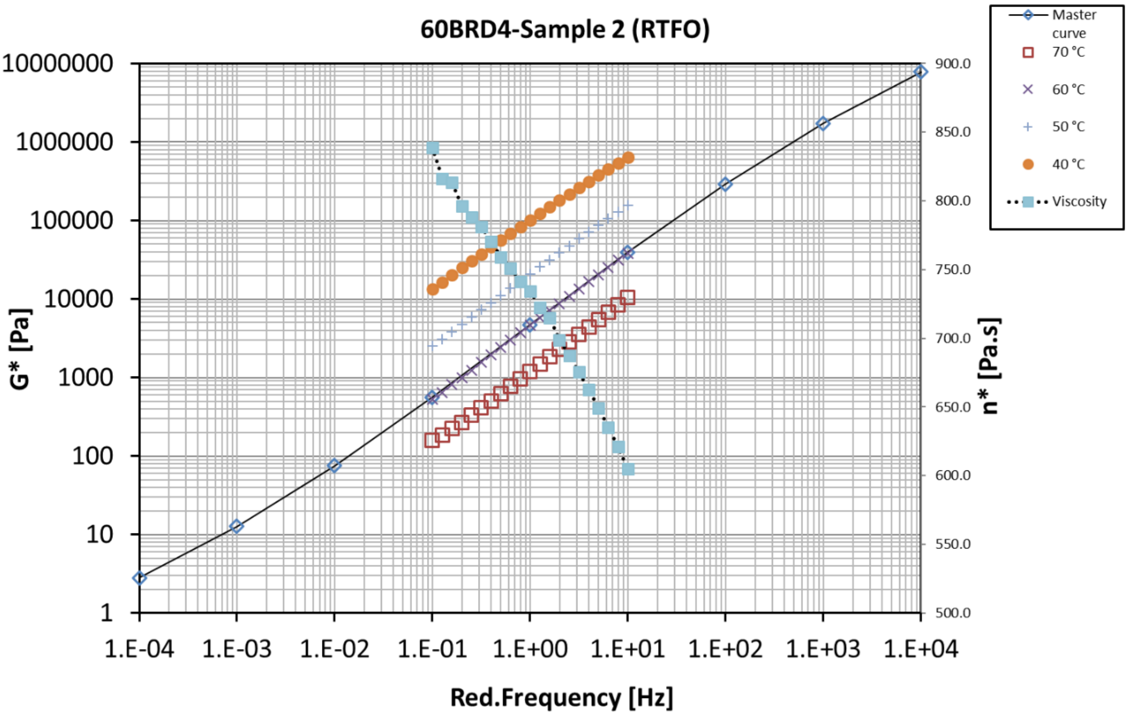

(II)

Figure B 22: Master curve of RTFO C320 + 6% NS (60nm) at 60 °C: (I) sample 1, (II) sample 2

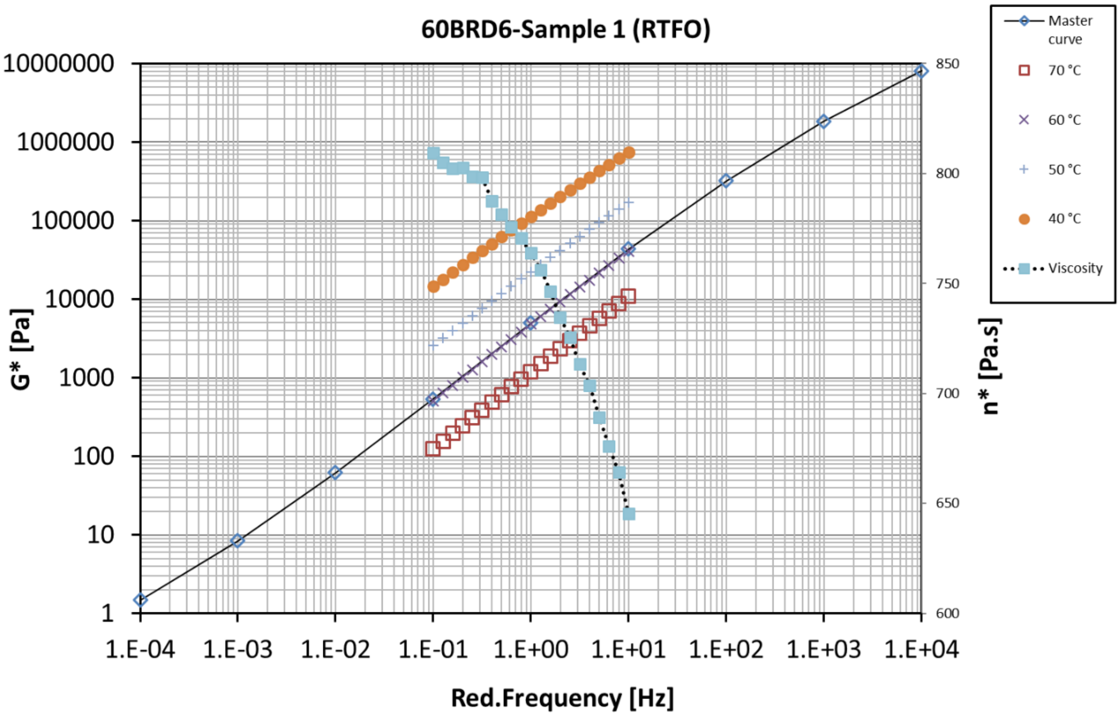

(I)

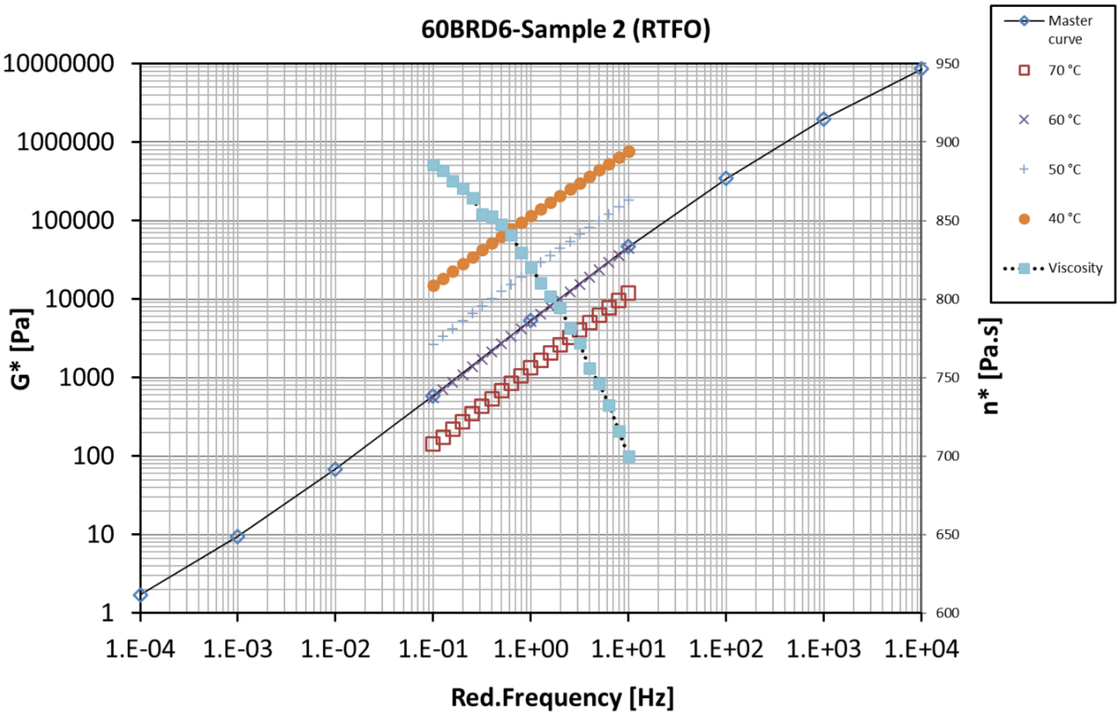

(II)

Figure B 23: Master curve of RTFO A15E at 60 °C: (I) sample 1, (II) sample 2

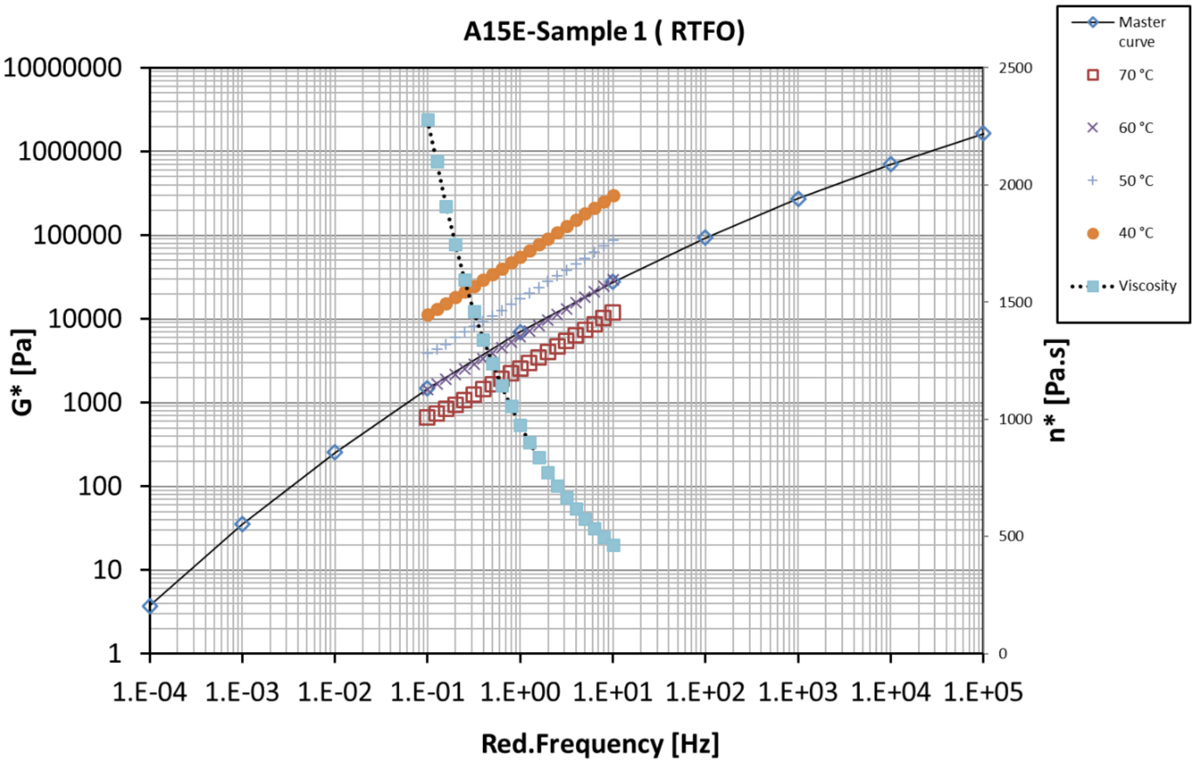

(I)

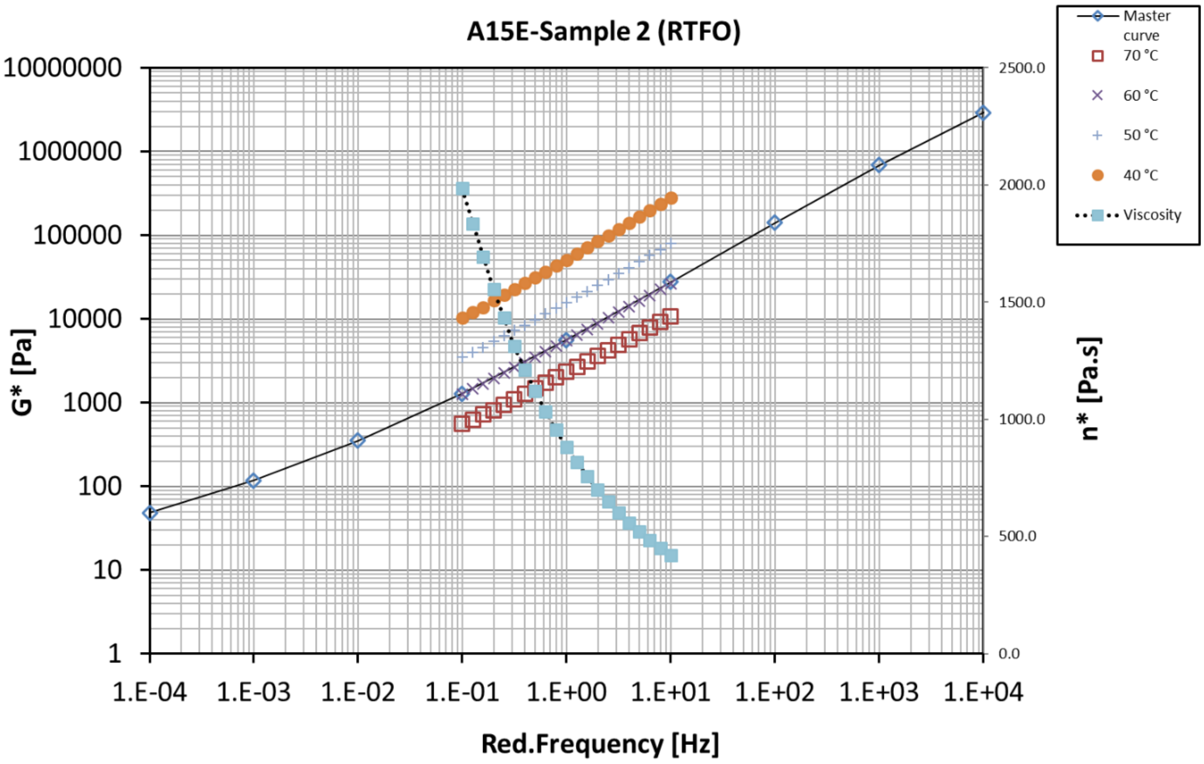

(II)

Figure B 24: Master curve of RTFO C600 at 60 °C: (I) sample 1, (II) sample 2

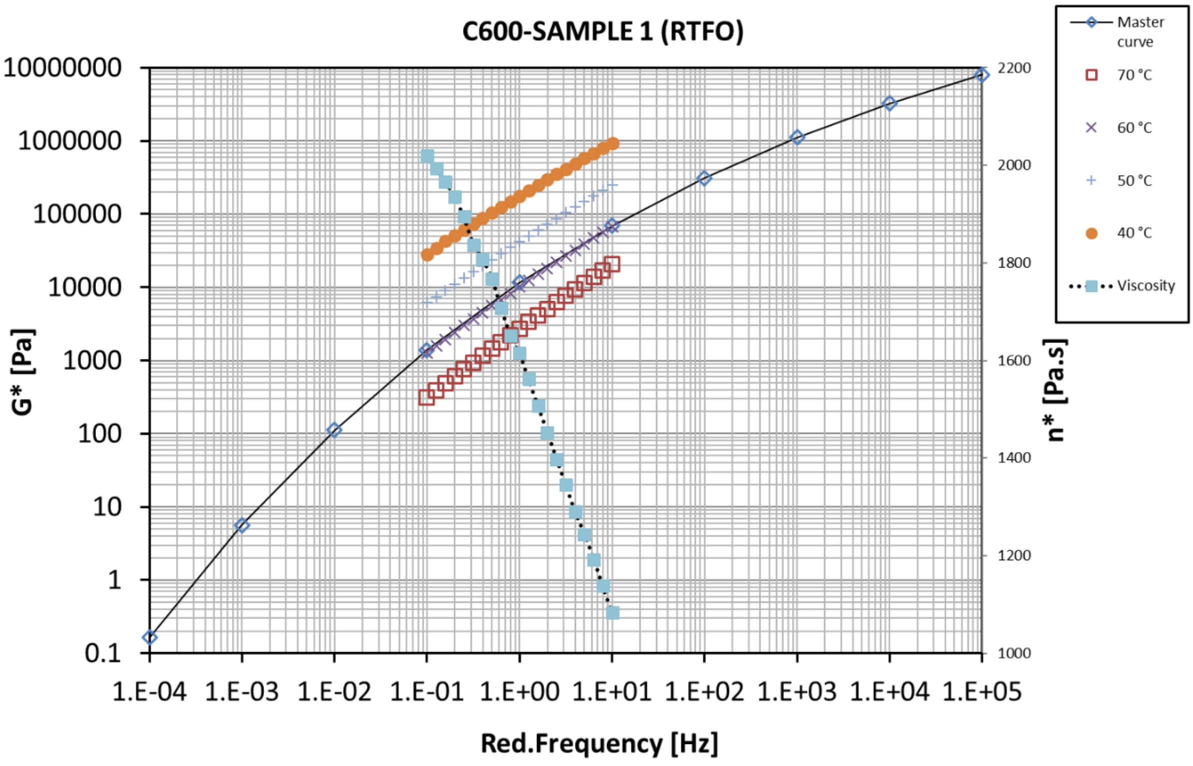

(I)

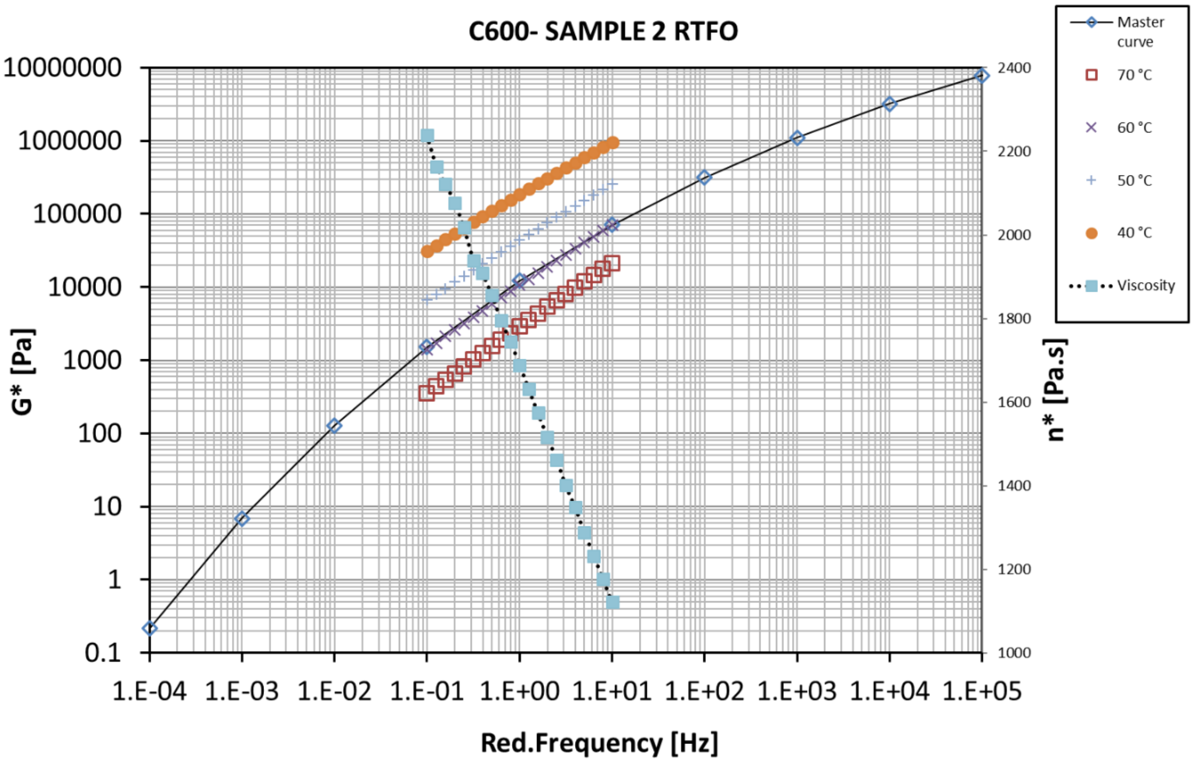

(II)

Figure B 25: Master curve of unaged C320 at 60 °C

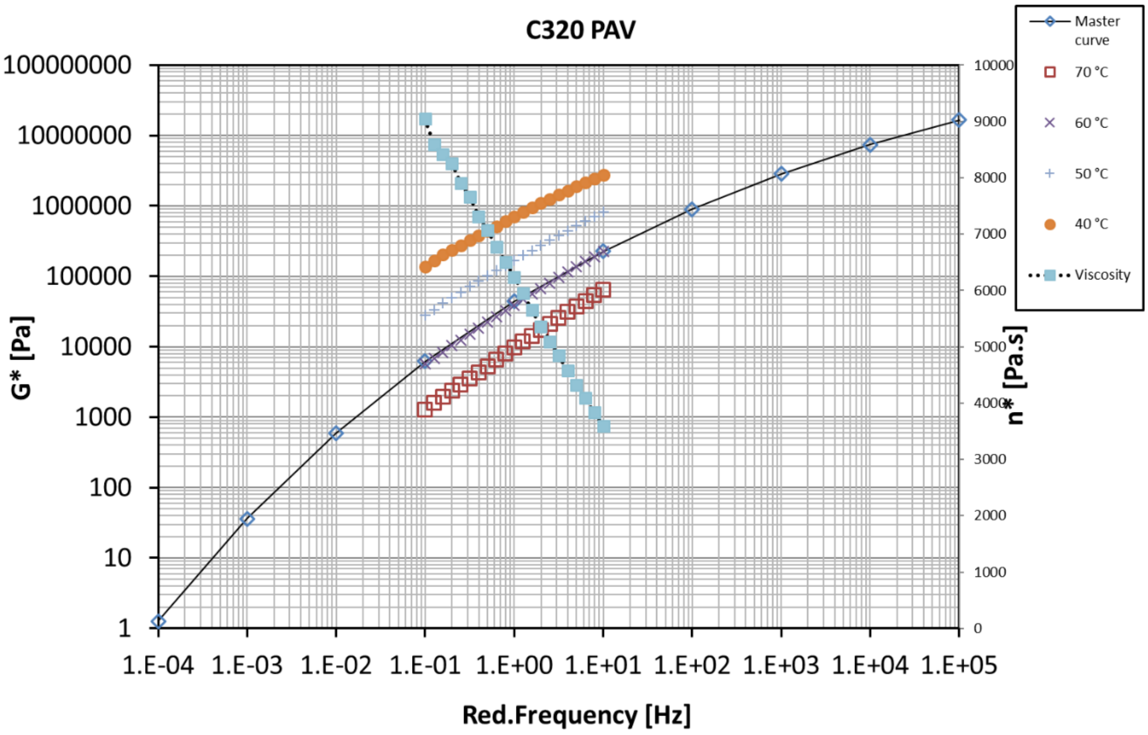

Figure B 26: Master curve of unaged C320 + 2% NS (20nm + KH550 couplant) at 60 °C

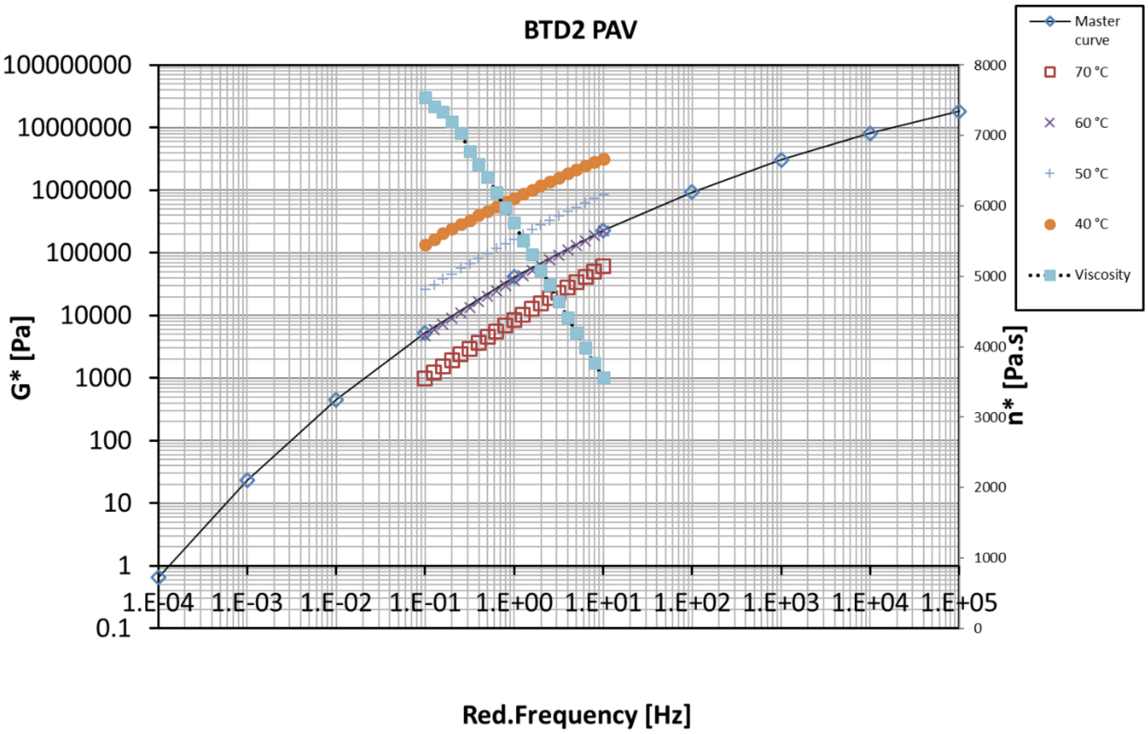

Figure B 27: Master curve of unaged C320 + 4% NS (20nm + KH550 couplant) at 60 °C: (I) sample 1, (II) sample 2

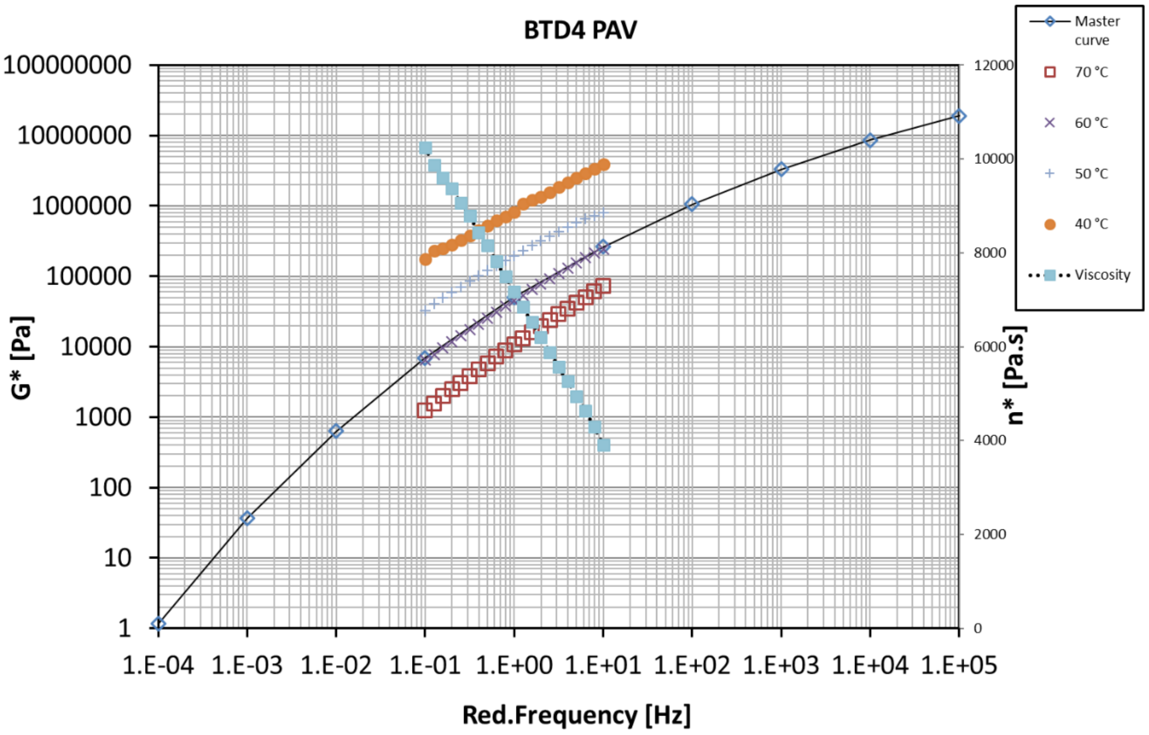

(I)

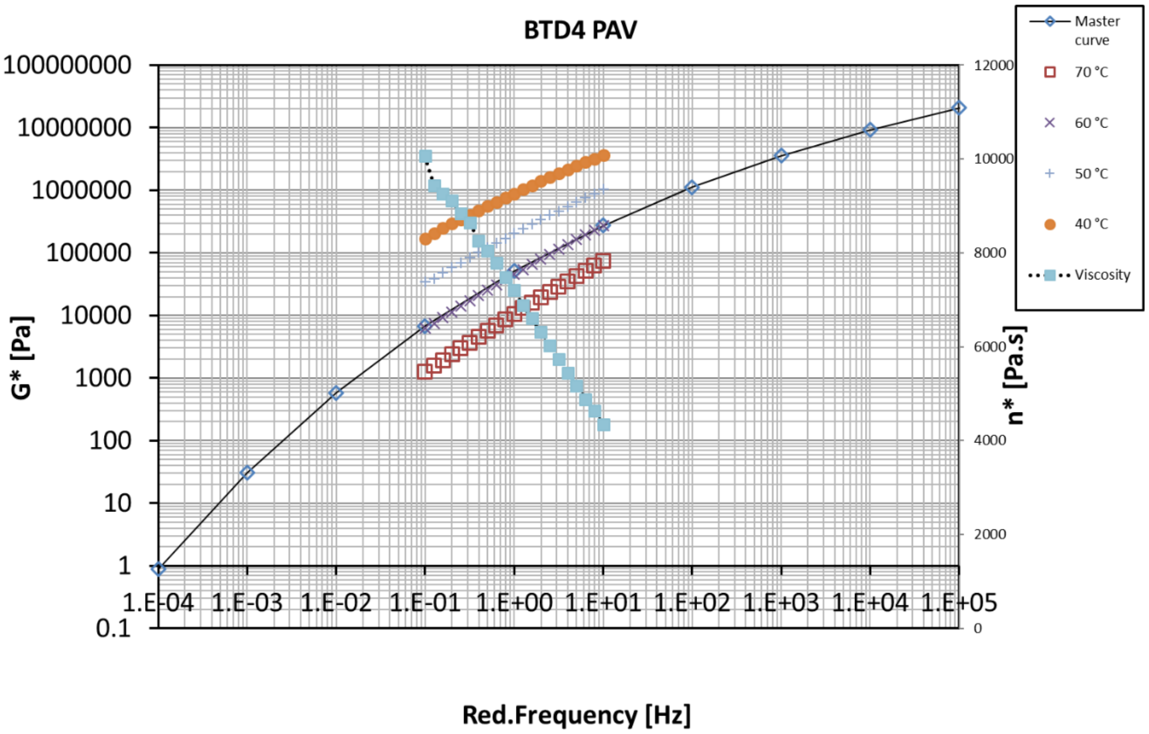

(II)

Figure B 28: Master curve of unaged C320 + 6% NS (20nm + KH550 couplant) at 60 °C: (I) sample 1, (II) sample 2

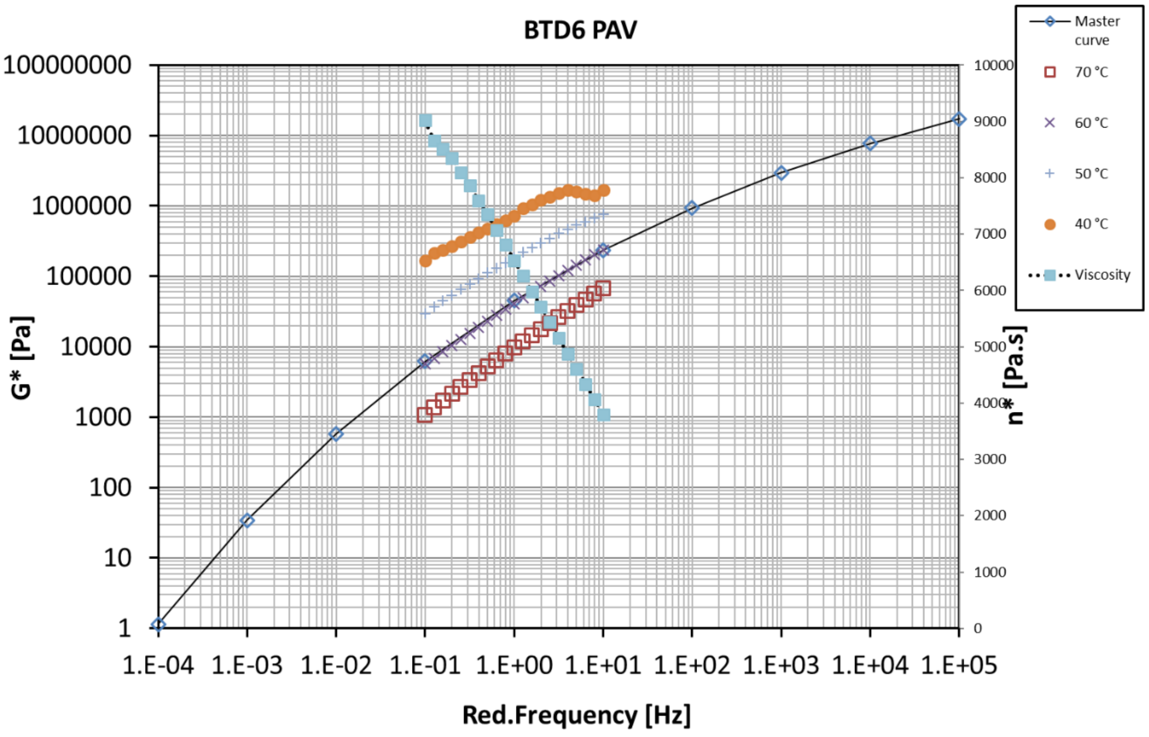

(I)

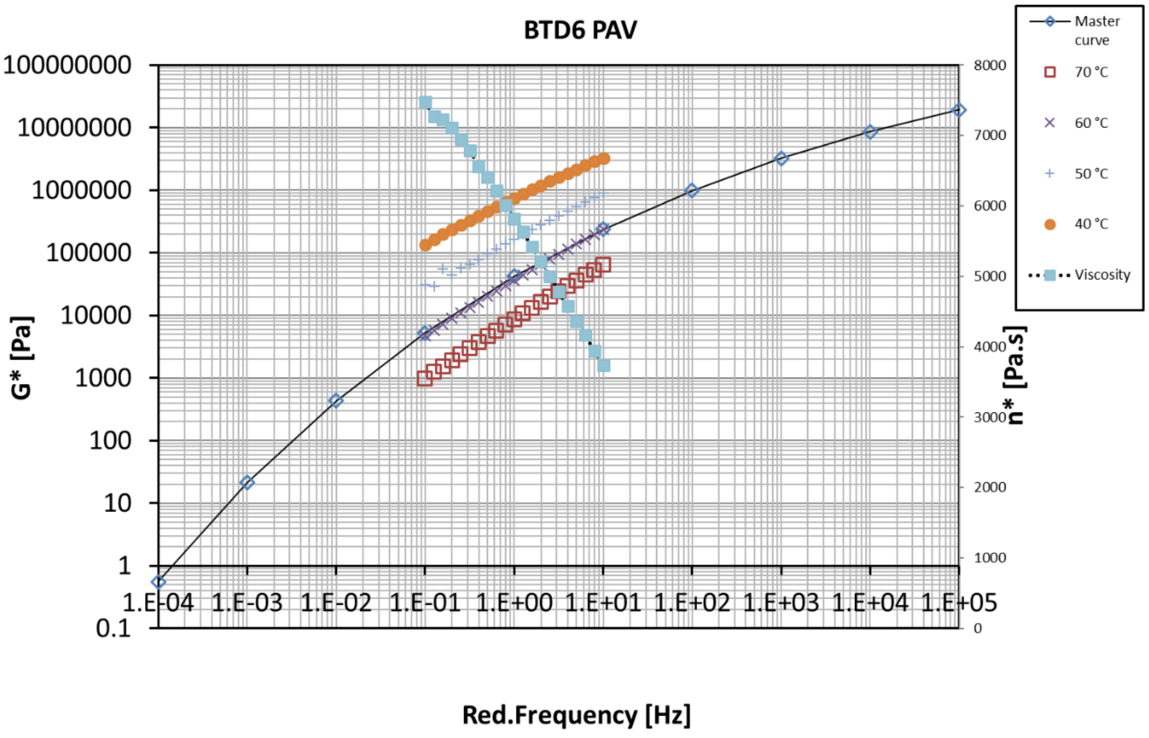

(II)

Figure B 29: Master curve of unaged C320 + 2% NS (20nm) at 60 °C: (I) sample 1, (II) sample 2

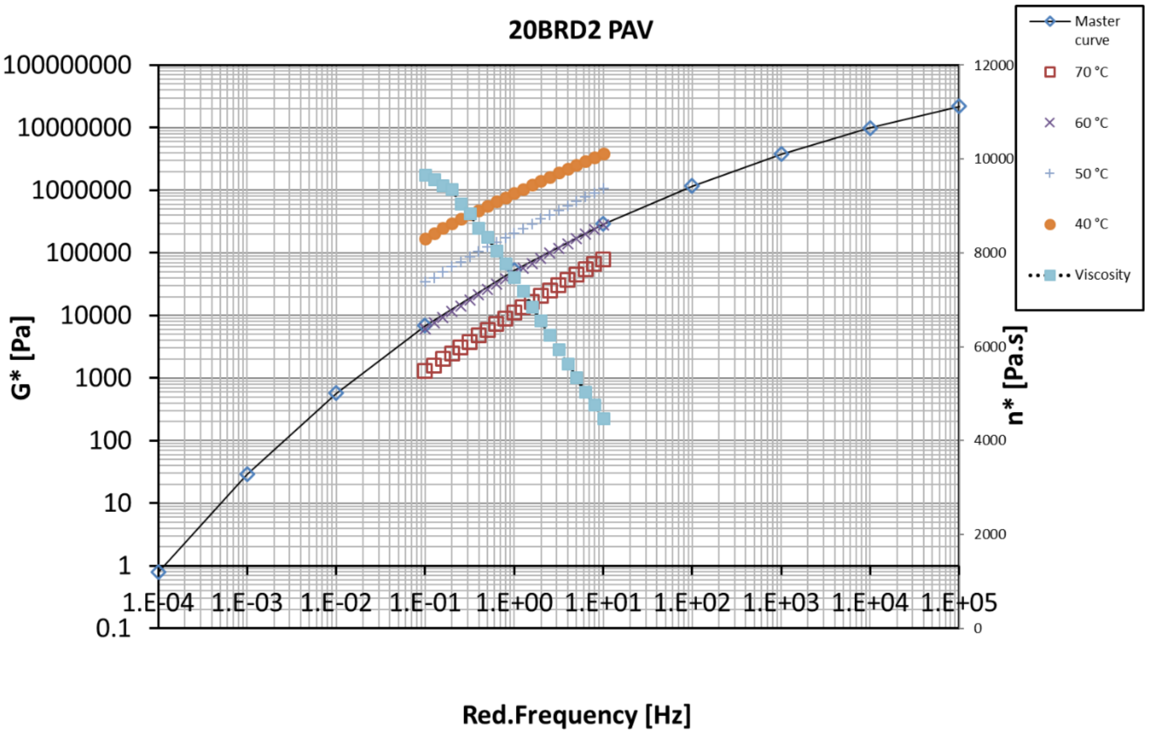

(I)

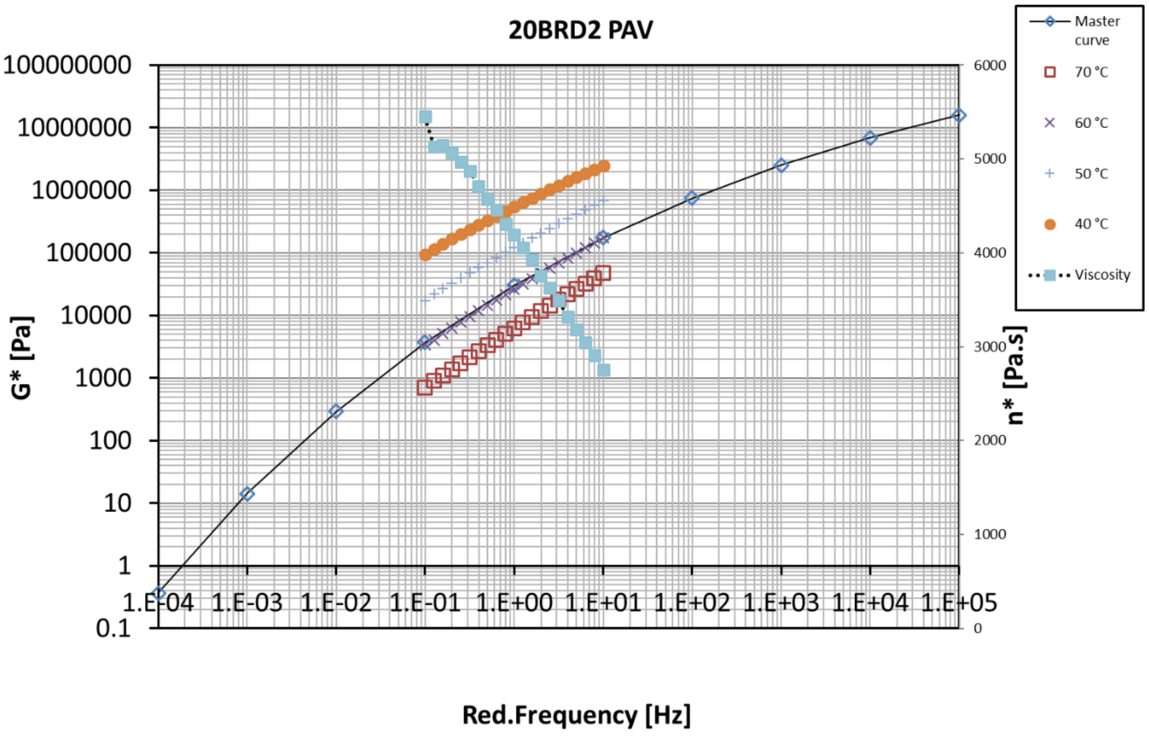

(II)

Figure B 30: Master curve of unaged C320 + 4% NS (20nm) at 60 °C: (I) sample 1, (II) sample 2

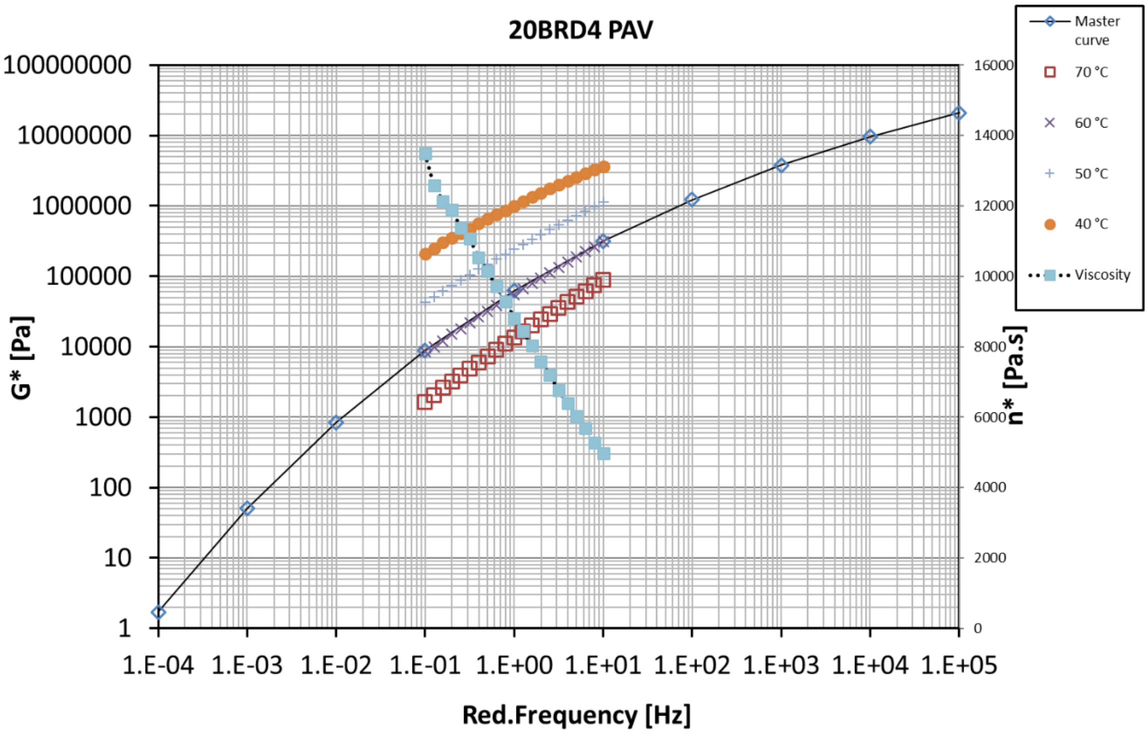

(I)

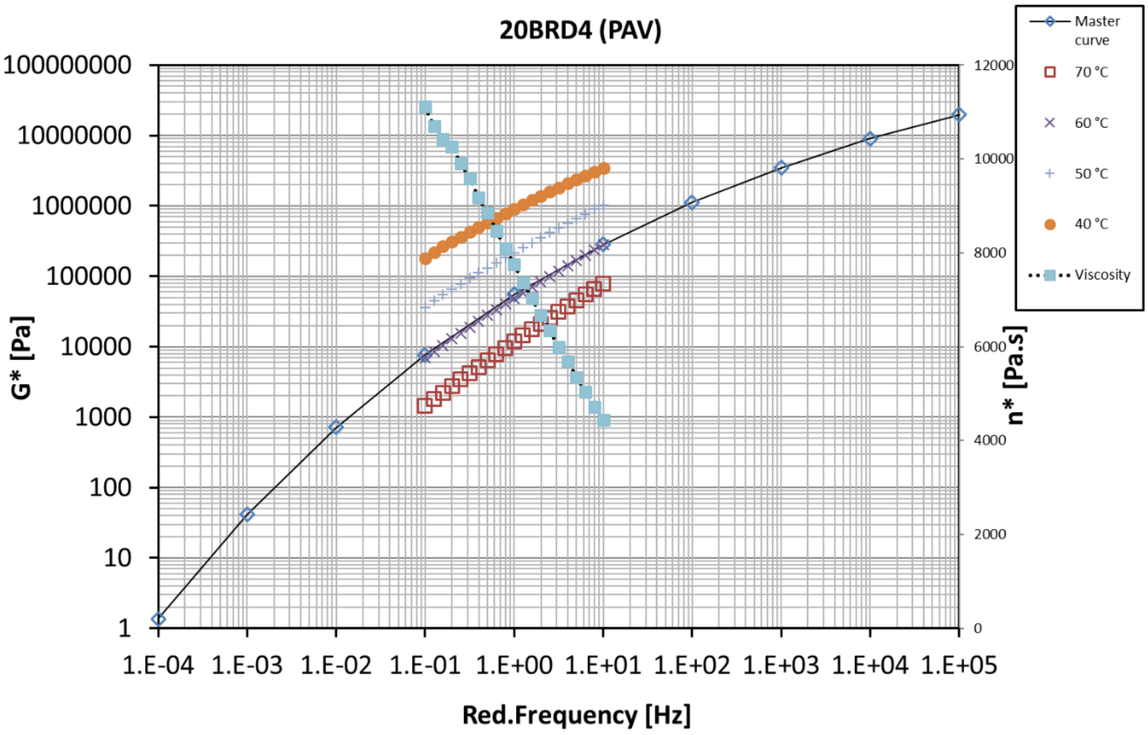

(II)

Figure B 31: Master curve of unaged C320 + 6% NS (20nm) at 60 °C: (I) sample 1, (II) sample 2

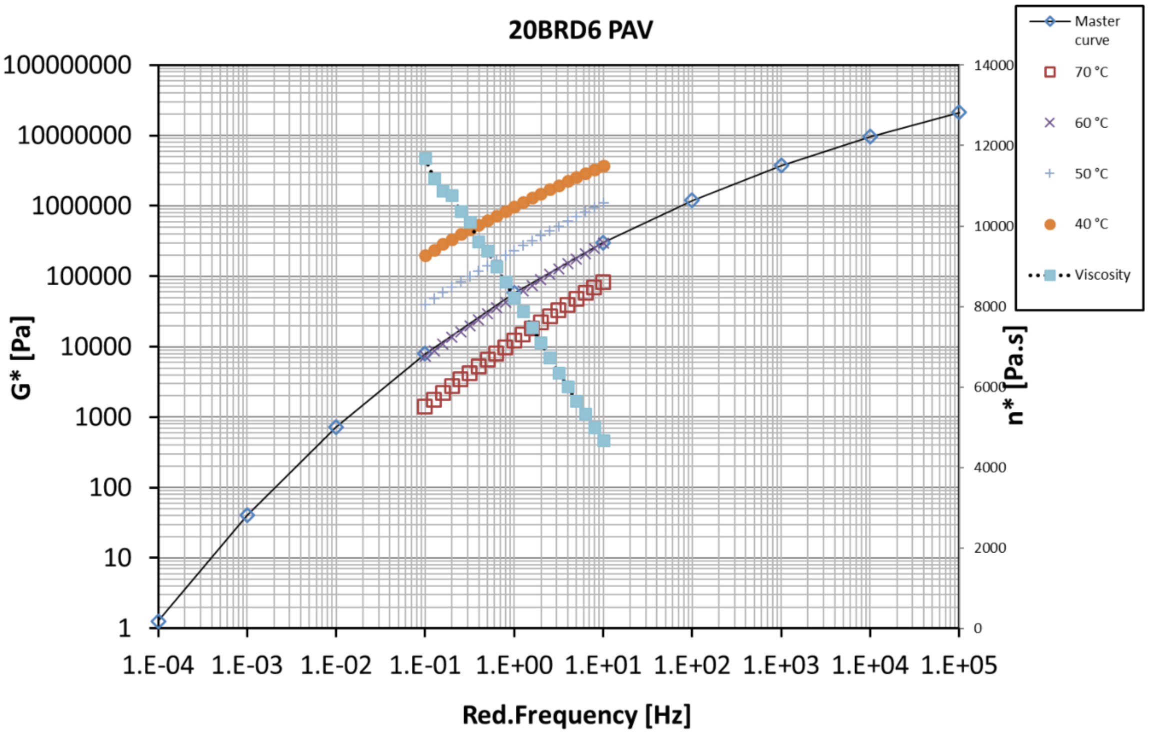

(I)

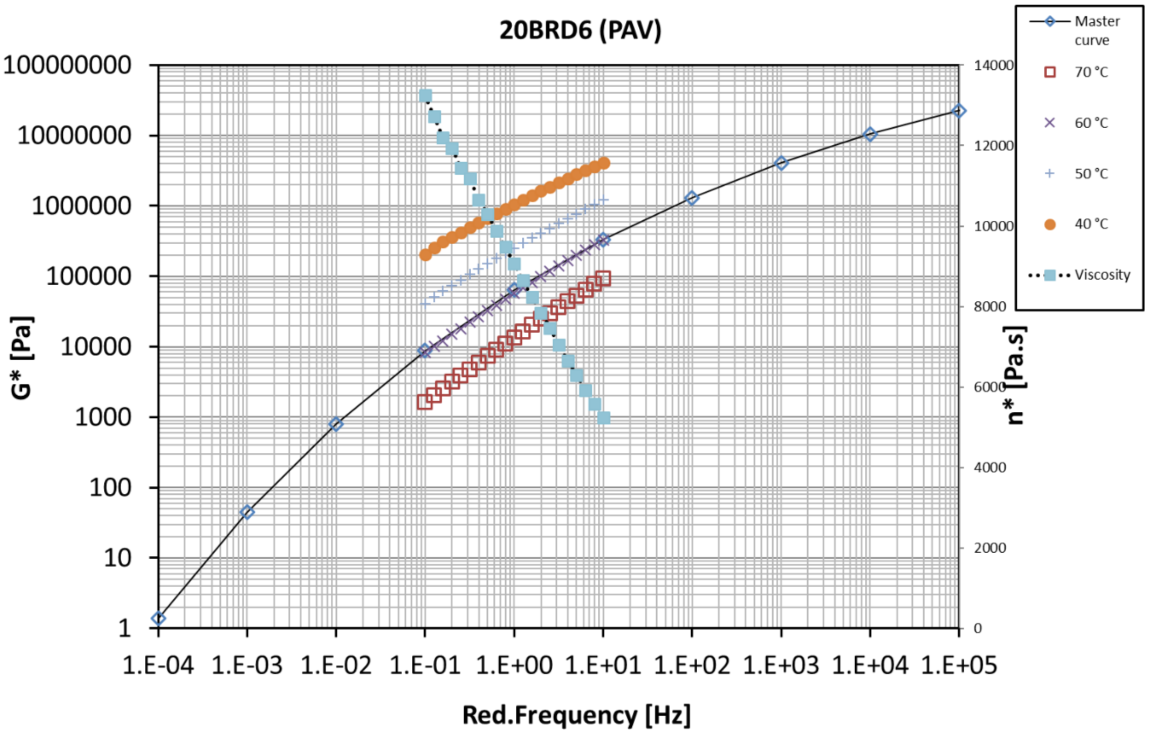

(II)

Figure B 32: Master curve of unaged C320 + 2% NS (60nm) at 60 °C: (I) sample 1, (II) sample 2

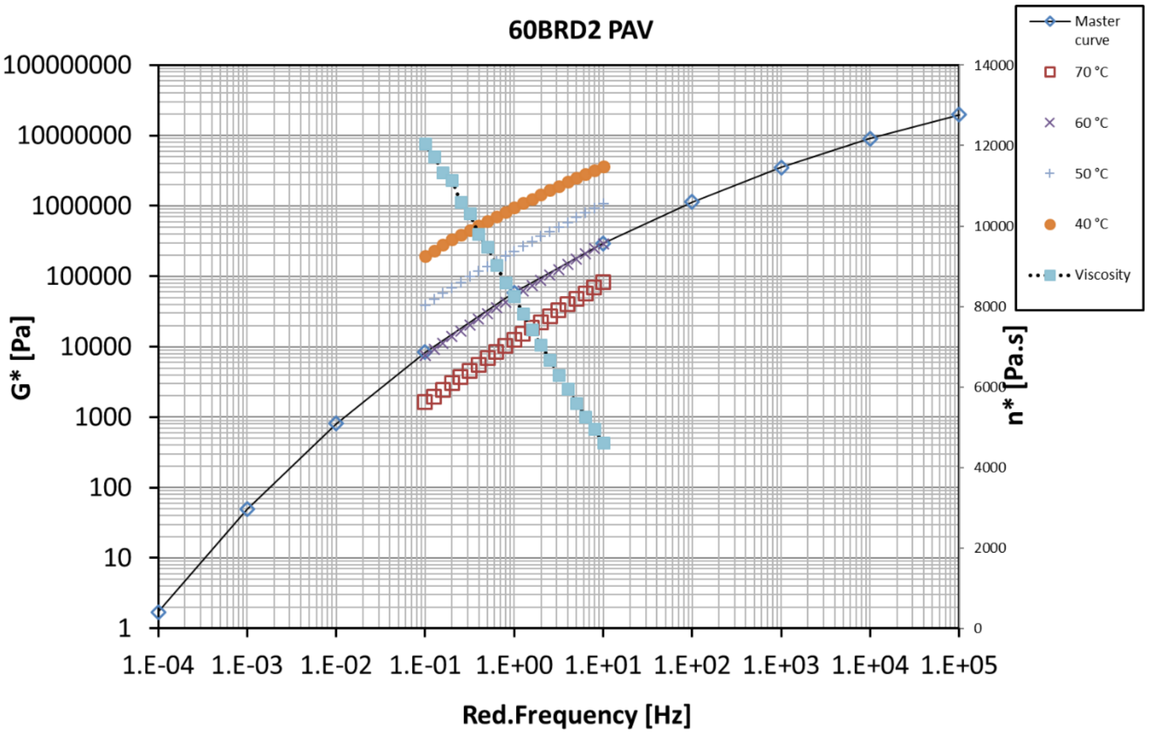

(I)

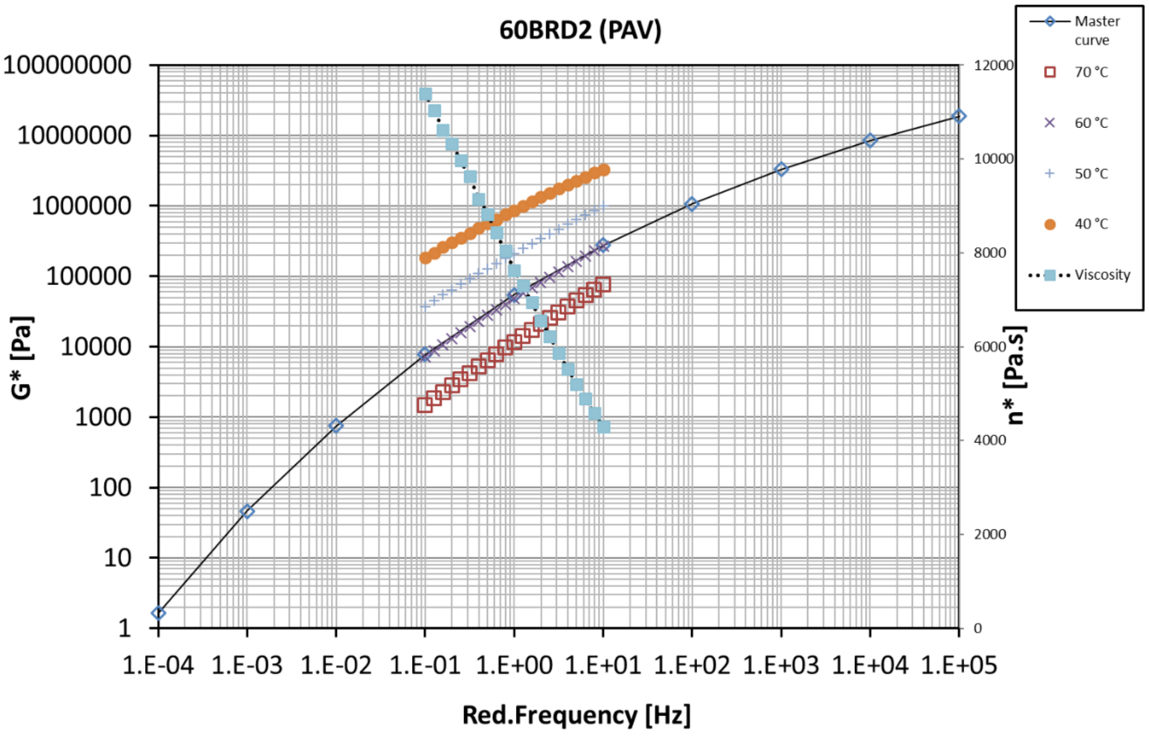

(II)

Figure B 33: Master curve of unaged C320 + 4% NS (60nm) at 60 °C: (I) sample 1, (II) sample 2

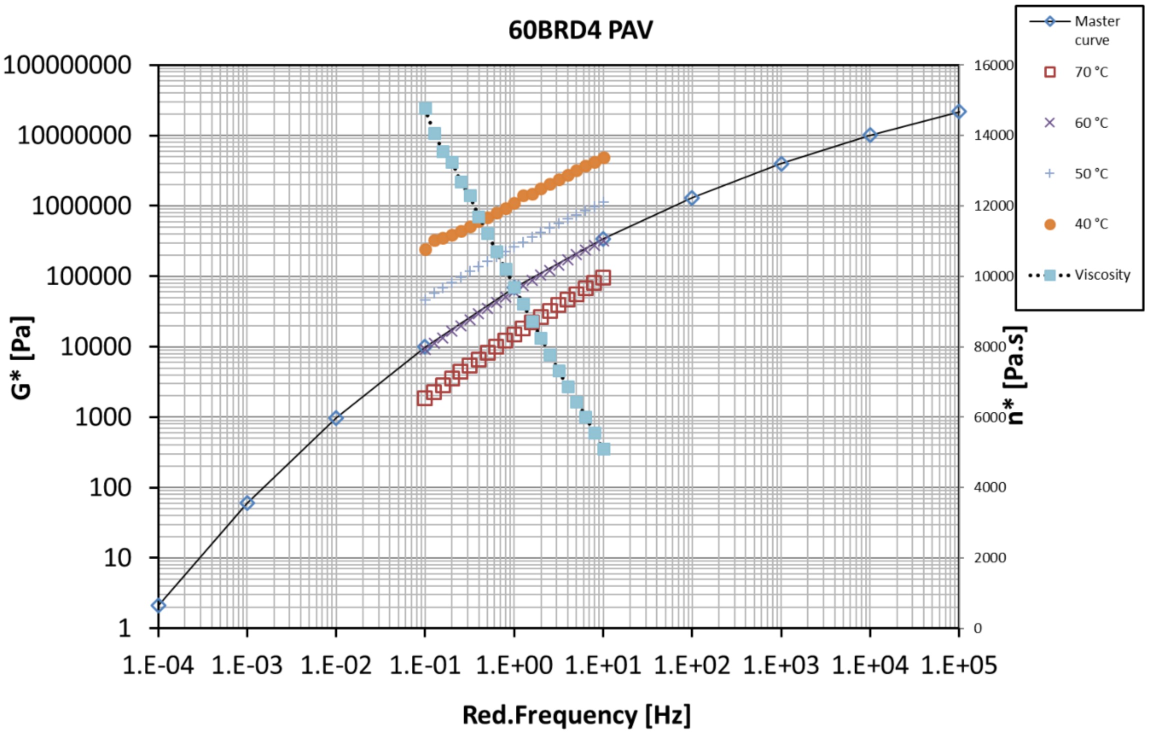

(I)

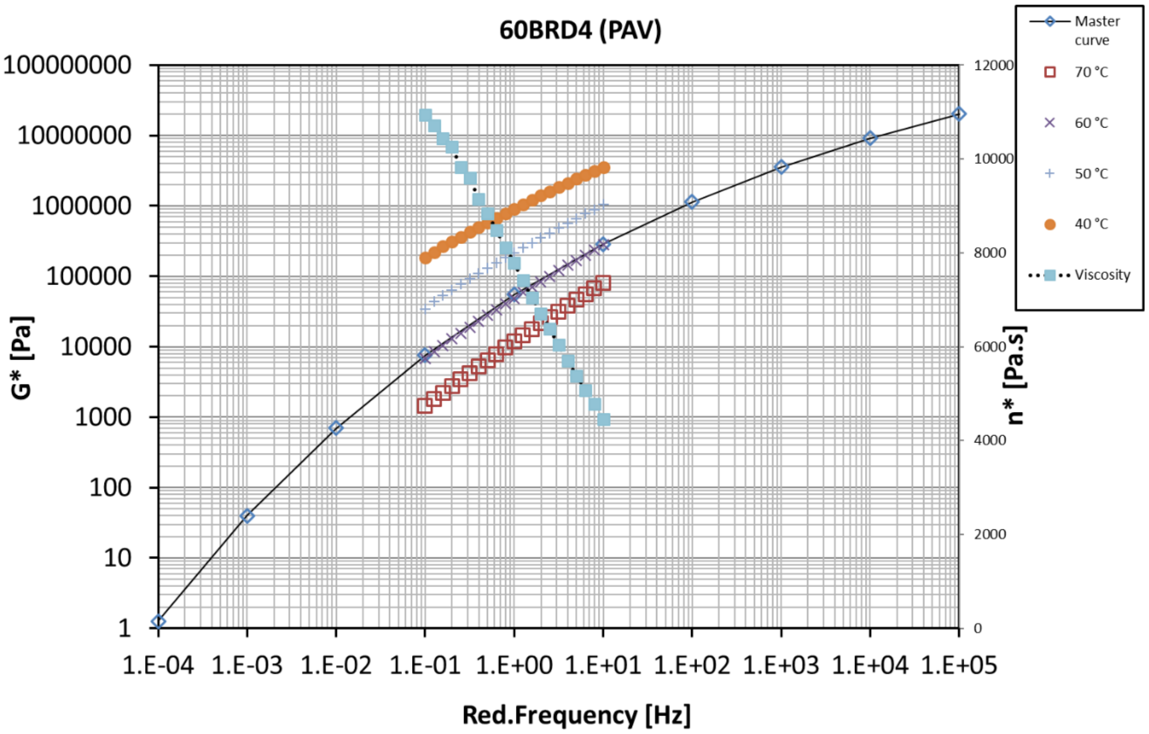

(II)

Figure B 34: Master curve of unaged C320 + 6% NS (60nm) at 60 °C: (I) sample 1, (II) sample 2

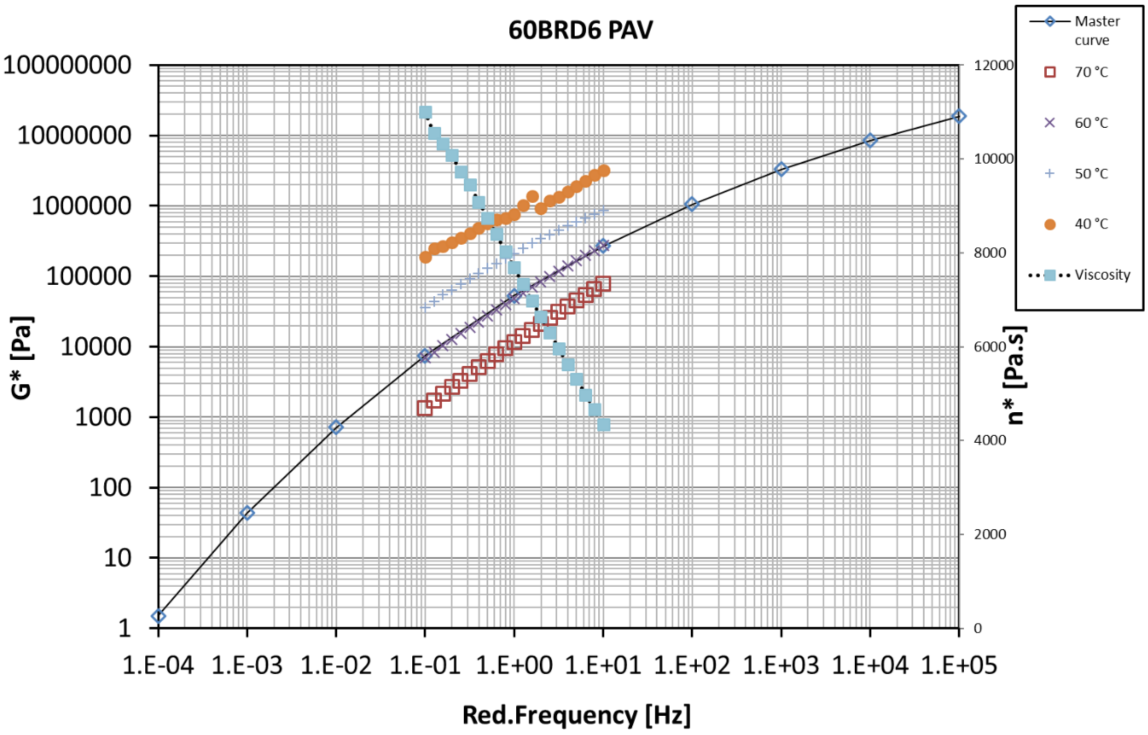

(I)

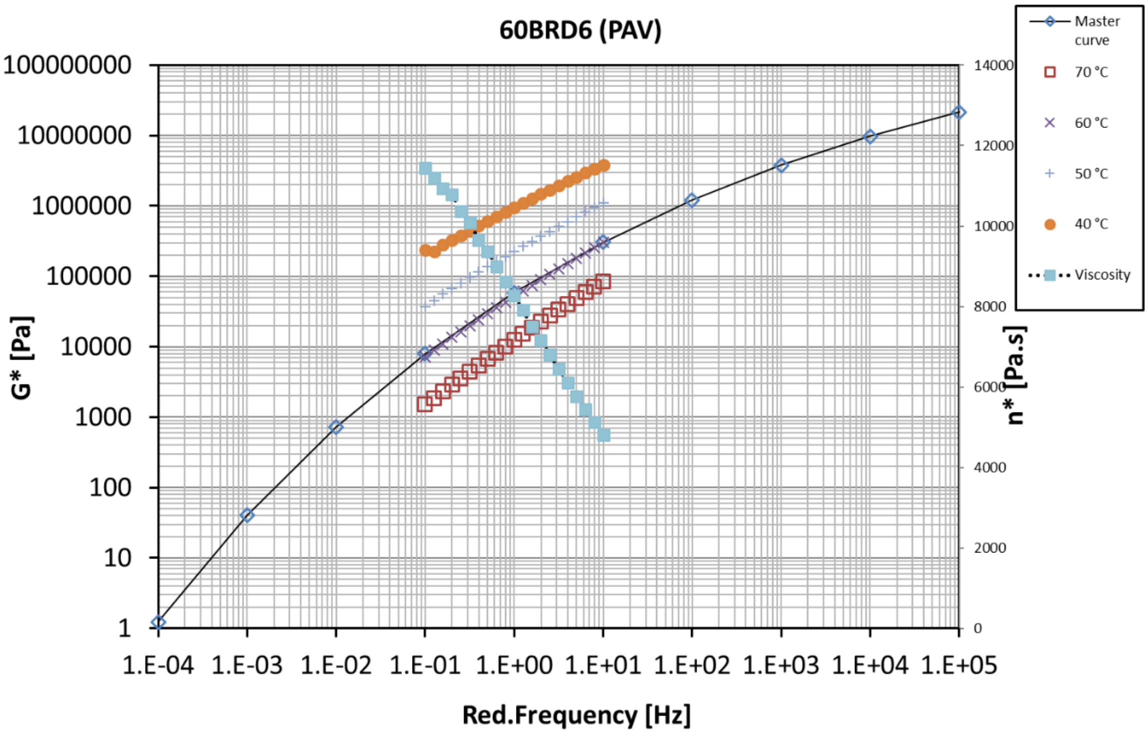

(II)

Figure B 35: Master curve of unaged C600 at 60 °C: (I) sample 1, (II) sample 2

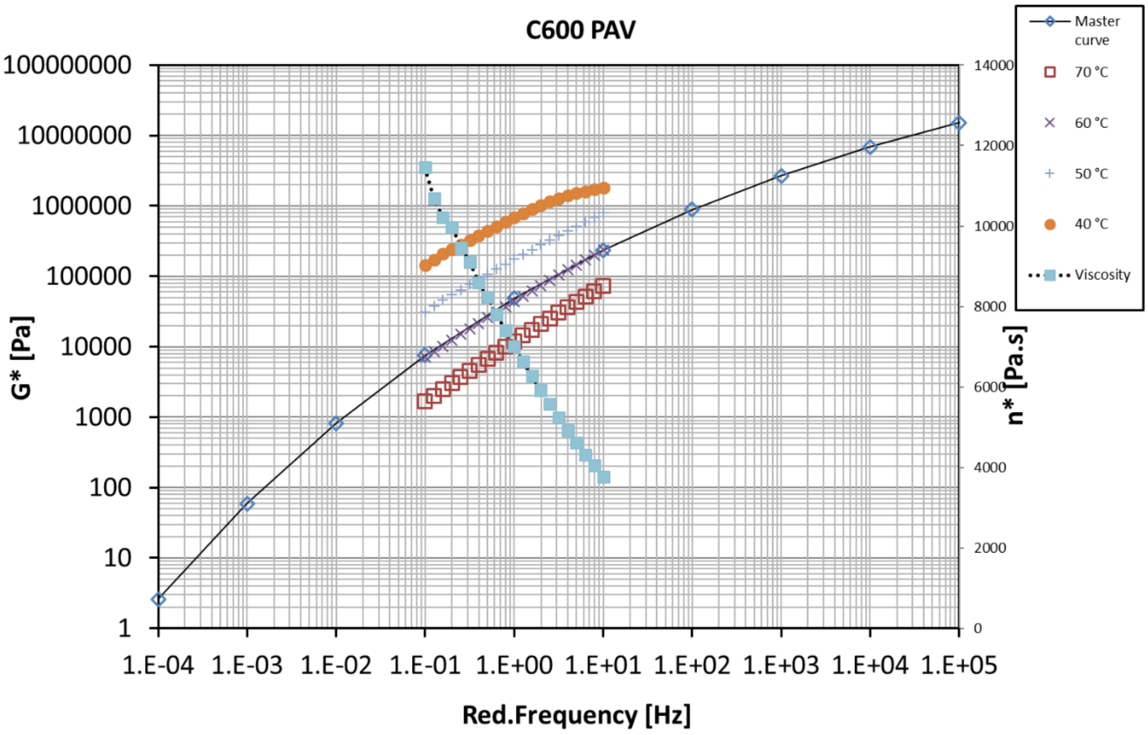

(I)

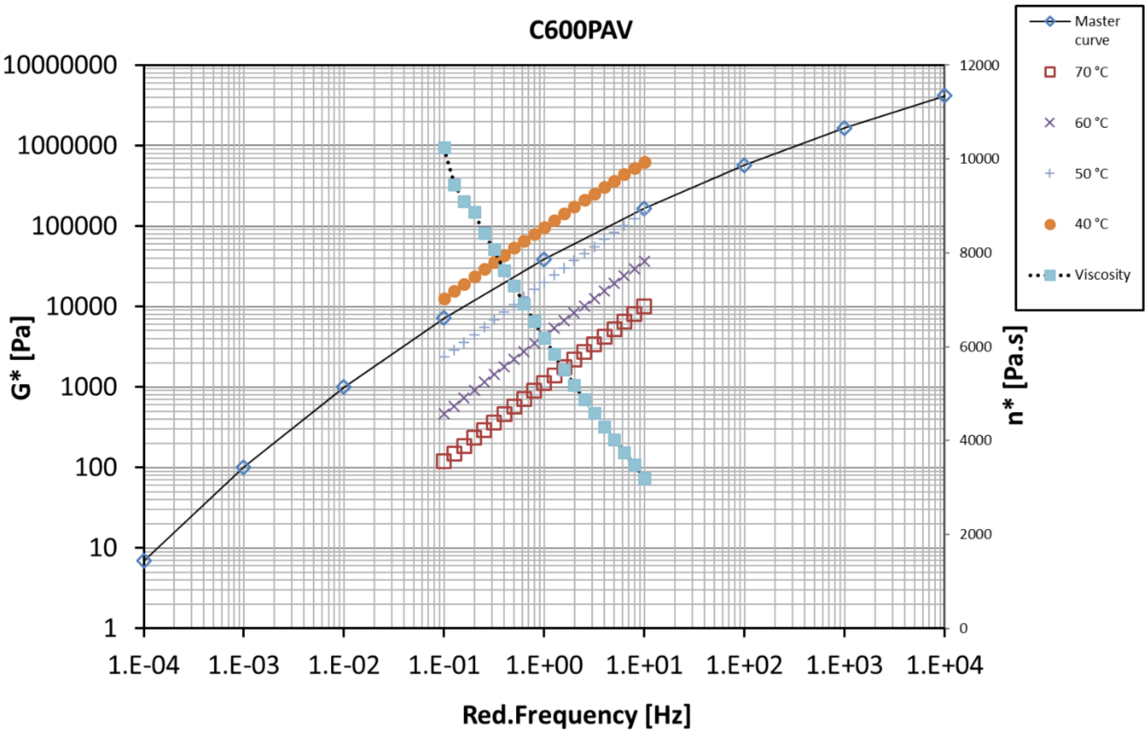

(II)

Figure B 36: Master curve of unaged A15E at 60 °C: (I) sample 1, (II) sample 2

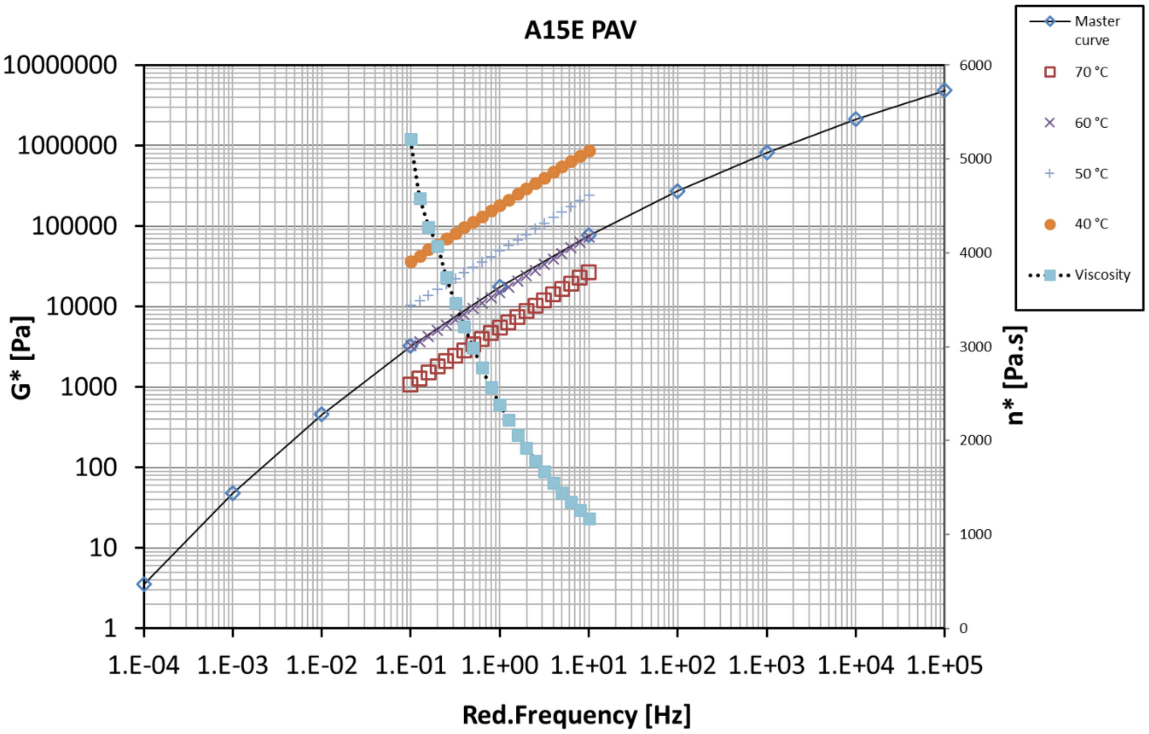

(I)

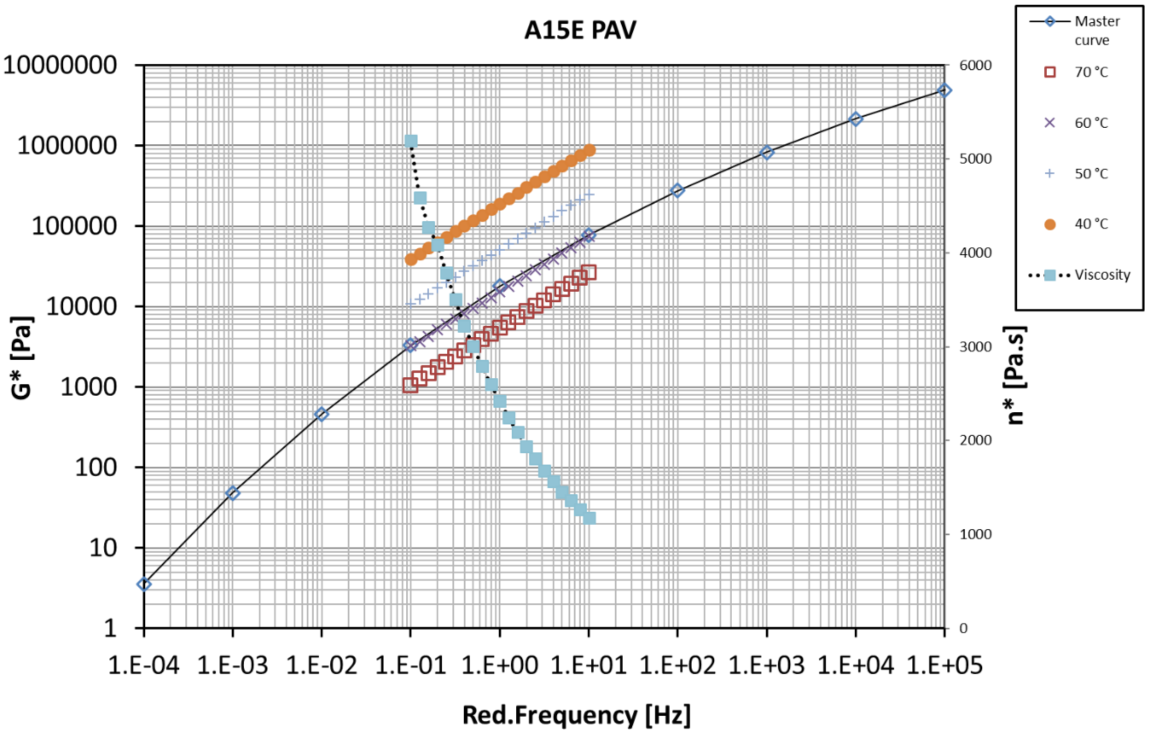

(II)

Figure B 37: Comparisons of master curves for different samples in the unaged condition

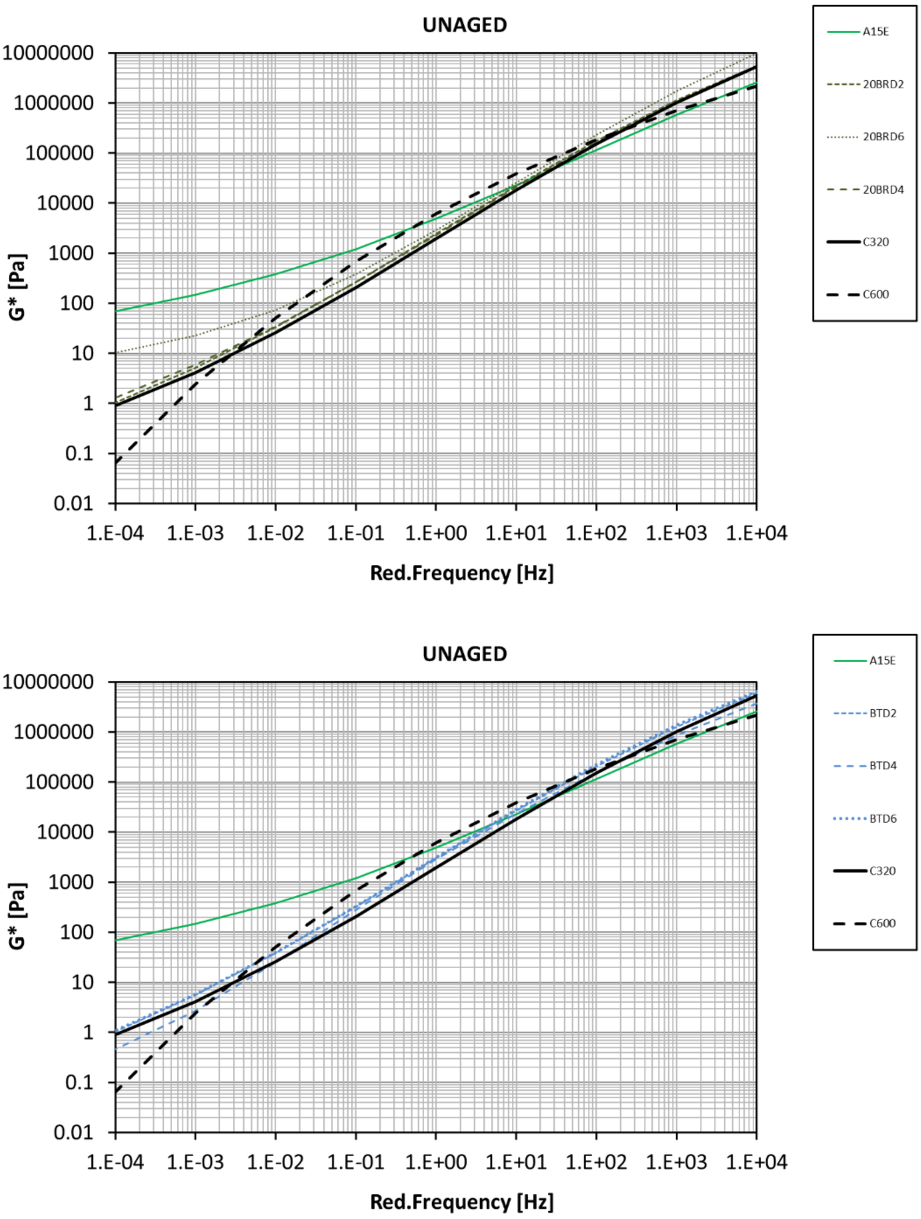

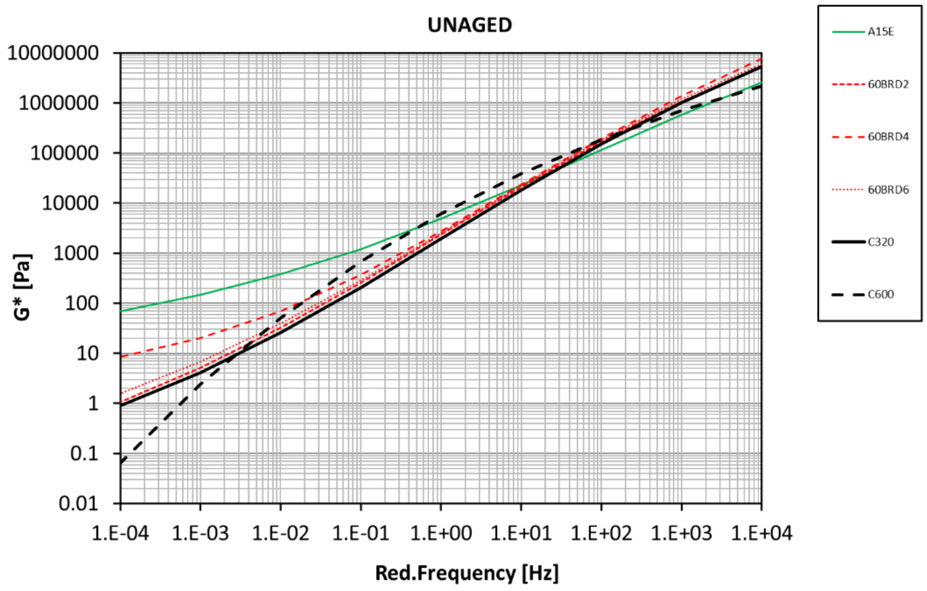
UNAGED
10000000
1000000
100000
10000
1000
100
10
1
0.1
0.01
G* [Pa]
1.E-04
1.E-03
1.E-02
1.E-01
1.E+00
1.E+01
1.E+02
1.E+03
1.E+04
Red.Frequency [Hz]
A15E
60BRD2
60BRD4
60BRD6
C320
C600

Figure B 38: Comparisons of master curves for different samples in the RTFO condition

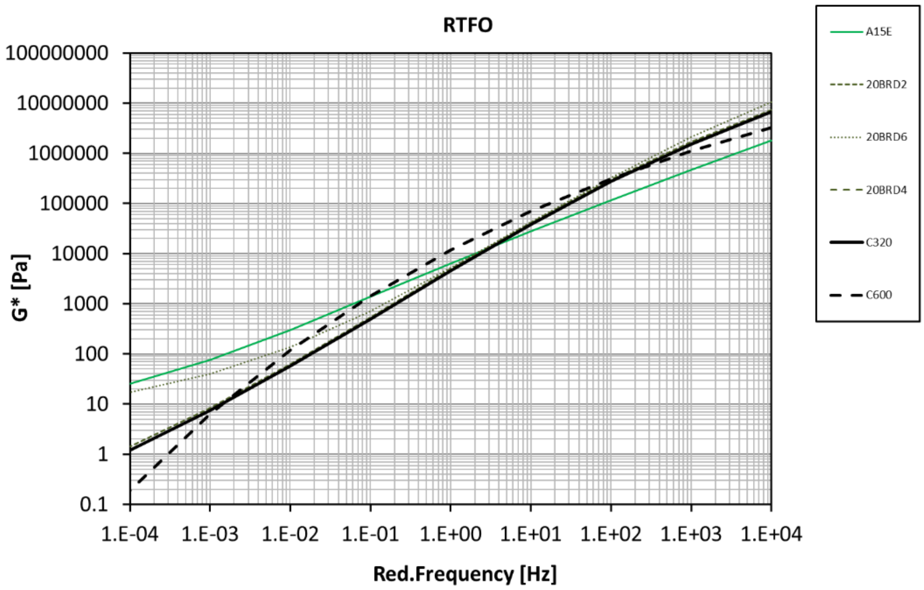

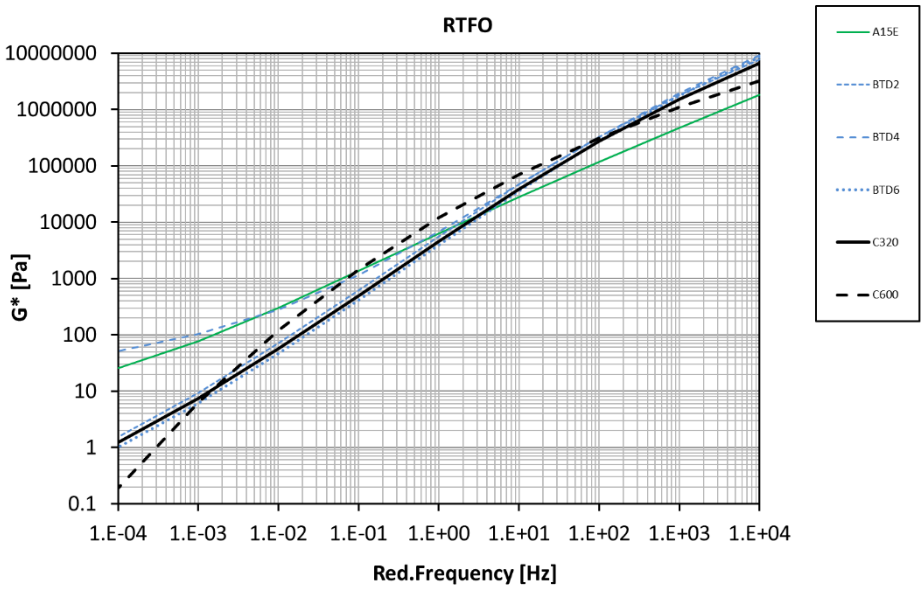

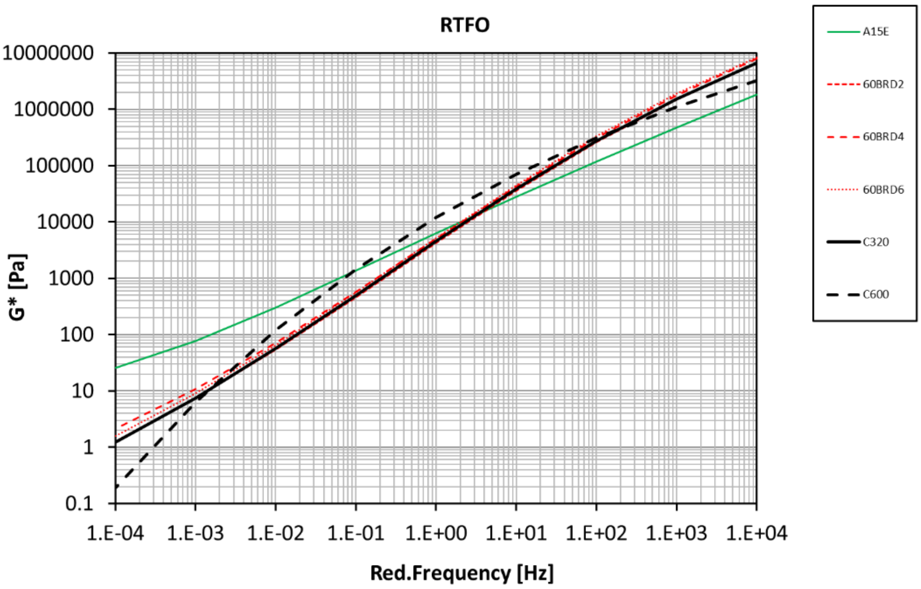
RTFO
10000000
1000000
100000
10000
1000
100
10
1
0.1
G* [Pa]
1.E-04
1.E-03
1.E-02
1.E-01
1.E+00
1.E+01
1.E+02
1.E+03
1.E+04
Red.Frequency [Hz]
A15E
60BRD2
60BRD4
60BRD6
C320
C600

Figure B 39: Comparisons of master curves for different samples in the PAV condition

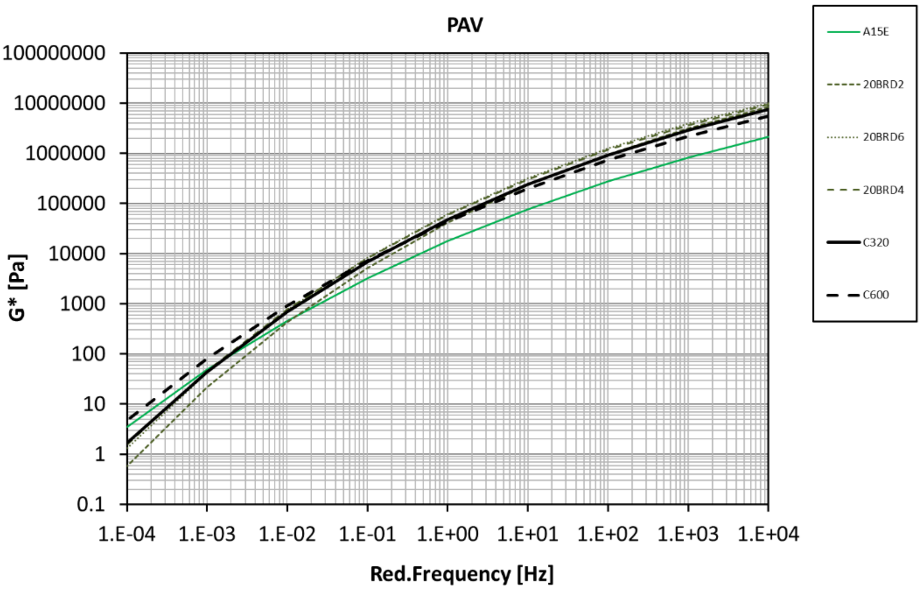

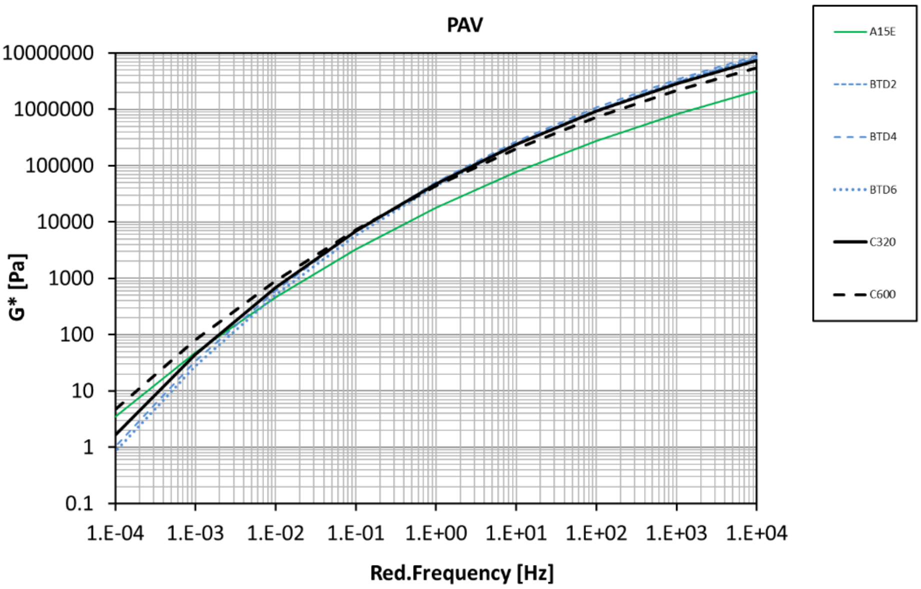

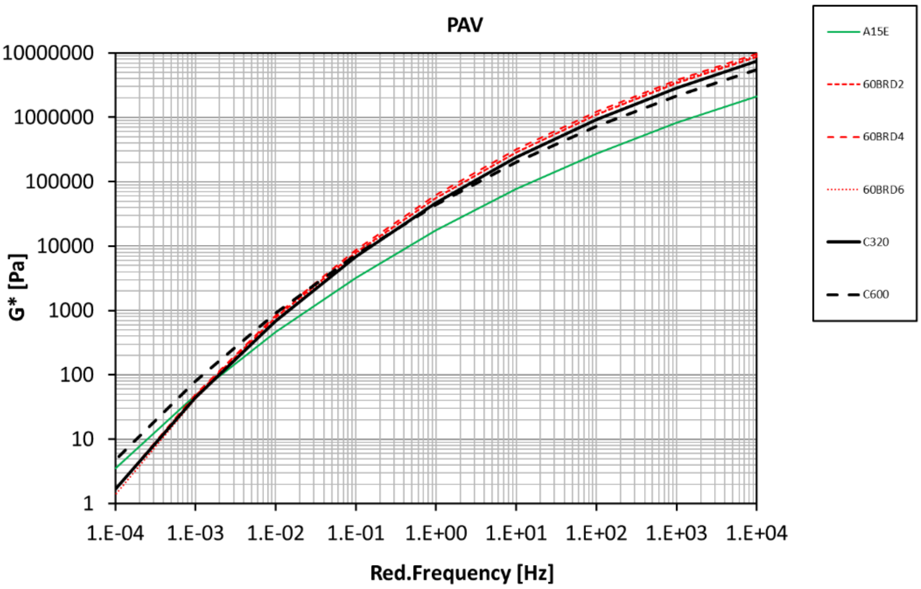

Figure B 40: Master curve of unaged C320 + 2% NS (20nm) at 60 °C – wet mixed

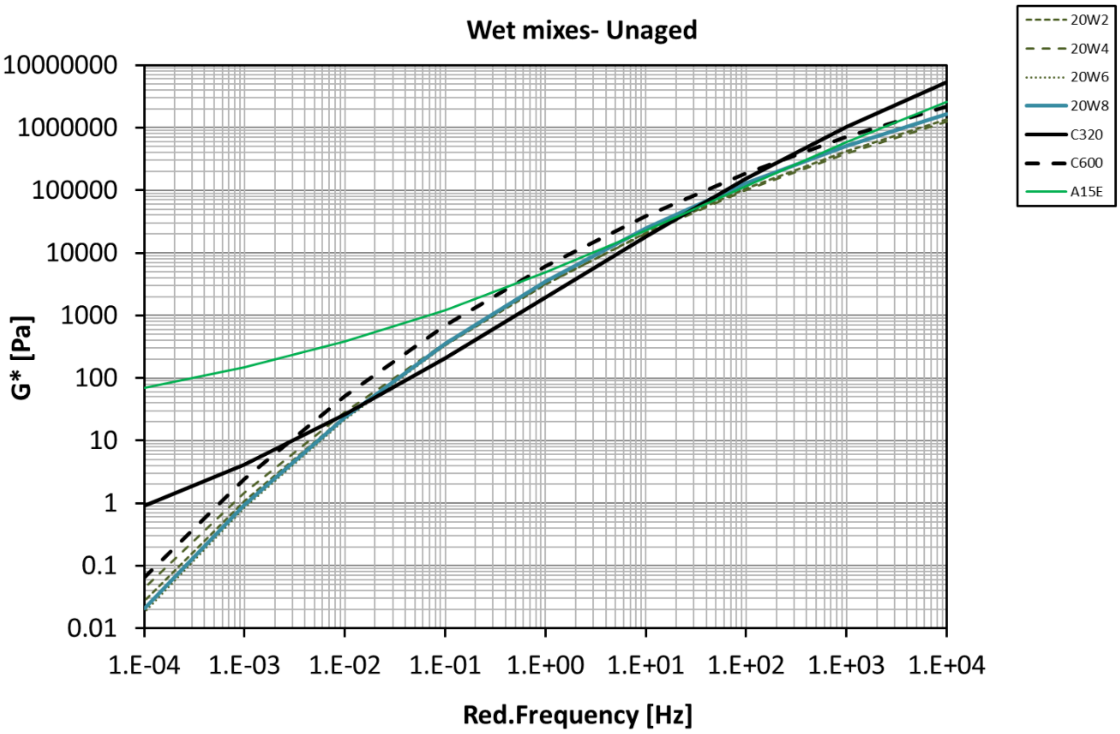

Figure B 41: Master curve of unaged C320 + 2% NS (20nm + KH550 couplant) at 60 °C – wet mixed

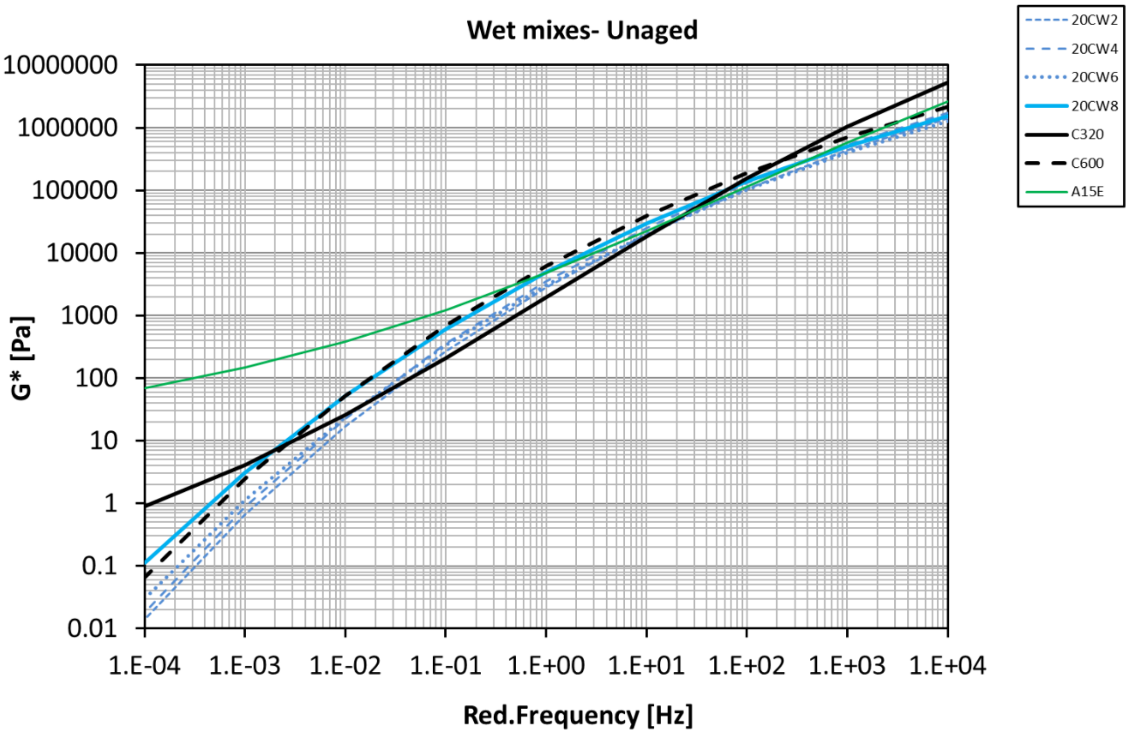

Figure B 42: Master curve of unaged C320 + NS (60nm) at 60 °C – wet mixed

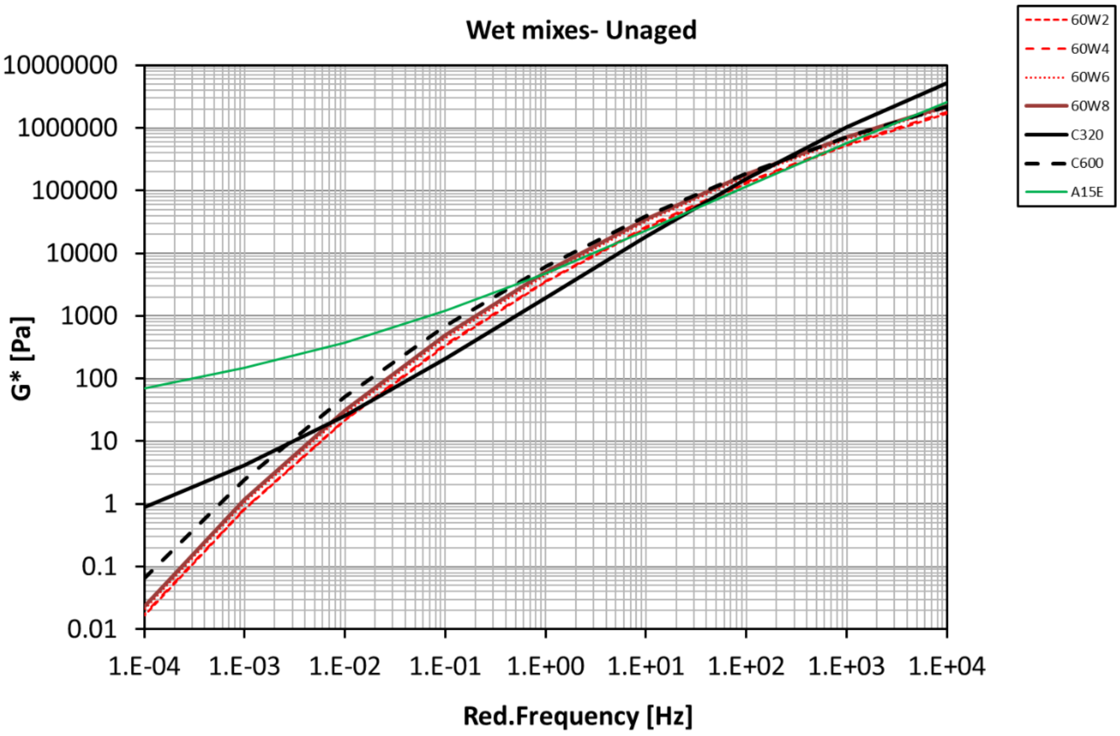

APPENDIX C SUMMARY OF RHEOLOGY

Figure C 1: Complex shear modulus of unaged samples at 60 °C (f = 10 rad/s)

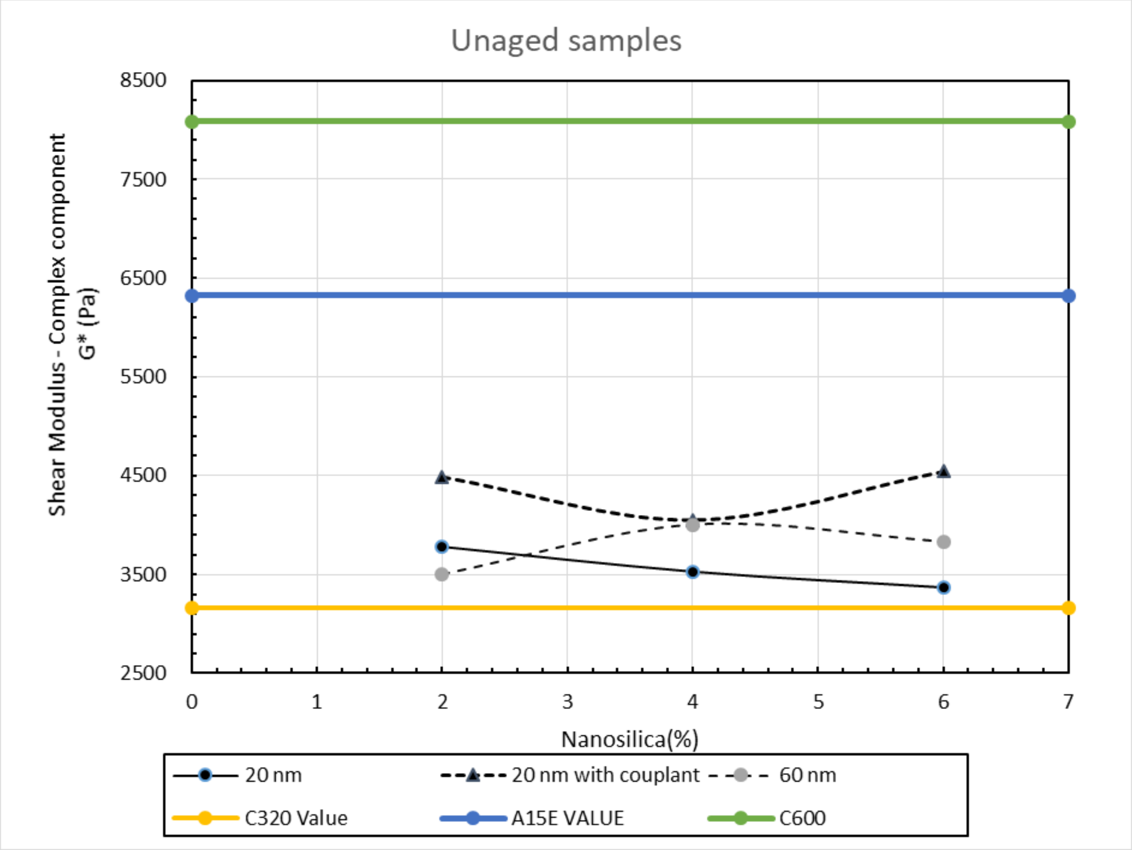

Figure C 2: Shear viscosity of unaged samples at 60 °C (f = 1 rad/s).

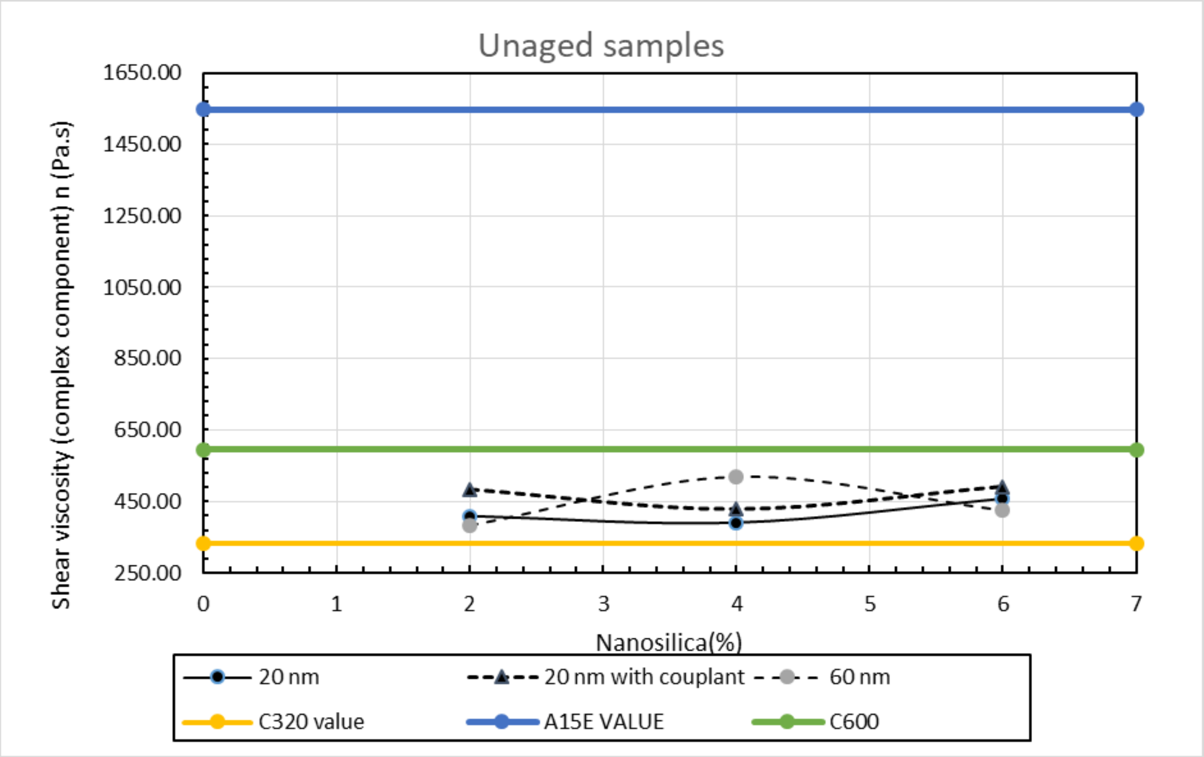

Figure C 3: Complex shear modulus of NS modified C320 over virgin C320 of unaged samples at 60 °C (f = 10 rad/s).

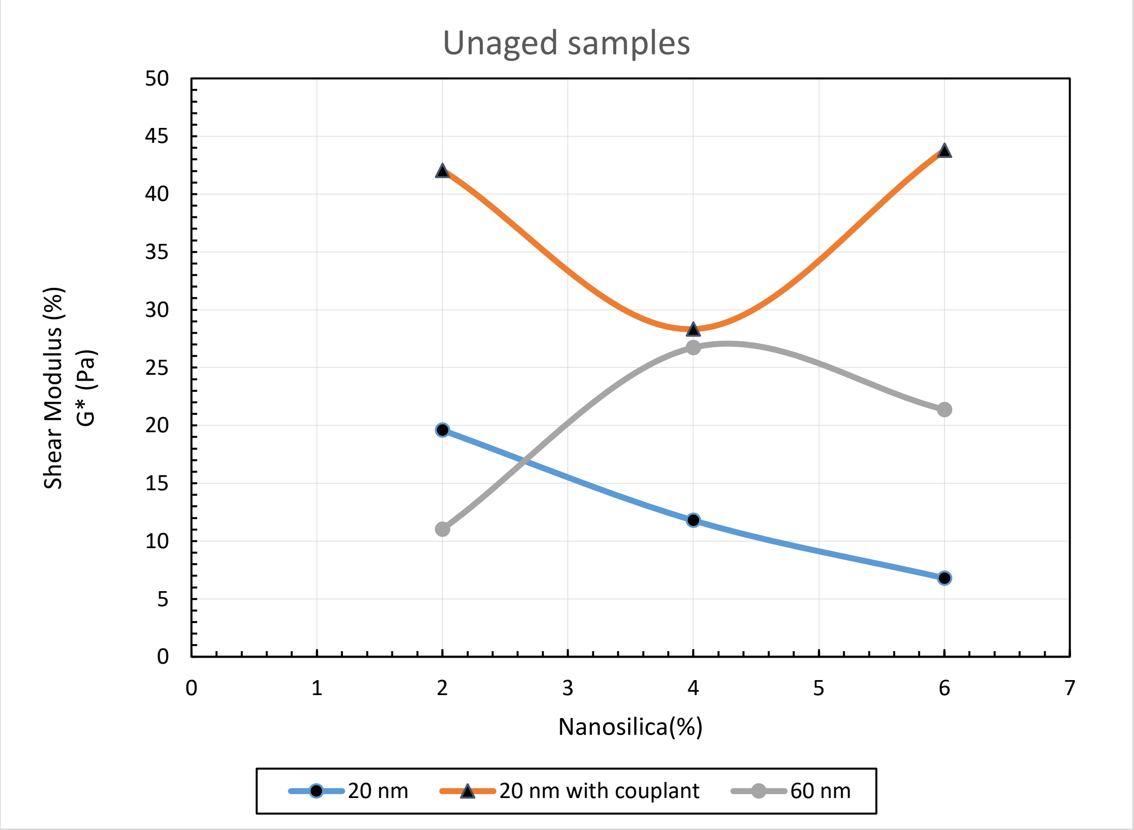

Figure C 4: Shear viscosity of NS modified C320 over virgin C320 of unaged samples at 60 °C (f = 1 rad/s).

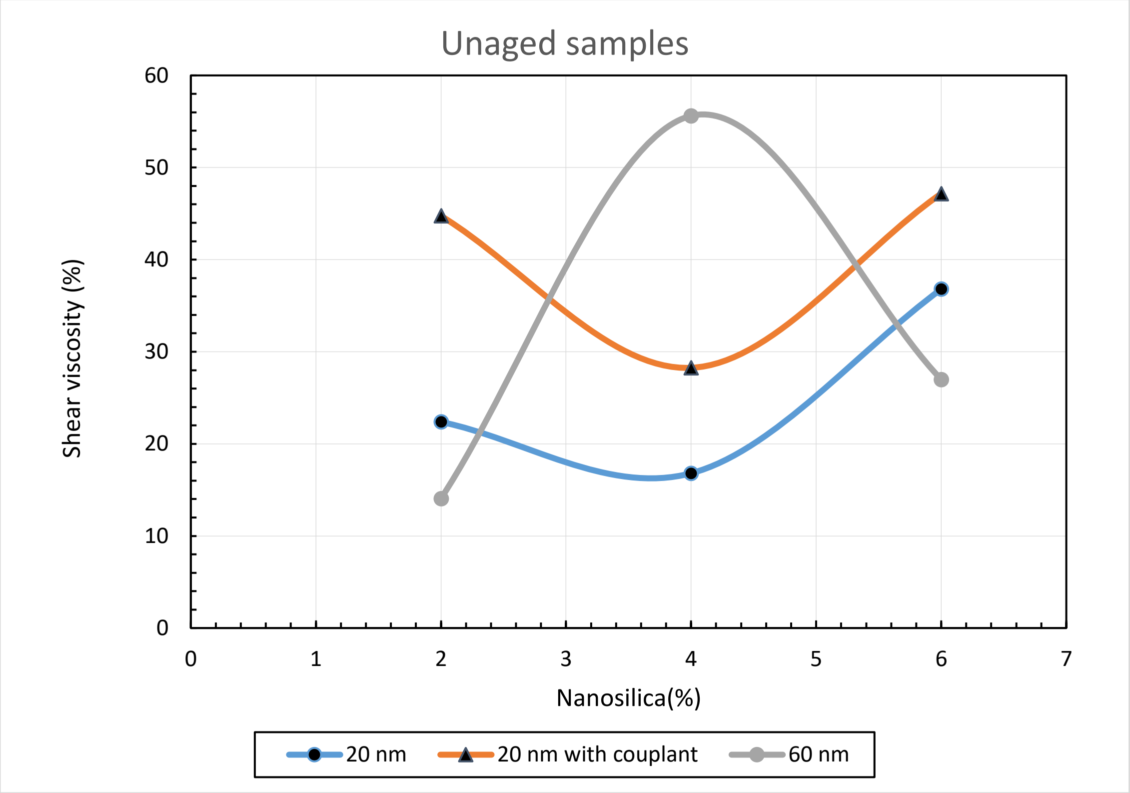

Figure C 5: Rutting parameter of unaged samples at 60 °C (f = 10 rad/s).

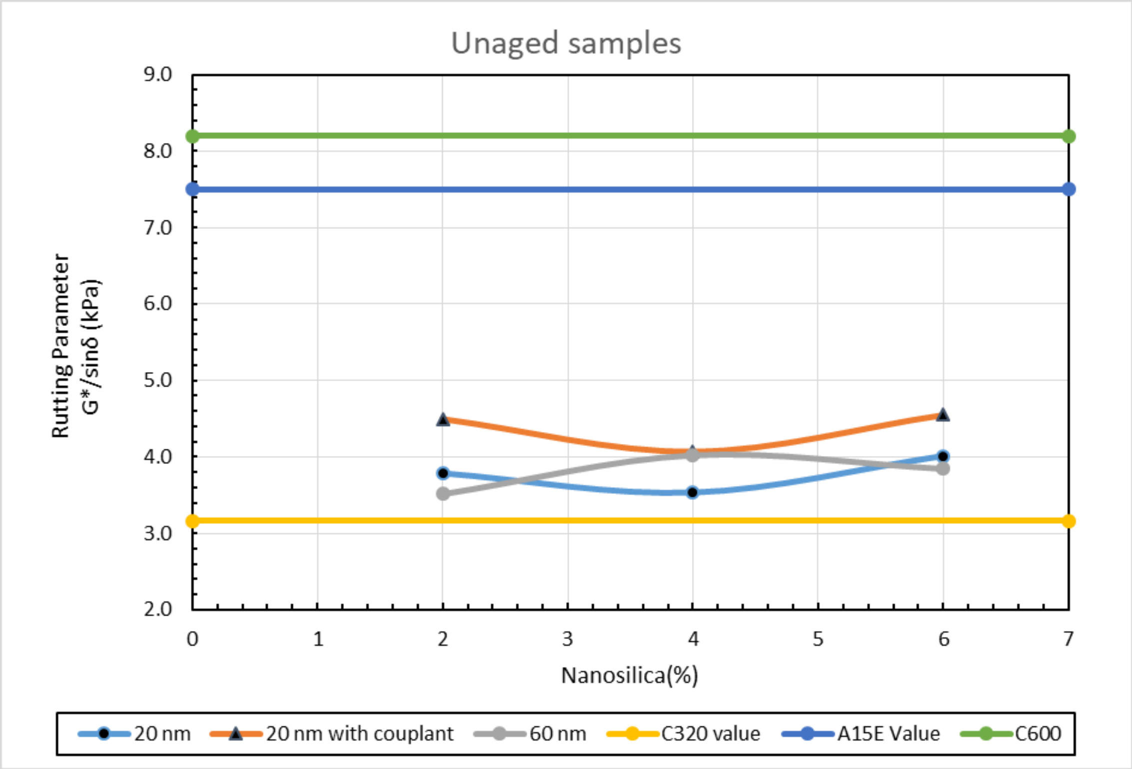

Figure C 6: Fatigue parameter of unaged samples at 60 °C (f = 10 rad/s).

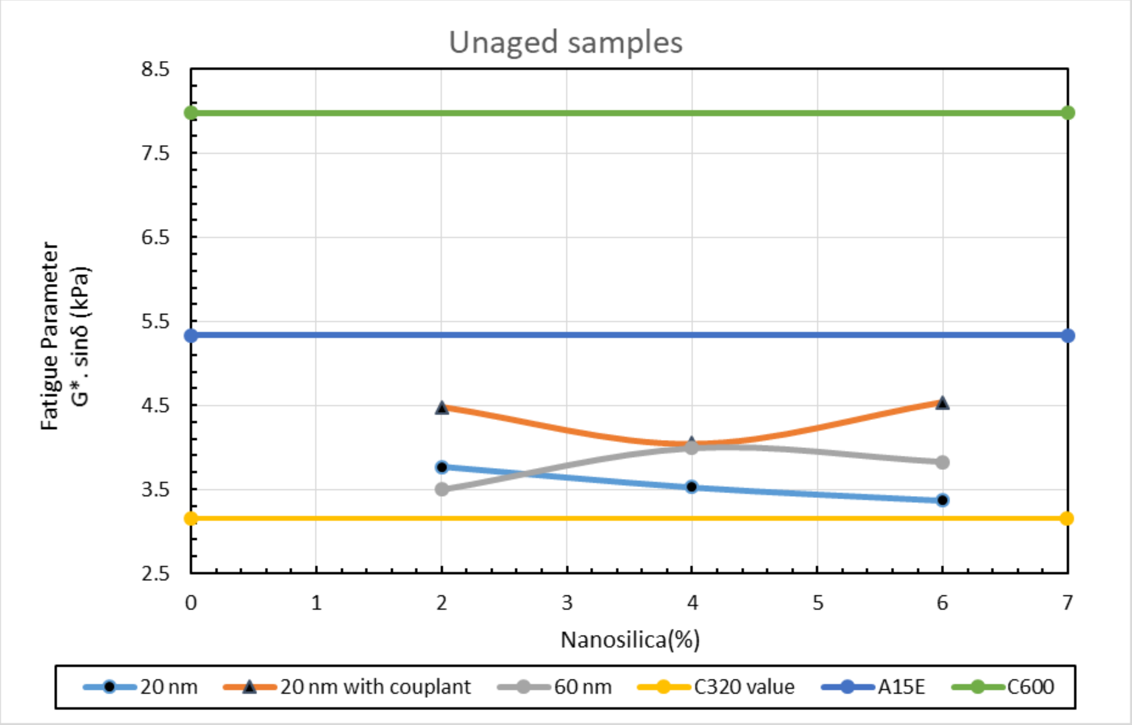

Figure C 7: Rutting parameter of NS modified C320 over virgin C320 of unaged samples at 60 °C (f = 10 rad/s).

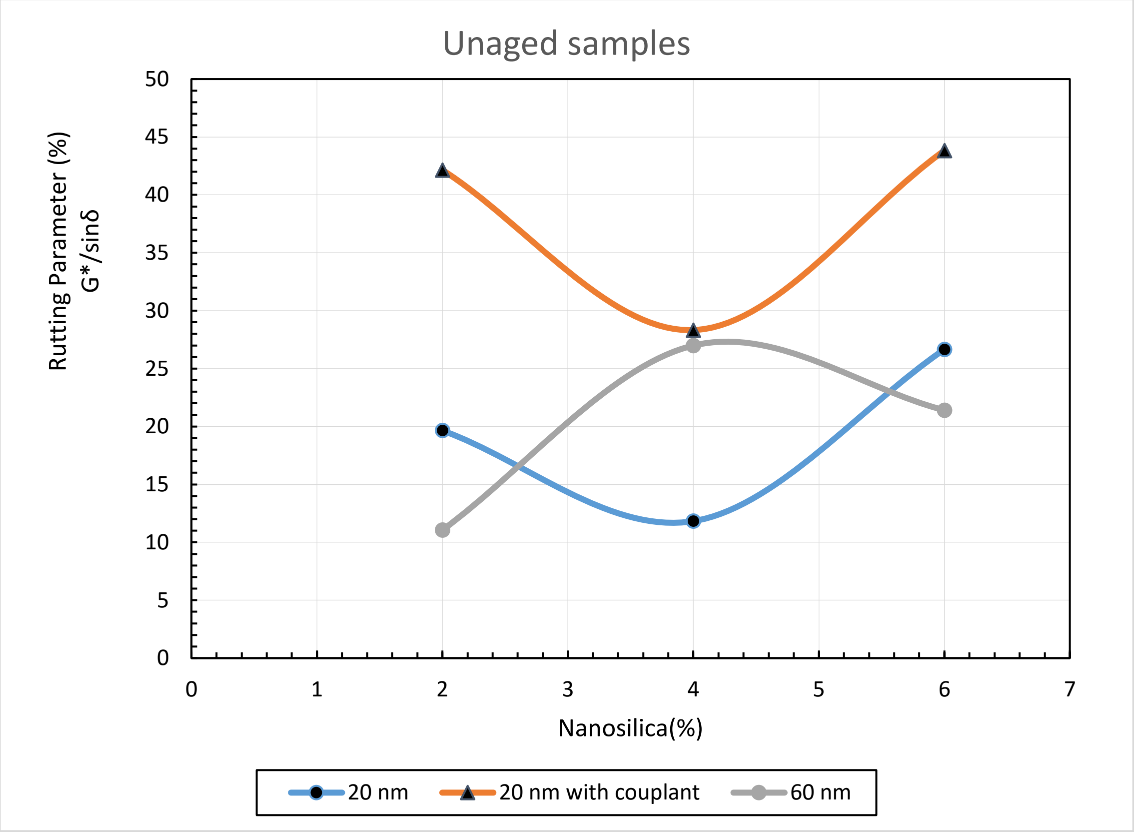

Figure C 8: Fatigue parameter of NS modified C320 over virgin C320 of unaged samples at 60 °C (f = 10 rad/s).

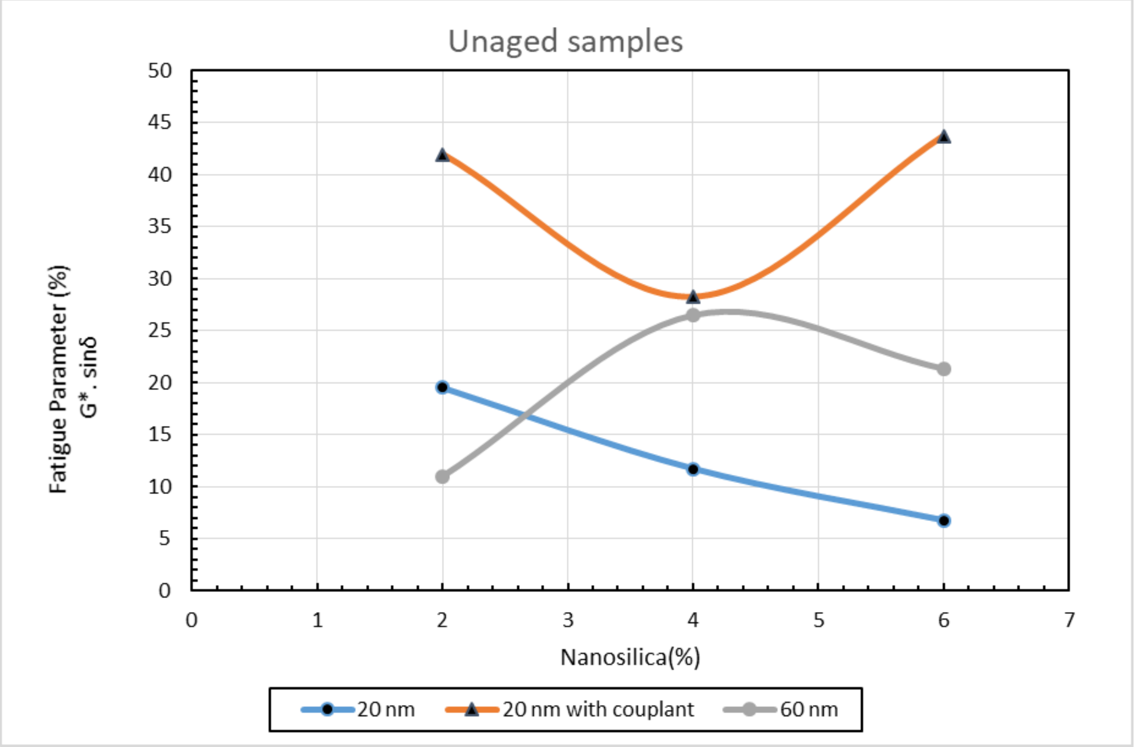

Figure C 9: Complex shear modulus of of RTFO Samples at 60 °C (f = 10 rad/s).

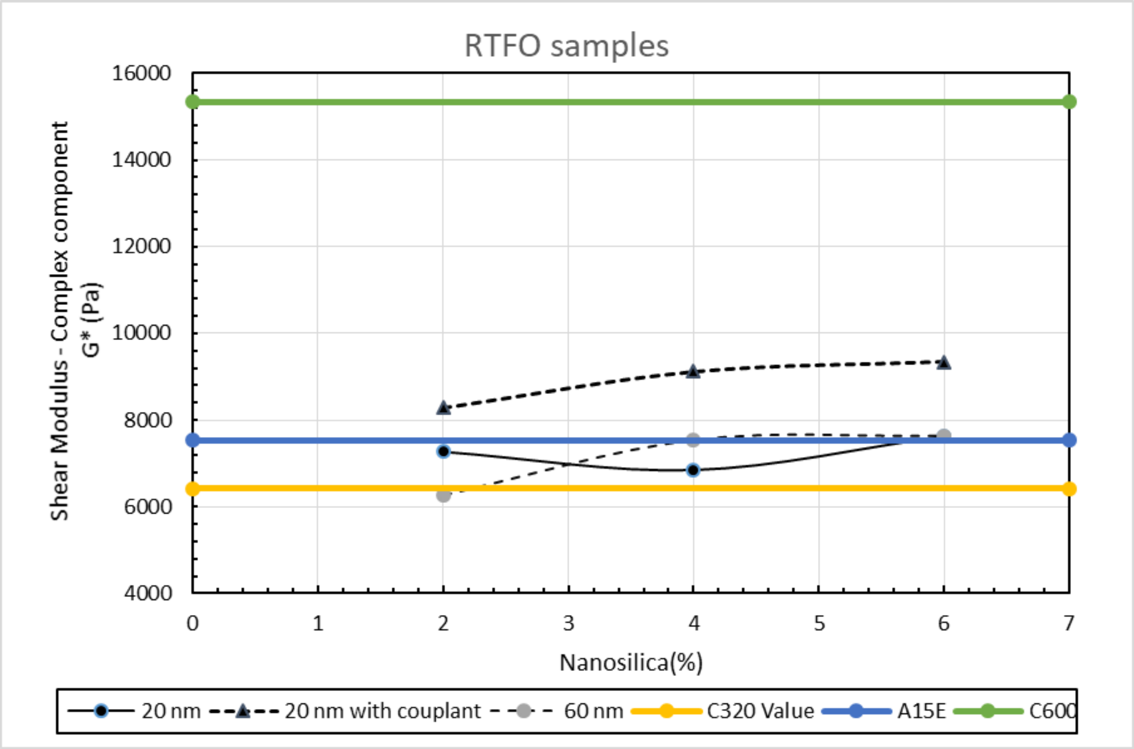

Figure C 10: Shear viscosity of RTFO samples at 60 °C (f = 1 rad/s).

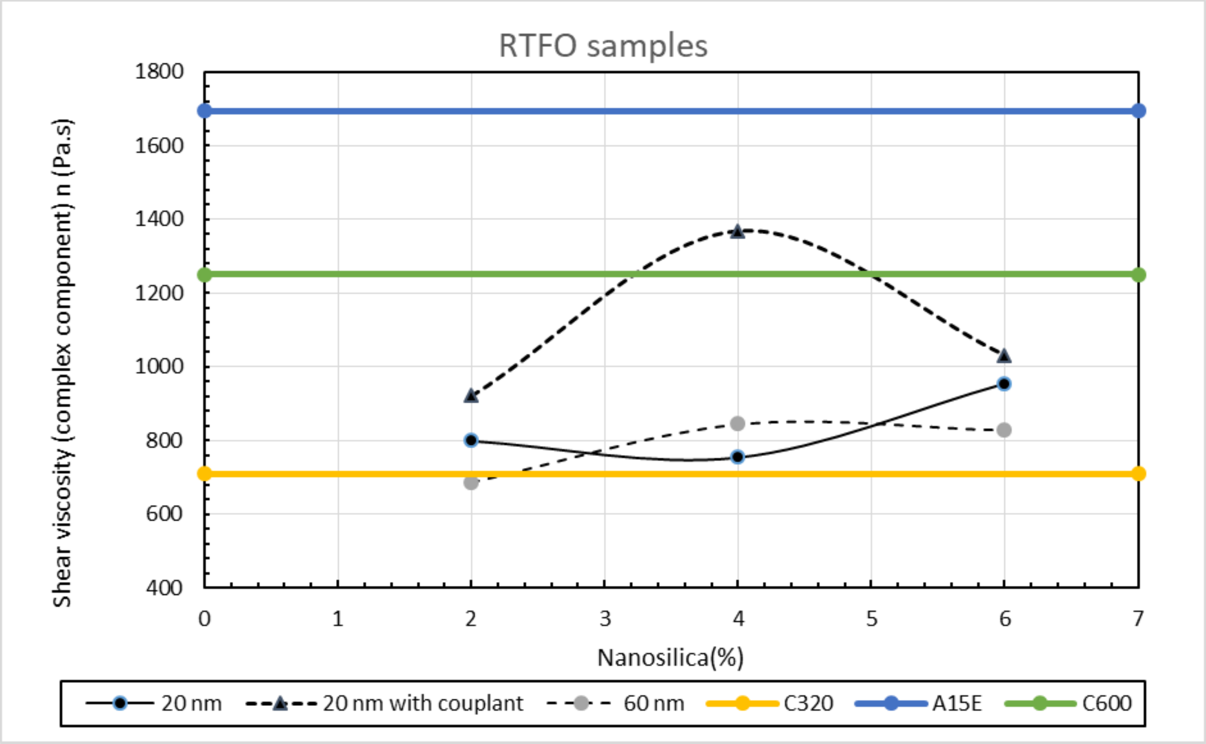

Figure C 11: Complex shear modulus of NS modified C320 over virgin C320 of RTFO samples at 60 °C (f = 10 rad/s).

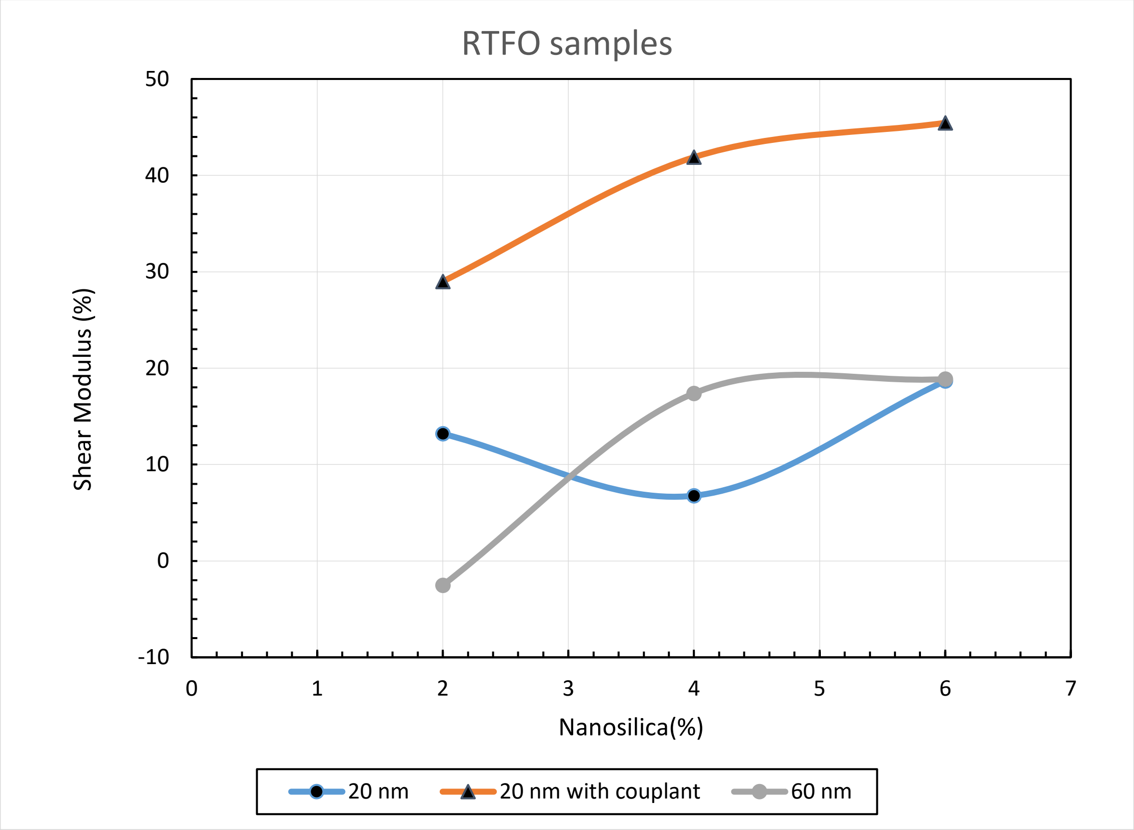

Figure C 12: Shear viscosity of NS modified C320 over virgin C320 of RTFO samples at 60 °C (f = 1 rad/s).

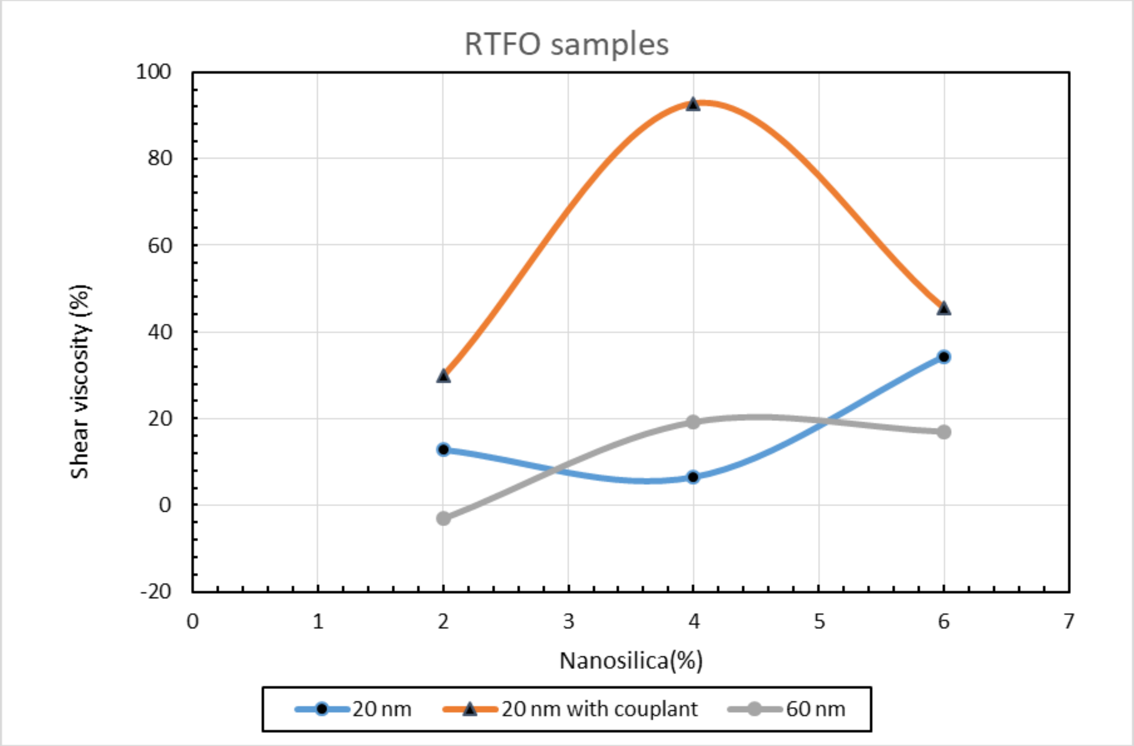

Figure C 13: Rutting parameter of RTFO samples at 60 °C (f = 10 rad/s).

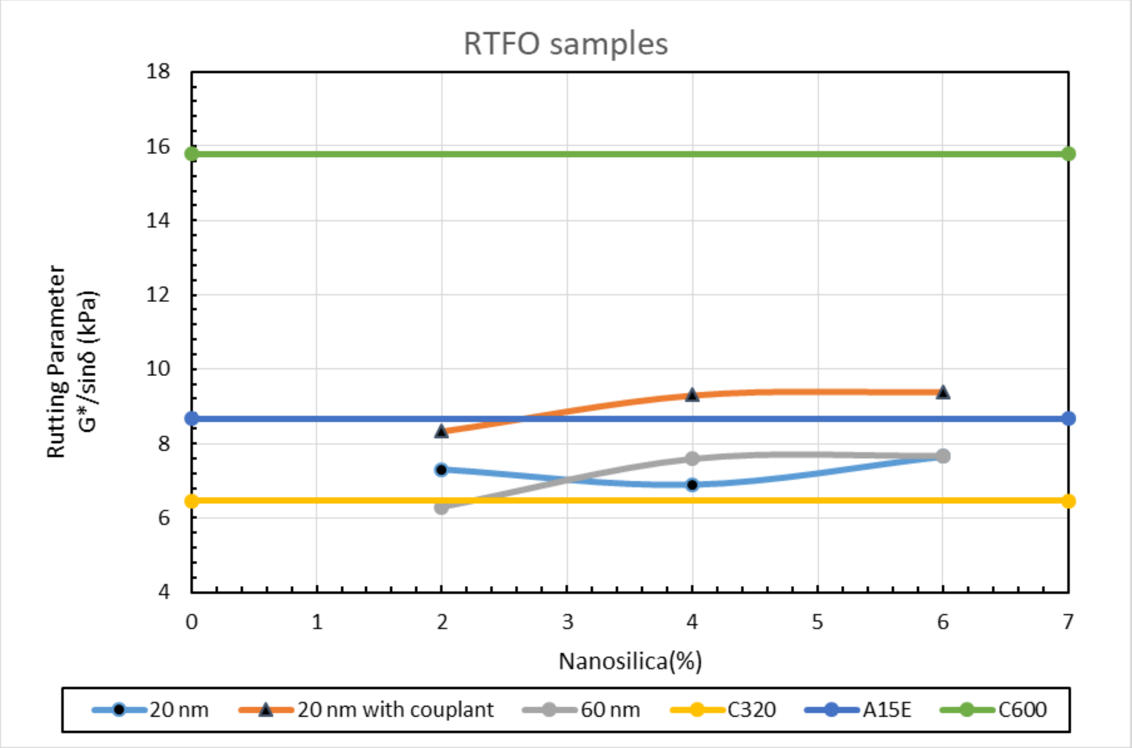

Figure C 14: Fatigue parameter of RTFO samples at 60 °C (f = 10 rad/s).

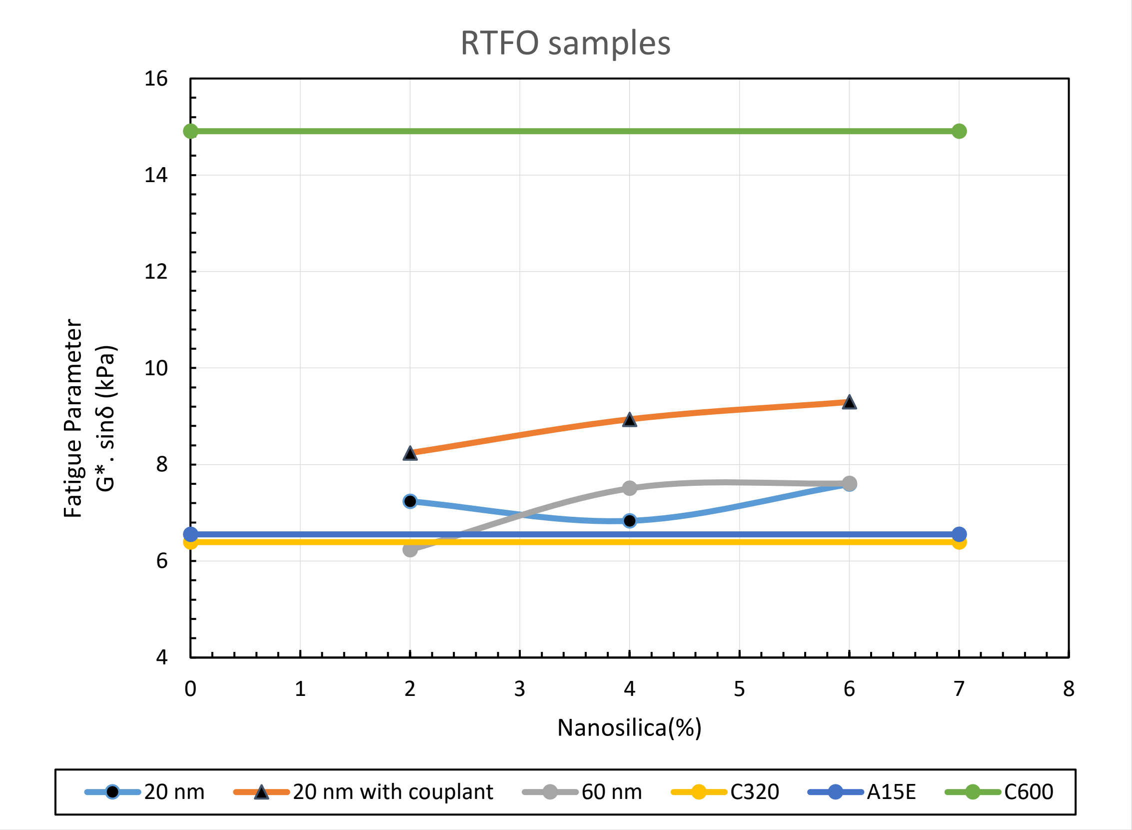

Figure C 15: Rutting parameter of NS modified C320 over virgin C320 of RTFO samples at 60 °C (f = 10 rad/s).

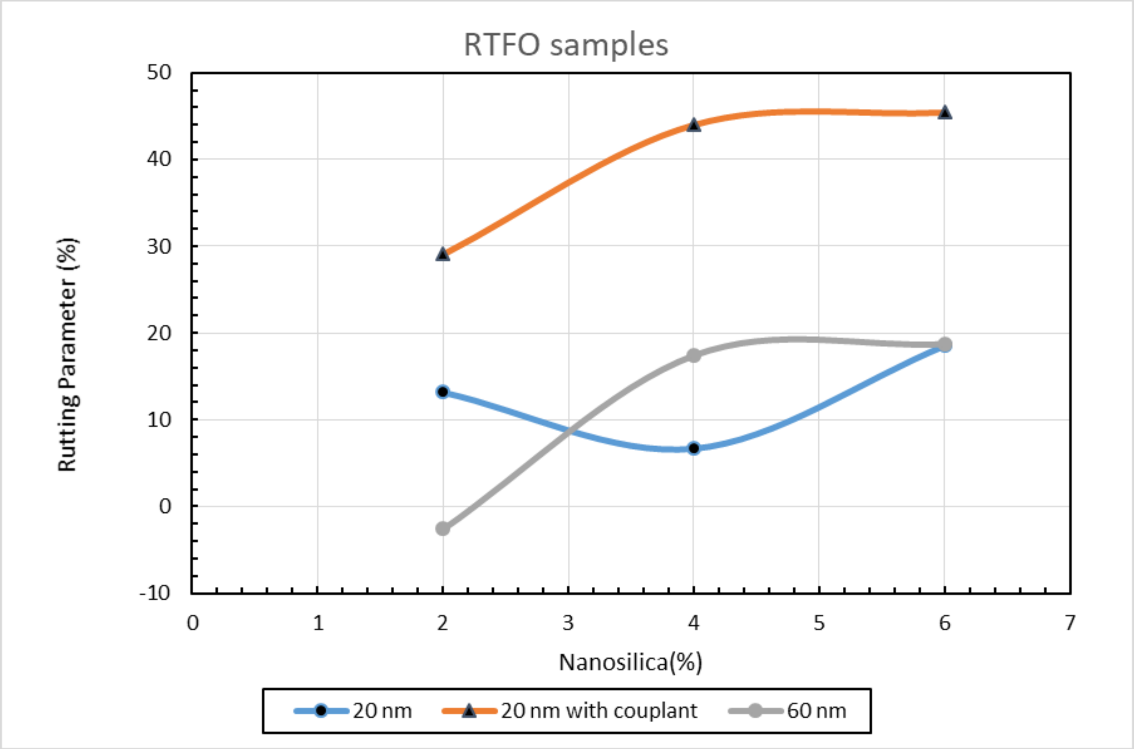

Figure C 16: Fatigue parameter of NS modified C320 over virgin C320 of RTFO samples at 60 °C (f = 10 rad/s).

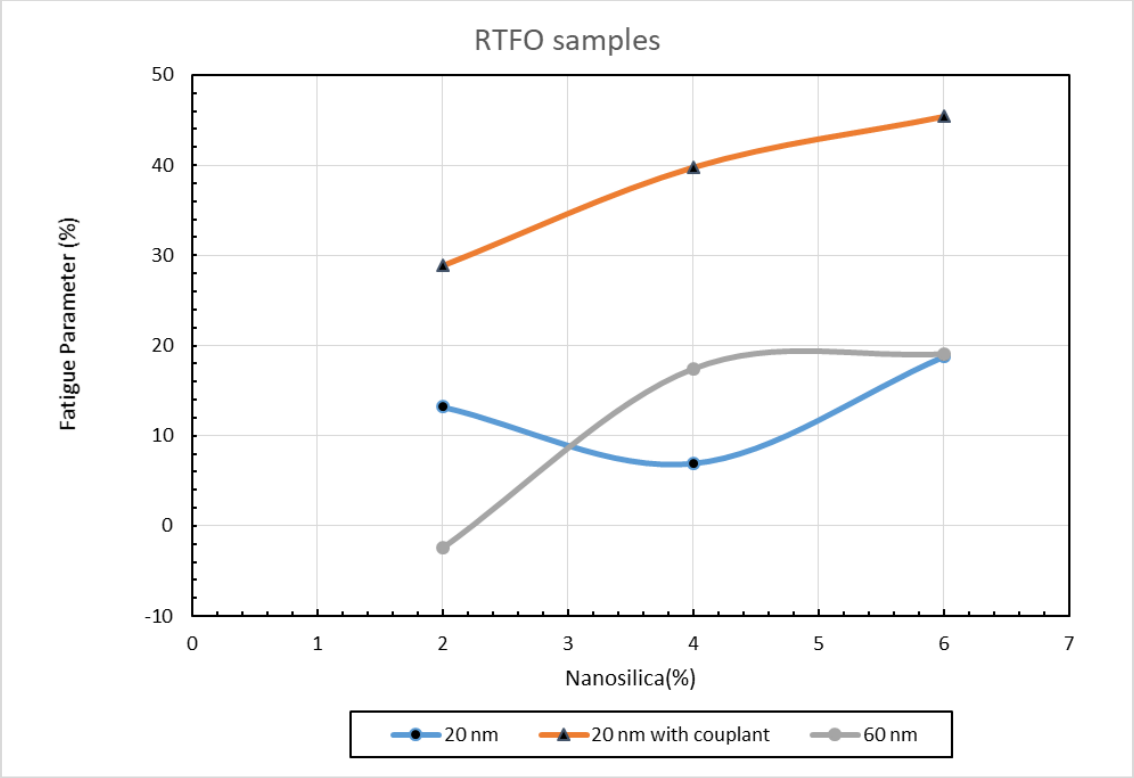

Figure C 17: Complex shear modulus of of PAV samples at 60 °C (f = 10 rad/s).

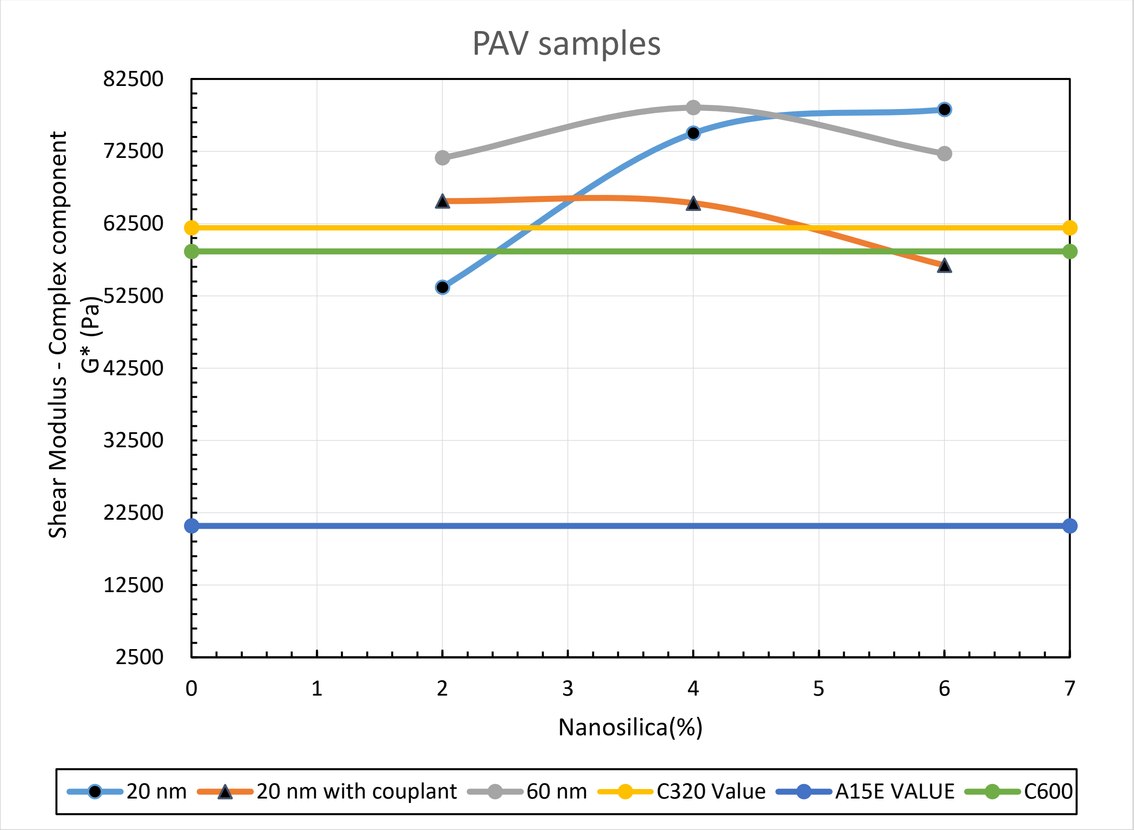

Figure C 18: Shear viscosity of PAV samples at 60 °C (f = 1 rad/s).

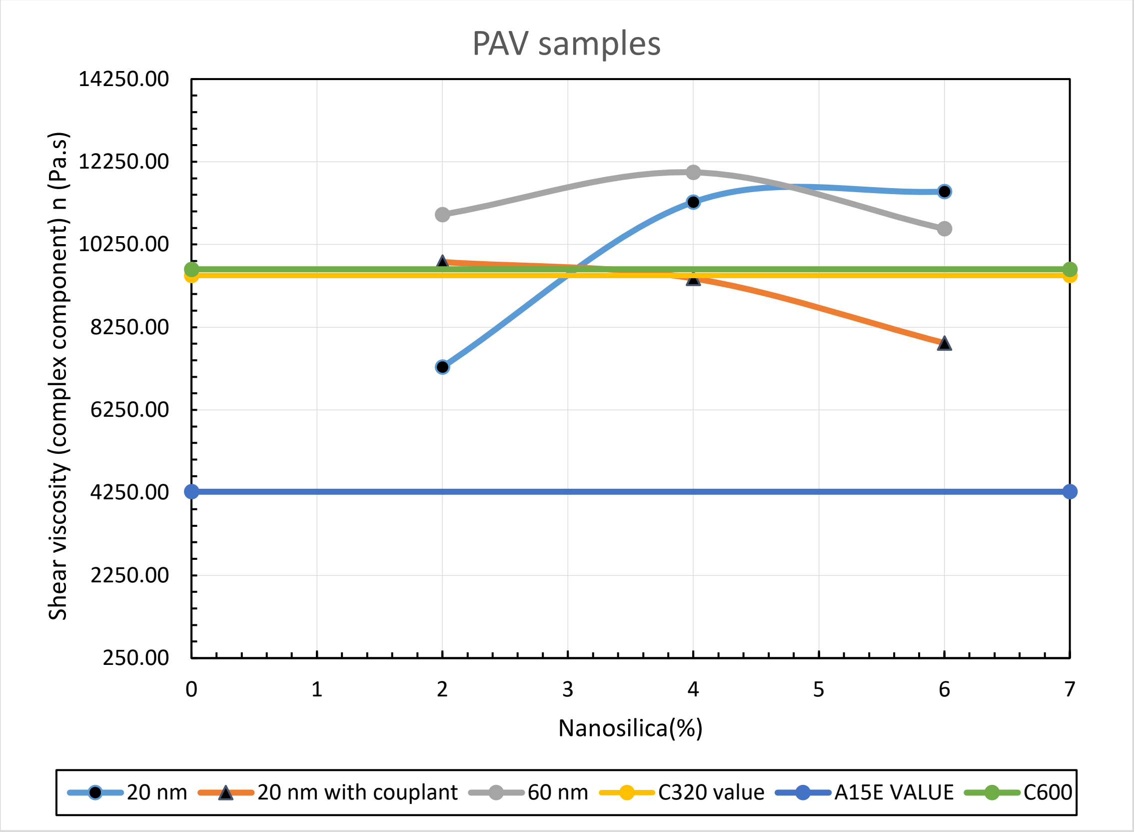

Figure C 19: Complex shear modulus of NS modified C320 over virgin C320 of PAV samples at 60 °C (f = 10 rad/s).

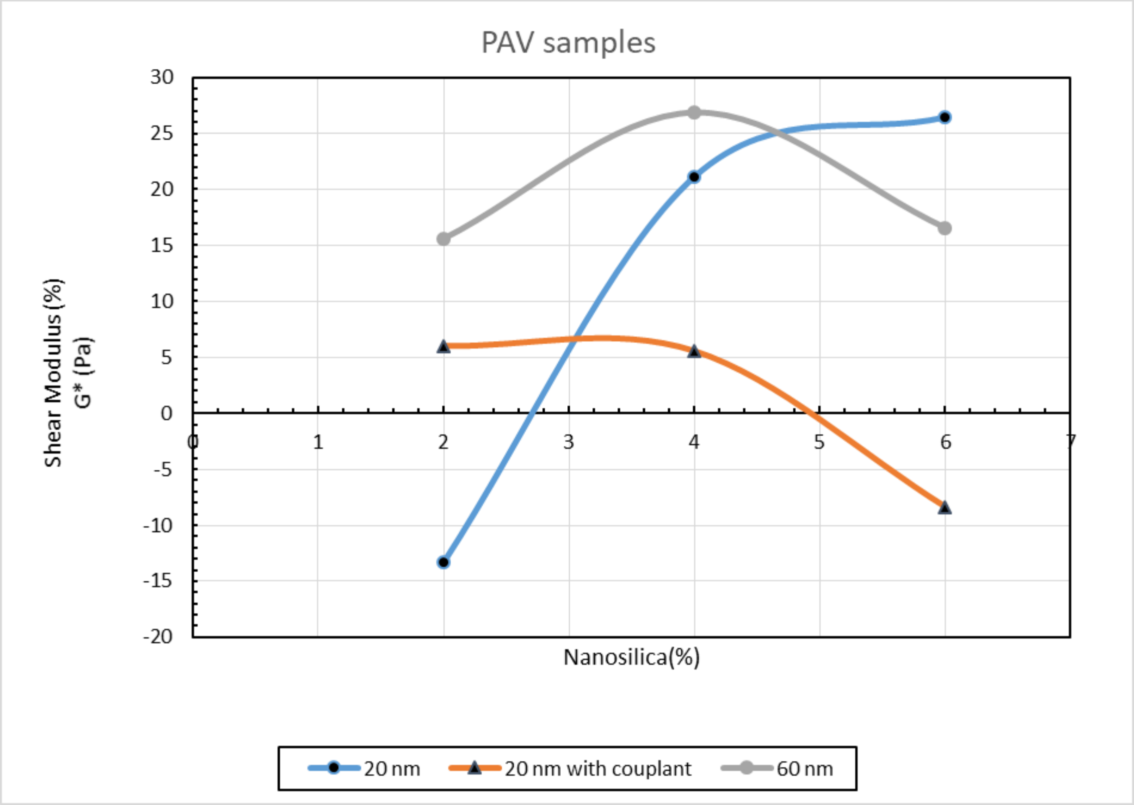

Figure C 20: Shear viscosity of NS modified C320 over virgin C320 of PAV samples at 60 °C (f = 1 rad/s).

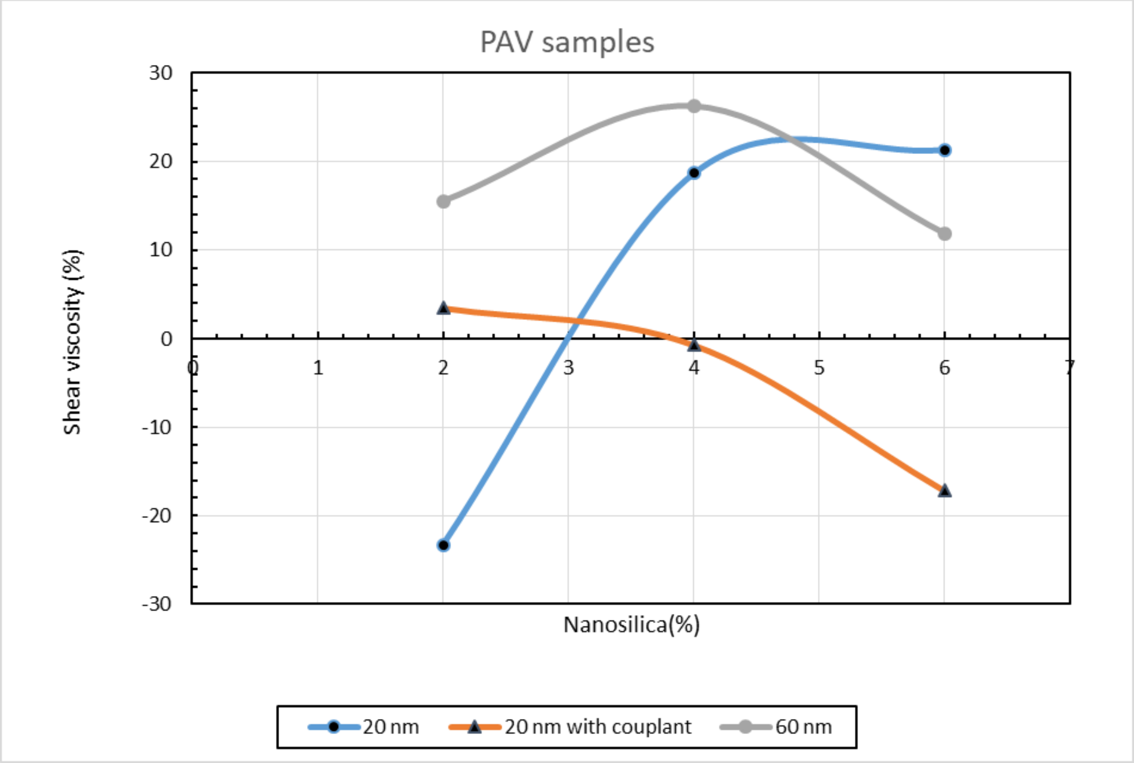

Figure C 21: Rutting parameter of PAV samples at 60 °C (f = 10 rad/s).

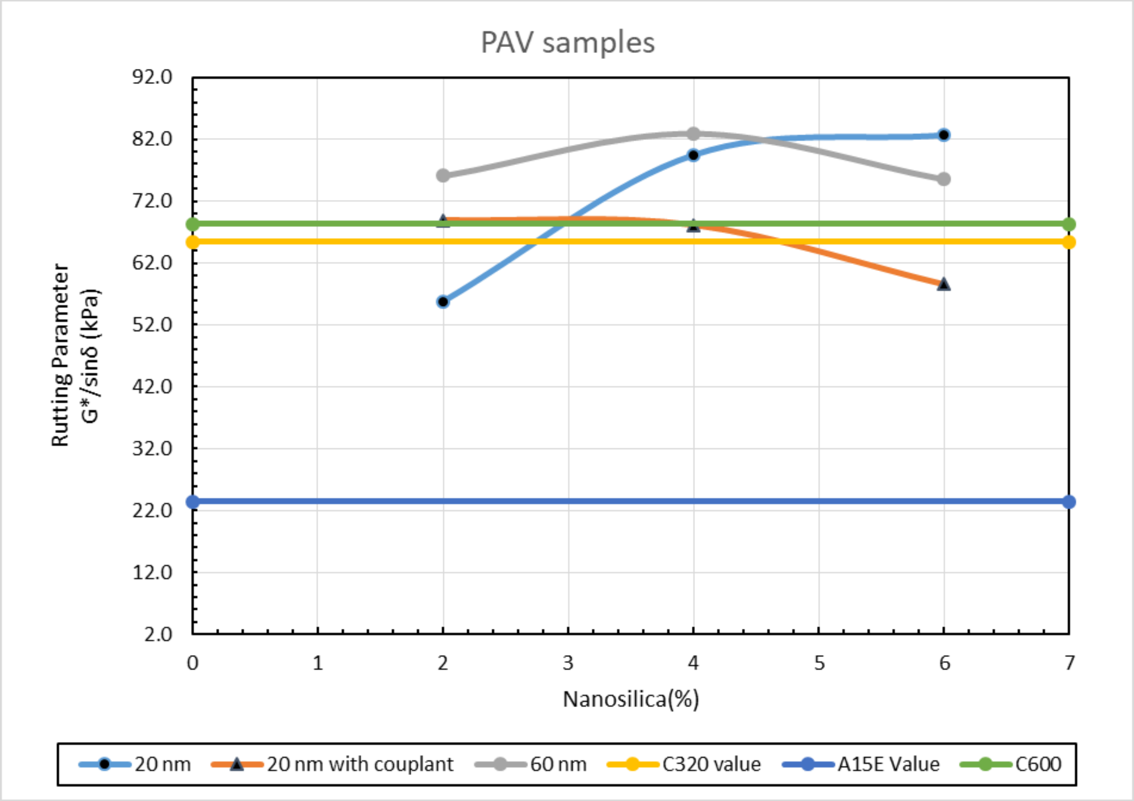

Figure C 22: Fatigue parameter of PAV samples at 60 °C (f = 10 rad/s).

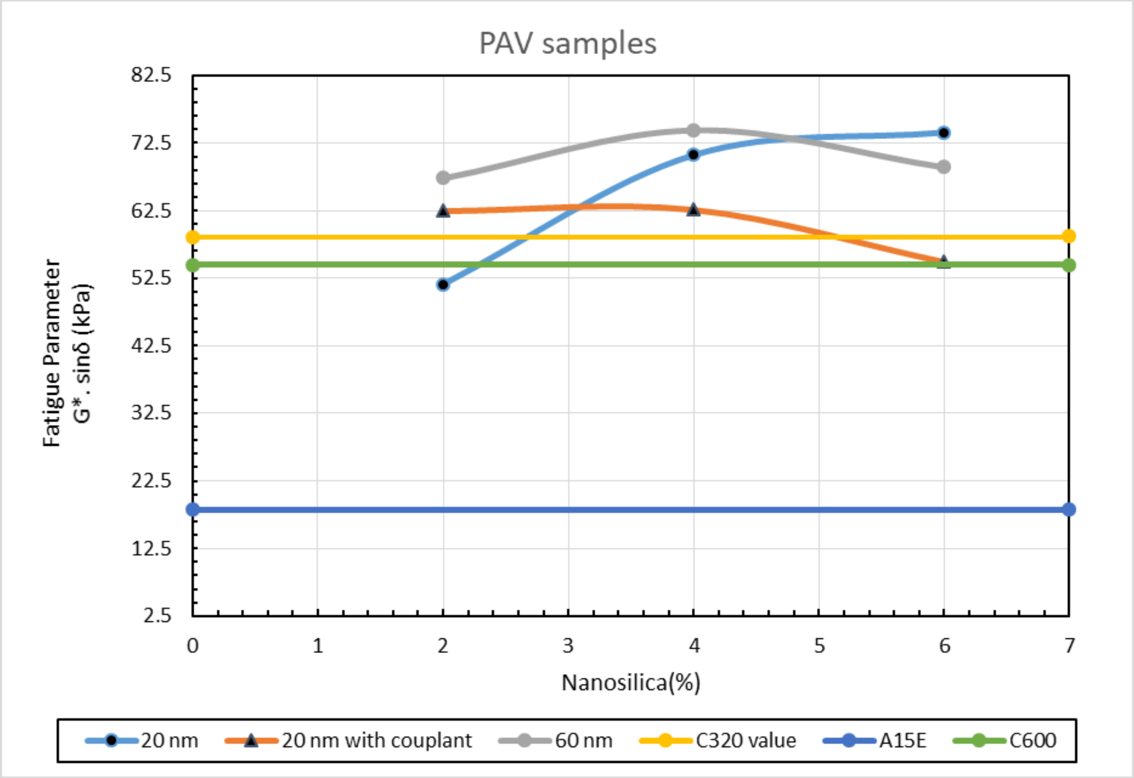

Figure C 23: Rutting parameter of NS modified C320 over virgin C320 of PAV samples at 60 °C (f = 10 rad/s).

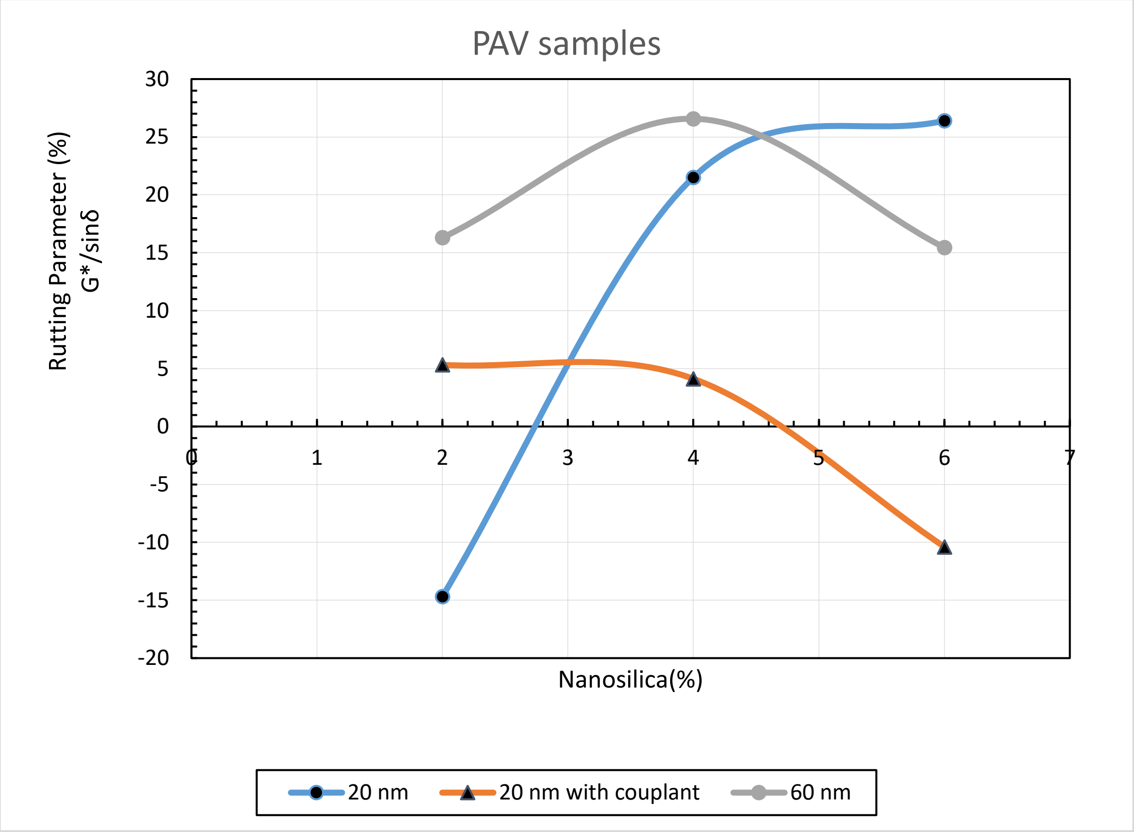

Figure C 24: Fatigue parameter of NS modified C320 over virgin C320 of PAV samples at 60 °C (f = 10 rad/s).

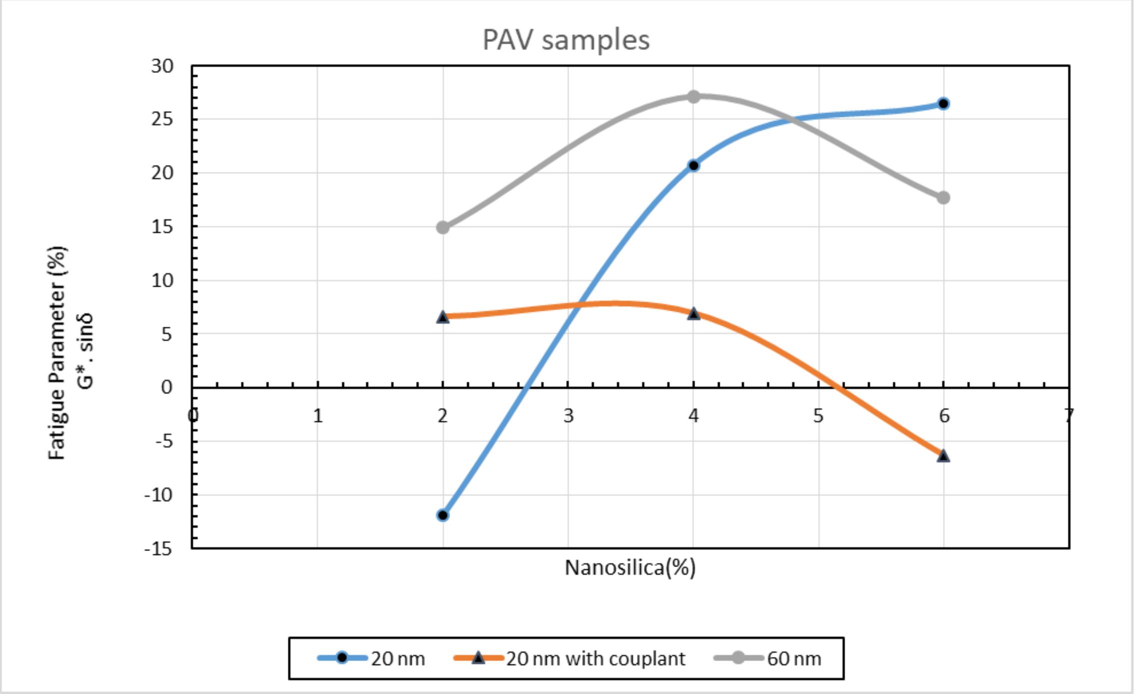

Figure C 25: Complex shear modulus of of wet samples at 60 °C (f = 10 rad/s).

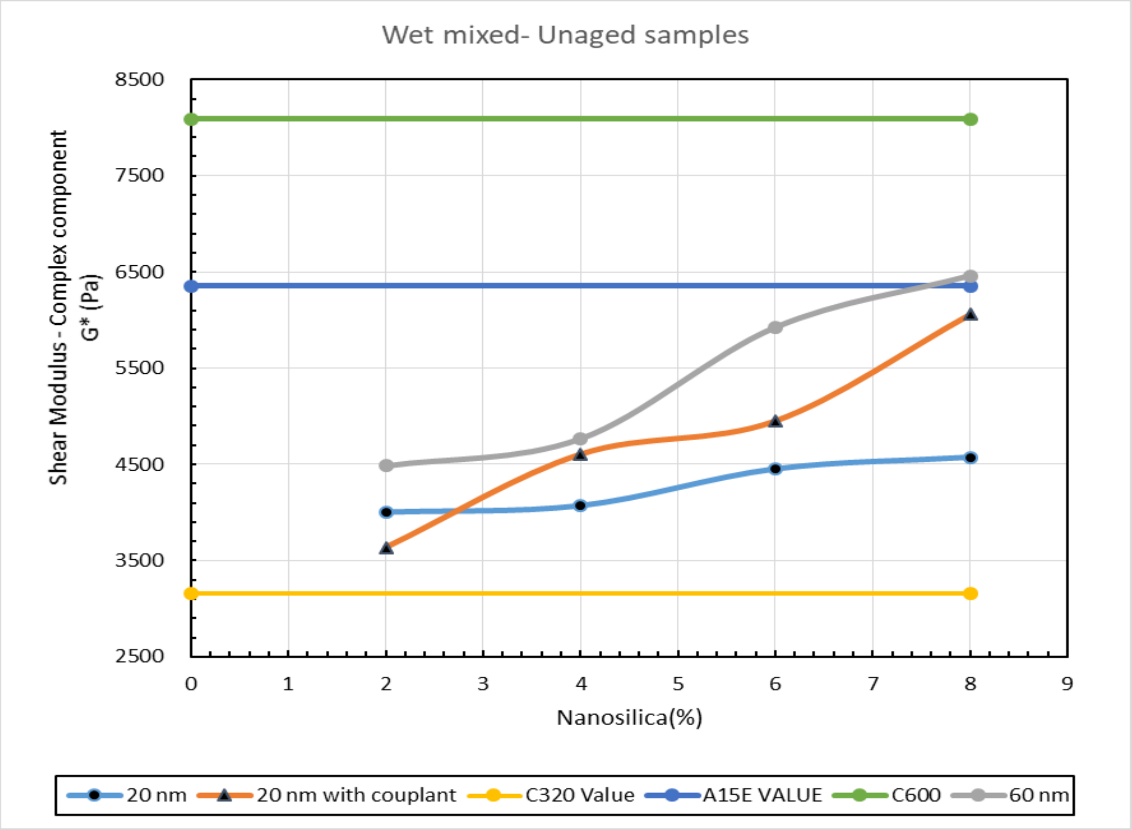

Figure C 26: Shear viscosity of wet samples at 60 °C (f = 1 rad/s).

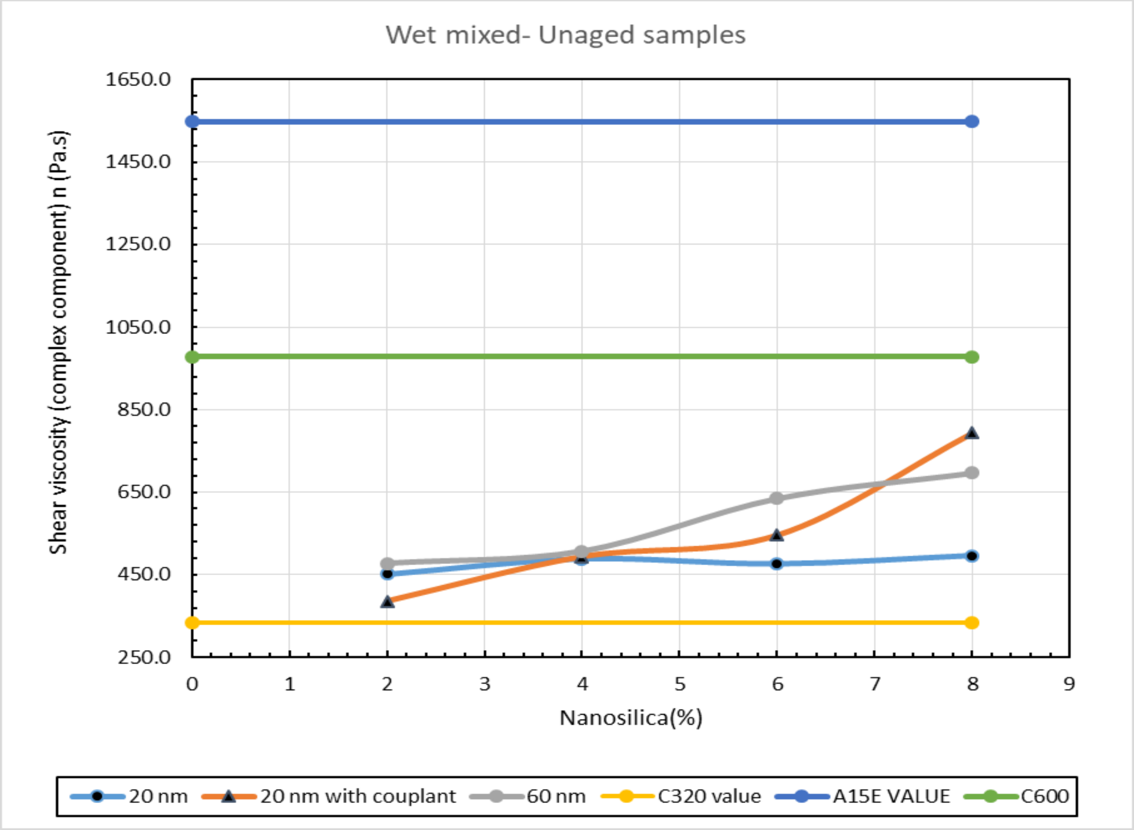

Figure C 27: Complex shear modulus of NS modified C320 over virgin C320 of wet samples at 60 °C (f = 10 rad/s).

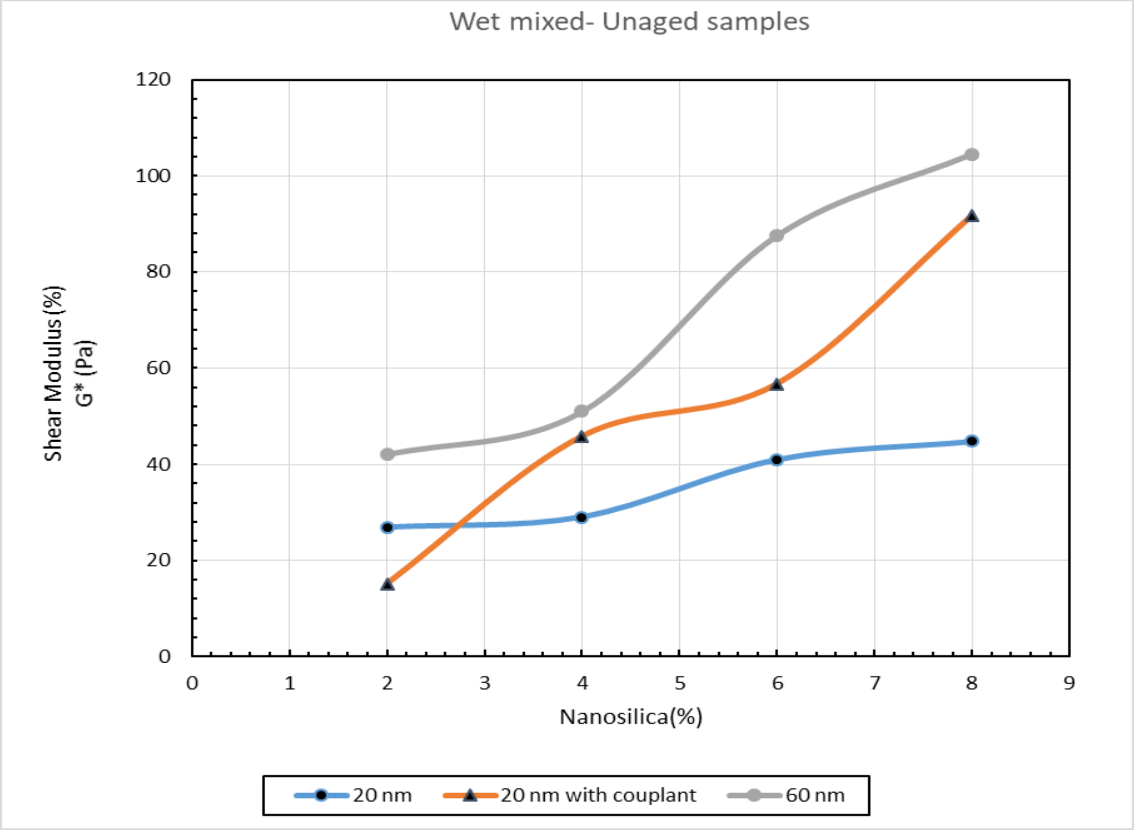

Figure C 28: Shear viscosity of NS modified C320 over virgin C320 of wet samples at 60 °C (f = 1 rad/s).

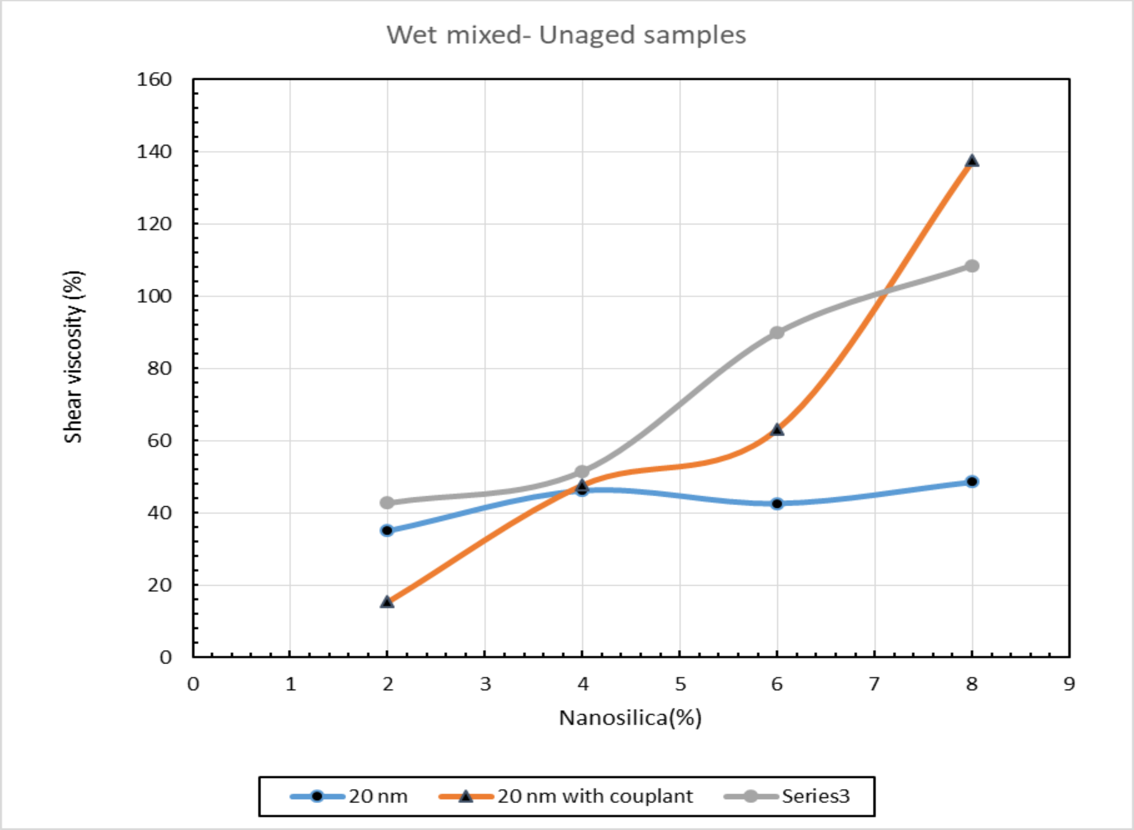

Figure C 29: Rutting parameter of wet samples at 60 °C (f = 10 rad/s).

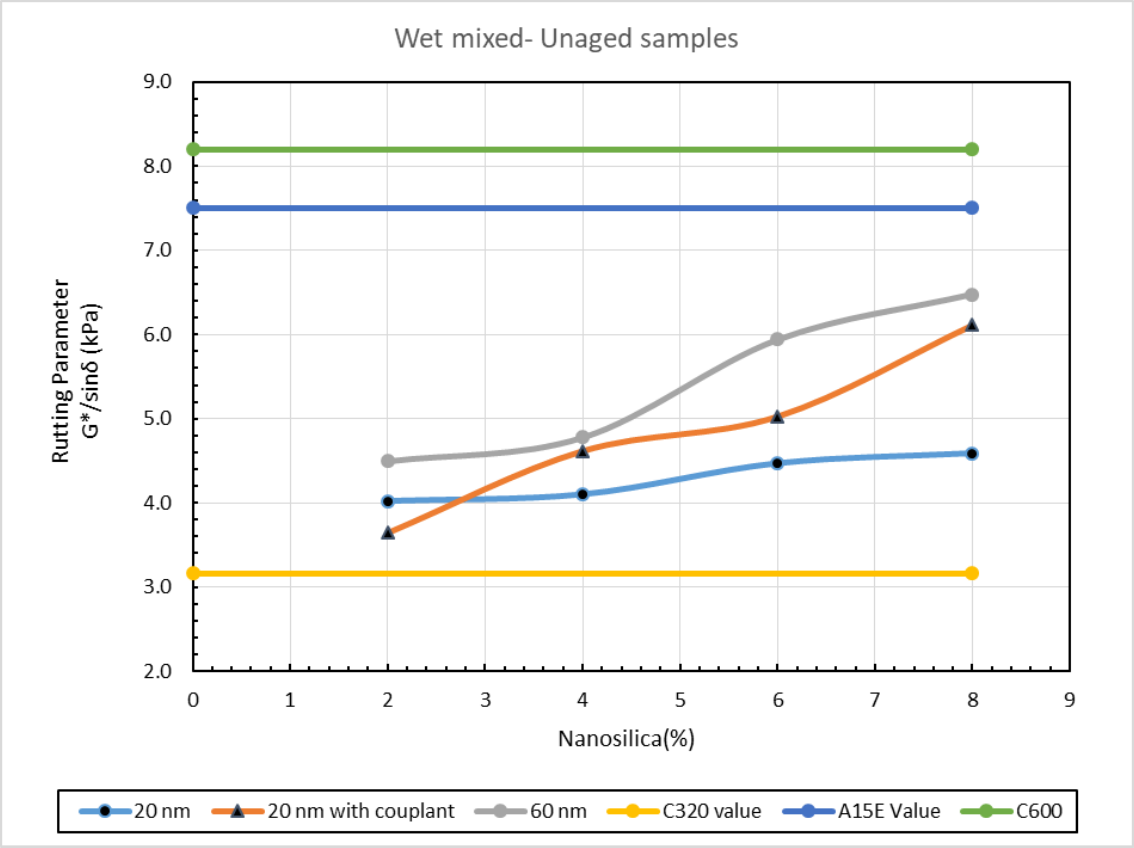

Figure C 30: Fatigue parameter of wet samples at 60 °C (f = 10 rad/s).

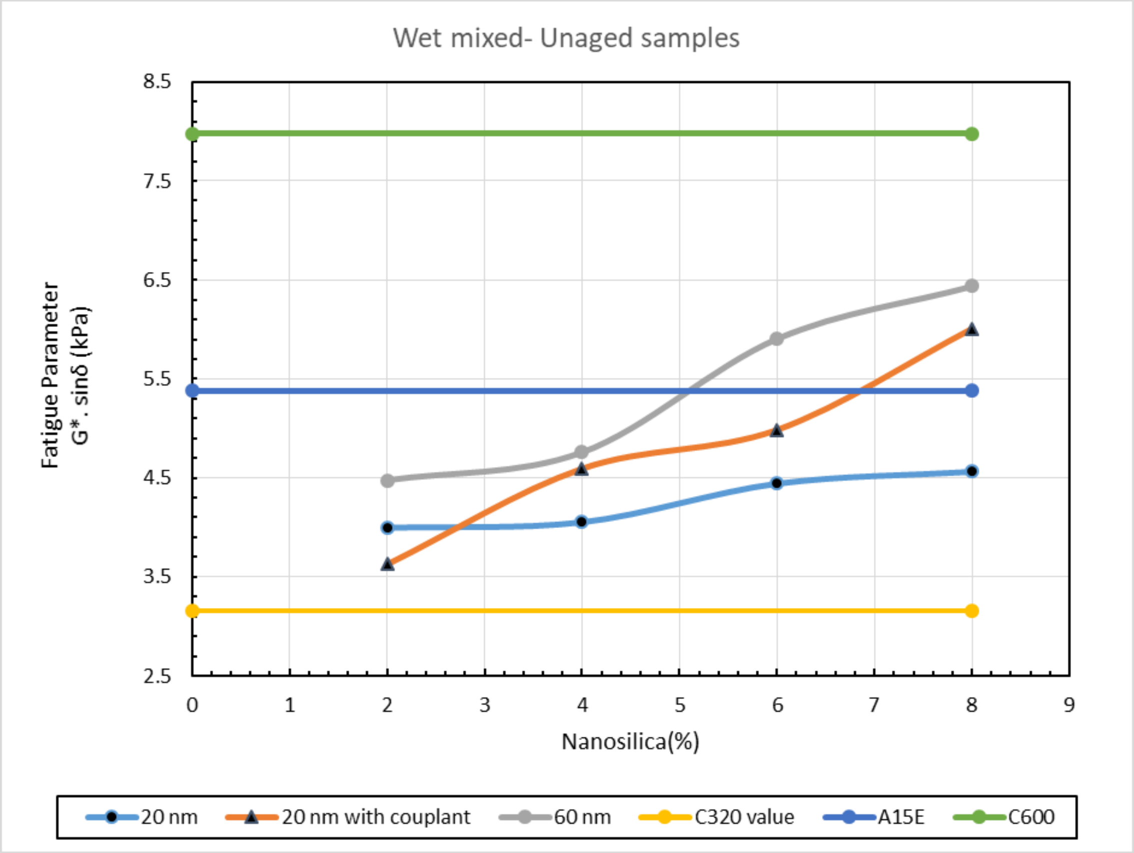

APPENDIX D TYPICAL OUTPUTS FROM MSCR TESTS

Figure D 1: MSCR test at 64 °C for unaged C320: (I) shear strain (II) recoverable strain (III) data

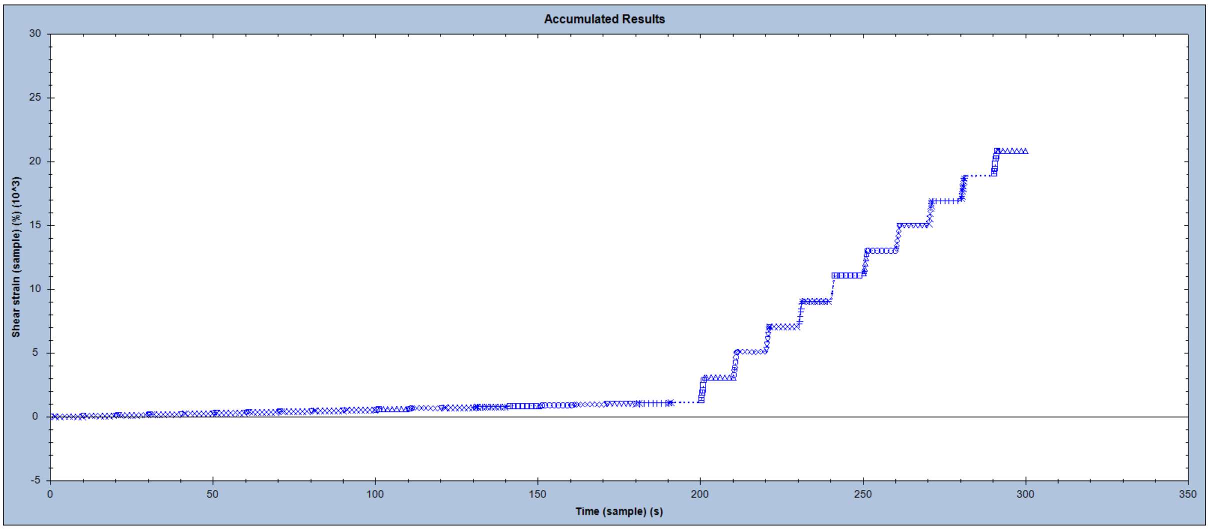

(I)

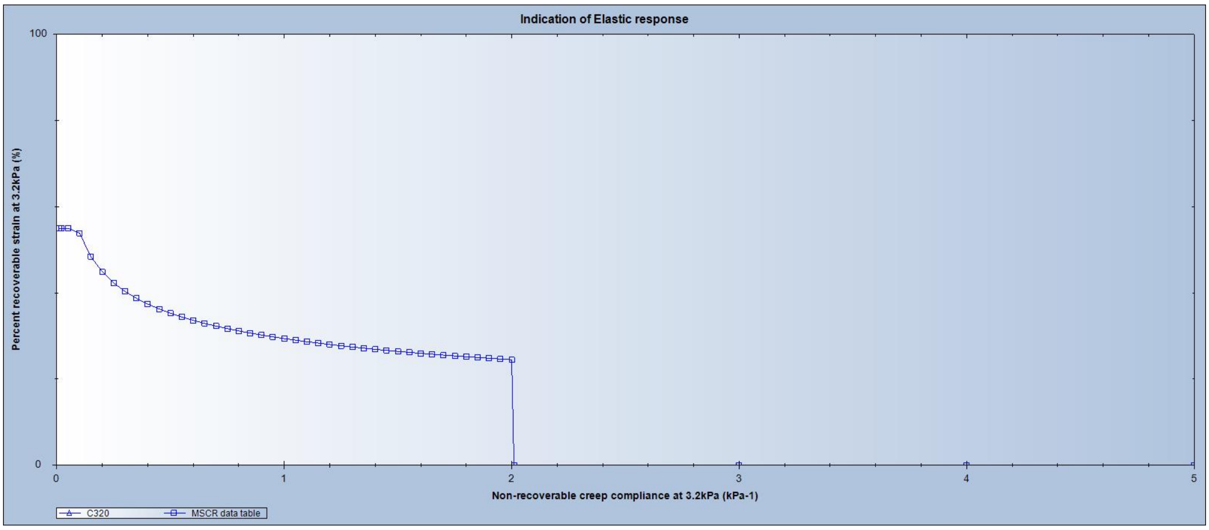

(II)

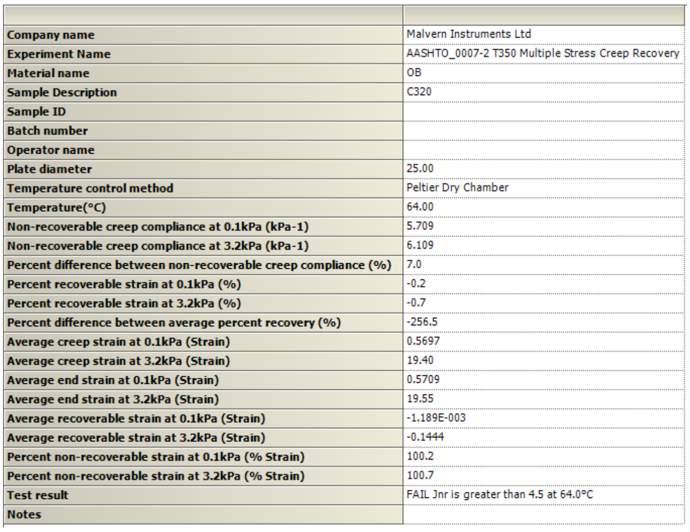

Company name	Malvern Instruments Ltd
Experiment Name	AASHTO_0007-2 T350 Multiple Stress Creep Recovery
Material name	OB
Sample Description	C320
Sample ID	
Batch number	
Operator name	
Plate diameter	25.00
Temperature control method	Peltier Dry Chamber
Temperature(°C)	64.00
Non-recoverable creep compliance at 0.1kPa (kPa-1)	5.709
Non-recoverable creep compliance at 3.2kPa (kPa-1)	6.109
Percent difference between non-recoverable creep compliance (%)	7.0
Percent recoverable strain at 0.1kPa (%)	-0.2
Percent recoverable strain at 3.2kPa (%)	-0.7
Percent difference between average percent recovery (%)	-256.5
Average creep strain at 0.1kPa (Strain)	0.5697
Average creep strain at 3.2kPa (Strain)	19.40
Average end strain at 0.1kPa (Strain)	0.5709
Average end strain at 3.2kPa (Strain)	19.55
Average recoverable strain at 0.1kPa (Strain)	-1.189E-003
Average recoverable strain at 3.2kPa (Strain)	-0.1444
Percent non-recoverable strain at 0.1kPa (% Strain)	100.2
Percent non-recoverable strain at 3.2kPa (% Strain)	100.7
Test result	FAIL Jnr is greater than 4.5 at 64.0°C
Notes	

(III)

Figure D 2: MSCR test at 64 °C for RTFO C320: (I) Accumulated Shear Strain (II) Data

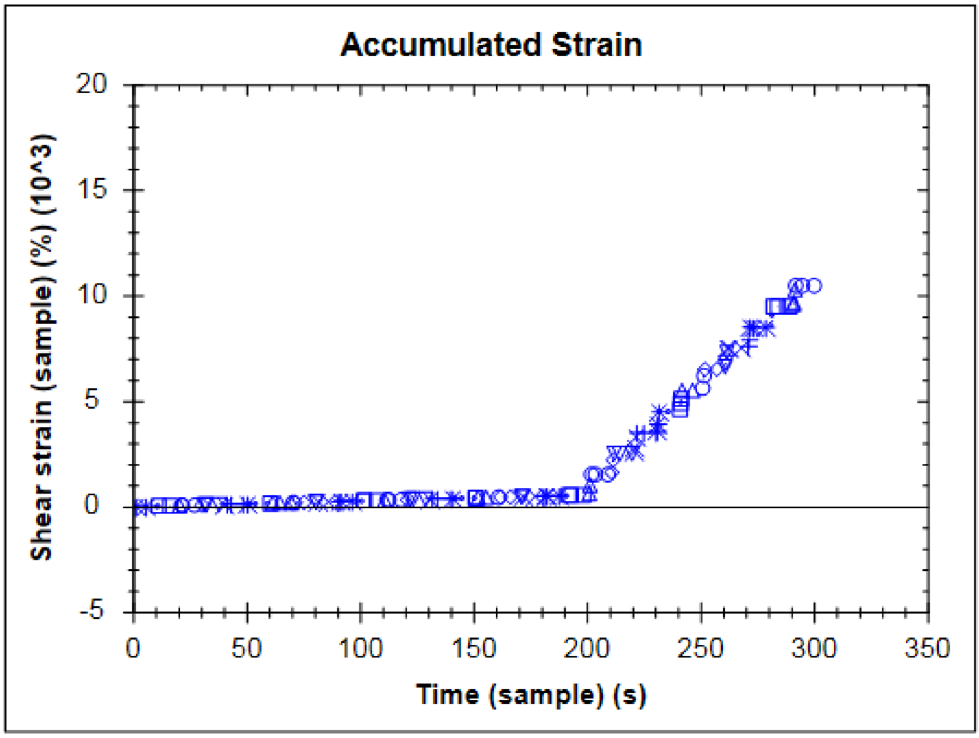

(I)

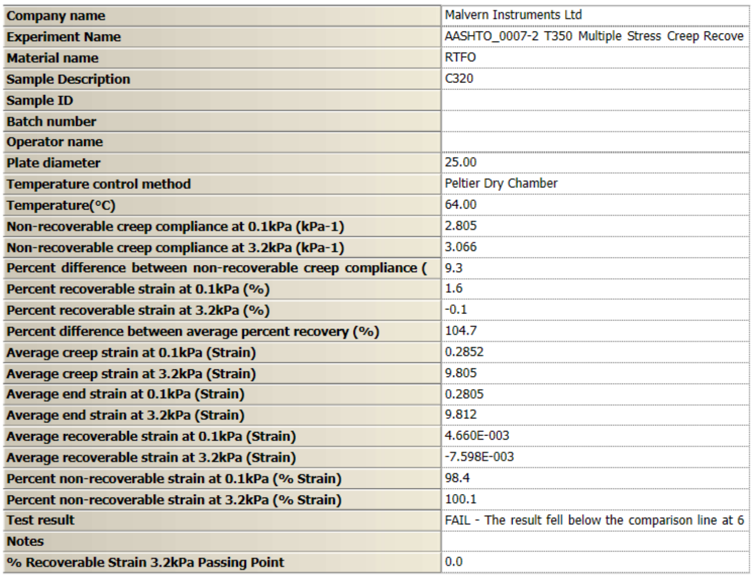

Company name	Malvern Instruments Ltd
Experiment Name	AASHTO_0007-2 T350 Multiple Stress Creep Recove
Material name	RTFO
Sample Description	C320
Sample ID	
Batch number	
Operator name	
Plate diameter	25.00
Temperature control method	Peltier Dry Chamber
Temperature(°C)	64.00
Non-recoverable creep compliance at 0.1kPa (kPa-1)	2.805
Non-recoverable creep compliance at 3.2kPa (kPa-1)	3.066
Percent difference between non-recoverable creep compliance (	9.3
Percent recoverable strain at 0.1kPa (%)	1.6
Percent recoverable strain at 3.2kPa (%)	-0.1
Percent difference between average percent recovery (%)	104.7
Average creep strain at 0.1kPa (Strain)	0.2852
Average creep strain at 3.2kPa (Strain)	9.805
Average end strain at 0.1kPa (Strain)	0.2805
Average end strain at 3.2kPa (Strain)	9.812
Average recoverable strain at 0.1kPa (Strain)	4.660E-003
Average recoverable strain at 3.2kPa (Strain)	-7.598E-003
Percent non-recoverable strain at 0.1kPa (% Strain)	98.4
Percent non-recoverable strain at 3.2kPa (% Strain)	100.1
Test result	FAIL - The result fell below the comparison line at 6
Notes	
% Recoverable Strain 3.2kPa Passing Point	0.0

(II)

APPENDIX E BLACK DIAGRAMS

Figure E 1: Black diagram for sample 20BRD2 in unaged, RTFO and PAV aged conditions

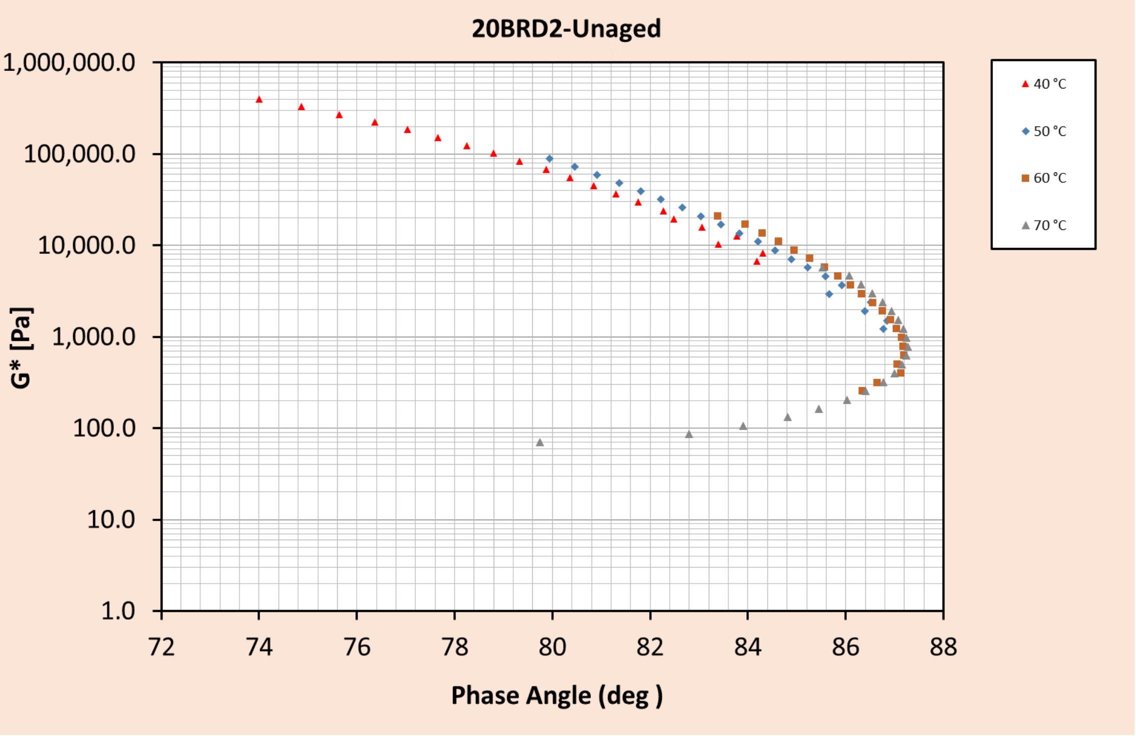

(I)

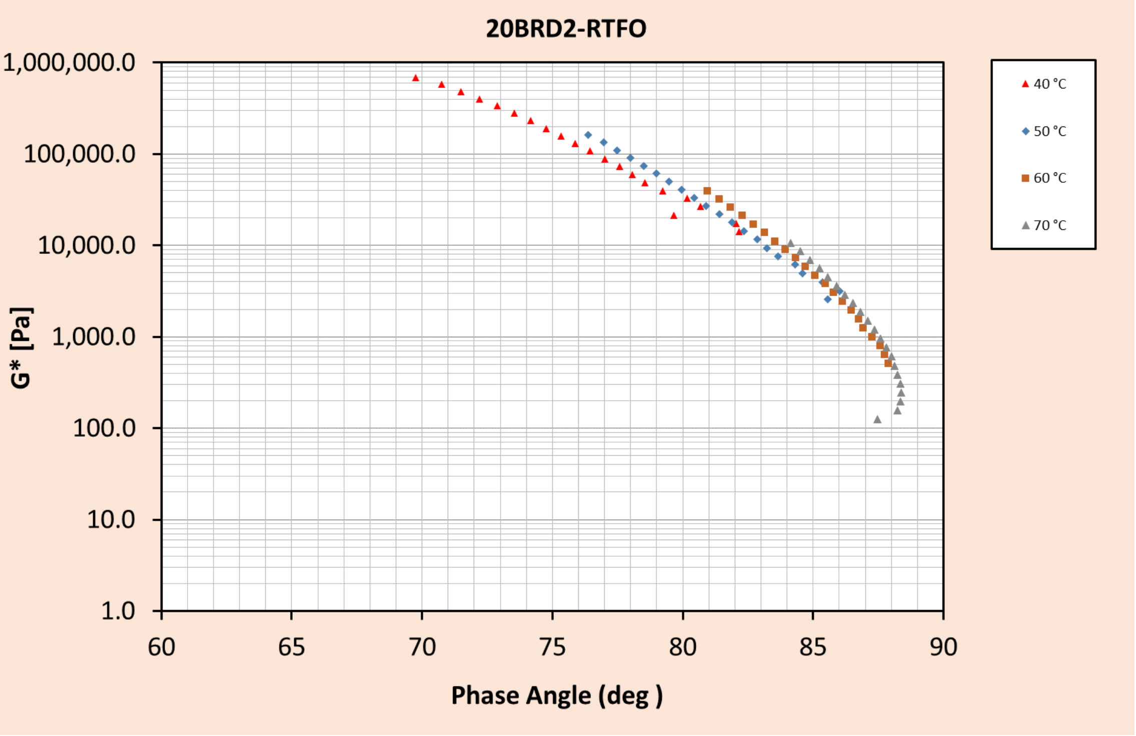

(II)

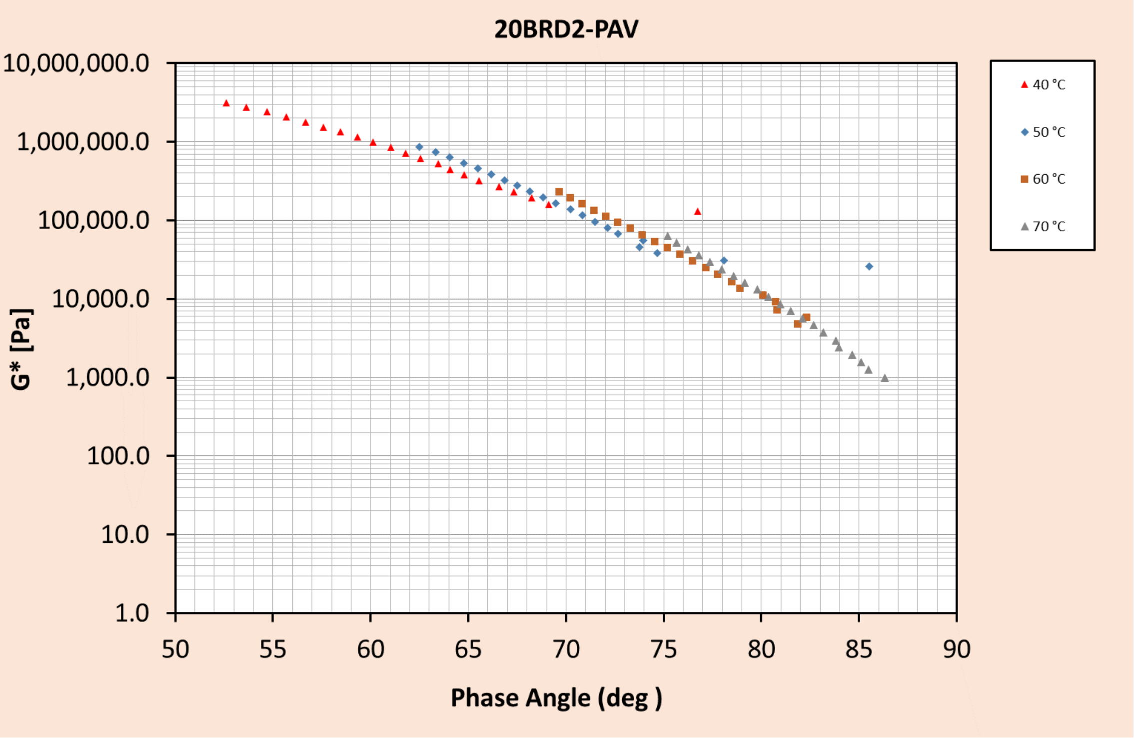

(III)

Figure E 2: Black diagram for Sample 20BRD4 in unaged, RTFOT and PAV aged conditions

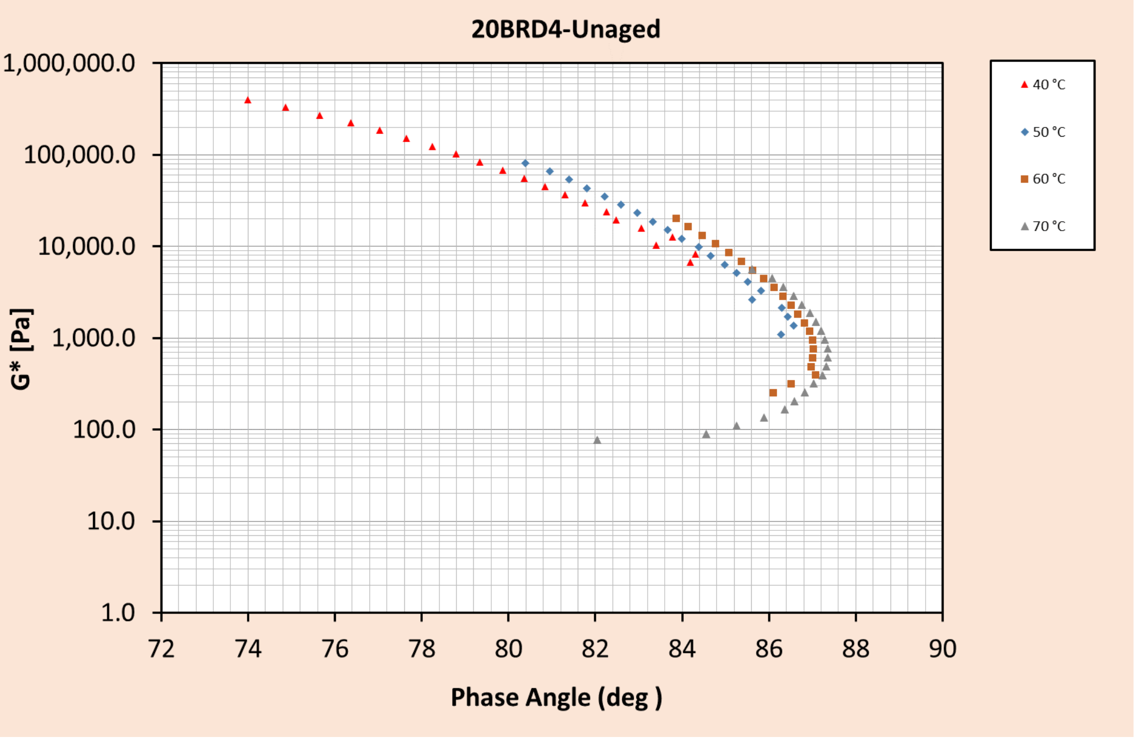

(I)

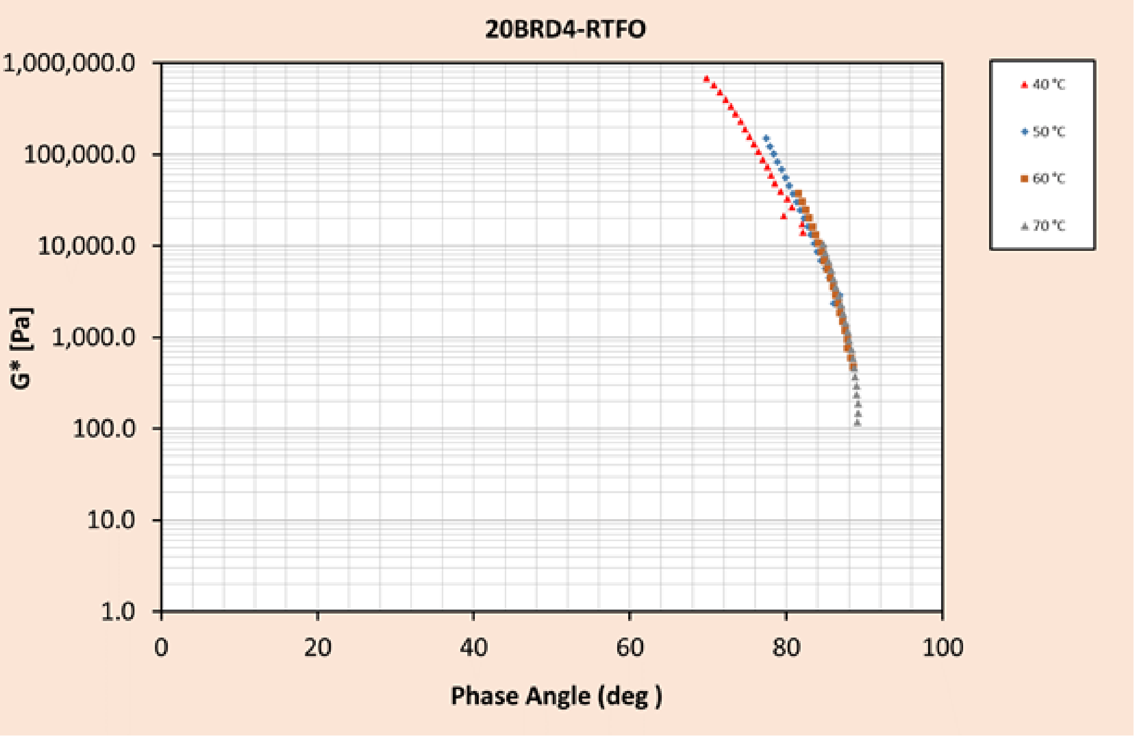
20BRD4-RTFO
G* [Pa]
1,000,000.0
100,000.0
10,000.0
1,000.0
100.0
10.0
1.0
0
20
40
60
80
100
Phase Angle (deg)
40 °C
50 °C
60 °C
70 °C

(II)

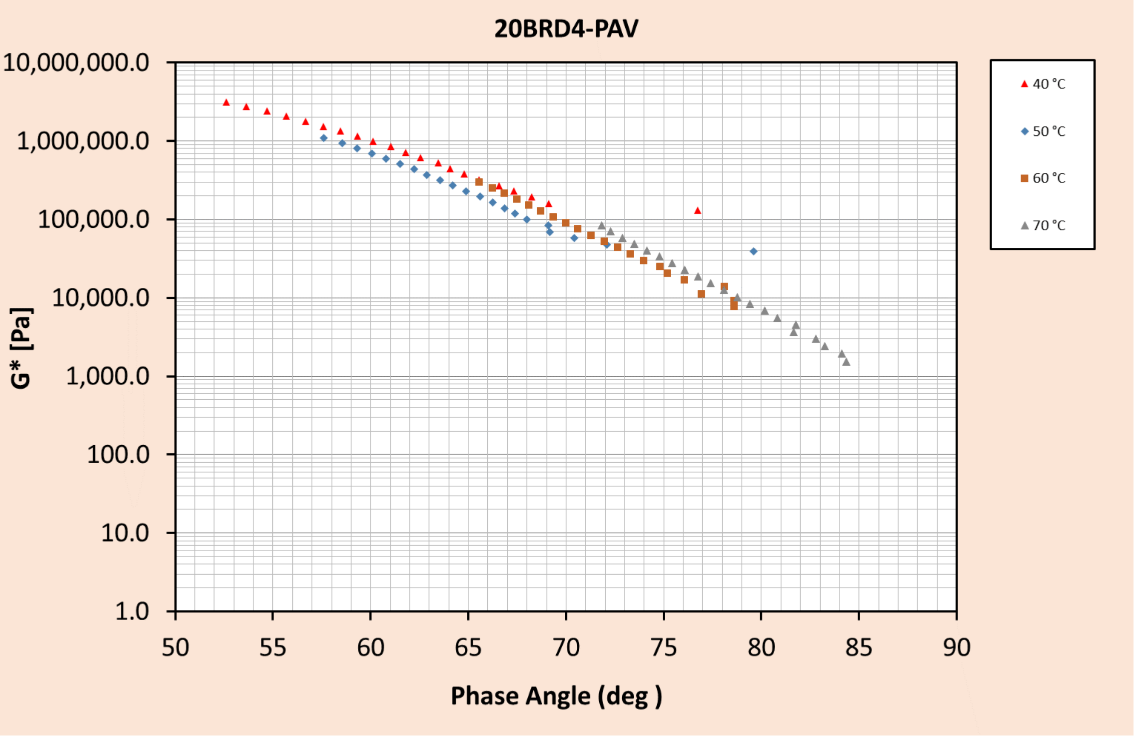
20BRD4-PAV
G* [Pa]
10,000,000.0
1,000,000.0
100,000.0
10,000.0
1,000.0
100.0
10.0
1.0
50
55
60
65
70
75
80
85
90
Phase Angle (deg)
40 °C
50 °C
60 °C
70 °C

(III)

Figure E 3: Black diagram for Sample 20BRD6 in unaged, RTFOT and PAV aged conditions

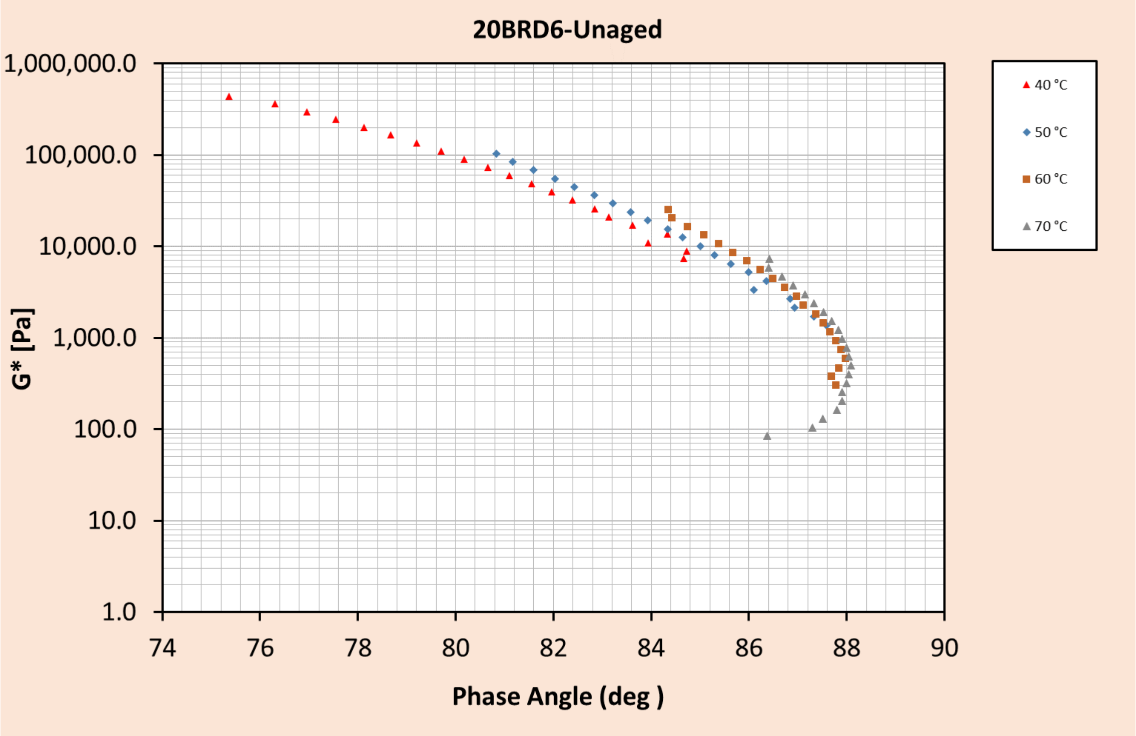

(I)

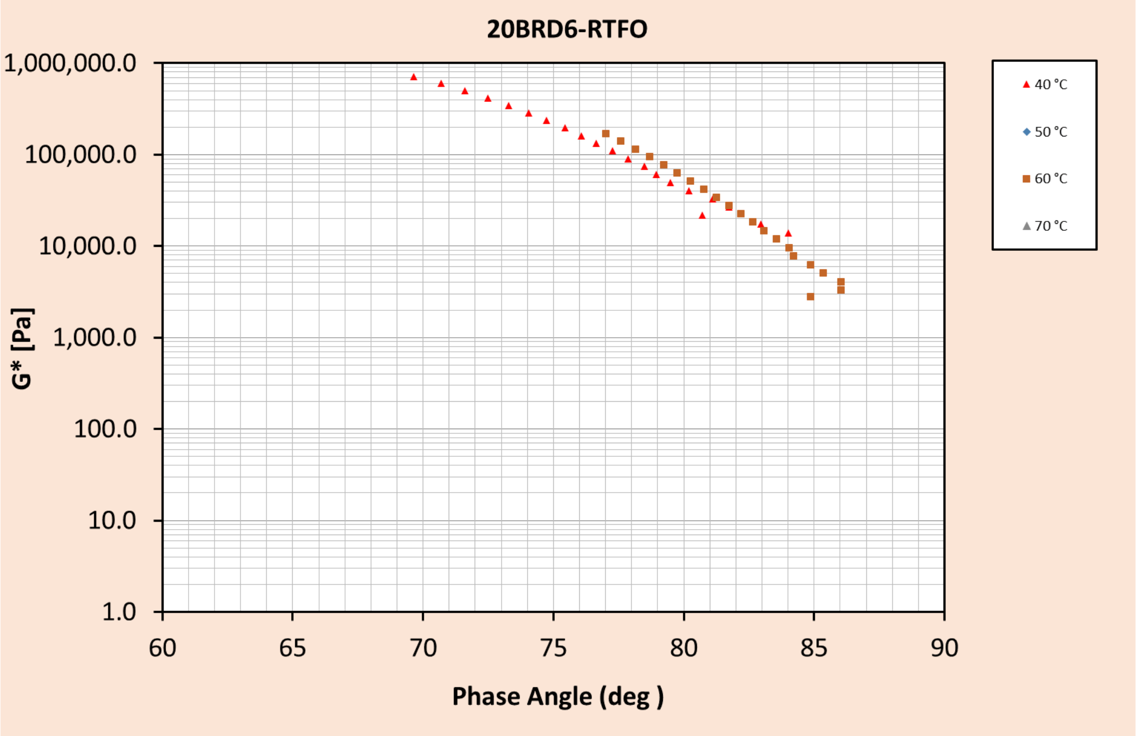

(II)

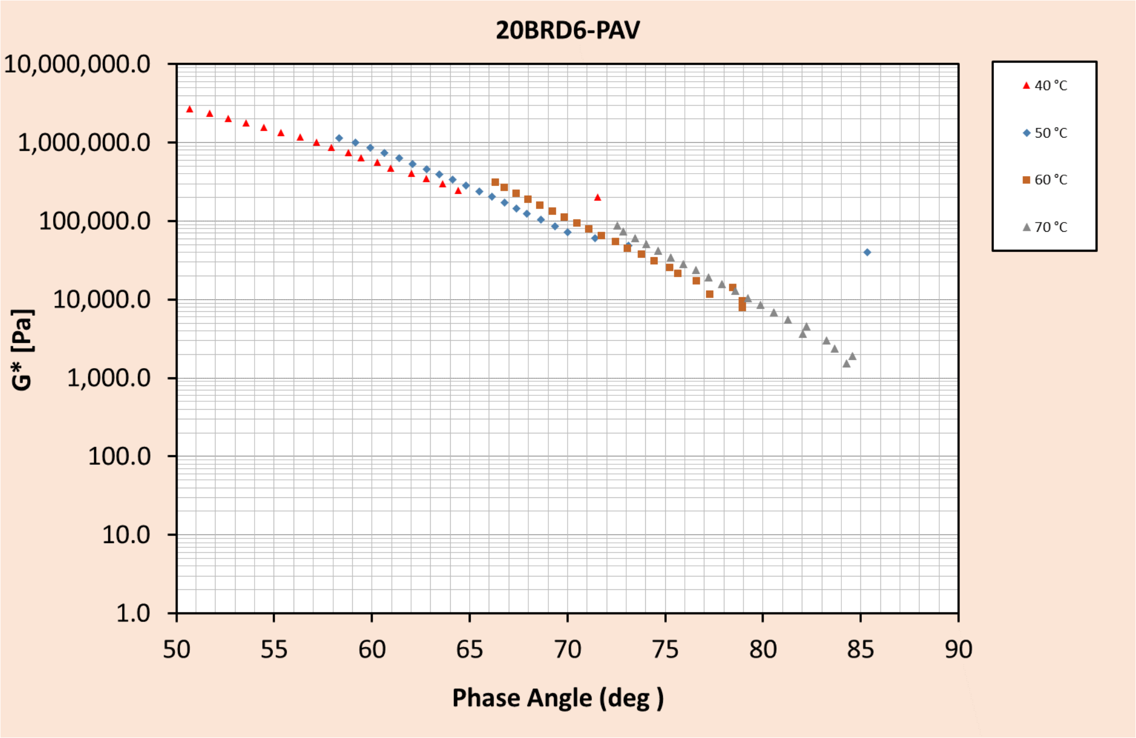

(III)

Figure E 4: Black diagram for Sample 60BRD2 in unaged, RTFOT and PAV aged conditions

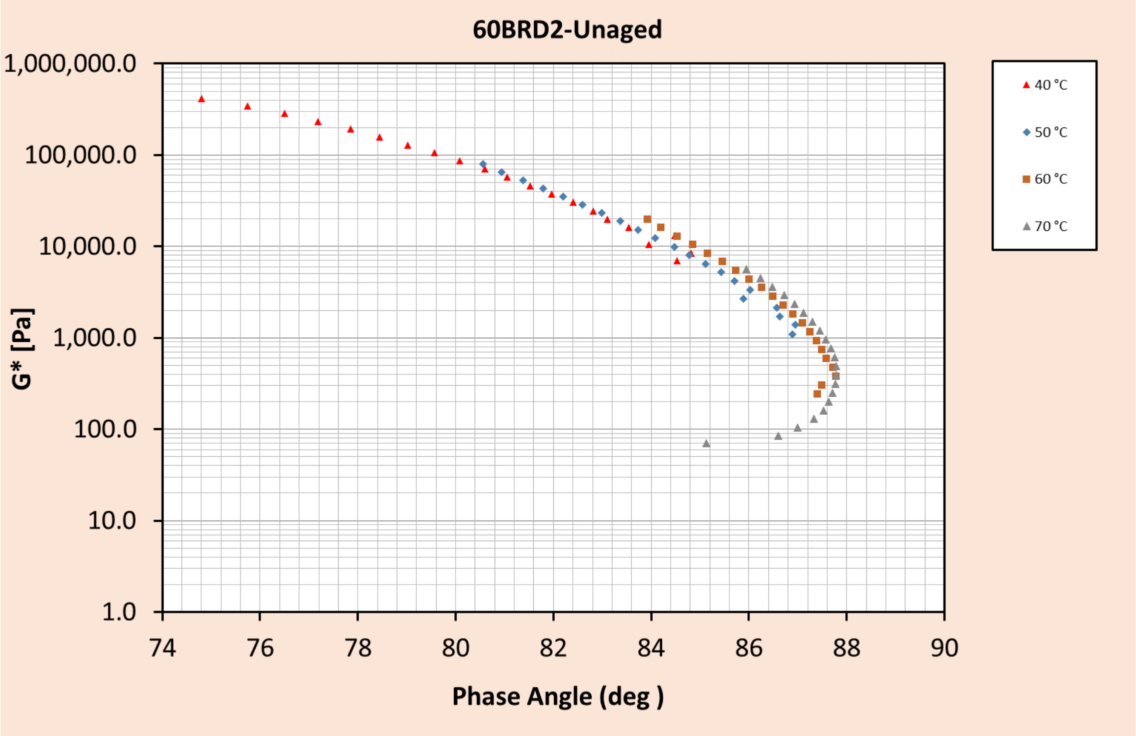

(I)

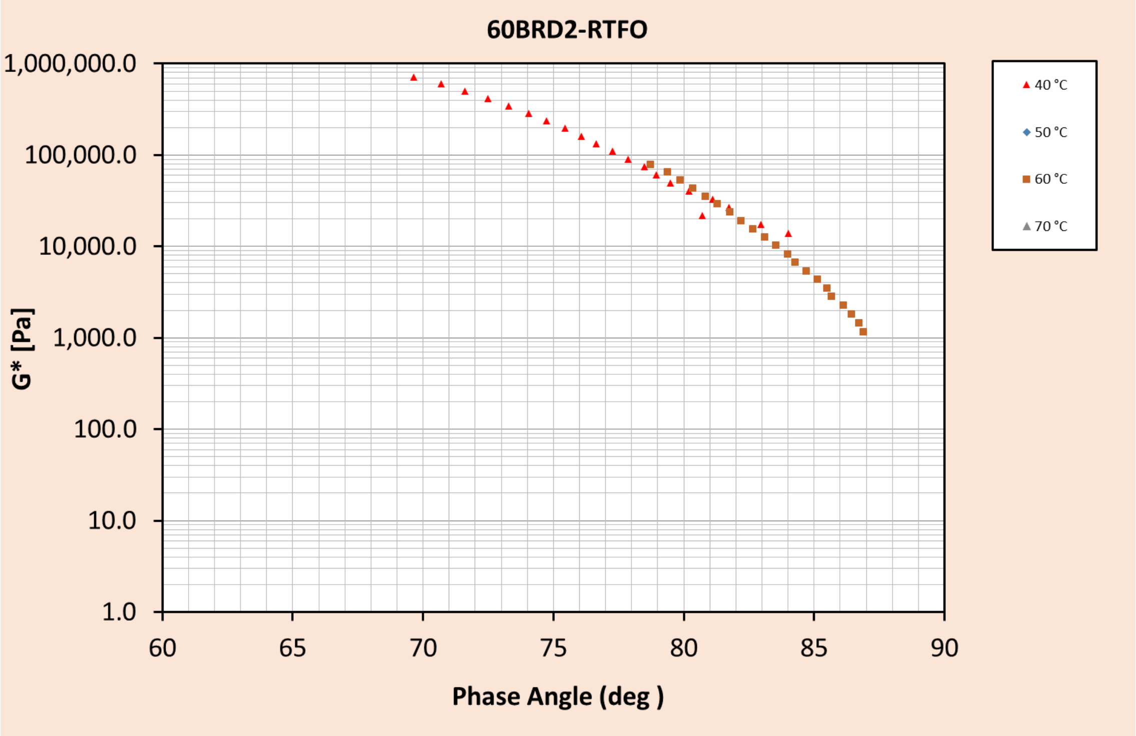
60BRD2-RTFO
1,000,000.0
100,000.0
10,000.0
1,000.0
100.0
10.0
1.0
G* [Pa]
60
65
70
75
80
85
90
Phase Angle (deg)
40 °C
50 °C
60 °C
70 °C

(II)

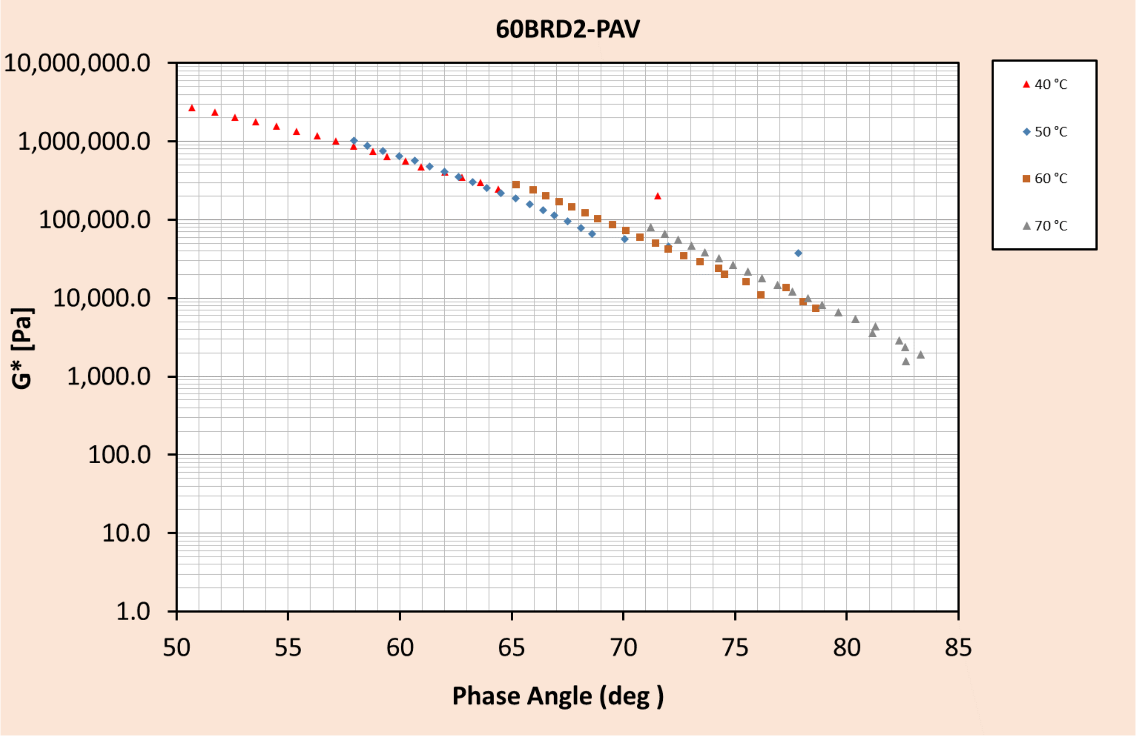
60BRD2-PAV
10,000,000.0
1,000,000.0
100,000.0
10,000.0
1,000.0
100.0
10.0
1.0
G* [Pa]
50
55
60
65
70
75
80
85
Phase Angle (deg)
40 °C
50 °C
60 °C
70 °C

(III)

Figure E 5: Black diagram for Sample 60BRD4 in unaged, RTFOT and PAV aged conditions

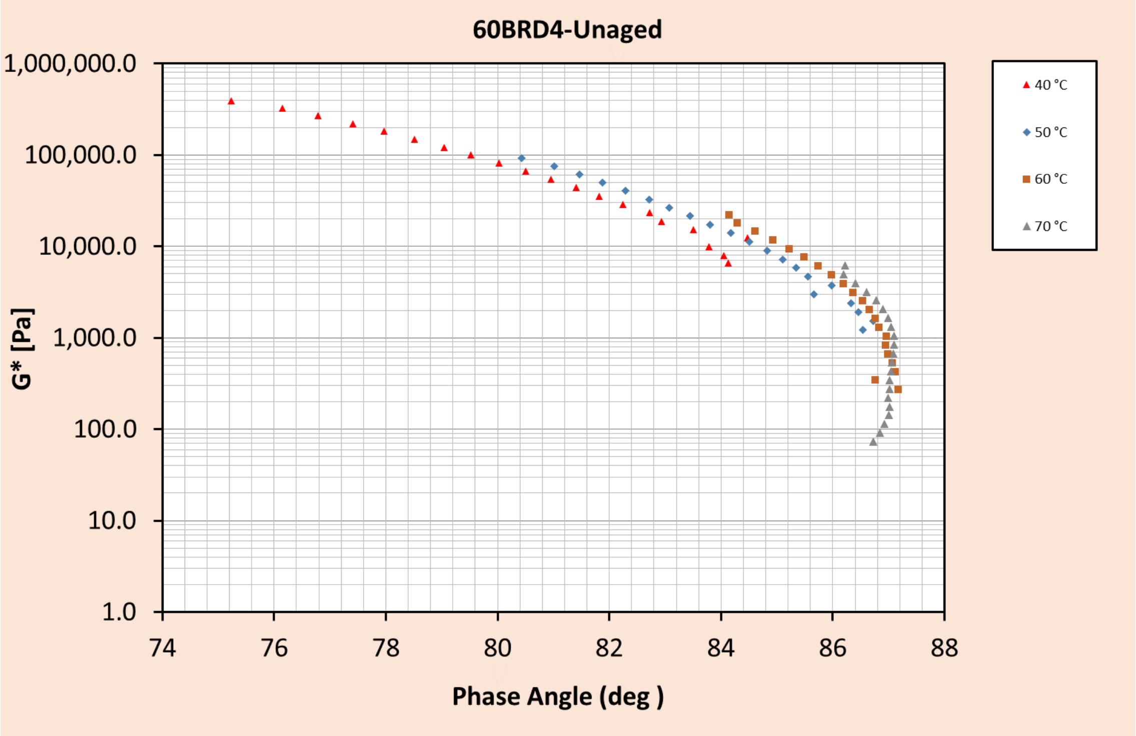

(I)

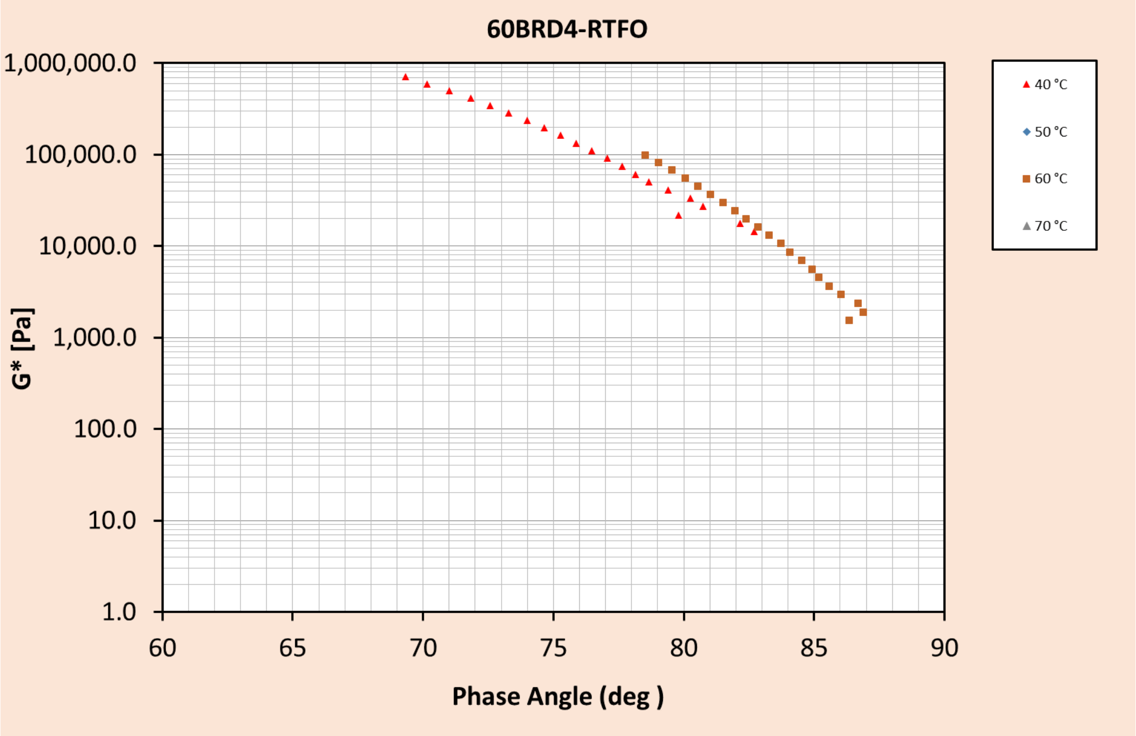

(II)

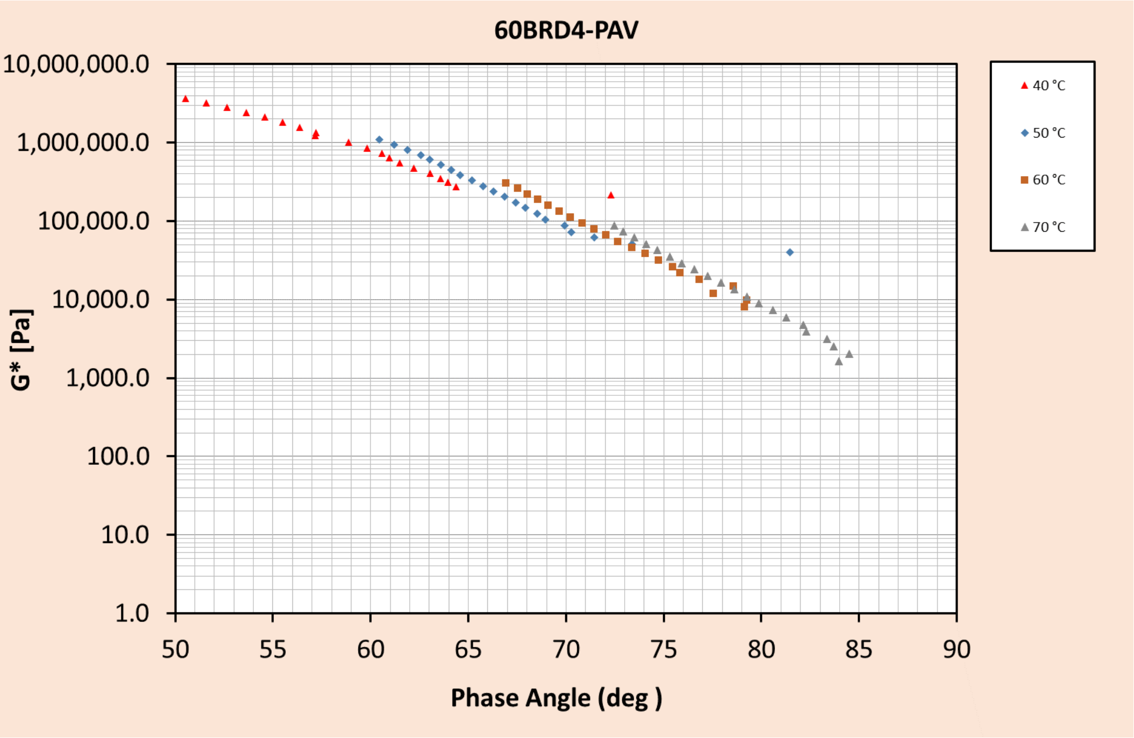

(III)

Figure E 6: Black diagram for Sample 60BRD6 in unaged, RTFOT and PAV aged conditions

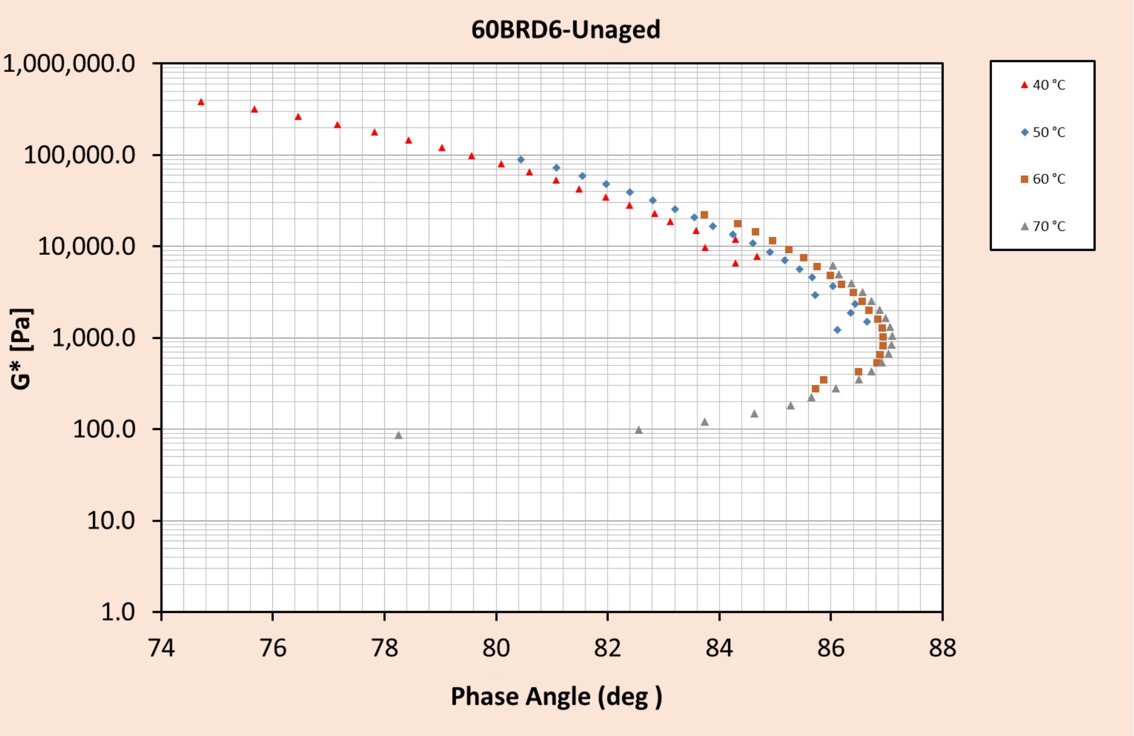

(I)

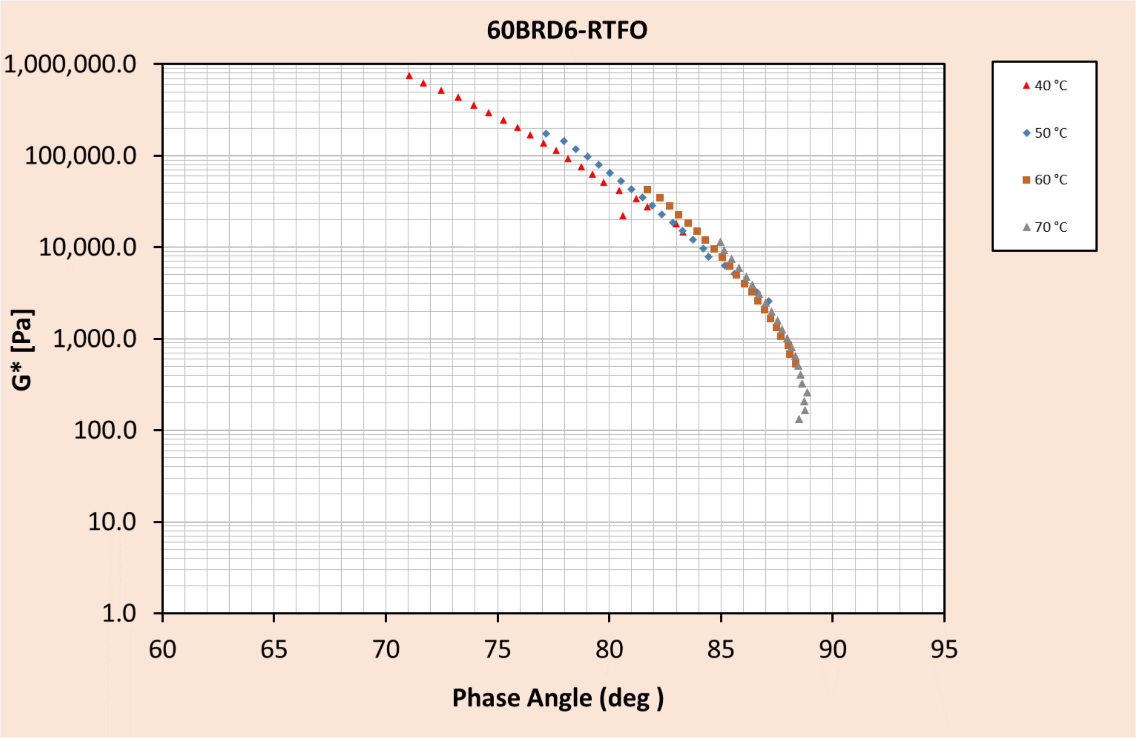
60BRD6-RTFO
G* [Pa]
1,000,000.0
100,000.0
10,000.0
1,000.0
100.0
10.0
1.0
60
65
70
75
80
85
90
95
Phase Angle (deg)
40 °C
50 °C
60 °C
70 °C

(II)

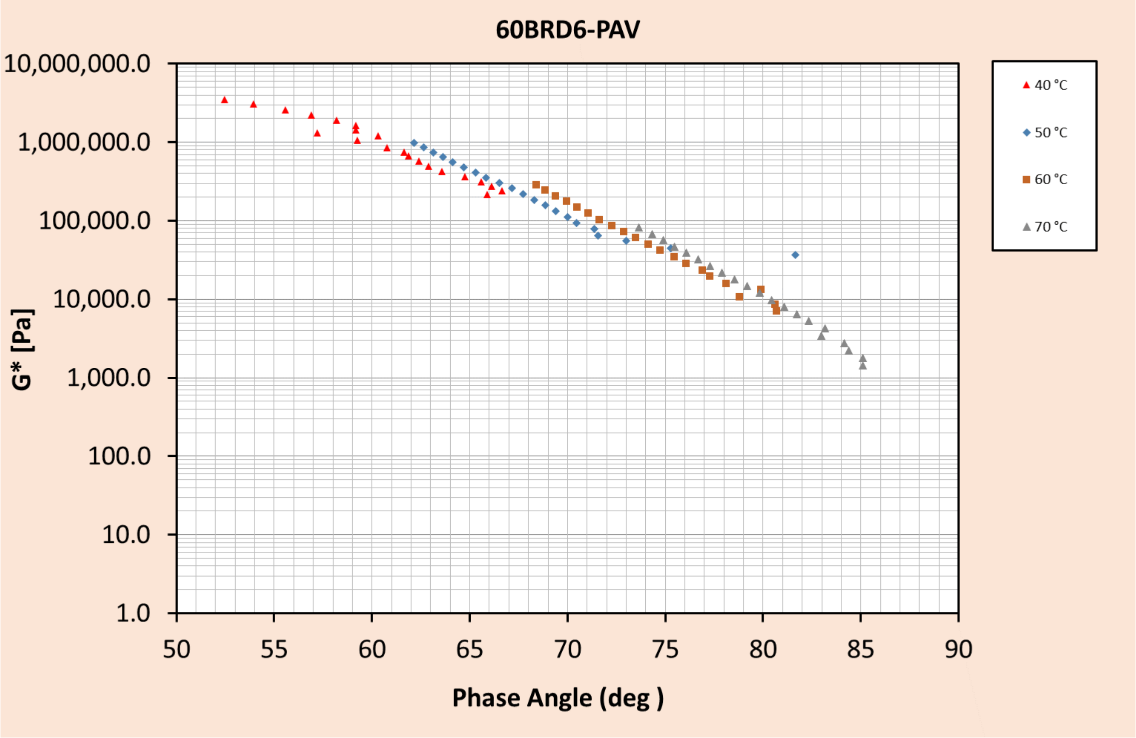
60BRD6-PAV
G* [Pa]
10,000,000.0
1,000,000.0
100,000.0
10,000.0
1,000.0
100.0
10.0
1.0
50
55
60
65
70
75
80
85
90
Phase Angle (deg)
40 °C
50 °C
60 °C
70 °C

(III)

Figure E 7: Black diagram for Sample A15E in unaged, RTFOT and PAV aged conditions

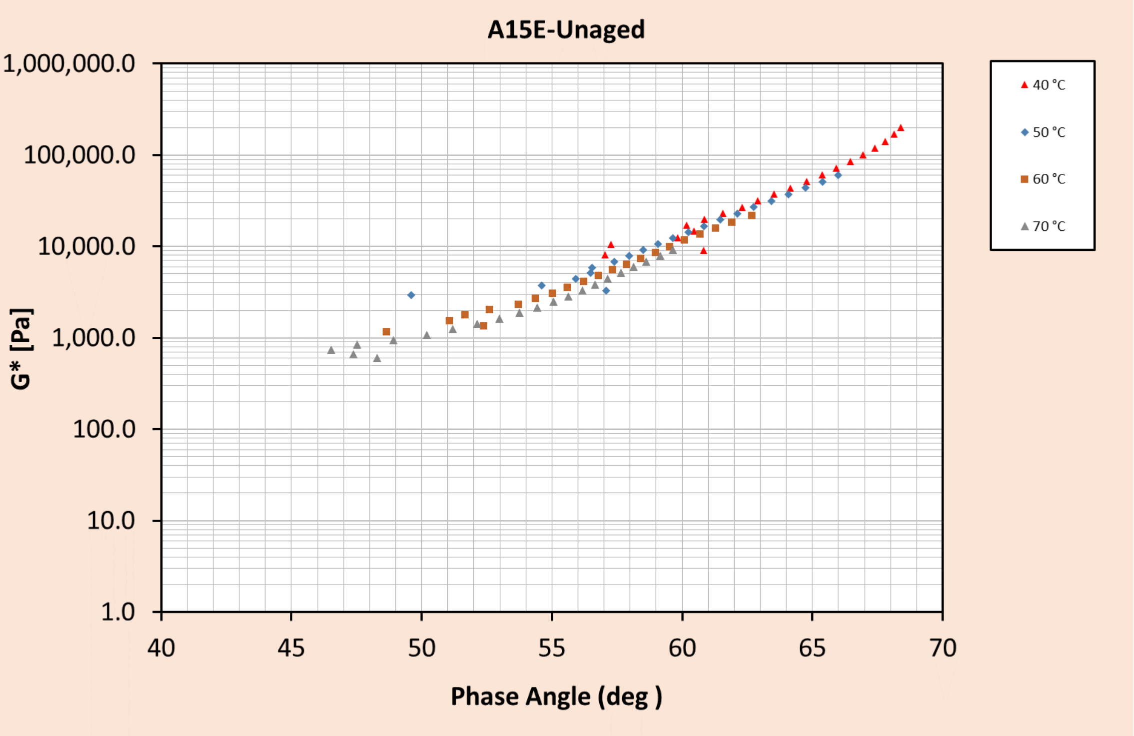

(I)

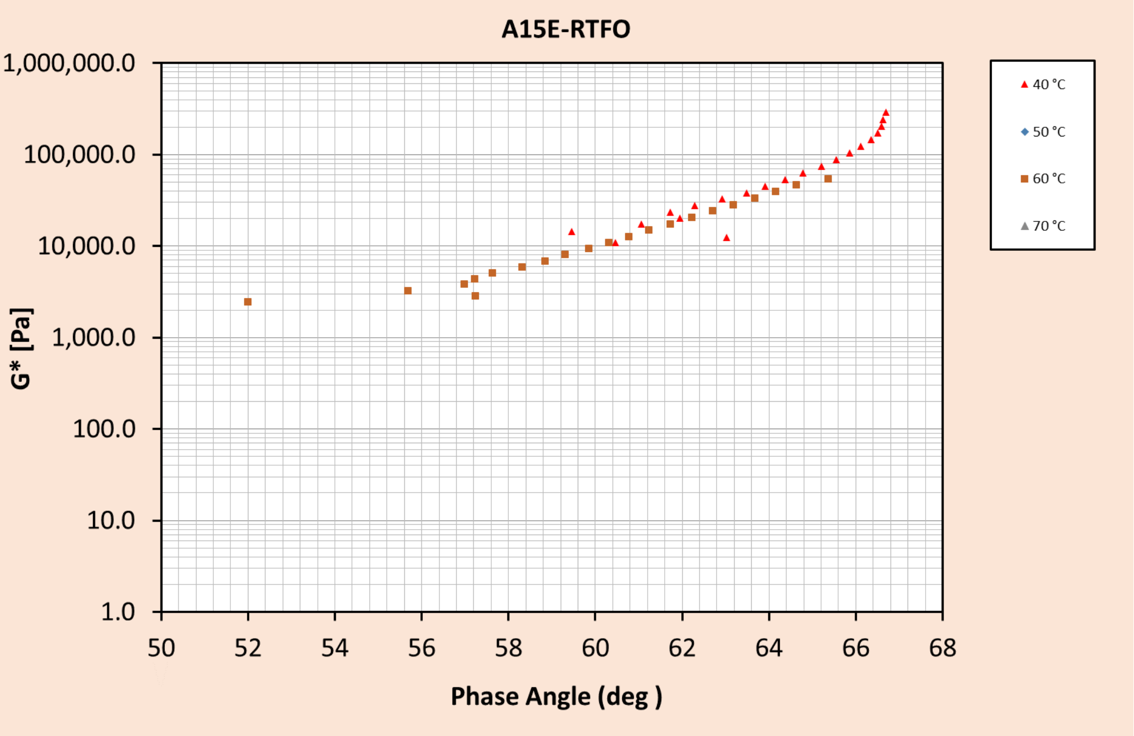

(II)

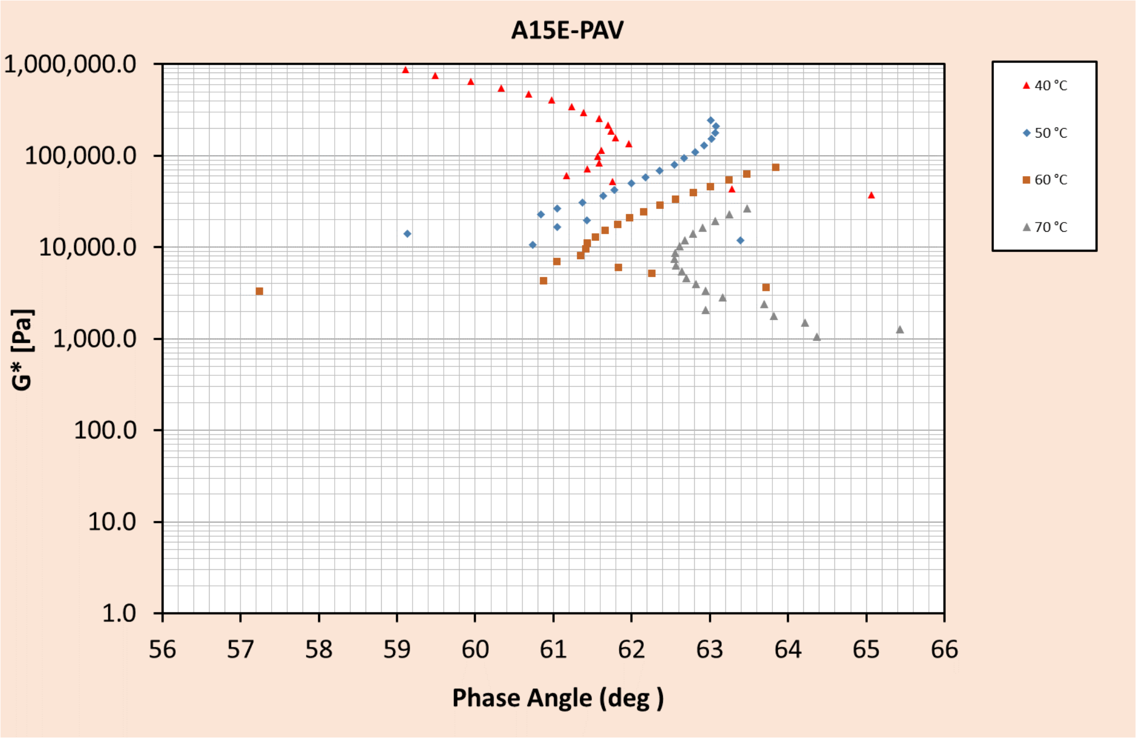

(III)

Figure E 8: Black diagram for Sample BTD2 in unaged, RTFOT and PAV aged conditions

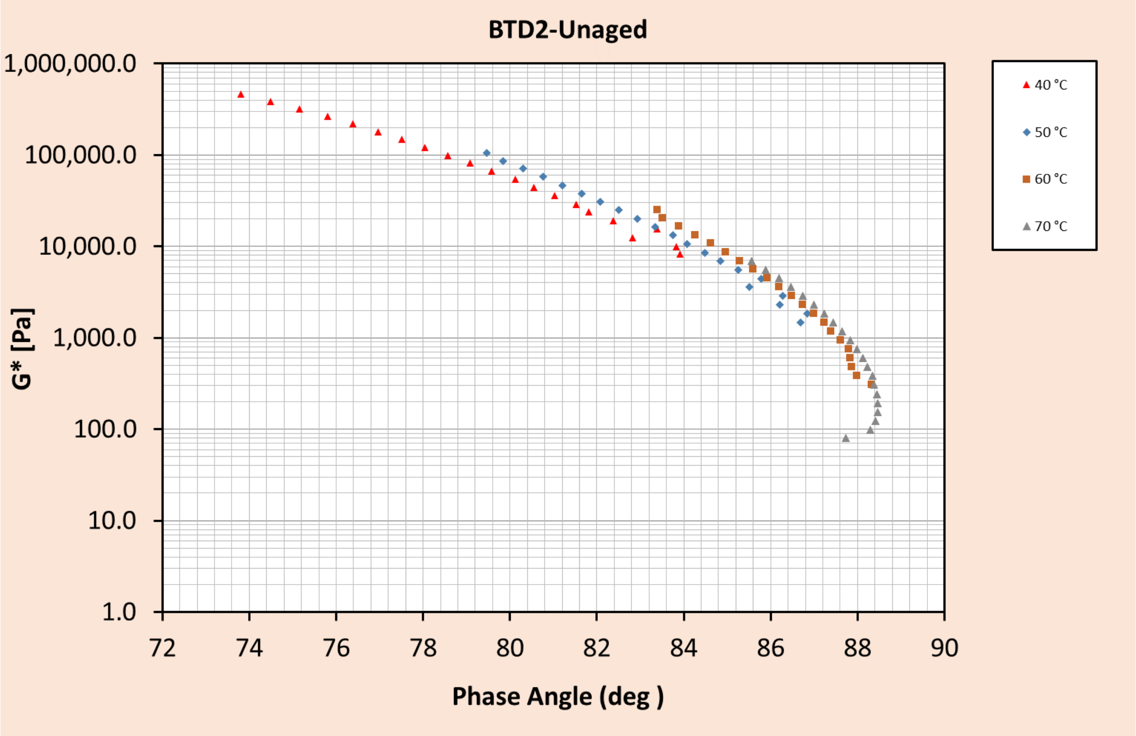

(I)

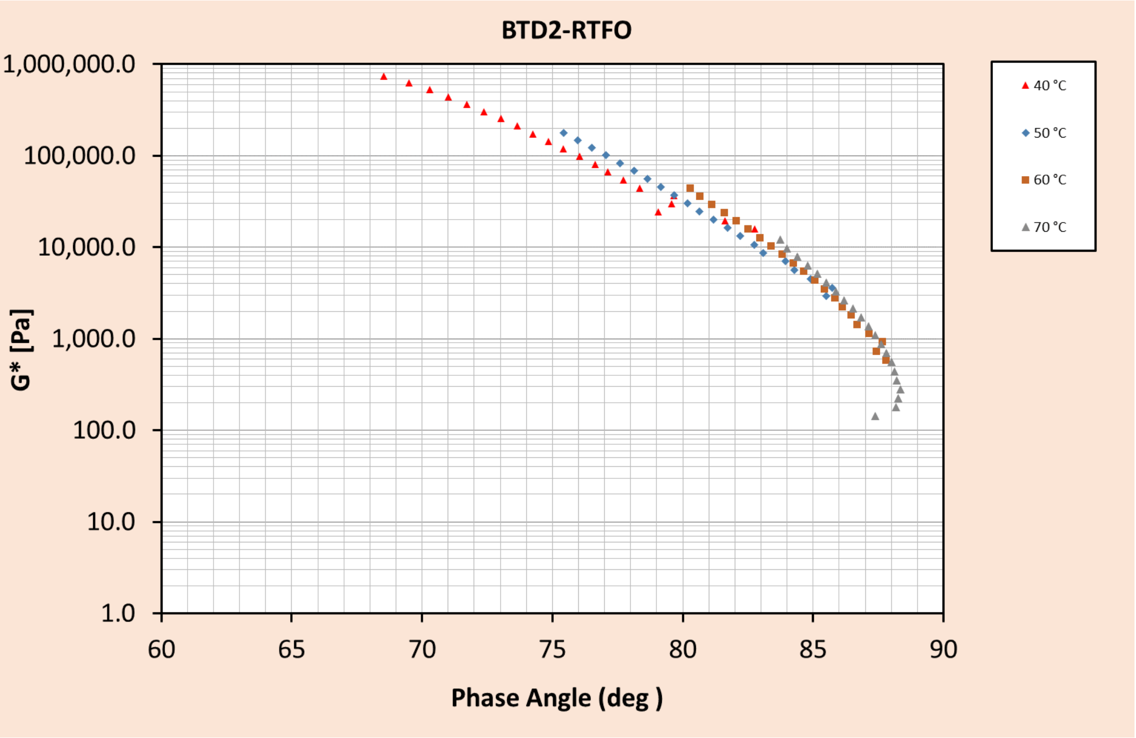
BTD2-RTFO
G* [Pa]
1,000,000.0
100,000.0
10,000.0
1,000.0
100.0
10.0
1.0
60
65
70
75
80
85
90
Phase Angle (deg)
40 °C
50 °C
60 °C
70 °C

(II)

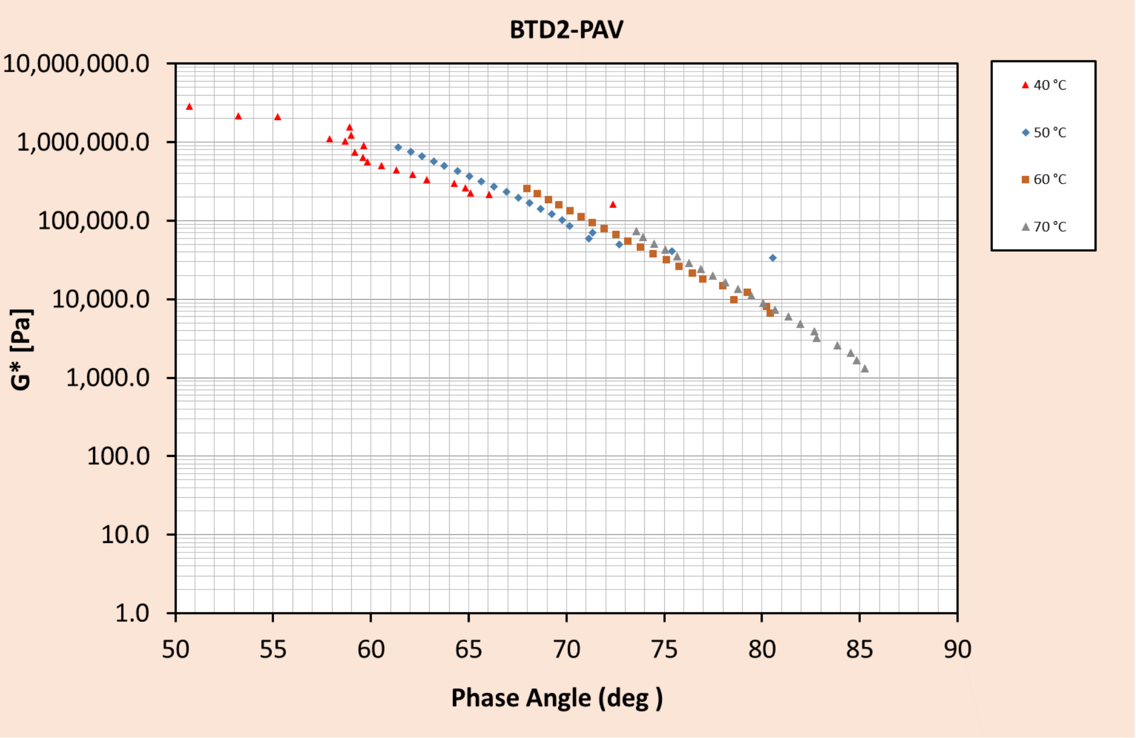
BTD2-PAV
G* [Pa]
10,000,000.0
1,000,000.0
100,000.0
10,000.0
1,000.0
100.0
10.0
1.0
50
55
60
65
70
75
80
85
90
Phase Angle (deg)
40 °C
50 °C
60 °C
70 °C

(III)

Figure E 9: Black diagram for Sample BTD4 in unaged, RTFOT and PAV aged conditions

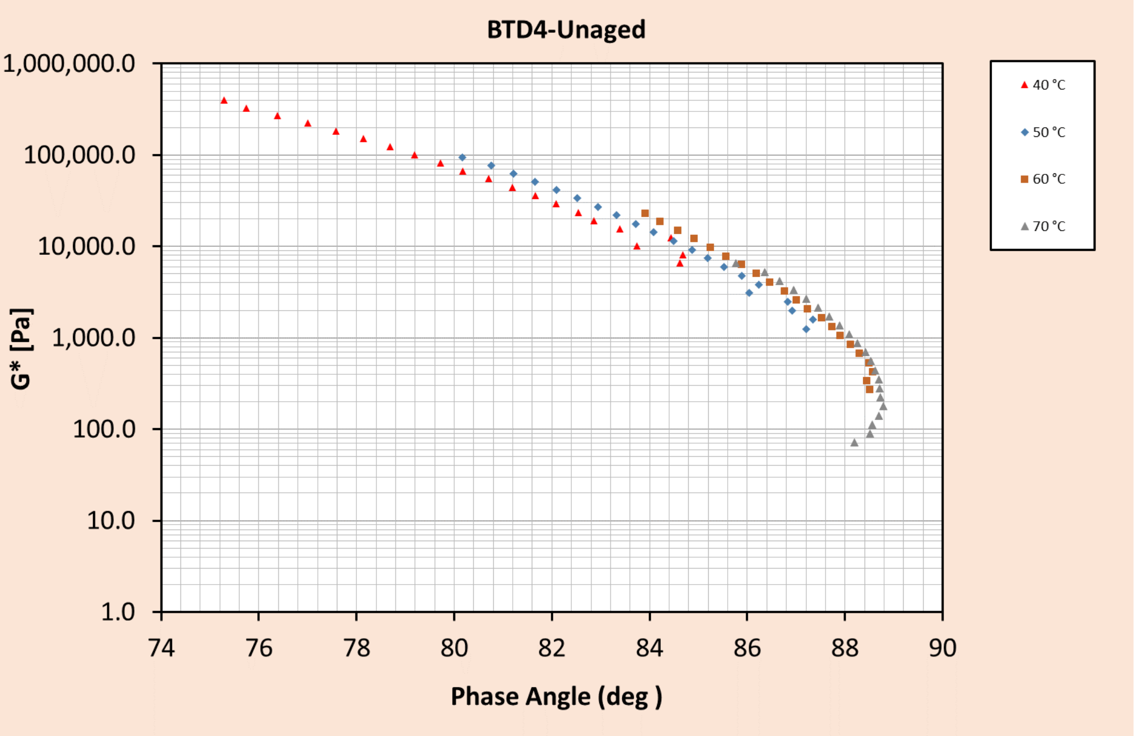

(I)

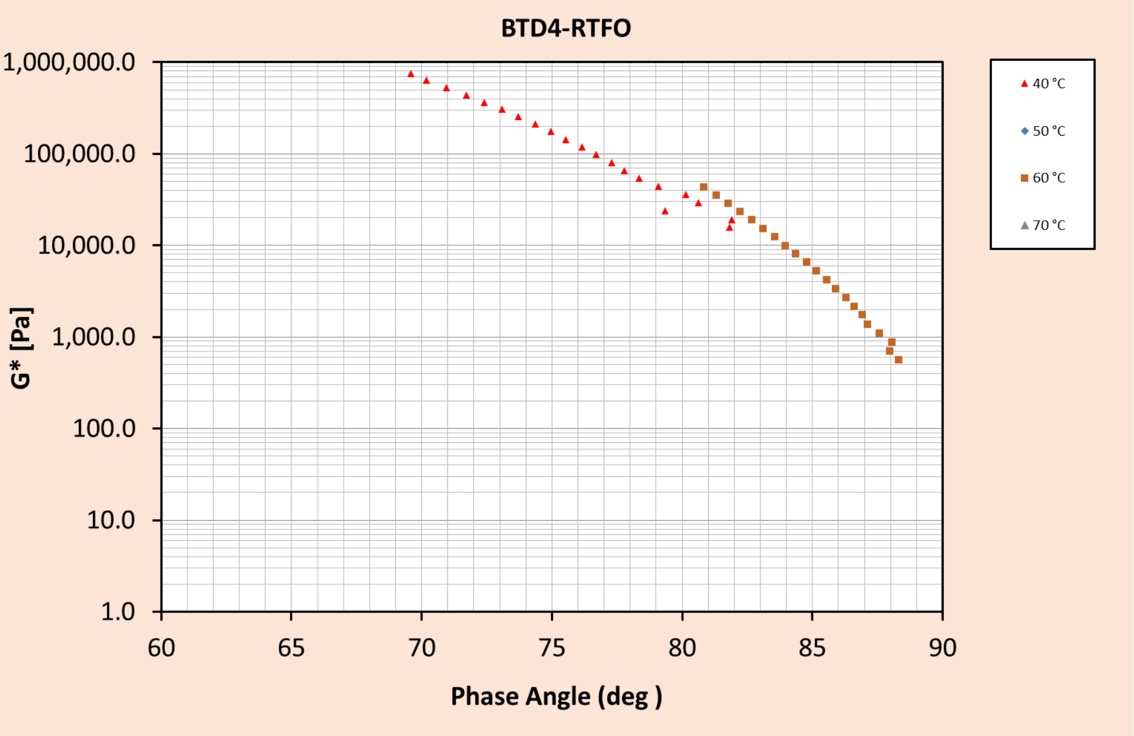

(II)

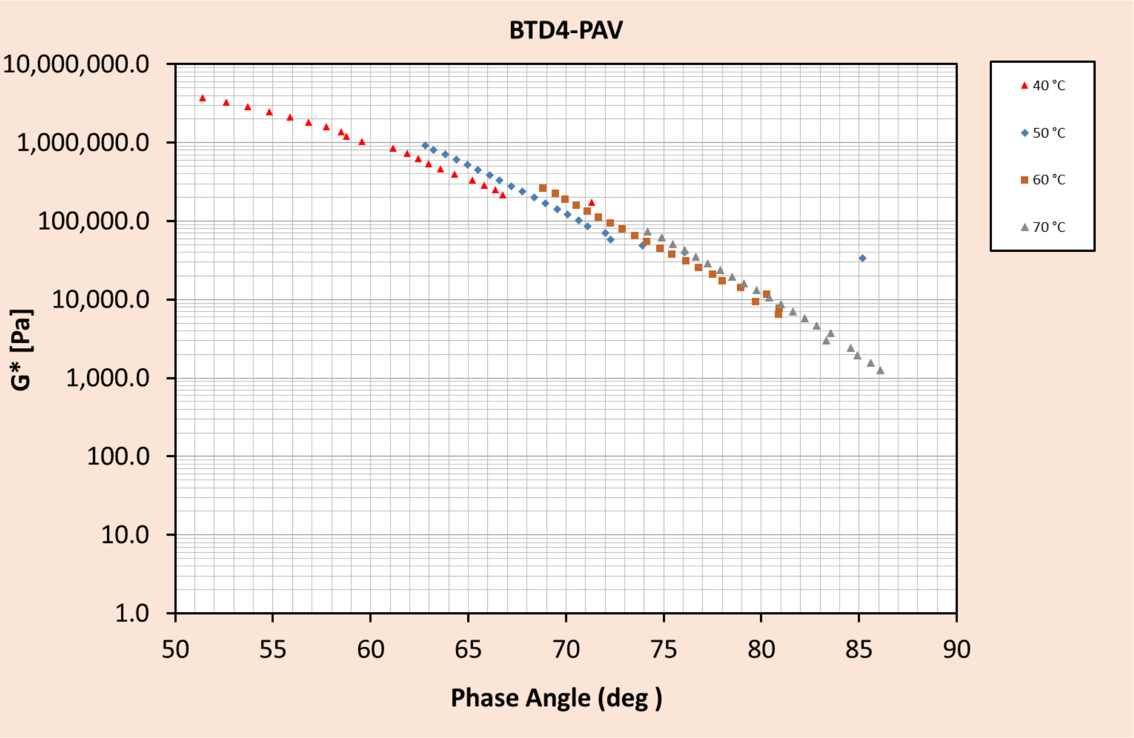

(III)

Figure E 10: Black diagram for Sample BTD6 in unaged, RTFOT and PAV aged conditions

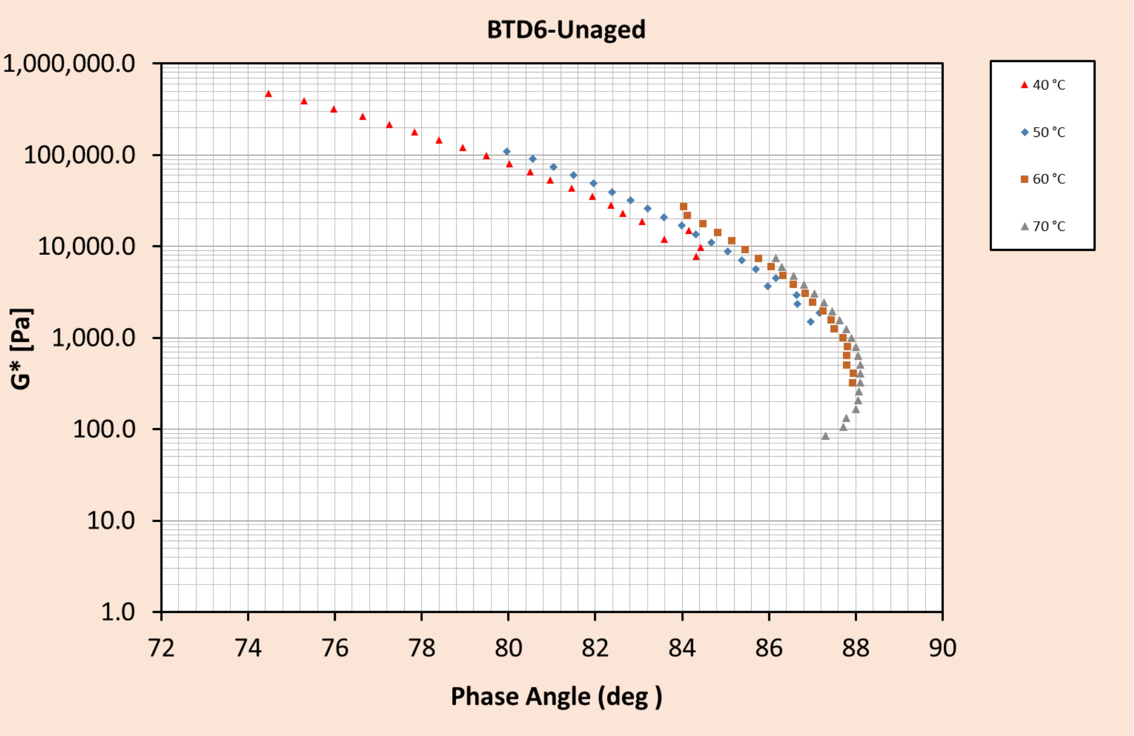

(I)

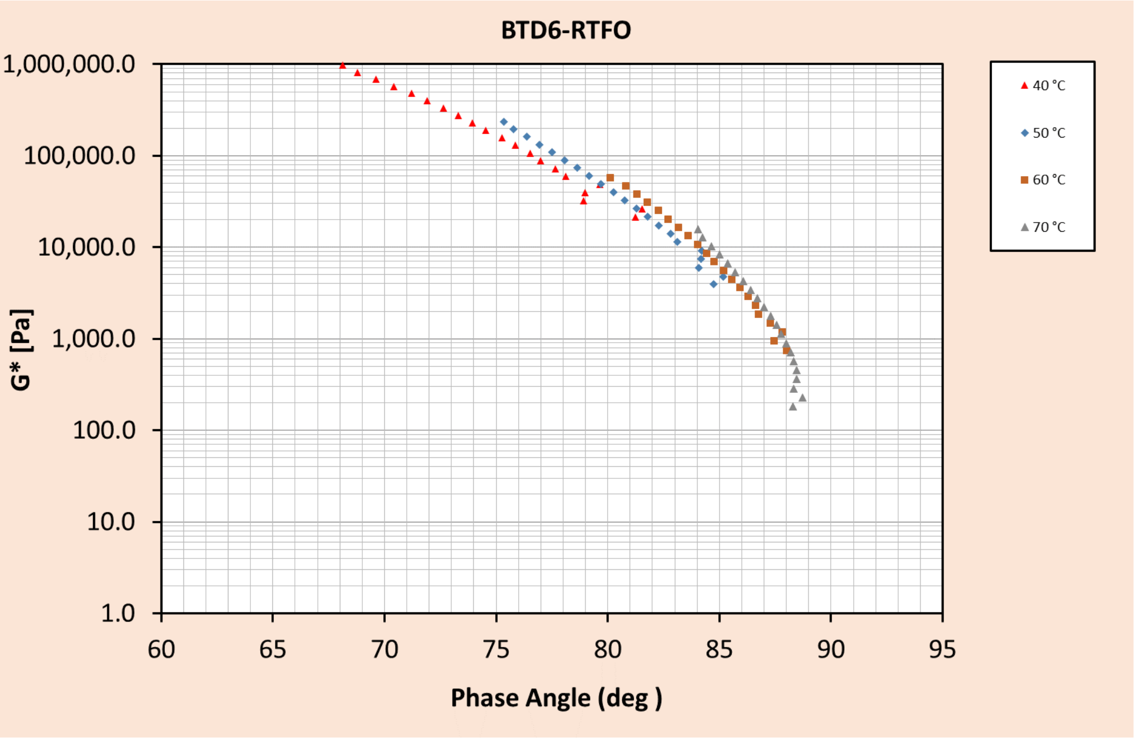
BTD6-RTFO
1,000,000.0
100,000.0
10,000.0
1,000.0
100.0
10.0
1.0
G* [Pa]
60
65
70
75
80
85
90
95
Phase Angle (deg)
40 °C
50 °C
60 °C
70 °C

(II)

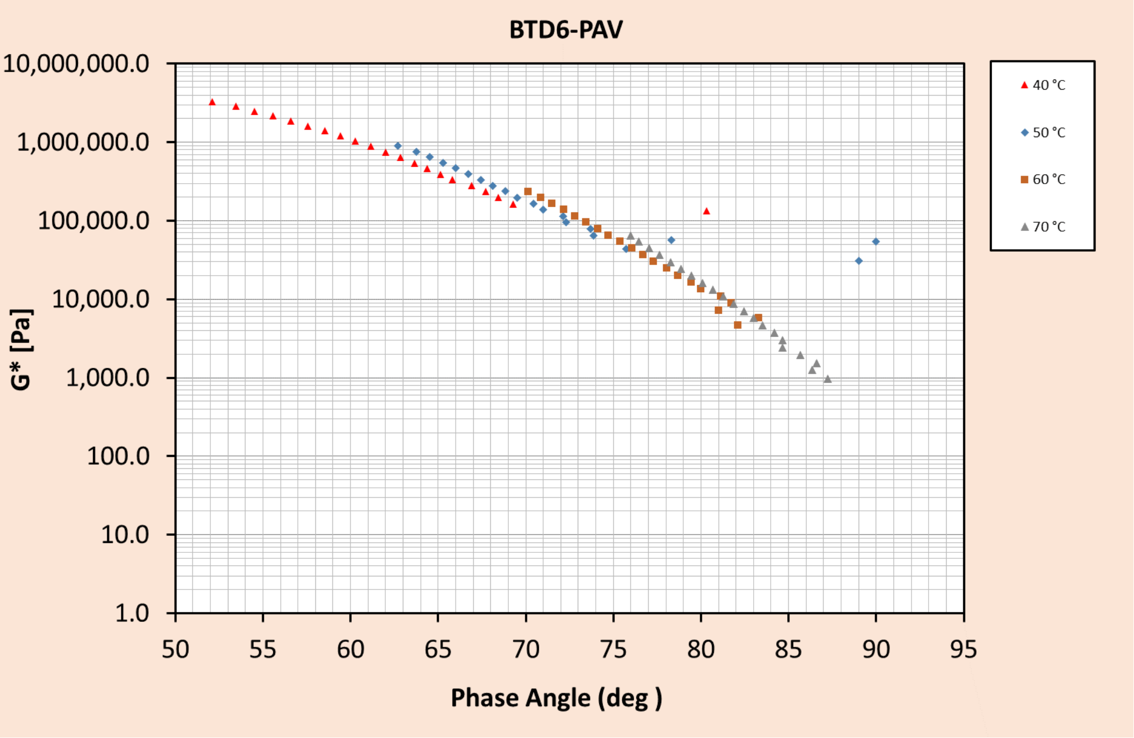
BTD6-PAV
10,000,000.0
1,000,000.0
100,000.0
10,000.0
1,000.0
100.0
10.0
1.0
G* [Pa]
50
55
60
65
70
75
80
85
90
95
Phase Angle (deg)
40 °C
50 °C
60 °C
70 °C

(III)

Figure E 11: Black diagram for Sample C320 in unaged, RTFOT and PAV aged conditions

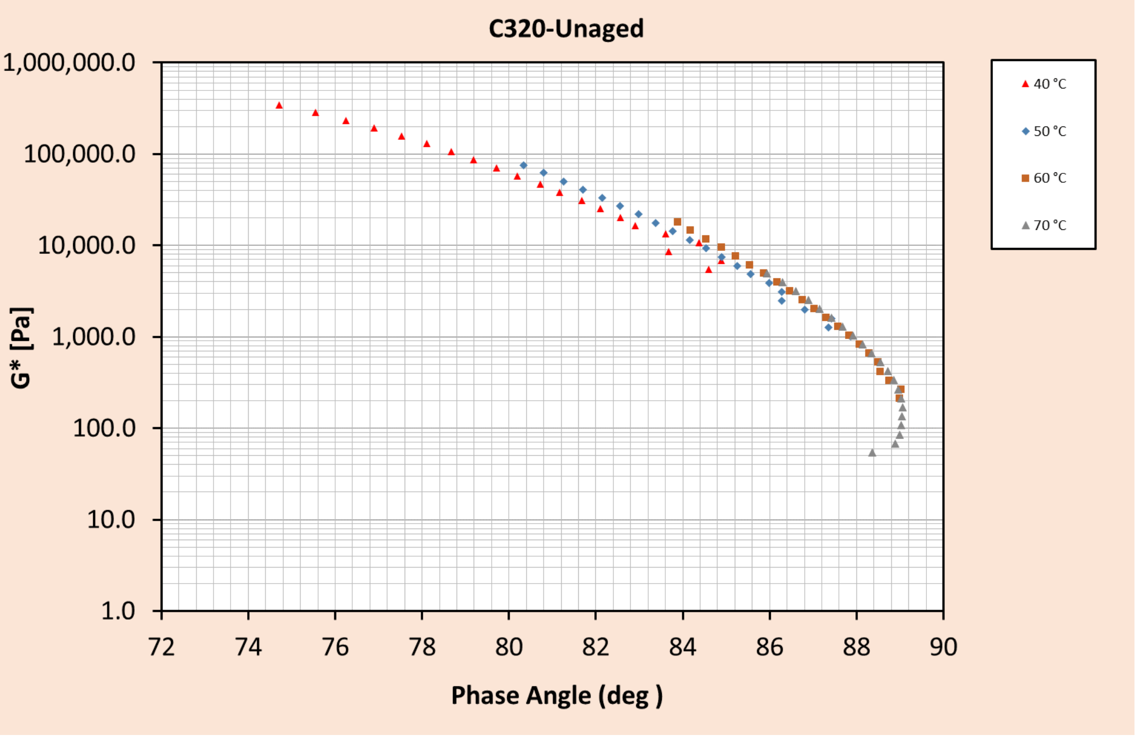

(I)

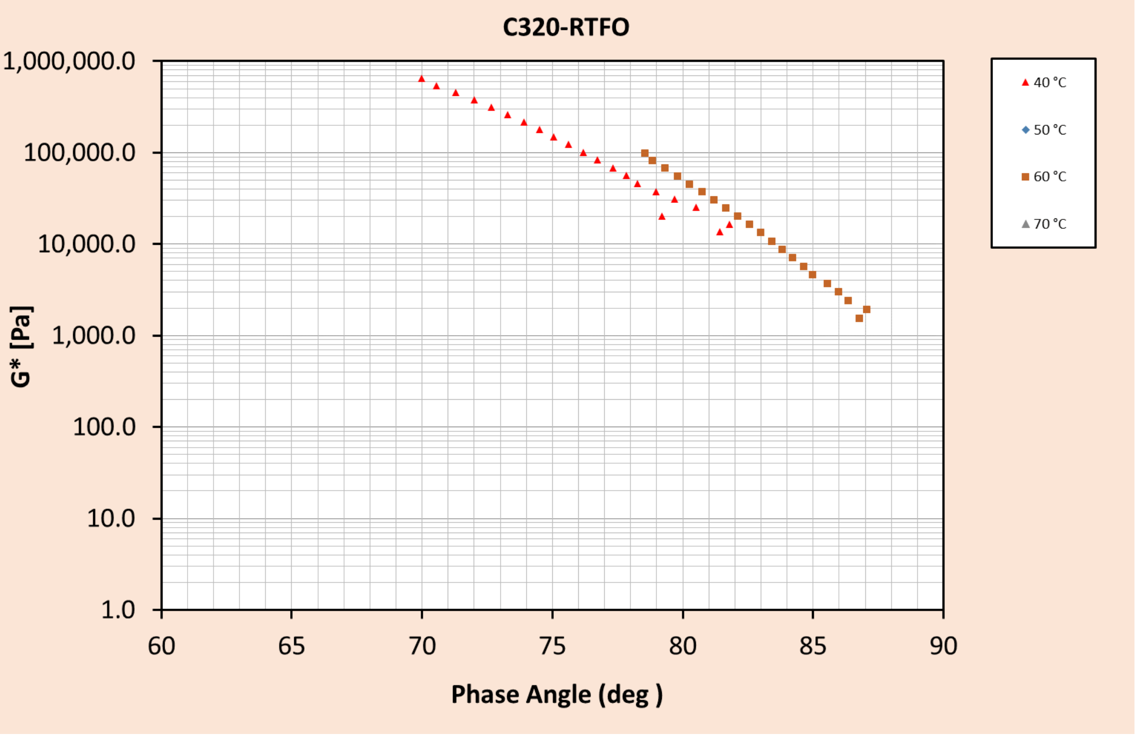

(II)

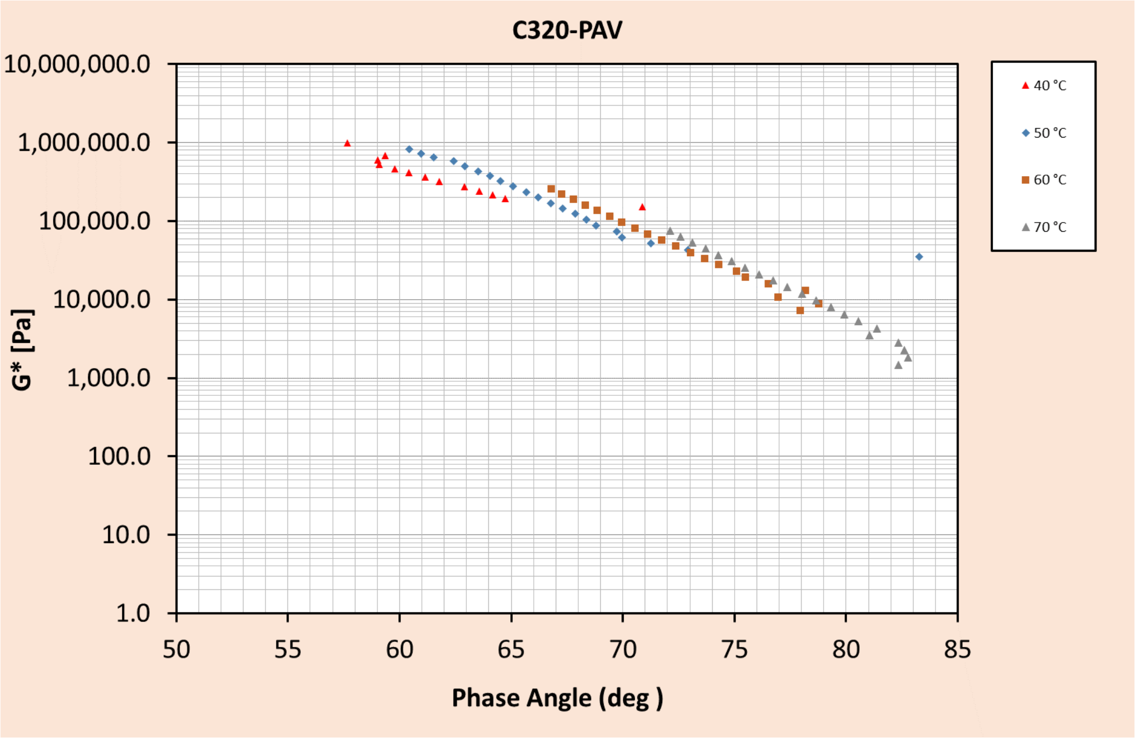

(III)

Figure E 12: Black diagram for Sample C600 in unaged, RTFOT and PAV aged conditions

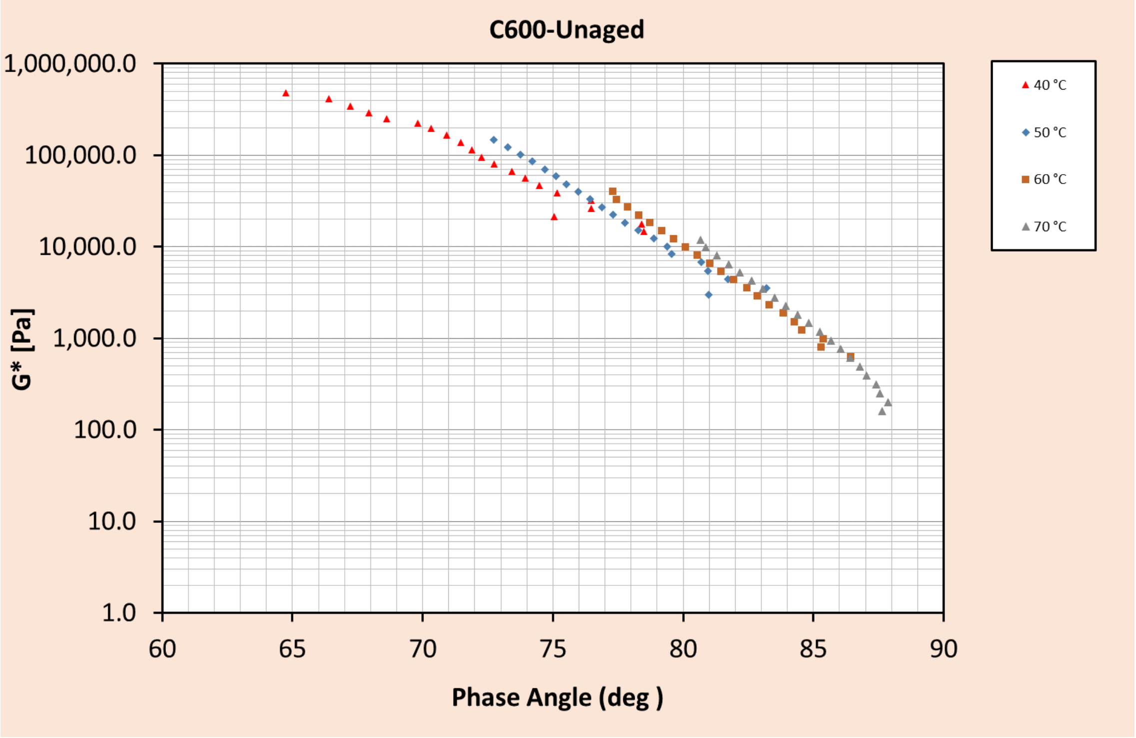

(I)

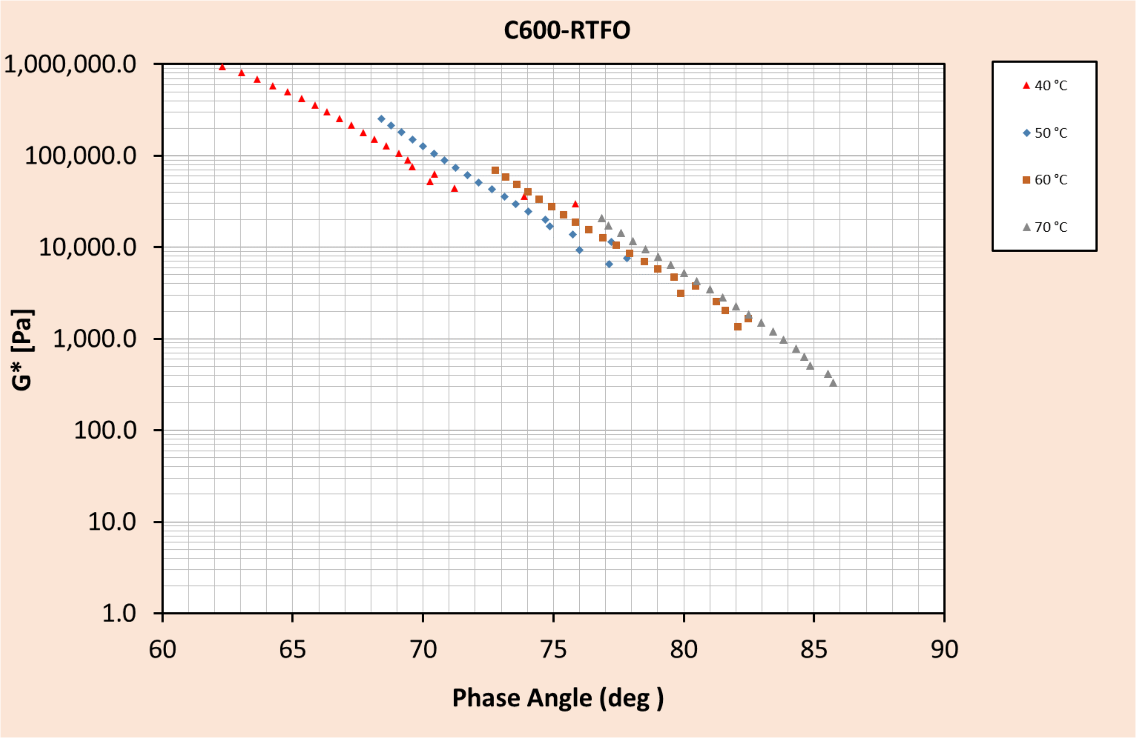
C600-RTFO
G* [Pa]
1,000,000.0
100,000.0
10,000.0
1,000.0
100.0
10.0
1.0
60
65
70
75
80
85
90
Phase Angle (deg)
40 °C
50 °C
60 °C
70 °C

(II)

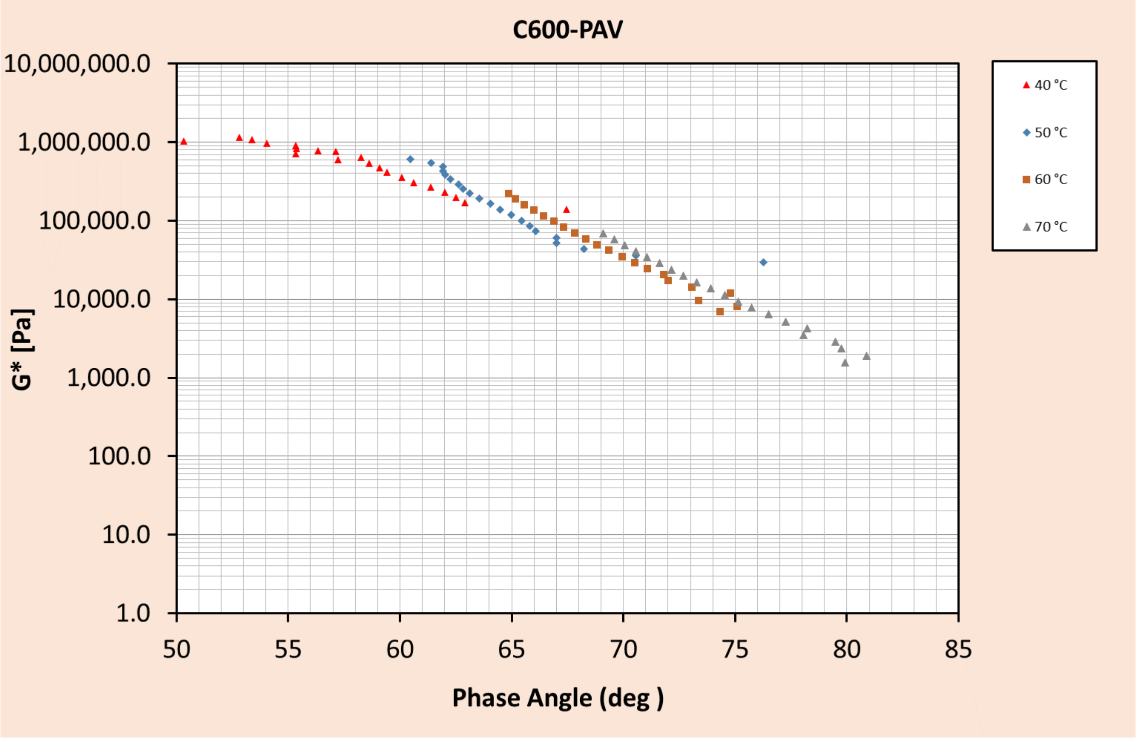
C600-PAV
G* [Pa]
10,000,000.0
1,000,000.0
100,000.0
10,000.0
1,000.0
100.0
10.0
1.0
50
55
60
65
70
75
80
85
Phase Angle (deg)
40 °C
50 °C
60 °C
70 °C

(III)

APPENDIX F IMAGING

F.1 Dry Mixing Images

Figure F 1: SE image – clusters of 20–30 nm NS with 3–4% KH550

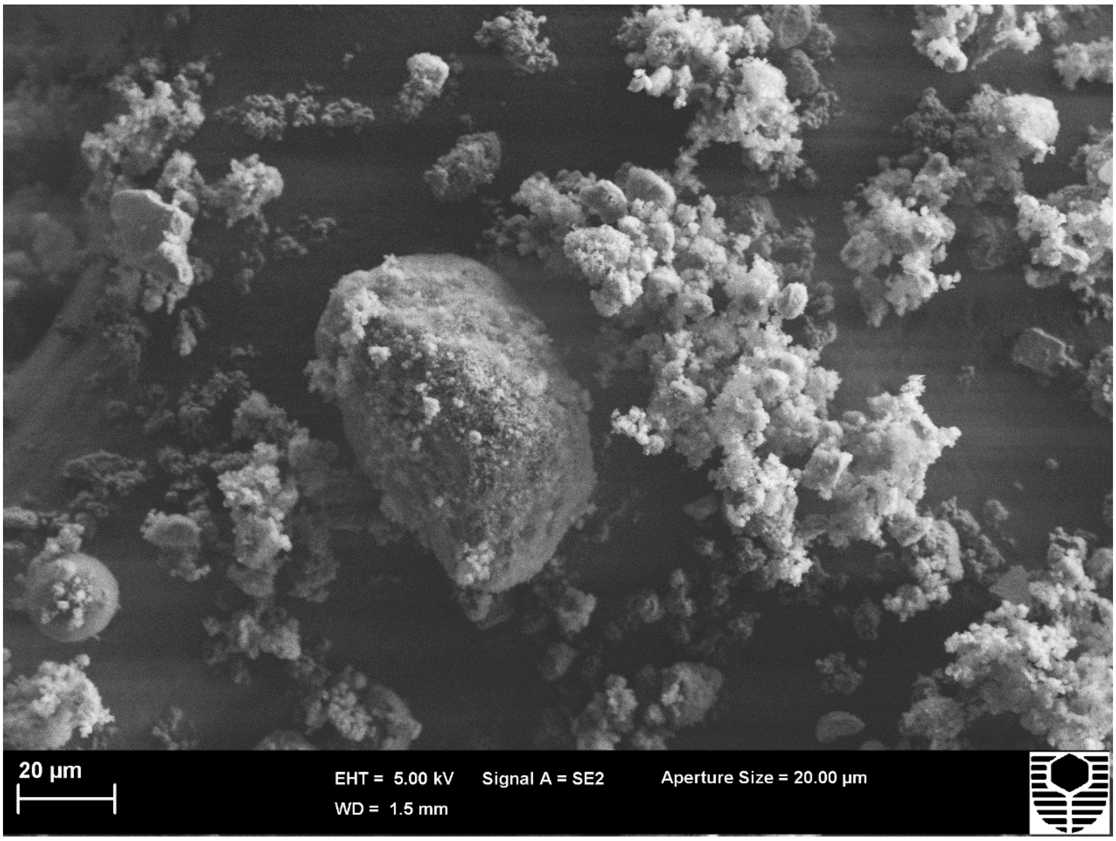

Figure F 2: SE image – surface of a cluster of 20–30 nm NS with 3–4% KH550

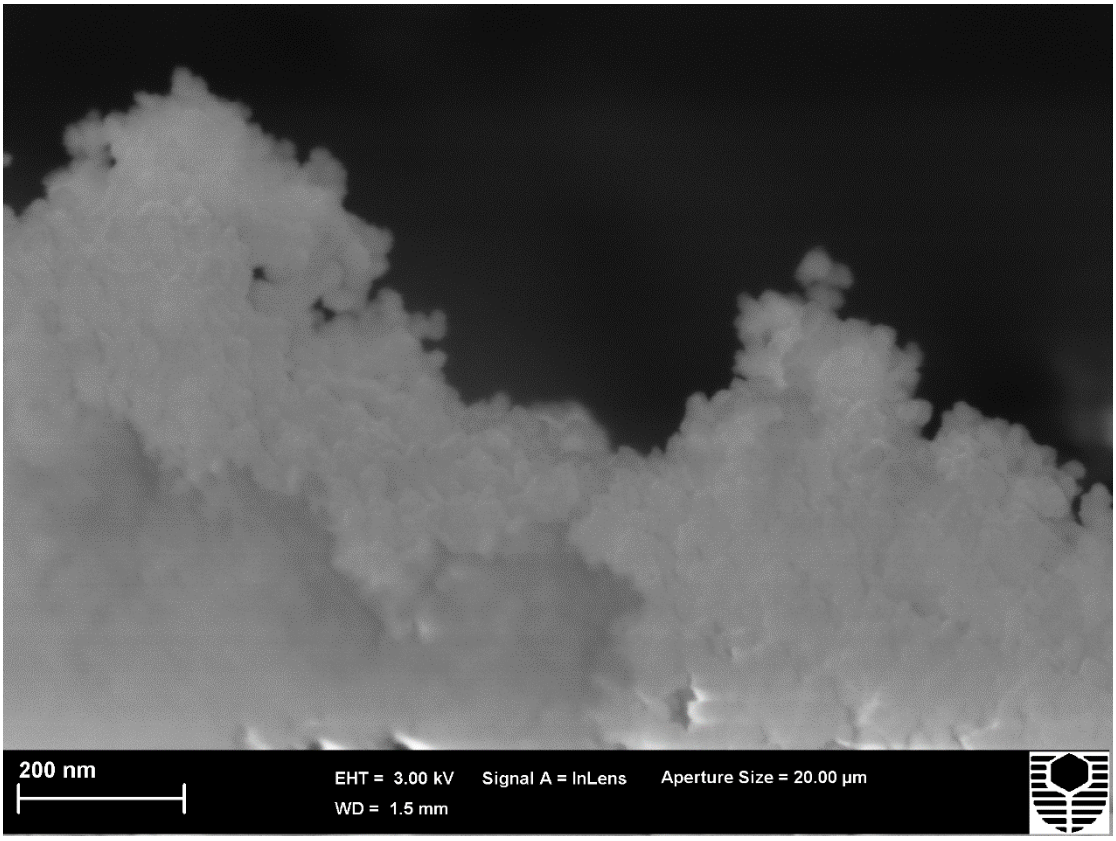

Figure F 3: SE image – clusters of 20–30 nm NS at low magnification

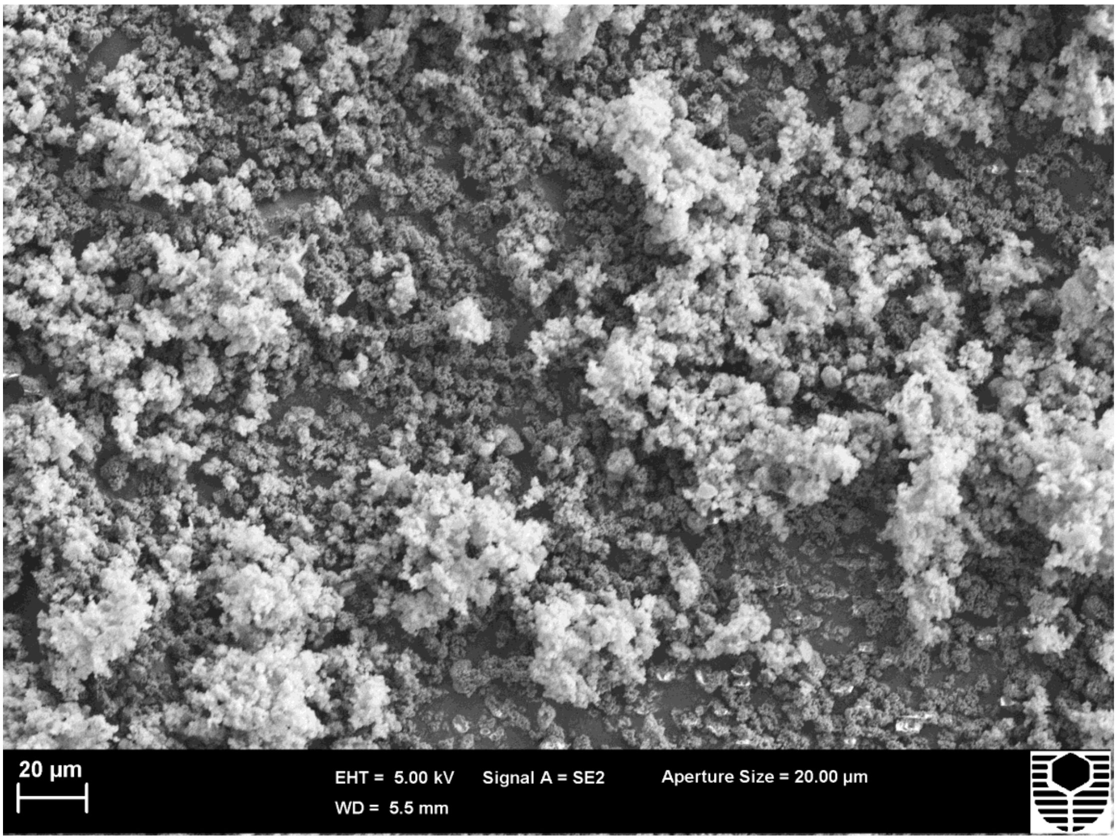

Figure F 4: SE image – surface of clusters of 20–30 nm NS at high magnification

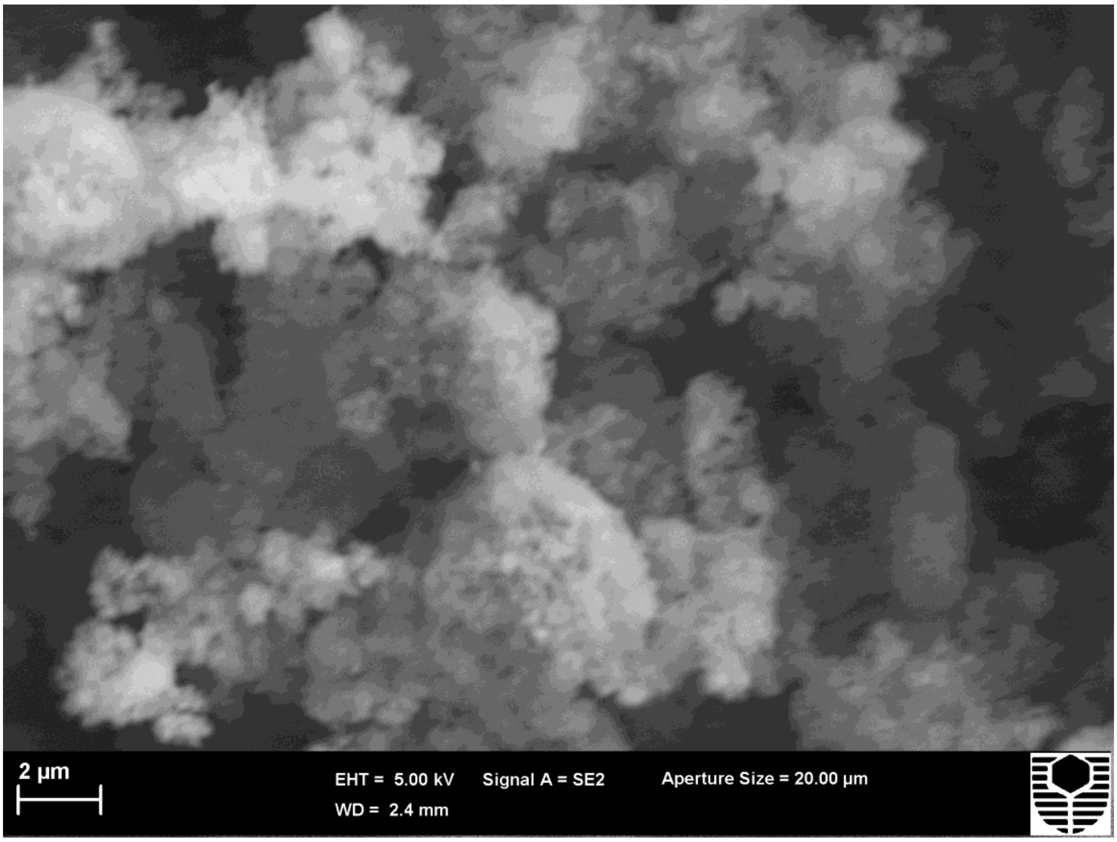

Figure F 5: SE image – clusters of 60–70 nm NS at low magnification

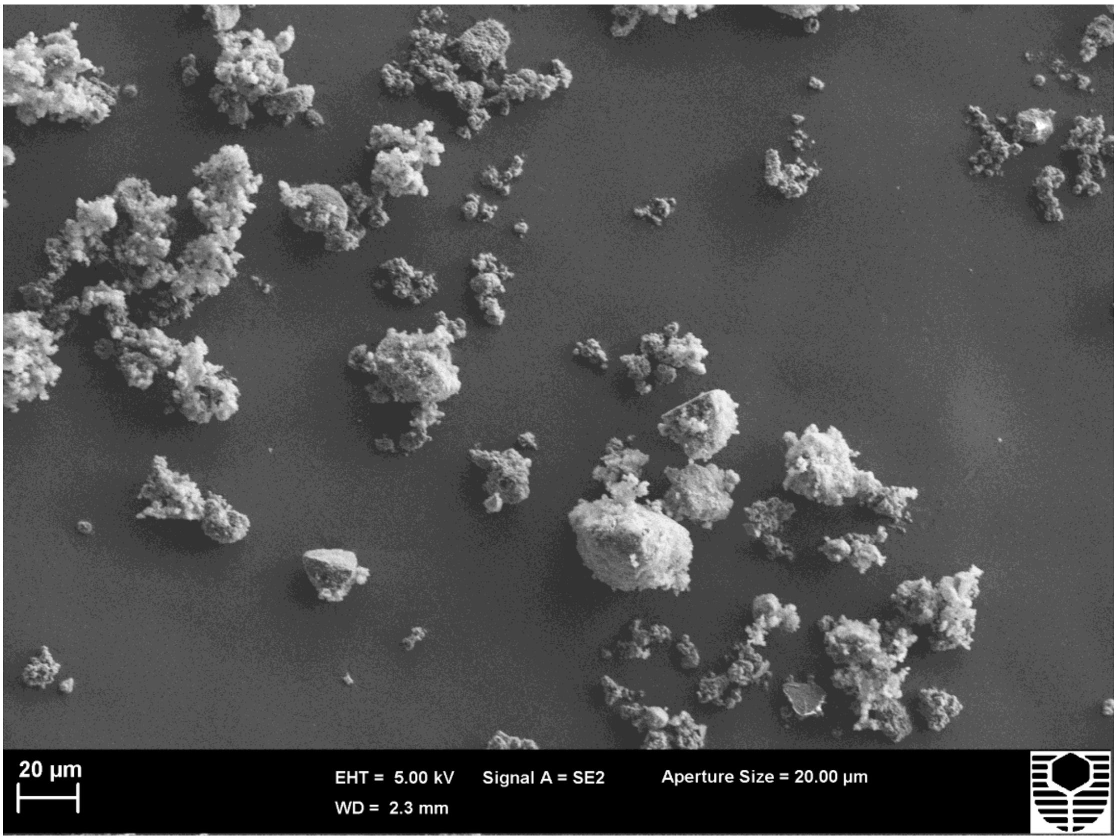

Figure F 6: SE image – surface of clusters of 60–70 nm NS at high magnification

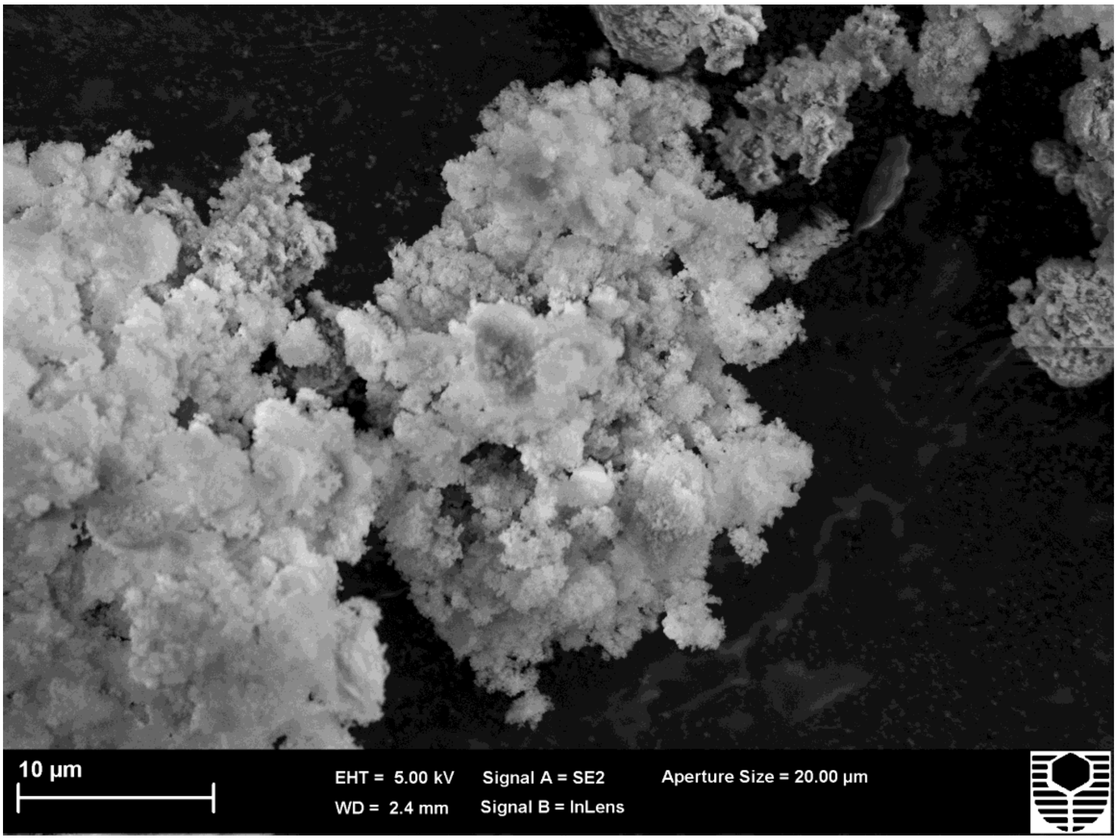

Figure F 7: SE image – mix of asphaltenes with 6% of 20–30 nm NS at low magnification

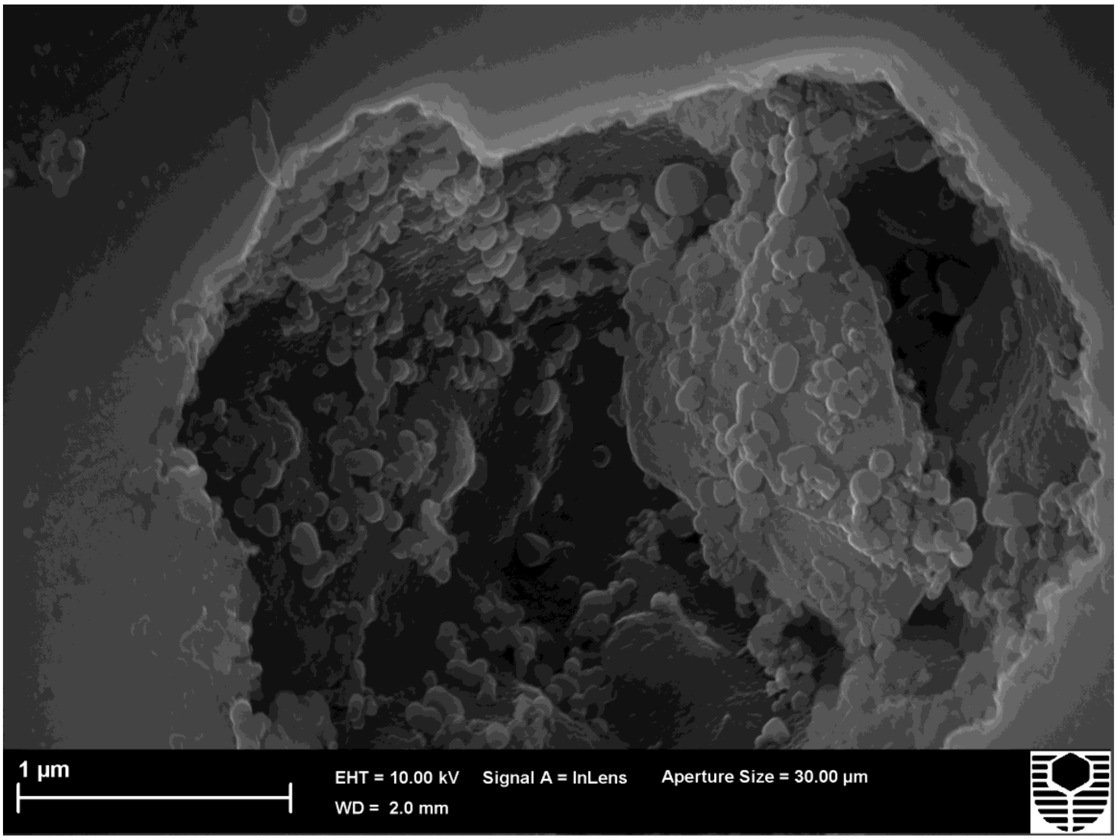

Figure F 8: SE image – mix of asphaltenes with 6% of 20–30 nm NS at high magnification

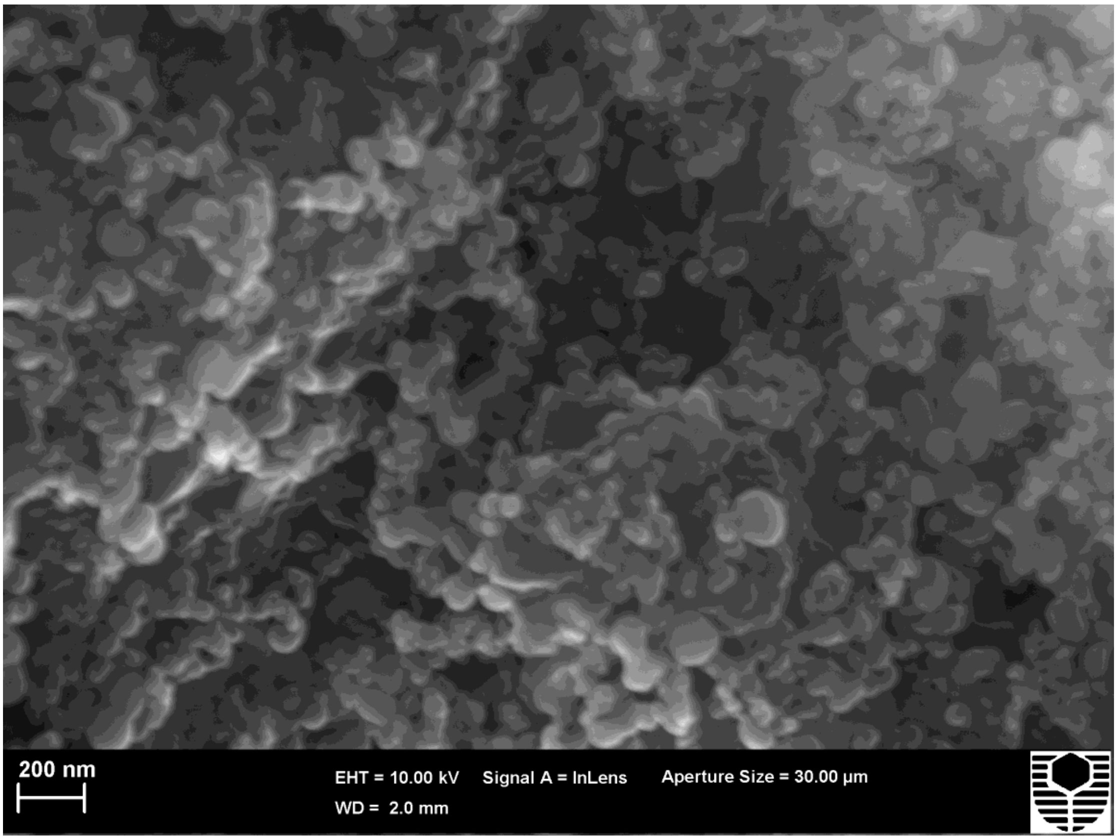

Figure F 9: BSE image – clusters in mix of asphaltenes with 6% of 20–30 nm NS at high magnification

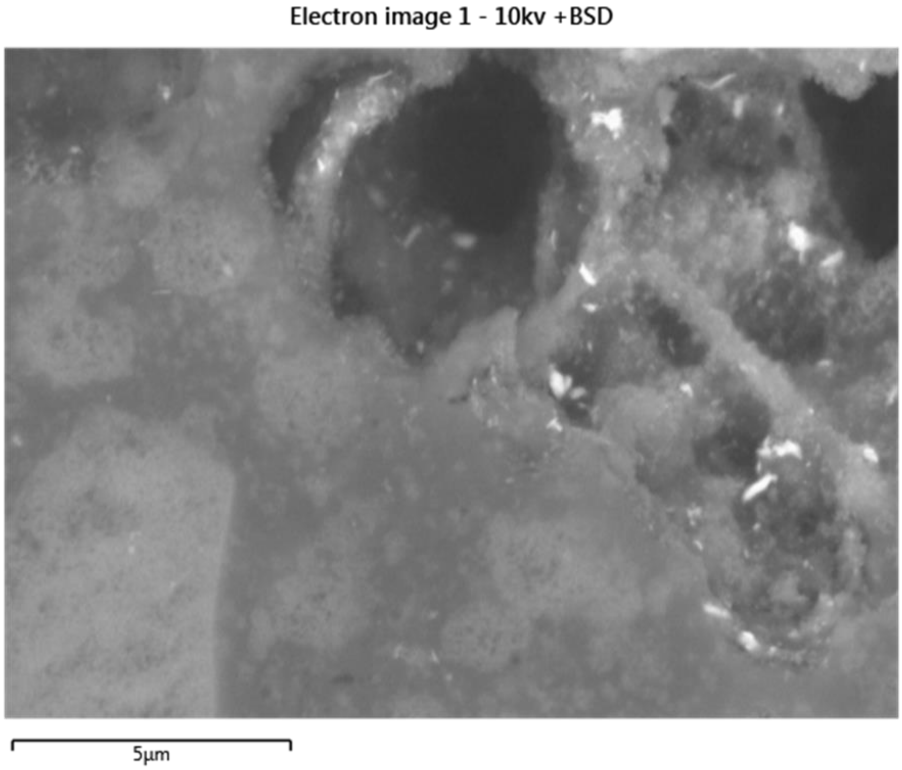

Figure F 10: EDS Map – X-ray map of asphaltenes with 6% of 20–30 nm NS at high magnification

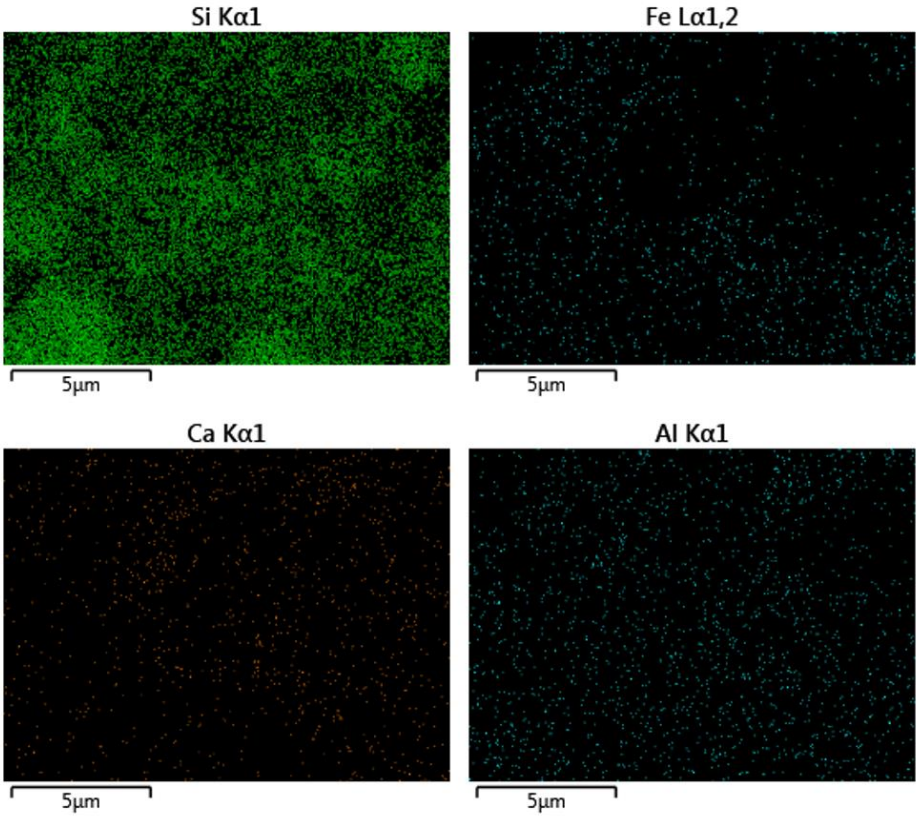

Figure F 11: SE image – clusters in asphaltenes with 6% of 20–30 nm NS at low magnification

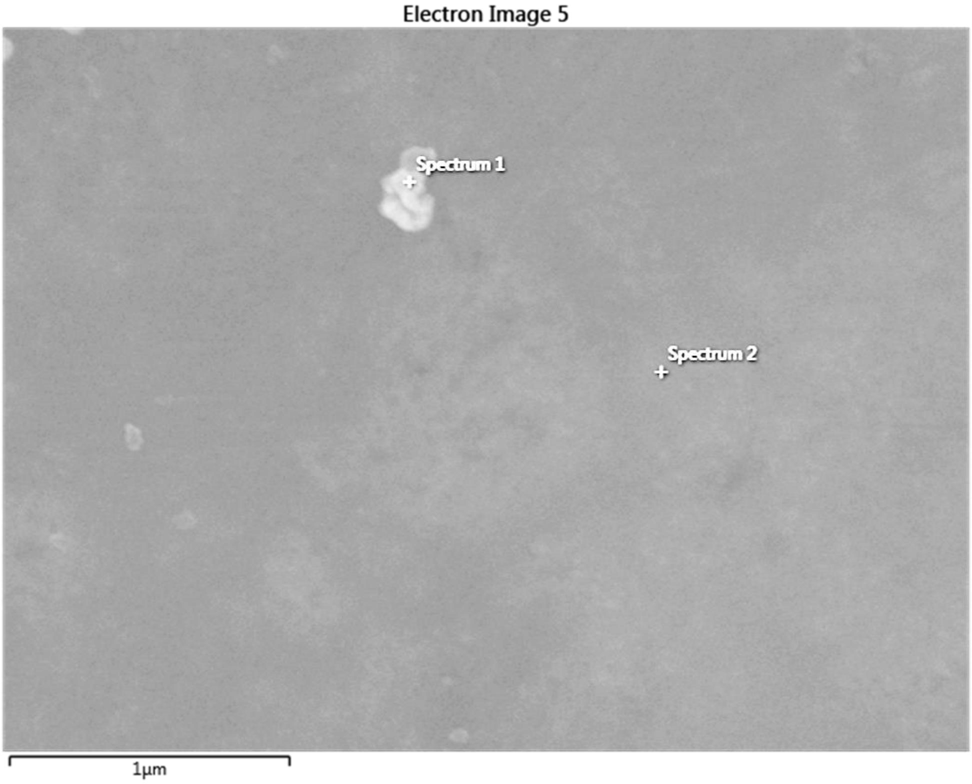

Figure F 12: EDS Spectrometry – high silica content in pointed cluster

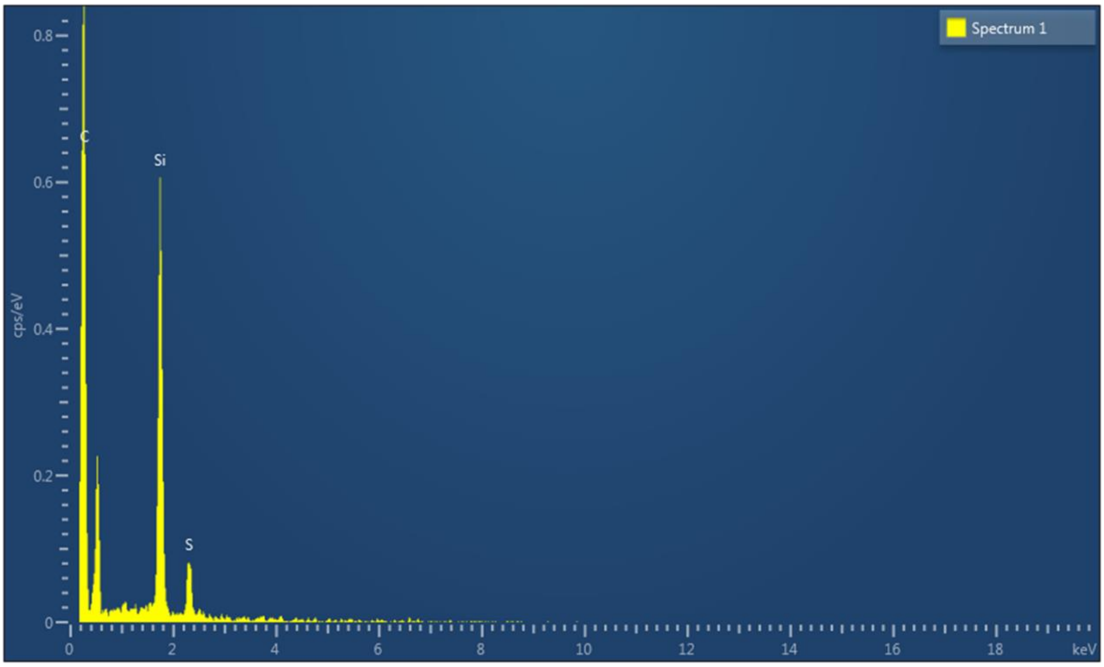

Figure F 13: EDS Spectrometry – low silica content in body

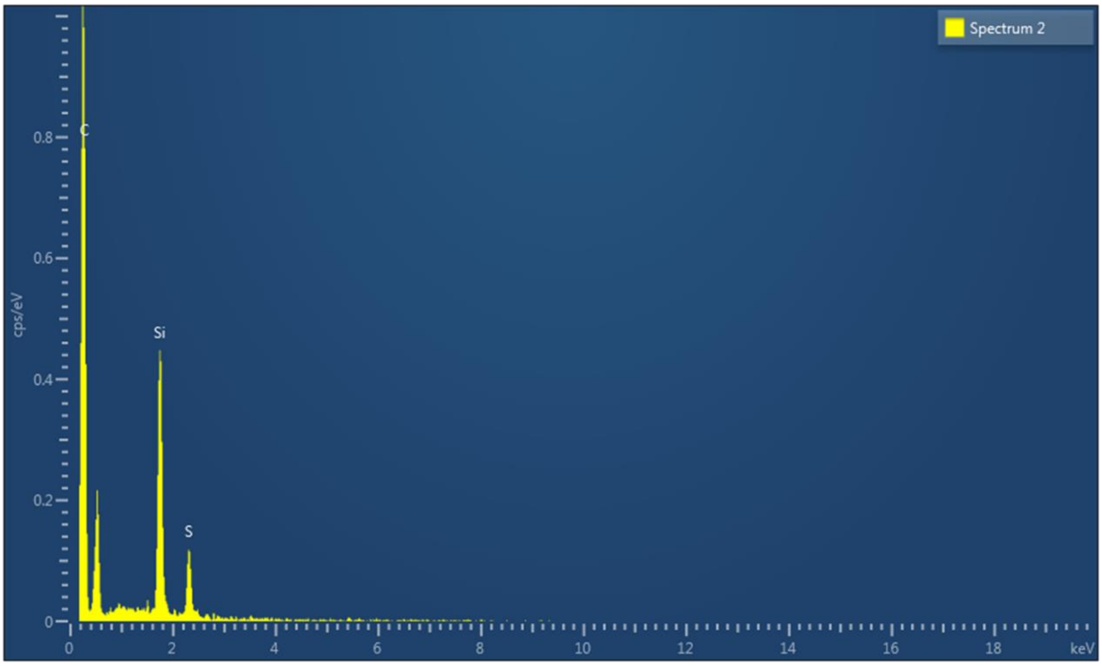

Figure F 14: BSE image – Clusters in asphaltenes with 6% of 20–30 nm NS at low magnification

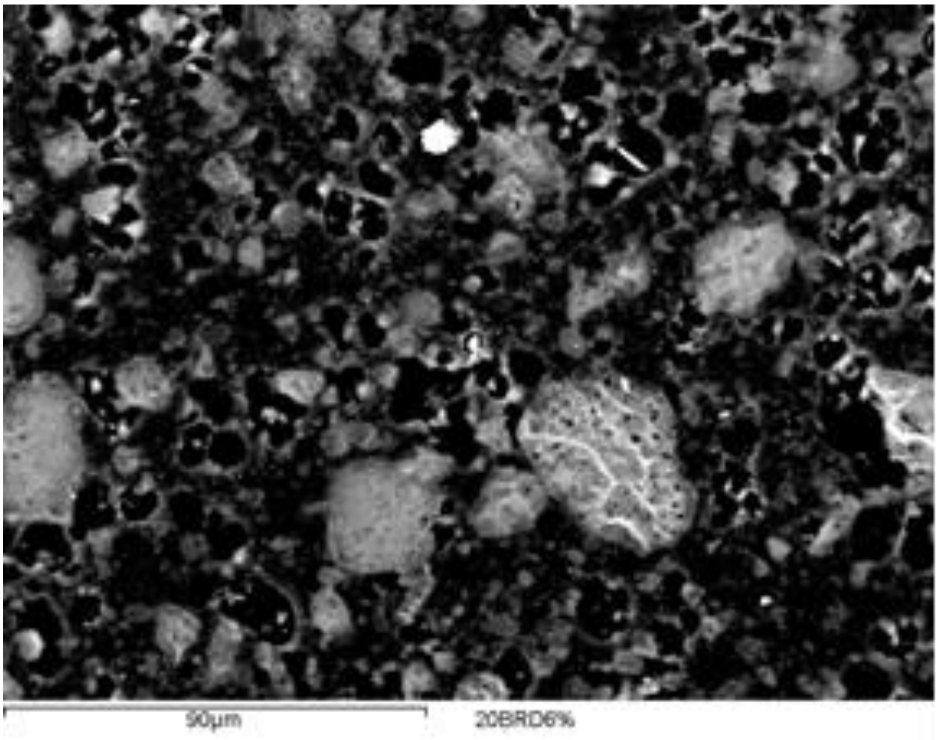

Figure F 15: EDS Map – X-ray map of asphaltenes with 6% of 20–30 nm NS at high magnification

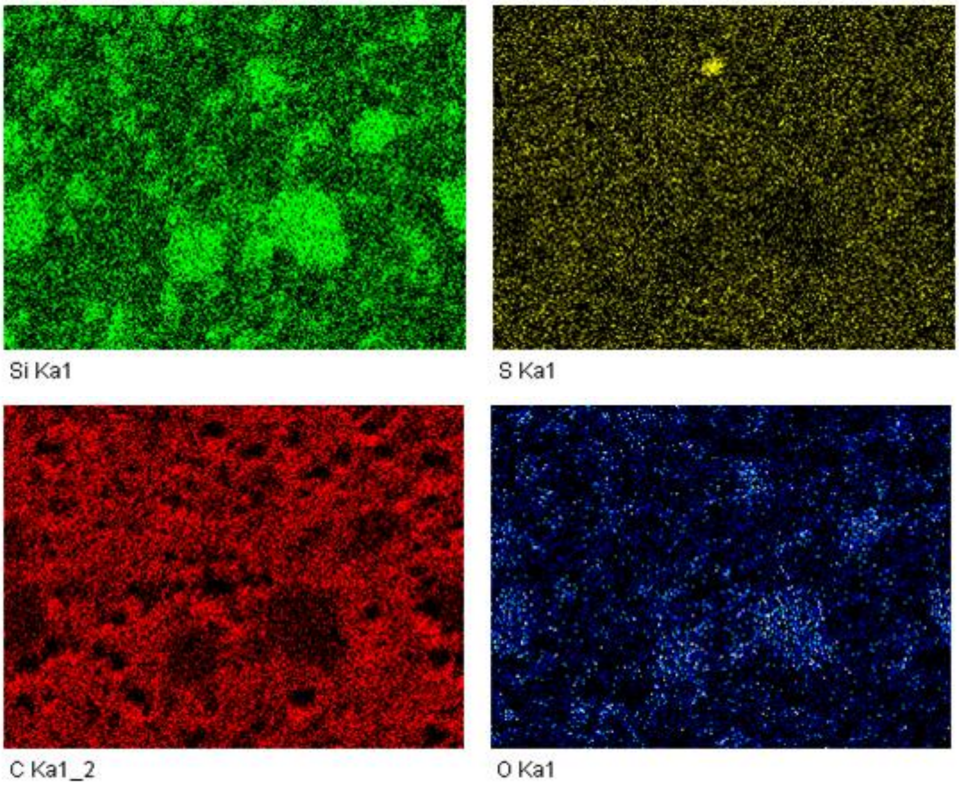

Figure F 16: EDS Map – X-ray map of frozen unaged C320 + 4% NS (20nm)

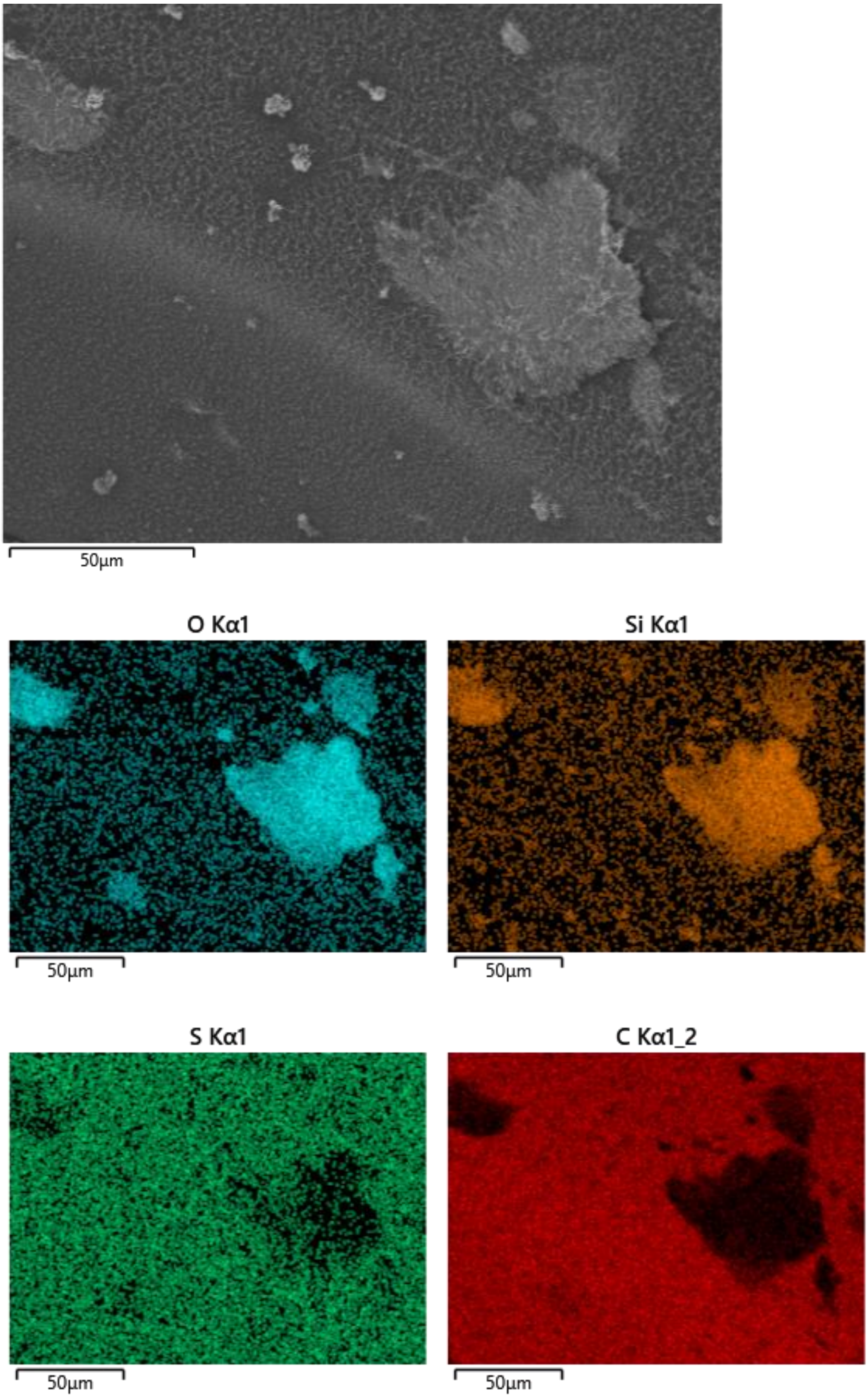

O Kα1

Si Kα1

S Kα1

C Kα1_2

Figure F 17: BSE image – frozen unaged C320 + 4% NS (20nm)

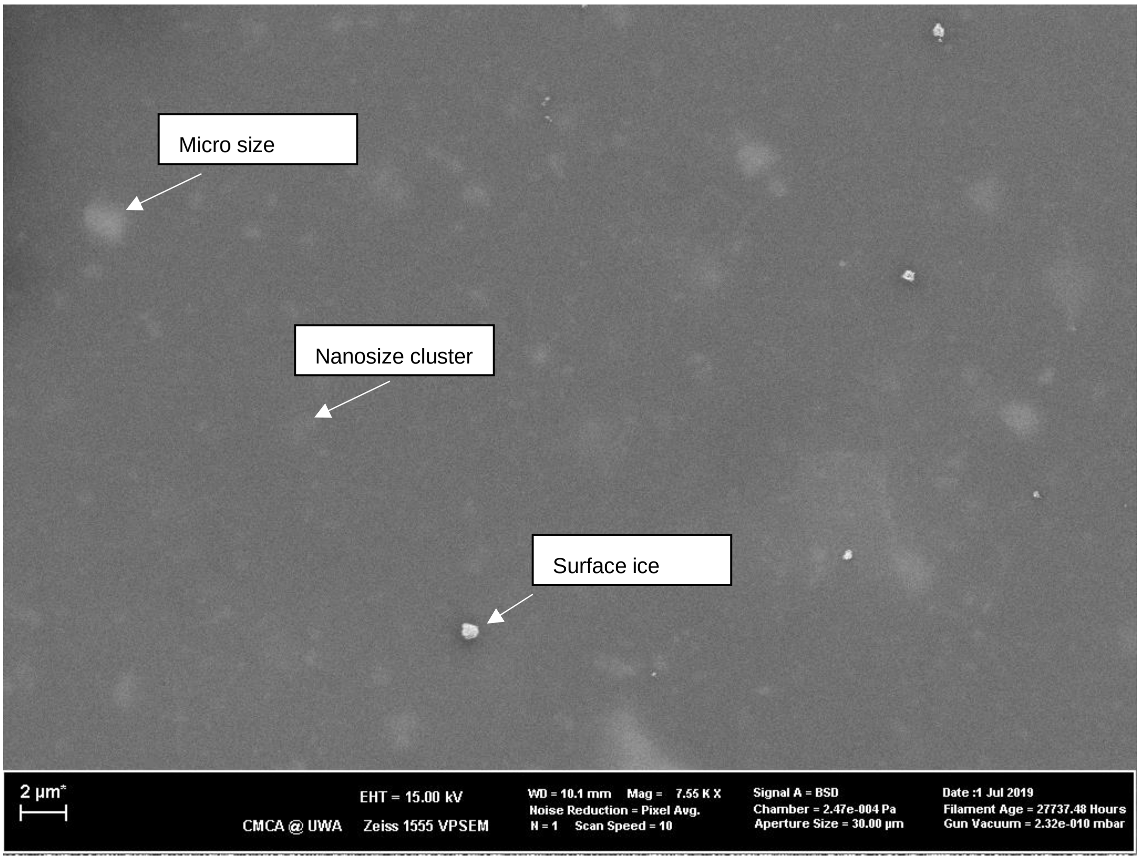

Figure F 18: BSE image – frozen unaged C320 + 2% NS (20nm + KH550 Couplant)

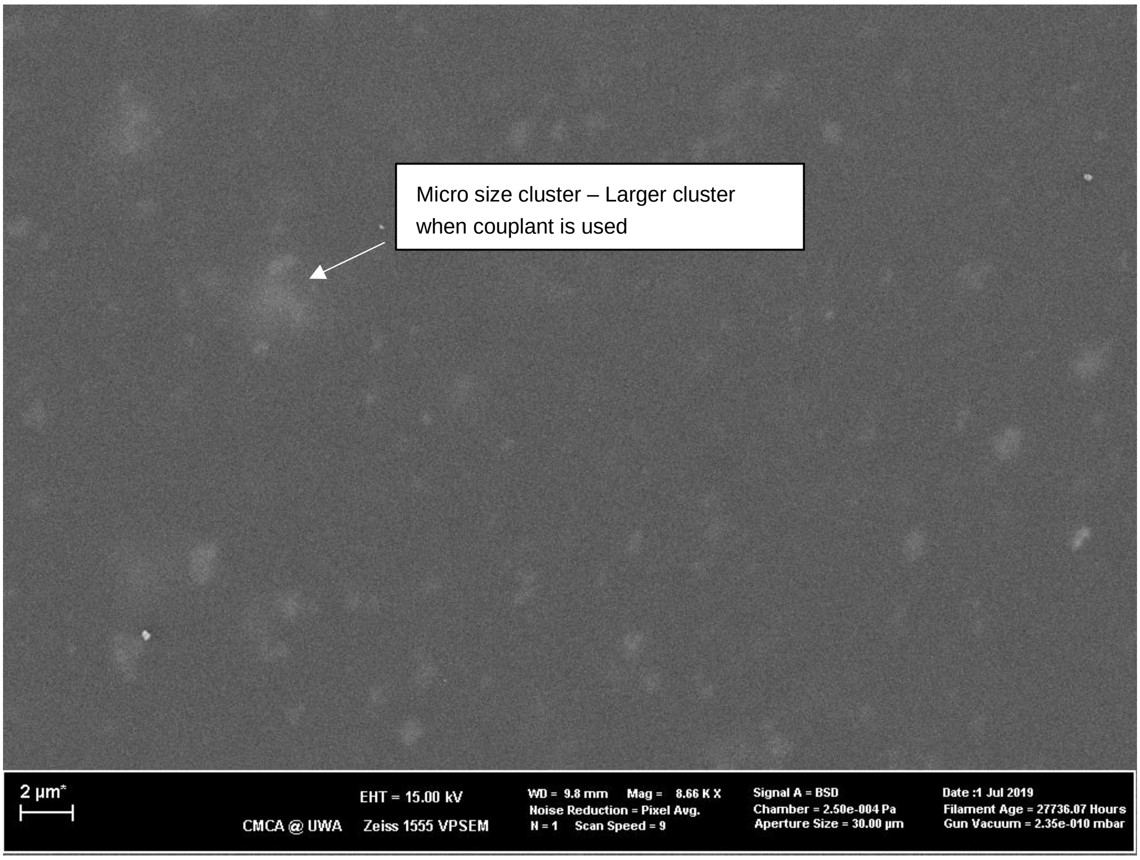

Micro size cluster – Larger cluster when couplant is used

Figure F 19: BSE image – frozen unaged C320 +2% NS (20nm + KH550 Couplant)

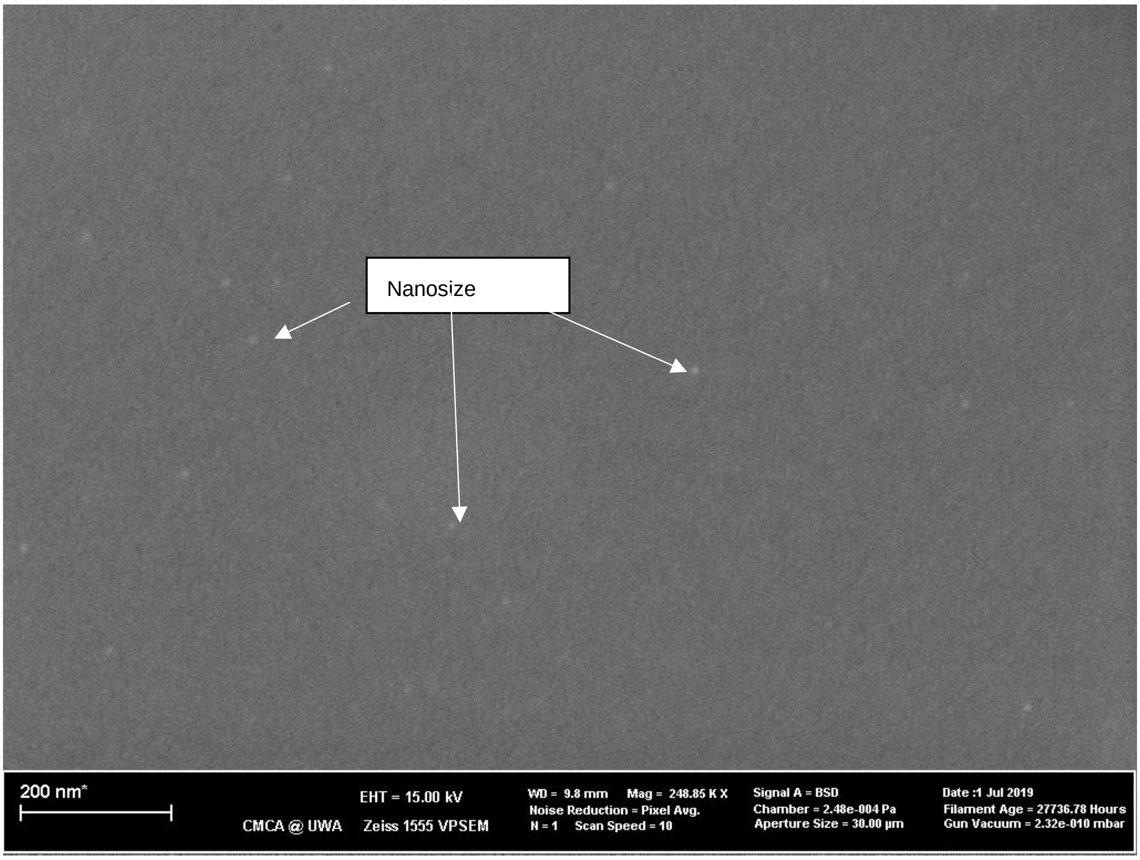

Figure F 20: SE image – frozen unaged C320 + 6% NS (20nm)

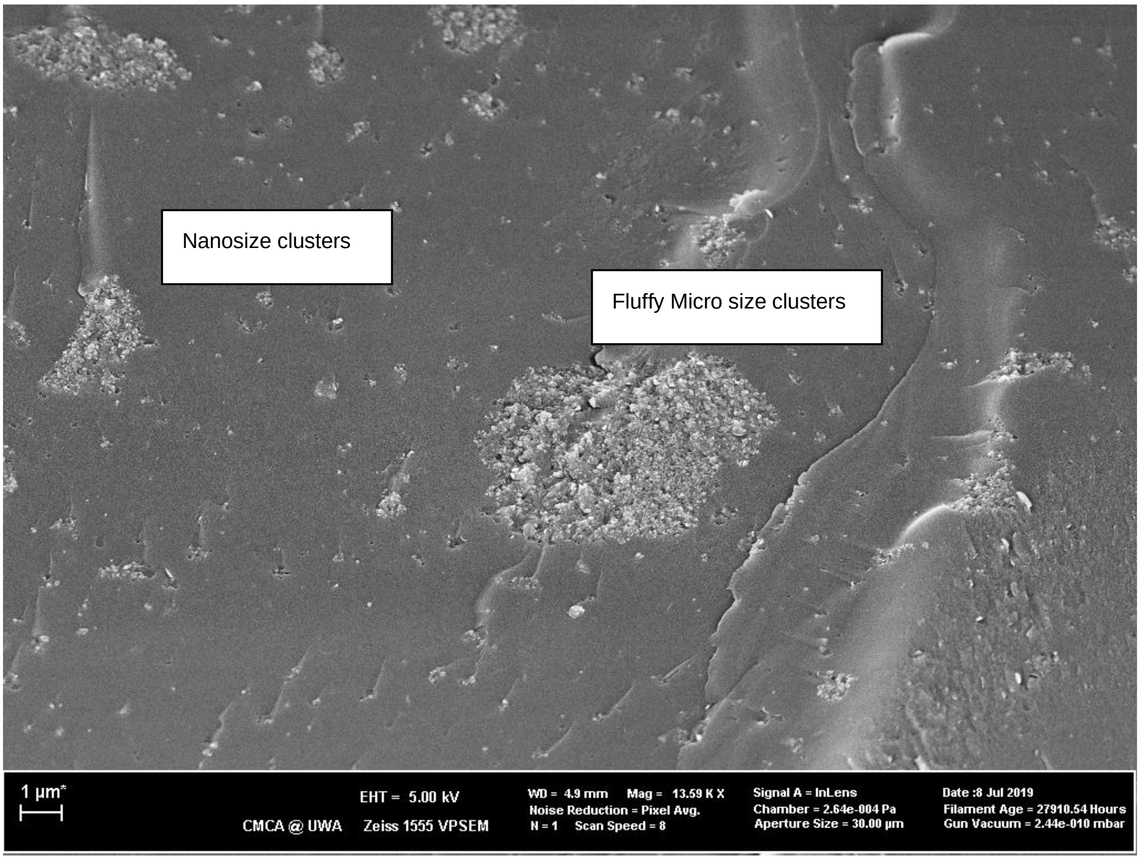

Figure F 21: SE image – frozen unaged C320 + 6% NS (20nm)

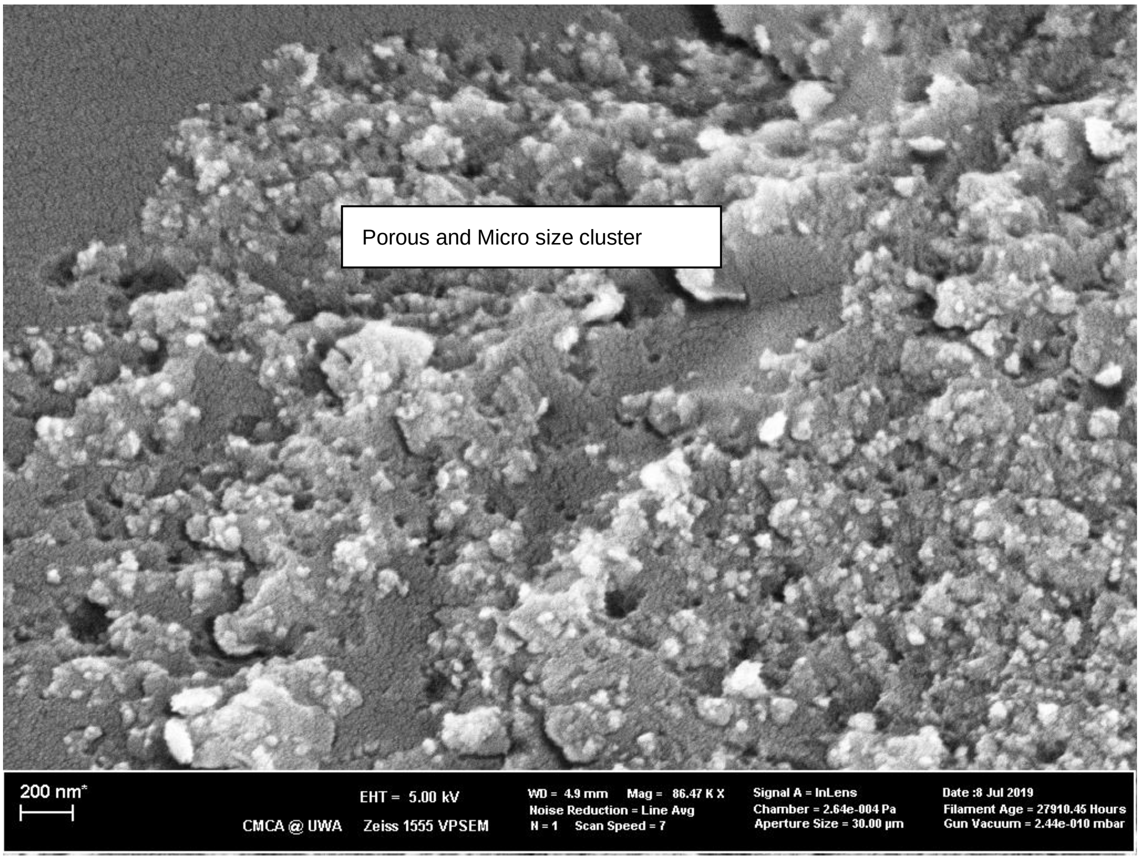

Porous and Micro size cluster

Figure F 22: SE image – frozen unaged C320 + 6% NS (20nm)

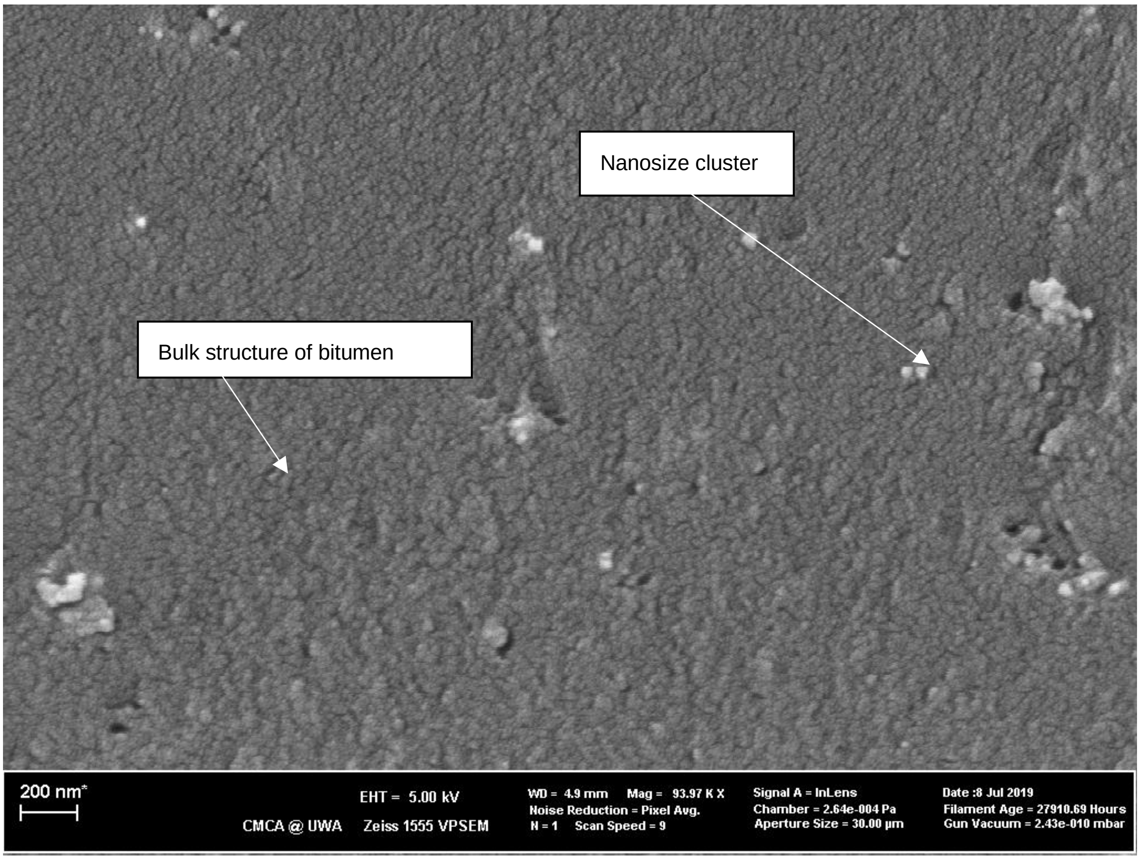
Nanosize cluster

Bulk structure of bitumen

Figure F 23: SE image – frozen unaged C320 + 6% NS (20nm + KH550 Couplant)

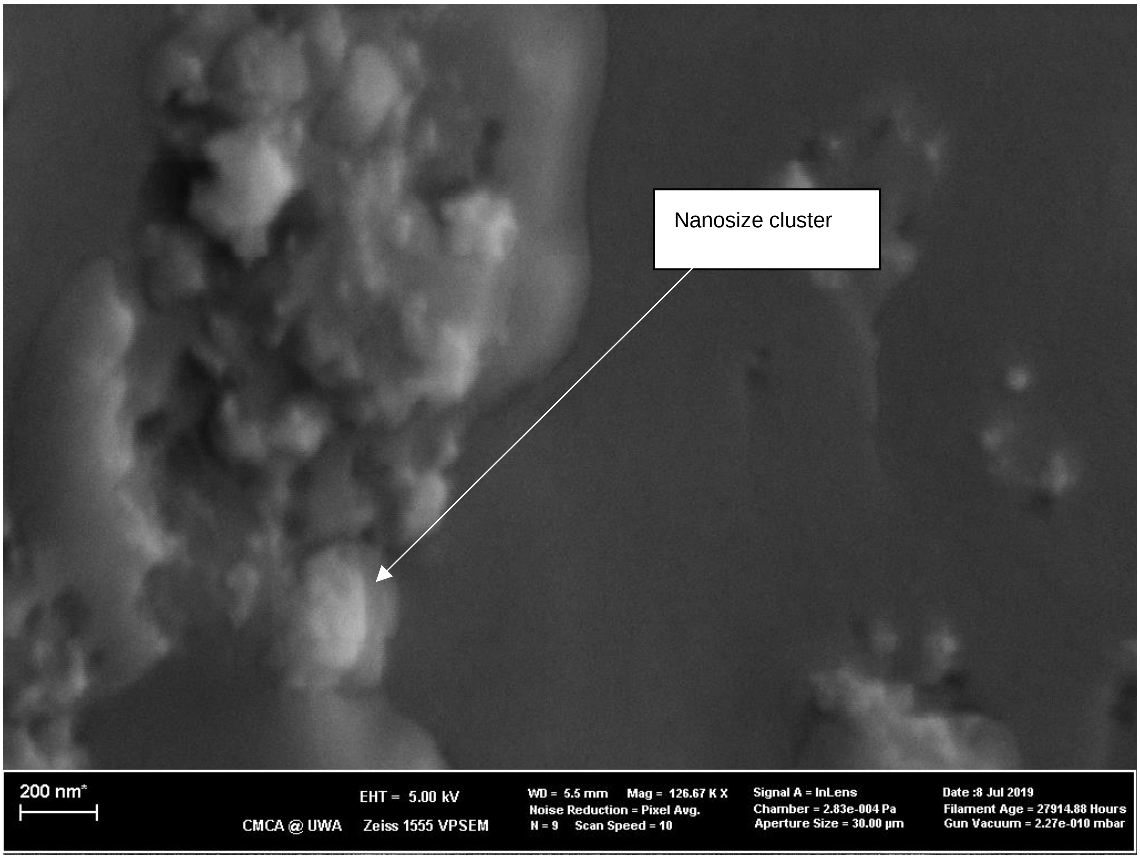

Figure F 24: SE image – frozen unaged C320 + 6% NS (60nm)

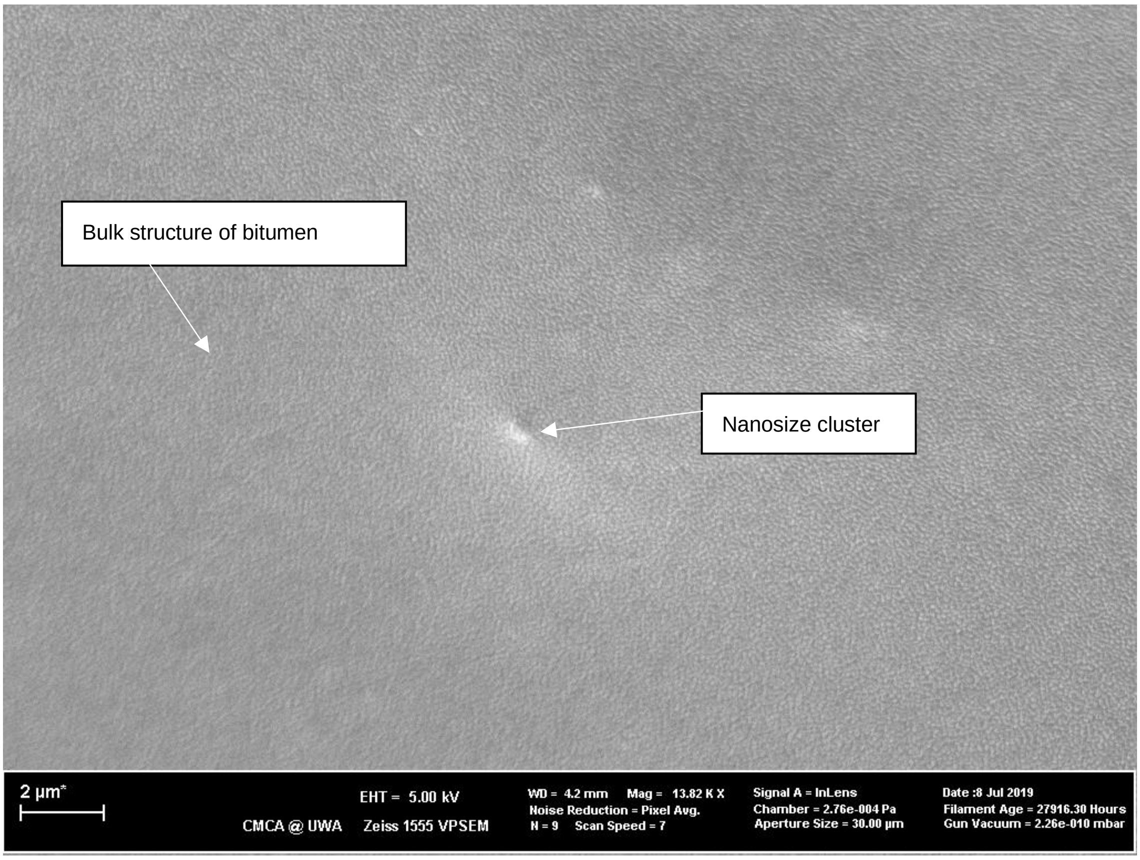

F.2 Wet Mixing images

Figure F 25: Agglomerates of asphaltenes with 6% of 60–70 nm NS (solved in unleaded petrol)

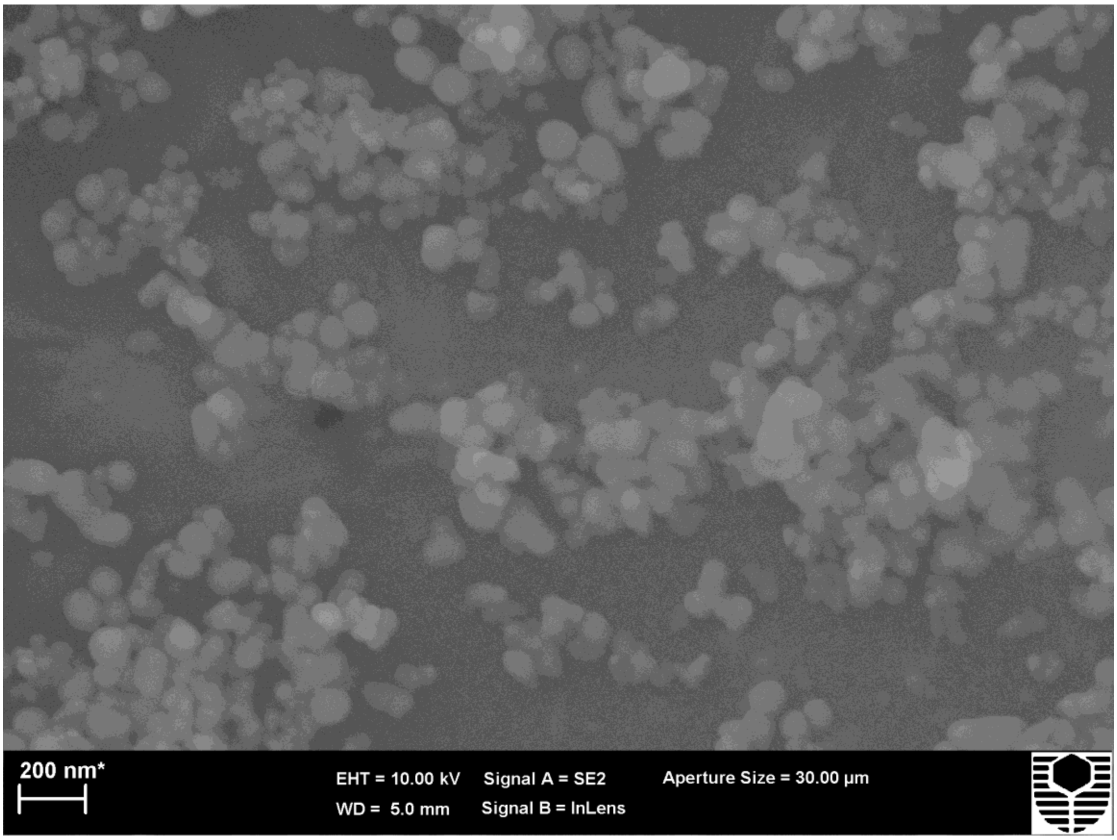

Figure F 26: Small agglomerates of asphaltenes with 6% of 60–70 nm NS (solved in unleaded petrol)

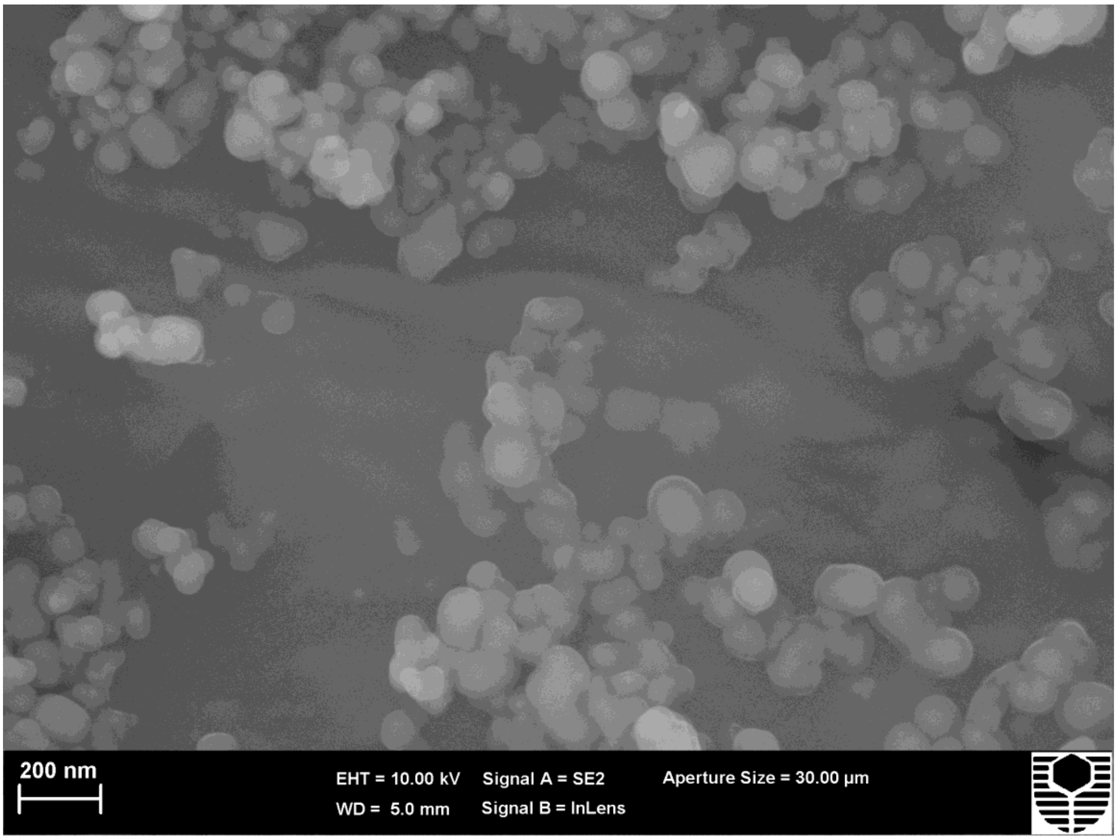

Figure F 27: SE image – frozen unaged C320 + 2% Ns (20nm + KH550 Couplant)

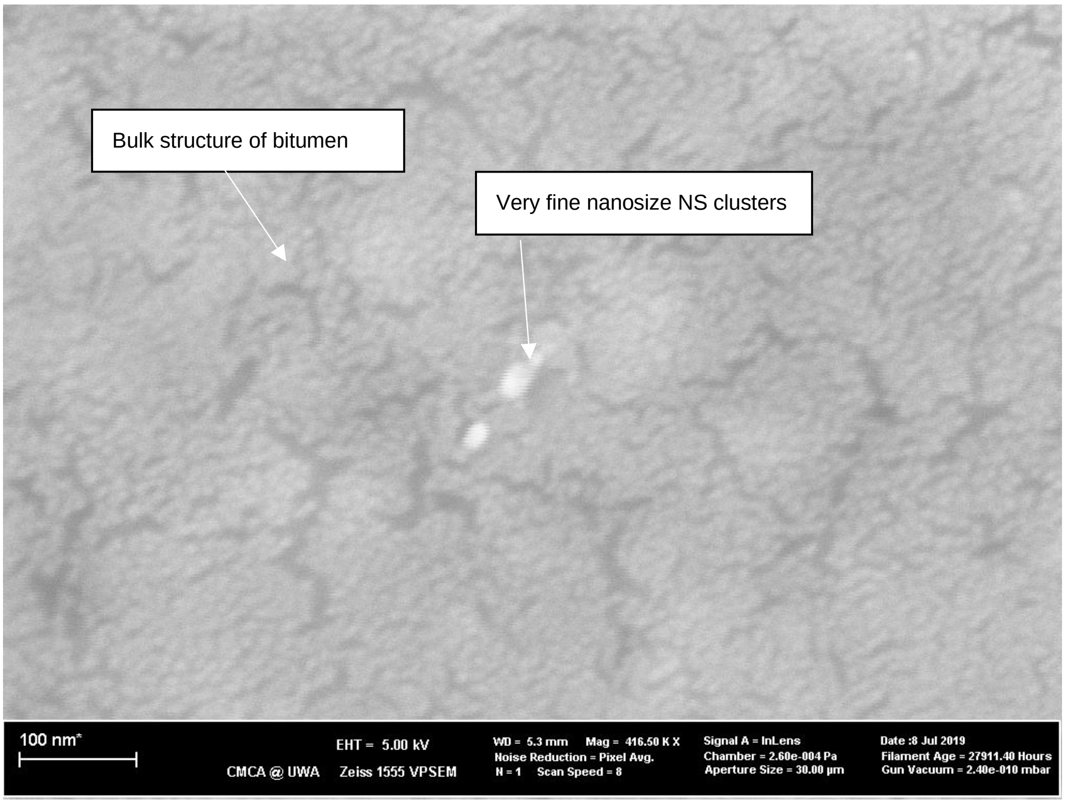

Figure F 28: SE image – frozen unaged C320 + 2% NS (20nm + KH550 Couplant)

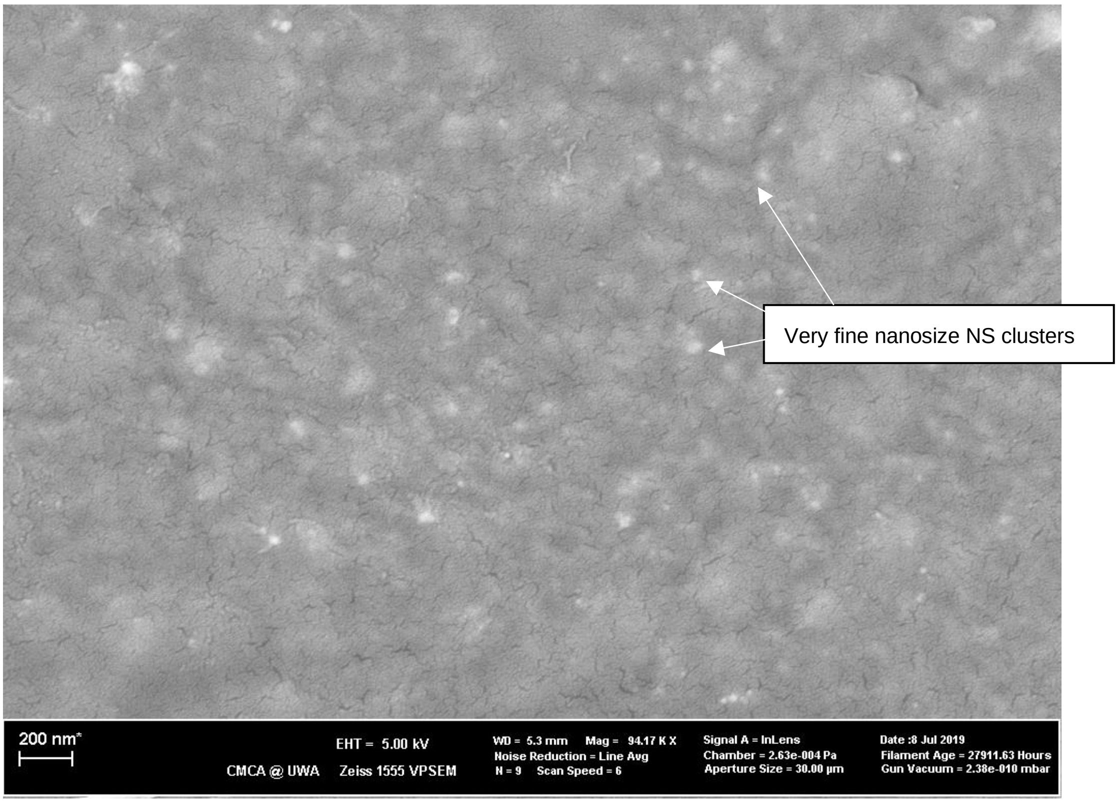

Figure F 29: EDS Map – X-ray map of frozen unaged C320 + 2% Ns (20nm + KH550 Couplant)

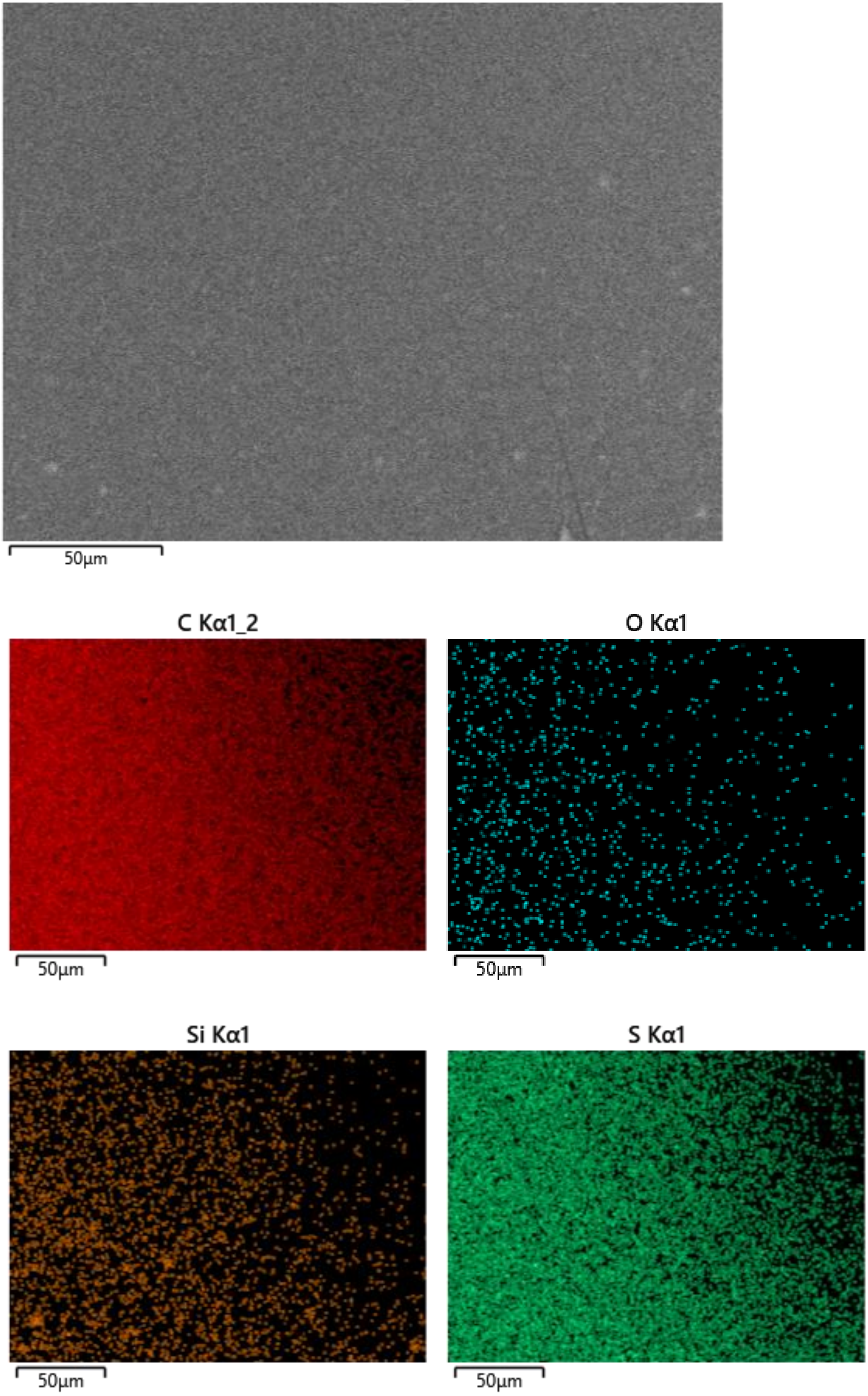

Figure F 30: SE image – frozen unaged C320 + 6% NS (20nm + KH550 Couplant)

Figure F 31: BSE image – frozen unaged C320 + 6% NS (20nm + KH550 Couplant)

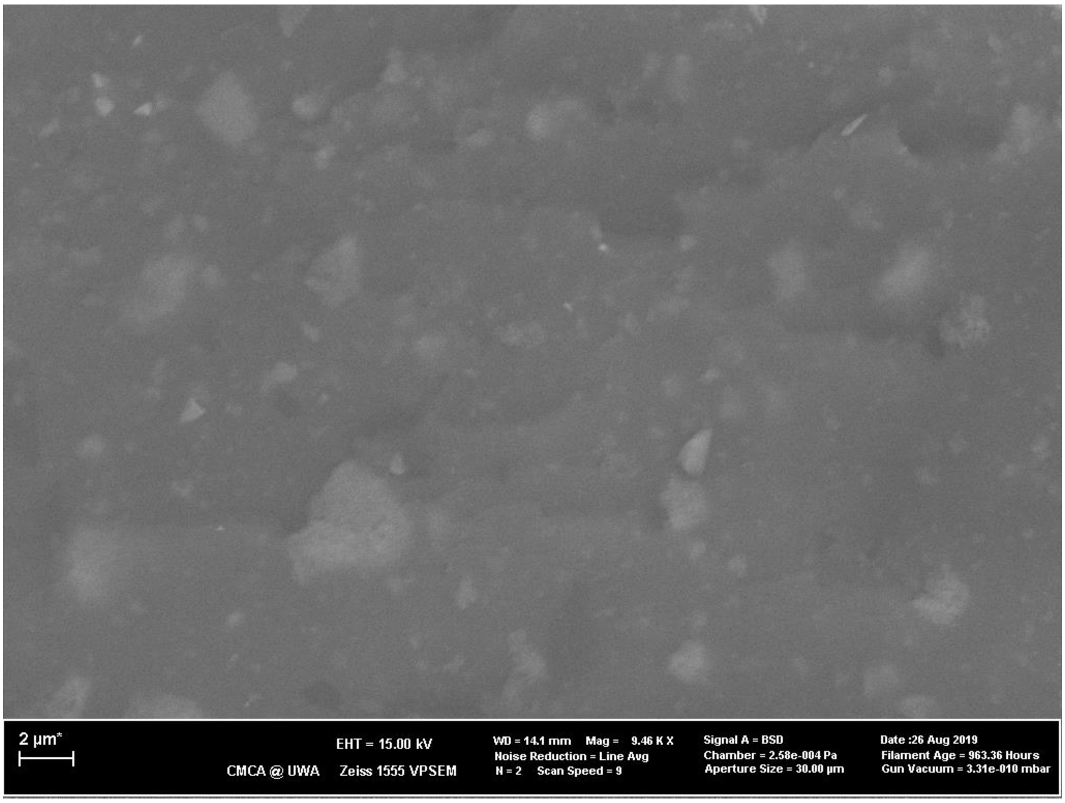

Figure F 32: BSE image – frozen unaged C320 + 6% NS (60nm)

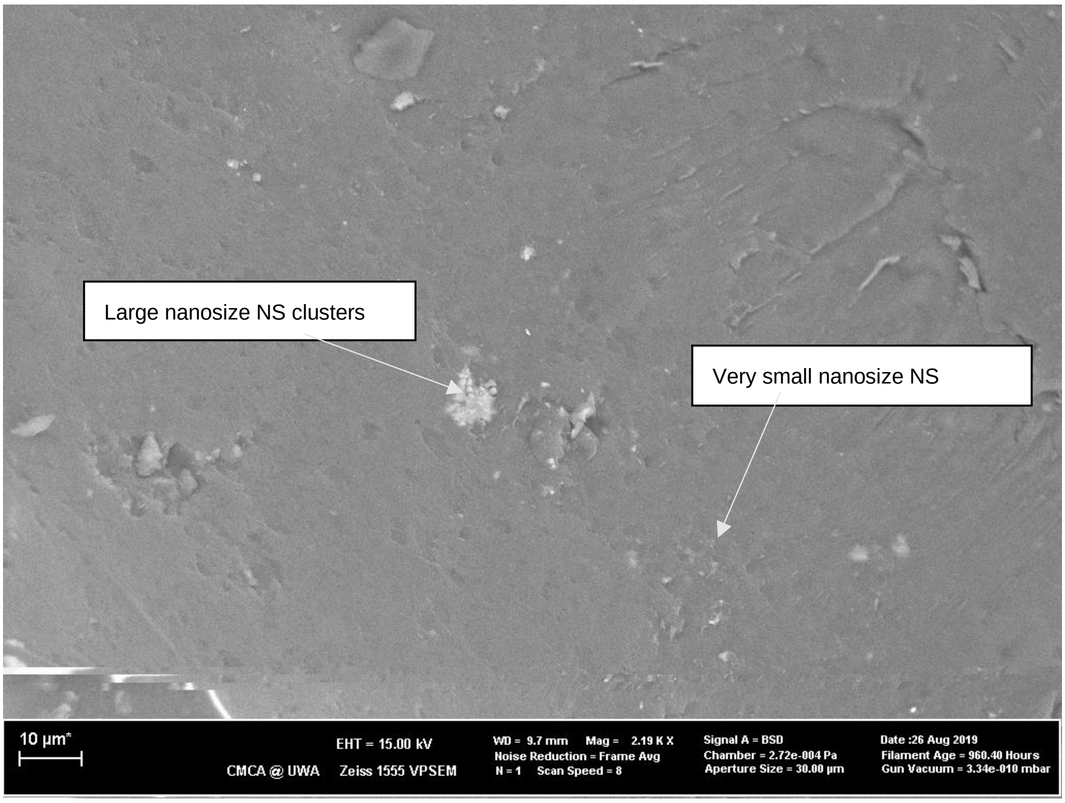

Figure F 33: SE image – frozen unaged C320 + 6% NS (60nm)

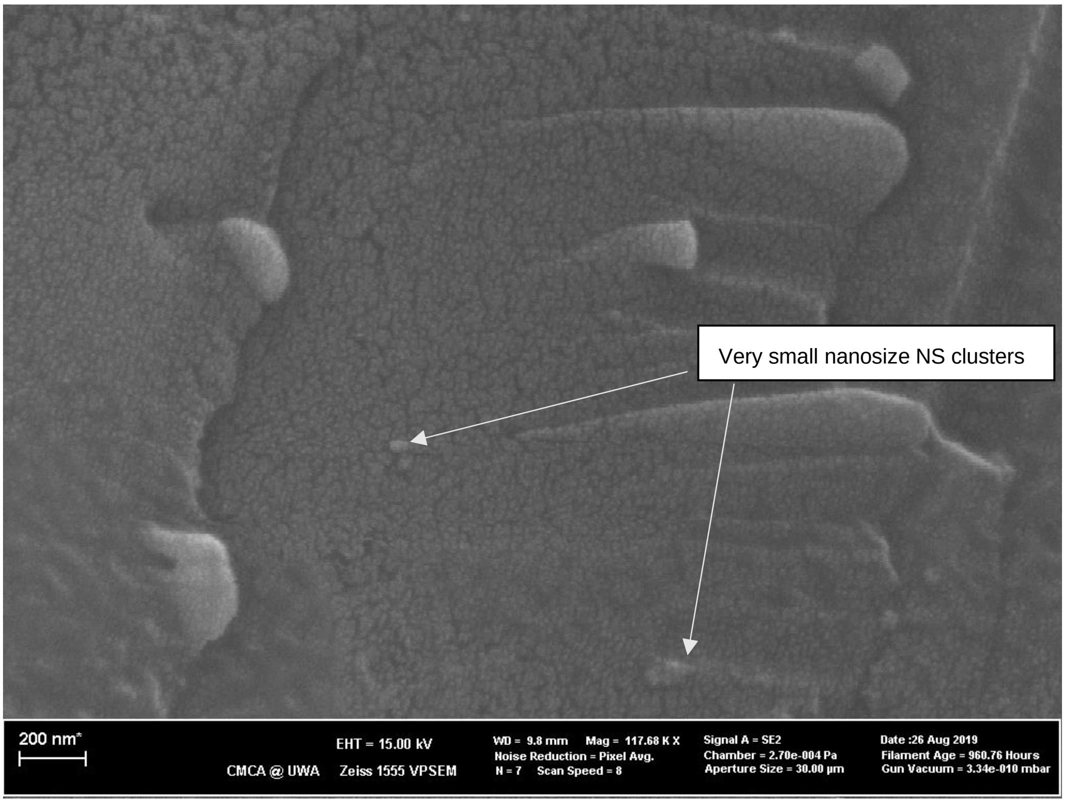

Very small nanosize NS clusters

Figure F 34: SE image – frozen unaged A15E

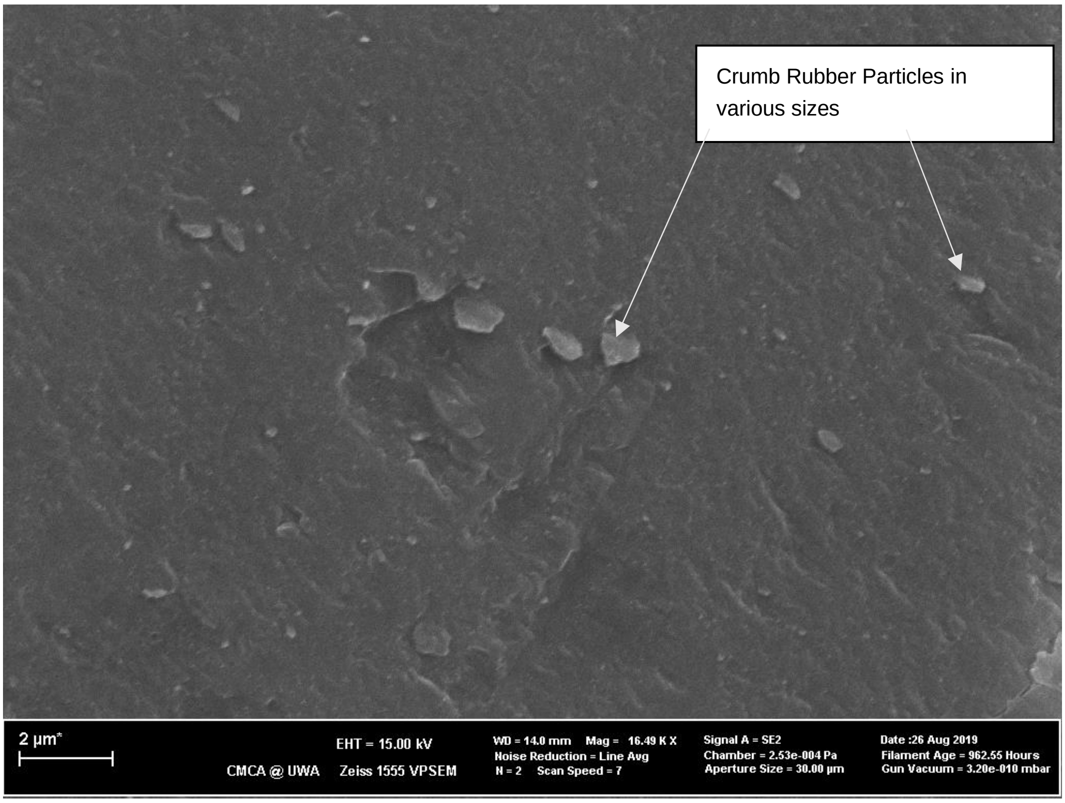

Figure F 35: BSE image – frozen unaged A15E